

EXPERIMENTS ON THE EFFECTS OF DILUTION AND FUEL
COMPOSITION ON IGNITION OF GASOLINE AND
ALTERNATIVE FUELS IN A RAPID COMPRESSION
MACHINE

By

Prasanna Chinnathambi

A DISSERTATION

Submitted to
Michigan State University
in partial fulfillment of the requirements
for the degree of

Mechanical Engineering - Doctoral of Philosophy

2019

ABSTRACT

EXPERIMENTS ON THE EFFECTS OF DILUTION AND FUEL COMPOSITION ON IGNITION OF GASOLINE AND ALTERNATIVE FUELS IN A RAPID COMPRESSION MACHINE

By

Prasanna Chinnathambi

In the first part of this work, ignition of methane-air mixtures under excess air dilution is studied. When excess air is used in SI engine operation, thermal efficiency is increased due to increase in compression ratio together with reduced pumping and heat losses. However, stable operation with excess air is challenging due to poor flammability of the resulting diluted mixture. Hence in order to achieve stable and complete combustion a turbulent jet ignition (TJI) system is used to improve combustion of lean methane-air mixtures. Various nozzle designs and operating strategies for a TJI system were tested in a rapid compression machine. 10-90% burn duration measurements were useful in assessing the performance of the nozzle designs while the 0-10% burn durations indicated if optimal air-fuel ratio is achieved within the pre-chamber at the time of ignition. The results indicated that distributed-jets TJI system offered faster and stable combustion while the concentrated-jets TJI system offered better dilution tolerance.

Knock in a SI engine occurs due to autoignition of the end gas mixture and typically occurs in the negative temperature coefficient (NTC) region of the fuel-air mixture. Dilution of intake charge with cold exhaust recirculation gases (EGR) reduces combustion temperatures and decreases mixture reactivity thereby reducing knocking tendency. This enables optimal spark timings to be used, thereby increasing efficiency of SI engines which would otherwise be knock limited. Effect of cold EGR dilution is studied in the RCM by measuring the autoignition delay times of gasoline and gasoline surrogate mixtures diluted with varying levels of CO₂. The autoignition experiments

in the RCM were performed using a novel direct test chamber (DTC) charge preparation approach. The DTC approach enabled mixture preparation directly within the combustion chamber and eliminated the need for mixing tanks. Effect of CO₂ dilution in retarding the autoignition delay times was more pronounced in the NTC region, while it was weaker in the low temperature and high temperature regions. The retarding effect was found to be dependent on both the octane number and the fuel composition of the gasoline being studied.

Finally, the effect of substituting ethanol(biofuel) in gasoline surrogates for up to 40% by volume is studied. Ethanol is an octane booster, but it blends antagonistically with aromatics such as toluene and synergistically with alkanes with respect to the resulting octane number of the blends. In order to study this blending effect, two gasoline surrogates containing only alkanes (PRF), and alkanes with large amounts of toluene (TRF) are blended with varying levels of ethanol. The ignition delay times of the resulting mixtures are measured in a rapid compression machine and kinetic analysis was carried out using numerical simulations. The kinetic analysis revealed that ethanol controlled the final stages of ignition for the PRF blends when more than 10% by volume of ethanol is present. However, in the TRF blends, toluene controlled the ignition until mole fractions of ethanol became higher than the toluene indicating the reason for the antagonistic blending nature. It was found that the RON values of the resulting blends matched the trend of the ignition delay times recorded at 740K and 21 bar compressed conditions. This enables qualitative assessment of the RON numbers for new biofuel blends by measuring their ignition delay times in the RCM.

ACKNOWLEDGEMENTS

First of all, I would like to thank my advisor Dr. Elisa Toulson for giving me this opportunity to pursue a PhD degree under her guidance. She has been a great supervisor and a mentor, always willing to share her knowledge and at the same time provoking me to come up with my own ideas. I also wanted to thank Dr. Sotirios Mamalis for encouraging and inspiring me to pursue a PhD degree. I am thankful for all the directions he has provided me so far. Many thanks to my colleagues and friends, Dr. Gerald Gentz, Dr. Masumeh Gholamishree and Bryce Thelen, for their guidance before and during my PhD program. I am extremely grateful to the members of my committee, Prof Indrek Wichman, Prof Farhad Jaberri and Prof Carl Lira, for their constructive feedback and guidance over all these years. A lot of credits go to Tom Stueken for his never-ending assistance with troubleshooting the RCM and sharing his knowledge about fittings, seals and everything else that moves in the ERC building. Without him maintaining the RCM in working condition would have been very difficult. Thanks to Kevin Moran and Brian Rowley for their generous assistance. And thanks to my teammates Chaitanya Wadkar and Berk Can Duva for being wonderful friends. I also would like to acknowledge Alexandra Ifkovits for her help with post-processing the RCM data and I wish her all the best for her future. Thanks to my past colleague Michael Bunce for being in touch and the insights he shared during these years. My greatest appreciation goes to my wife Sakthi Janaki and my parents for always supporting my endeavors. I am forever indebted to them for their efforts and sacrifices.

TABLE OF CONTENTS

LIST OF TABLES	viii
LIST OF FIGURES	ix
KEY TO ABBREVIATIONS.....	xvi
Chapter 1 Introduction and Background	1
1.1 SI Engines Current Trend and Outlook.....	1
1.2 Efficiency Gains Through Air Dilution	2
1.3 Ignition Enhancement – TJI	4
1.4 Knock in SI Engines.....	8
1.4.1 Knock and Fuel Chemistry	10
1.4.2 Oxidation Chemistry of Hydrocarbon	14
1.5 Cold EGR Dilution Strategy in SI Engines.....	19
1.6 Effects of Dilution and Fuel Composition on Ignition Delay Times of Natural Gas-Air Mixtures	21
1.7 Relationship Between Fuel’s Ignition Delay Times and Their Octane Numbers	25
1.8 Research Questions and Objectives	26
1.9 Outline of the Dissertation	27
Chapter 2 Experimental Setup	30
2.1 MSU Rapid Compression Machine.....	30
2.2 TJI Experimental Configuration.....	32
2.2.1 Testing Protocol for TJI Experiments.....	34
2.3 Experimental Configuration for Autoignition Studies	35
2.3.1 Testing Protocol for Autoignition Experiments.....	38
Chapter 3 Nozzle Design Evaluation for TJI Applications in Natural Gas Engines	39
3.1 Introduction	39
3.2 Research Questions	39
3.3 Background and Literature Review.....	40
3.3.1 Natural Gas as Fuel for Heavy Duty Applications	40
3.3.2 Ultra-Lean Burn Strategy for Natural Gas Engines using TJI.....	42
3.3.3 Prechamber Ignition for Natural Gas Engines	45
3.4 Experimental Setup	47
3.5 Testing Methodology	48
3.6 Nozzle Configurations.....	49
3.7 Results and Discussions	51
3.7.1 Main Chamber Pressure Analysis.....	51
3.7.2 High Speed Image Analysis.....	58
3.7.3 Image Analysis Methodology - Flame Area and Edge	61
3.8 Chapter Summary.....	65

Chapter 4 Performance Metrics for Fueled and Unfueled Turbulent Jet Igniters in a Rapid Compression Machine	67
4.1 Introduction	67
4.2 Research Questions	67
4.3 Background and Literature Review.....	68
4.4 Testing Strategy.....	70
4.5 TJI Nozzle Descriptions	73
4.6 Results and Discussions	75
4.6.1 Passive TJI images	75
4.6.2 Active TJI images	76
4.6.3 Flame Area Analysis.....	79
4.6.4 Jet Penetration Analysis	81
4.6.5 Prechamber Lambda Sweep.....	84
4.6.6 Effect of Initial Pressure on Jet Penetration.....	85
4.6.7 Main Chamber Pressure Analysis	86
4.6.8 Burn Rate Data.....	91
4.6.9 Characteristic Times	98
4.7 Chapter Summary.....	110
 Chapter 5 Impact of CO₂ Dilution on Ignition Delay Times of Iso-Octane at 15% and 30% Dilution Levels in a Rapid Compression Machine	 113
5.1 Introduction	113
5.2 Research Questions	114
5.3 Background and Literature Review.....	114
5.4 Experimental Setup	118
5.5 Data Interpretation.....	120
5.5.1 Ignition Delay Definition	120
5.5.2 Measurement of Compressed Temperatures.....	120
5.6 Direct Test Charge Approach.....	123
5.6.1 Fuel Calibration	123
5.6.2 Mixture Preparation	124
5.7 Results and discussions	125
5.7.1 Validation with Other RCM Data	125
5.7.2 Effect of Equivalence Ratio	126
5.7.3 NTC Region Analysis.....	127
5.7.4 Delta Ignition Delay Times.....	128
5.7.5 Effect of CO ₂ Dilution at Fixed Equivalence Ratio.....	130
5.7.6 Pressure Dependence of NTC Region	131
5.7.7 Image Analysis.....	134
5.7 Chapter Summary.....	135
 Chapter 6 Impact of CO₂ Dilution on Ignition Delay Times of Full Blend Gasolines in a Rapid Compression Machine.....	 137
6.1 Introduction	137
6.2 Research Questions	138
6.3 Literature Review	139

6.4	Experimental Methodology.....	142
6.4.1	Mixture Preparation	142
6.4.2	Fuel Characterization and Handling	143
6.4.3	GCMS Study.....	143
6.5	Results and Discussions	147
6.5.1	Effect of Equivalence Ratio and Pressure.....	147
6.5.2	Effect of CO ₂ dilution and comparison with surrogate (iso-octane).....	150
6.5.3	Effect of Octane Number	156
6.6	Chapter Summary.....	159
Chapter 7 Impact of CO₂ Dilution on Ignition Delay Times of Multicomponent Gasoline Surrogates in a Rapid Compression Machine.....		161
7.1	Introduction	161
7.2	Research Questions	161
7.3	Literature Review.....	162
7.4	Test Data Interpretation.....	164
7.5	Surrogate Formulation.....	166
7.6	Results and Discussions	167
7.6.1	Effect of Equivalence Ratio and Pressure.....	167
7.6.2	Performance of Surrogates and Effect of Dilution	170
7.6.3	Effect of Octane Numbers	176
7.6.4	Impact of Dilution on First Stage Delay Times	180
7.7	Chapter Summary.....	183
Chapter 8 Effect of Ethanol Substitution on Ignition Delay Times and Ron Values for PRF and TRF Blends for Up To 40% by Volume		185
8.1	Introduction	185
8.2	Background and Literature Review.....	186
8.3	Research Questions	188
8.4	Methodology	189
8.5	RCM Test Conditions	191
8.6	Surrogate Composition.....	193
8.7	Simulations.....	194
8.8	Results and Discussions	196
8.8.1	RCM Experiments	196
8.8.2	HO ₂ ROP Analysis.....	209
8.8.3	Average Pressure Rise Rate (PRR) Analysis.....	211
8.9	Chapter Summary.....	214
Chapter 9 Summary and Conclusions		216
9.1	Recommendation for Future Work	220
APPENDIX.....		223
BIBLIOGRAPHY.....		228

LIST OF TABLES

Table 1-1- Components present in a typical commercial grade gasoline (~98 RON) at greater than 1% by weight [7].	13
Table 1-2- Types of elementary reactions and their meanings [50].	15
Table 2-1 RCM conditions used for achieving the target compressed condition.	36
Table 3-1- RCM experimental set-up.	48
Table 4-1- Overview of RCM experimental setup and initial conditions.	72
Table 4-2- Prechamber fueling strategy.	72
Table 8-1- RON, MON and sensitivity values of the surrogate blends used in this study.	190

LIST OF FIGURES

Figure 1-1 Illustration of TJI with a single orifice nozzle as visualized from a RCM experiment [36].	7
Figure 1-2 Plane of pre-chamber cavity and location of supporting hardware on a cylinder head b) Unburned hydrocarbon emissions (UHC) with different pre-chamber fuel [27] c) Optical visualization of gasoline combustion ignited by turbulent jets issued from pre- chamber (as viewed from bottom of the piston) [38].	8
Figure 1-3 Combustion parameters - normal vs knocking cycle [39].	10
Figure 1-4 Ignition delay times of stoichiometric n-heptane-air mixtures at various pressures conditions [48].	14
Figure 1-5 Possible pathways for low-temperature oxidation of hydrocarbons [51].	17
Figure 1-6 Ignition delay times and ON plotted for a) 835K and 20 bar b) 825K and 25 bar compressed conditions in a RCM for stoichiometric TPRF-air mixtures[61].	19
Figure 1-7 Ratio of specific heats as a function of the amount of dilution and temperature [62].	21
Figure 1-8 Ignition delay times of CH ₄ -air mixtures at 10 and 20 atm for stoichiometric conditions [71].	23
Figure 1-9 Ignition delay times of stoichiometric natural-gas-air mixtures (diamonds) vs methane-air mixtures (circles) [72].	25
Figure 2-1 Cross section of various chambers within the RCM test facility showing the TJI system installed.	30
Figure 2-2 RCM test facility at MSU showing the autoignition setup.	31
Figure 2-3 Optical imaging setup with high speed camera aligned in front of quartz window.	33
Figure 2-4 Enlarged view of RCM head fitted with optical window and TJI igniter.	34
Figure 2-5 View of RCM combustion cylinder with component locations and connections for autoignition studies.	37
Figure 2-6 View of RCM with stepped metal window used for increasing or decreasing TDC volume.	37
Figure 3-1 Exploded view of components used in the TJI igniter.	47
Figure 3-2 Sectional and bottom views of the nozzle configurations used in the TJI igniter with L ₁ =13.2mm, L ₂ =3.2mm and L ₃ =17.2mm.	50
Figure 3-3 Sample pressure trace indicating derived pressure quantities and timing of various events during RCM operation.	52

Figure 3-4 Experimental pressure traces for single jet nozzle configuration.....	55
Figure 3-5 Experimental pressure traces for diverging jets nozzle configuration.	55
Figure 3-6 Experimental pressure traces for converging jets nozzle configuration.....	56
Figure 3-7 Average experimental pressure trace for single jet, dual diverging and dual converging jets nozzle configurations.	56
Figure 3-8 0-10% mean burn durations for single jet, dual diverging and dual converging jets nozzle configurations.	57
Figure 3-9 10-90% mean burn durations for single jet, dual diverging and dual converging jets nozzle configurations.	57
Figure 3-10 RCM experiment pressure trace (blue) and rate of pressure change (pink) overlaid with high speed images at respective time interval.....	58
Figure 3-11- Montage comparing high speed images for single jet, dual diverging and dual converging jets nozzle configurations. Images within the orange dashed border are enhanced (equally) for better clarity.	60
Figure 3-12- Comparison for flame propagation pattern through extracted flame edges for single jet, dual diverging jets and dual converging jets nozzle configurations at $\lambda = 1.78$	64
Figure 3-13- Comparison of normalized flame area across jet configurations for $\lambda = 1.78$	65
Figure 4-1 Sectional and bottom views of nozzle configurations used in the TJI igniter for this study with $L_1=13.16\text{mm}$, $L_2=3.175\text{mm}$ and $L_3=17.22\text{mm}$	74
Figure 4-2 Cross sectional view of the TJI igniter installed in RCM head.....	74
Figure 4-3 High speed images showing mainchamber combustion in passive TJI mode for all five nozzles at $\lambda=1.5$. Images are enhanced for better visualization.	77
Figure 4-4 High speed images showing combustion in active TJI mode for global $\lambda=1.78$. Images are enhanced for better visualization.	78
Figure 4-5 Comparison of normalized flame area in active TJI mode for all nozzle configurations at $\lambda=1.78$	80
Figure 4-6 Comparison of normalized flame area in passive TJI mode for all nozzle configurations at $\lambda=1.5$	80
Figure 4-7 High speed images showing jet penetration and main chamber combustion for the large hole nozzle configuration at $\lambda = 1.00$	81

Figure 4-8 Normalized jet penetration values for the small hole nozzle (left) and the large hole nozzle (right) for active and passive TJI systems.....	83
Figure 4-9 Normalized jet penetration values for the diverging nozzles with the left plot corresponding to the left hole and the right plot corresponding to the right hole for the active and passive TJI systems.	83
Figure 4-10 Normalized jet penetration values for the converging nozzle for active and passive TJI systems.....	84
Figure 4-11 Normalized jet penetration curves for the diverging nozzle showing the effect of varying pre-chamber lambda for a fixed mainchamber $\lambda=1.8$	85
Figure 4-12 Normalized jet penetration curves for the diverging nozzle showing the effect of varying prechamber lambda and increasing mainchamber pressure for a fixed mainchamber λ of 1.8.	86
Figure 4-13 Main chamber pressure for TJI nozzles in the passive configuration at $\lambda=1$. The x-axis 0 ms corresponds to the spark discharge event.....	89
Figure 4-14 Main chamber pressure for TJI nozzles in the passive configuration at $\lambda=1.25$. The x-axis 0 ms corresponds to the spark discharge event.	89
Figure 4-15 Main chamber pressure for TJI nozzles in the passive configuration at $\lambda=1.5$. The x-axis 0 ms corresponds to the spark discharge event.....	90
Figure 4-16 Comparison of averaged main chamber pressure curves in the active TJI mode for up to a global lambda value of 2.48.....	90
Figure 4-17 Pressure for the small hole nozzle showing prechamber operation mode changing from passive to active (past $\lambda=1.5$) until lean limit is achieved.....	91
Figure 4-18 0-10% burn duration comparison for the passive TJI (no auxiliary injection) test points.	92
Figure 4-19 10-90% burn duration comparison for the passive TJI test points.	93
Figure 4-20: 0-10% burn duration comparison for the active TJI configuration.	94
Figure 4-21 10-90% burn duration comparison for the active TJI configuration.	95
Figure 4-22 0-10% burn duration comparison for the dual diverging nozzle in the active TJI configuration for fixed main chamber lambda and varying prechamber lambda. The x-axis indicates the prechamber lambda value.	97
Figure 4-23 10-90% burn duration comparison for the dual diverging nozzle in the active TJI configuration for fixed main chamber lambda and varying prechamber lambda. The x-axis indicates the prechamber lambda value.	97
Figure 4-24 Pressure and derivatives of the pressure curves illustrating inflection points during the jet ignition phase and the main chamber combustion phase for the diverging nozzle in active TJI mode.	99

Figure 4-25 The maximum values for the 1 st derivative of pressure during the jet ignition phase (1 st dP/dt) for the passive TJI mode.	102
Figure 4-26 The maximum values for the 1 st derivative of pressure during the main chamber combustion phase (2 nd dP/dt) for the passive TJI mode.	103
Figure 4-27 The maximum values for the 1 st derivative of pressure during the jet ignition phase (1 st dP/dt) for the active TJI mode	105
Figure 4-28 The maximum values for the 1 st derivative of pressure during the main chamber combustion phase (2 nd dP/dt) for the active TJI mode.....	106
Figure 4-29 Maximum values for 1 st derivative of the pressure during the jet ignition phase (1 st dP/dt) for a prechamber lambda sweep study in the active TJI mode.	107
Figure 4-30 The maximum values for the 1 st derivative of pressure during the main chamber combustion phase (2 st dP/dt) for a prechamber lambda sweep study in the active TJI mode.	108
Figure 4-31 Jet ignition duration measurements for the passive TJI mode.	109
Figure 4-32 Jet ignition duration measurements for the active TJI mode – prechamber lambda sweep study.....	110
Figure 5-1 Sample pressure and dP/dt curve (top) illustrating ignition delay definition and pressure traces showing experimental repeatability for various dilution levels (bottom).	122
Figure 5-2 Fuel injector calibration curve showing pulse width vs mass injected information.....	124
Figure 5-3 Results comparing several RCM ignition delay data for iso octane as reported in [157] overlaid with total ignition times form our current study at 20±0.6 bar compressed pressure.	126
Figure 5-4 Ignition delay times shown in Arrhenius form for $\Phi=0.6, 0.8, 1.0$ and 1.3 for 0%(upper), 15%(middle) and 30%(lower) CO ₂ dilution levels at compressed pressure of 20±0.5 bar....	129
Figure 5-5 Bar charts showing average increase in ignition delay times with increasing dilution using 0% dilution delay times as baseline @ T _c =800K.	130
Figure 5-6 Ignition delay times shown in Arrhenius form for 0%, 15%, and 30% CO ₂ dilution levels for $\Phi=0.6$ (8a), $\Phi=0.8$ (8b), $\Phi=1.0$ (8c) and $\Phi=1.3$ (8d) at compressed pressure of 20±0.5 bar.....	132
Figure 5-7 Ignition delay times at $\Phi=1.3$ (top) and $\Phi=1.0$ (bottom) comparing the effect of pressure on ignition delay times for 10±0.5 bar vs 20±0.5 bar.	133
Figure 5-8 Ignition delay times at $\Phi=1.3$ for 10±0.5 bar comparing the effect of dilution. Connecting lines not shown for the dilution cases due to long ignition times in the NTC region.....	133
Figure 5-9 High speed images illustrating autoignition events at $\Phi=1.0$ (top row) and $\Phi=0.5$ (bottom row). First frame corresponds to ~0.3ms before total ignition delay time and each frame is spaced 0.1ms apart.	135

Figure 6-1 Results from GCMS analysis showing normalized concentration values of n-alkanes in the gas phase sample of low RON fuel.	145
Figure 6-2 GCMS results showing normalized concentration values of n-alkanes measured in the gas phase sample of the high RON fuel.	146
Figure 6-3 Ignition delay times shown in Arrhenius form for high RON fuel (left column) and low RON fuel (right column) for 0% (upper), 15% (middle) and 30% (lower) CO ₂ dilution levels at a compressed pressure of 20±0.5 and 10±0.5 bar. Line type indicates different experimental sets.	149
Figure 6-4 Ignition delay times of high RON fuel (green) and surrogate (iso-octane) shown in Arrhenius form for 0% (circles), 15% (squares) and 30% (triangles) CO ₂ dilution levels for $\Phi=0.6$, $\Phi=1.0$ and $\Phi=1.3$ at a compressed pressure of 20±0.5 bar (column) and 10±0.5 (left column) bar. Line type indicates different experimental sets.	154
Figure 6-5 Ignition delay times of low RON fuel (red) and surrogate (iso-octane) shown in Arrhenius form for 0% (circles), 15% (squares) and 30% (triangles) CO ₂ dilution levels for $\Phi=0.6$, $\Phi=1.0$ and $\Phi=1.3$ at a compressed pressure of 20±0.5 bar (right column) and 10±0.5 (left column) bar. Line type indicates different experimental sets.	155
Figure 6-6 Ignition delay times of low RON fuel (red) and high RON fuel (green) shown in Arrhenius form for 0% (circles), 15% (squares) and 30% (triangles) CO ₂ dilution levels for $\Phi=0.6$, $\Phi=1$ and $\Phi=1.3$ at a compressed pressure of 20±0.5 bar (right column) and 10±0.5 (left column) bar. Line type indicates different experimental sets.	158
Figure 7-1 Sample pressure and dP/dt curve illustrating durations of ignition events.	165
Figure 7-2 Pressure traces showing repeatability and influence of CO ₂ dilution. Line type indicates different experimental sets.	166
Figure 7-3 Ignition delay times shown in Arrhenius form for high RON surrogate (left column) and low RON surrogate (right column) for 0% (upper), 15% (middle) and 30% (lower) CO ₂ dilution levels at a compressed pressure of 20±0.5 and 10±0.5 bar. Line type indicates different experimental sets.	169
Figure 7-4 Ignition delay times of fuels and their surrogates, iso-octane and multicomponent, (high RON-top, low RON-bottom) shown in Arrhenius form for 0% (circles), 15% (squares) and 30% (triangles) CO ₂ dilution levels for $\Phi=0.6$, $\Phi=1.0$ and $\Phi=1.3$ at compressed pressure of 20±0.5 bar (right column) and 10±0.5 (left column) bar. Line type indicates different experimental sets.	173
Figure 7-5 Ignition delay times of high RON fuel (green) and its surrogate (orange) shown in Arrhenius form for 0% (circles), 15% (squares) and 30% (triangles) CO ₂ dilution levels for $\Phi=0.6$, $\Phi=1.0$ and $\Phi=1.3$ at compressed pressure of 20±0.5 bar (right column) and 10±0.5 (left column) bar. Line type indicates different experimental sets.	174
Figure 7-6 Ignition delay times of low RON fuel (red) and its surrogate (blue) shown in Arrhenius form for 0% (circles), 15% (squares) and 30% (triangles) CO ₂ dilution levels for $\Phi=0.6$, $\Phi=1.0$ and $\Phi=1.3$ at compressed pressure of 20±0.5 bar (right column) and 10±0.5 (left column) bar. Line type indicates different experimental sets.	175

Figure 7-7 Ignition delay times of low RON surrogate (orange) and high RON surrogate (blue) shown in Arrhenius form for 0% (circles), 15% (squares) and 30% (triangles) CO ₂ dilution levels for $\Phi=0.6$, $\Phi=1$ and $\Phi=1.3$ at compressed pressure of 20 ± 0.5 bar (right column) and 10 ± 0.5 (left column) bar. Line type indicates different experimental sets.....	178
Figure 7-8 Average diluted ignition delay times of the high RON and low RON gasoline (top) and corresponding surrogates (bottom) normalized with their respective undiluted delay times for $\Phi=1$ at $P_c = 20\pm0.5$ with T_c chosen within the NTC region. X axis labels indicates compressed temperatures.....	179
Figure 7-9 Averaged first stage delay times (top) and total delay times (bottom) of fuel and surrogates at $T_c=750K$ and $P_c=20$ bar for various equivalence ratios.....	182
Figure 8-1 RON and MON trajectory extracted from [192] with the green line indicating the test conditions covered in this study.....	192
Figure 8-2 Volume fraction (top) and mole fractions (bottom) of various fuel components present in the PRFE mixtures and the TRFE mixtures tested in this study.....	194
Figure 8-3 Comparison of pressure from RCM experiment and CHEMKIN-PRO simulation for TRFE40-air mixture at stoichiometric conditions for $P_c=21$ bar and $T_c=736K$	196
Figure 8-4 Comparison of total ignition delay times from RCM experiments (filled circles), variable volume (dashed line) and constant volume (solid line) numerical simulations for PRF91 with varying ethanol % by volume.	197
Figure 8-5 Comparison of total ignition delay times from RCM experiments (filled circles), variable volume (dashed line) and constant volume (solid line) numerical simulations for TRF91 with varying ethanol % by volume.	199
Figure 8-6 Average IDTs obtained from experiments for PRF and TRF surrogates substituted with ethanol for up to 40% by volumes.	202
Figure 8-7 IDTs obtained from constant volume simulations for various PRF and TRF surrogates substituted with ethanol for up to 40% by volumes.....	202
Figure 8-8 RON vs IDT relationship obtained at $T_c=740K$ and $P_c=21$ bar for PRFE and TRFE mixtures. RON values, sensitivity values and ethanol % are shown for each data point. Note: Data shown for PRFE40 is at $T_c=750K$, $P_c=21$ bar.	204
Figure 8-9 OH consumption rate by fuel components at different temperatures at 80% of ignition delay time for PRFE10 (top), PRFE20 (middle) and PRFE40 (bottom).	207
Figure 8-10 OH consumption rate by fuel components at different temperatures at 80% of ignition delay time for TRFE10(top), TRFE20(middle) and TRFE40(bottom).	208
Figure 8-11 HO ₂ consumption rate by toluene and ethanol at different temperatures at 80% of ignition delay time for TRFE10(top), TRFE20(middle) and TRFE40(bottom).....	210

Figure 8-12 Average pressure rise rates (PRR) for all the tested fuels at CR9.6 (top) and CR13.8 (bottom).	213
Figure A-1 Bar charts showing average increase in ignition delay times with increasing dilution levels with 0% dilution delay times used as baseline with $T_c = 650\text{K}$ and 700K and $P_c = 20 \pm 0.5\text{bar}$. (Chapter 5)	224
Figure A-2 Bar charts showing average increase in ignition delay times with increasing dilution levels with 0% dilution delay times used as baseline with $T_c = 750\text{K}$ and 800K and $P_c = 20 \pm 0.5\text{bar}$.	225
Figure A-3 Bar charts showing average increase in ignition delay times with increasing dilution levels with 0% dilution delay times used as baseline with $T_c = 850$ and 900K and $P_c = 20 \pm 0.5\text{bar}$.	226
Figure A-4 Ignition delay times of anisole-air mixtures at stoichiometric condition and 20 bar compressed pressure. Preliminary experimental and numerical results for chapter 9	227

KEY TO ABBREVIATIONS

AFR	Air-Fuel Ratio
Ar	Argon
BDC	Bottom Dead Center
CAD	Crank Angle Degrees
CH ₄	Methane
CNG	Compressed Natural Gas
CO	Carbon Monoxide
CO ₂	Carbon Dioxide
CR	Compression Ratio
DTC	Direct Test Charge
EGR	Exhaust Gas Recirculation
EOC	End of Compression
GCMS	Gas Chromatography Mass Spectrometry
GDI	Gasoline Direct Injection
HAJI	Hydrogen Assisted Jet Ignition
HC	Hydrocarbon
H ₂ O	Water
H ₂ O ₂	Hydrogen Peroxide
JPIC	Jet Plume Injection Combustion
KLSA	Knock Limited Spark Advance
LAG	Lavinnia Aktyvatsia Gorenia (Avalanche Activated Combustion)
LNG	Liquid Natural Gas
LTC	Low Temperature Combustion
MBT	Maximum Brake Torque

MON	Motor Octane Number
N ₂	Nitrogen
NO _x	Oxides of Nitrogen
N ₂ O	Nitrous Oxide
NO	Nitric Oxide
NTC	Negative Temperature Coefficient
O ₂	Oxygen
OFR	Oxidizer Fuel Ratio
OH	Hydroxyl Radical
ON	Octane Number
PRF	Primary Reference Fuel
Q	Alkyl radical minus one H atom
R	Alkyl Radical
QOOH	hydroperoxyl alkyl radical
RON	Research Octane Number
RCM	Rapid Compression Machine
SI	Spark Ignition
TDC	Top Dead Center
TJI	Turbulent Jet Ignition
TTL	Transistor Transistor Logic
TWC	Three-Way Catalytic
UHC	Unburned Hydrocarbon Emission
VI	Virtual Instrument
λ	Relative Air-to Fuel Ratio: Actual/Stoichiometric

Chapter 1 Introduction and Background

Currently 95% of the energy used for transportation is provided by liquid fuels obtained from petroleum refineries out of which spark ignition (SI) engines, running on gasoline, account for about 35% of the global transportation energy [1]. Next generation SI engines are under more scrutiny than ever before due to the rising concerns over global warming due to CO₂ emissions. CO₂ emissions are a consequence of burning hydrocarbon (HC) fuels such as gasoline and emission reduction is possible only through increasing engine efficiency or by widespread adoption of alternative and carbon neutral biofuels [2,3]. The transition to biofuels has already begun with the incorporation of ethanol into gasoline, however, for the foreseeable future liquid fossil fuels will continue to remain the prime mover for transportation [4]. Also, alternative fuels such as natural gas are now cheaper due to the recent discoveries of shale gas reserves and remain a viable option in heavy duty transport with strong potential to replace diesel engines [5]. Hence next generation combustion technology development targets must include higher efficiency, reduced emissions, and with flexibility to use existing, alternative and non-petroleum-based fuels.

1.1 SI Engines Current Trend and Outlook

As mentioned above, engine efficiency is directly related to fuel economy and to CO₂ emissions. Techniques such as engine downsizing, gasoline direct injection (GDI) and exhaust gas recirculation (EGR) currently drives modern SI engine development [6]. Besides CO₂, emissions such as unburned hydrocarbons (UHC), carbon monoxide (CO) and nitrogen oxides (NO_x) contribute to environmental and health hazards and hence are regulated. SI engines are inherently less efficient than diesel engines for several reasons, including operating at lower compression ratios and increased pumping losses associated with throttling at lower loads. Reduction in

throttling losses can be addressed by boosted downsized engines although this is normally associated with reduced compression ratios due to the occurrence of knock, thereby limiting further efficiency gains. Moreover, in order to realize the full potential of boosted downsized engines, high octane fuels are required. The usage of high-octane fuels results in additional expenses for consumers and such fuels tend to have reduced well to wheel efficiencies when compared to their lower octane counterparts [7]. Dilution of the intake charge either by supplying excess air or using EGR can help address pumping losses since the load can be controlled with diluent concentration instead of throttling [8]. Air and EGR dilution is also known to reduce knocking tendency in engines as they add an inert component to the mixture [9,10].

1.2 Efficiency Gains Through Air Dilution

The lean burn concept involves the addition of excess air (when compared to the stoichiometric condition) to the same amount of fuel. This concept enables a similar amount of air to enter the engine at both lower and higher load points and as a result, the pumping work reduces since load is limited by the amount of fuel[11]. Lean burn conditions typically occur at partial engine loads, while stoichiometric combustion is used at higher engine loads [12].

An important parameter that determined engine efficiency are the specific heats of the working fluid. Thermodynamic analysis of a spark ignited engine is based on the Otto cycle, and consequently, the increase of compression ratio increases the engine efficiency ($\varepsilon \approx 1 - 1/C_R^{k-1}; k = \frac{c_p}{c_v}$) [11,13]. Since burning lean contributes to an increase in the ratio of the specific heats of the mixture, it directly increases the efficiency [14]. It is possible to run engines lean with current GDI technology since the in-cylinder mixture preparation can be targeted in such a way that rich mixtures can be located around spark plug to aid in ignition but the overall mixture can

be operated lean [15]. One disadvantage of mixture stratification is the presence of pockets of fuel rich regions, which can increase NO_x emissions [16]. Also, UHC emissions can become an issue under highly stratified conditions resulting in very lean regions of air-fuel mixtures that remain unburned at the end of the cycle [17]. In addition, stratified combustion has been linked to increased soot emissions [18]. Homogeneous lean combustion ($1 < \lambda < \sim 1.5$) in modern SI engines has been proven to increase thermal efficiency, however, it produces elevated NO_x emissions, necessitating efficient but costly lean-NO_x aftertreatment systems since three-way catalyst systems are only effective at stoichiometric conditions. [11,19]. Operating in a homogeneous ultra-lean combustion mode ($\lambda > 1.5$) has been shown to both increase thermal efficiency and significantly reduce NO_x emissions due to the relatively cooler combustion with high levels of dilution [19,20]. Ultra-lean combustion has the potential to not only increase overall engine efficiency but also to enable a reduction in the scope of the lean-NO_x aftertreatment solution. The major limitation in developing lean and ultra-lean combustion systems is the less favorable ignition quality of the mixture and incompatibility with three-way catalyst systems. Reduced laminar flame speed with lean or dilute combustion strategies leads to combustion instabilities causing increases in HC emissions [21]. One method to overcome this is ignition enhancement, which involves increasing the ignition energy in order to improve the burning characteristics of the mixture. As a result ignition enhancement techniques with additional ignition energy or distributed ignition sources are required [22]. Technologies such as microwave spark ignition [23], plasma-assisted ignition [24], divided chamber stratified charge [2] and prechamber ignition systems are classified as advanced ignition systems. Among all of these systems, turbulent jet ignition (TJI), which is a type of prechamber ignition systems shows great promise in enabling low temperature combustion

(LTC), through both lean and/or dilute combustion while requiring minimum modifications to existing engine designs.

1.3 Ignition Enhancement – TJI

Lean burn engines generally require high ignition energy, long duration of ignition and a wide dispersion of ignition source in order to achieve fast burn rates [22]. SI engines with combustion initiated within prechamber cavities started appearing during first part of the twentieth century with the introduction of the 2-stroke Ricardo dolphin engine [30]. Jet ignition applications of IC engines have a long history and contain several documented studies. Around 1950, studies were conducted at the USSR Academy of Sciences Institute of Chemical Physics under the guidance of N.N Semyonov leading to development of Lavinnai Aktyvatsia Gorenia (LAG) or avalanche-activated combustion by Gussak [25]. The goal was to develop engines capable of achieving relatively high compression ratios without knock, using gasoline with an octane number around 70. Gussak's extensive studies revealed the importance of active radicals in the jet ignition process and lead to an engine that was mass produced and provided service for decades. Gussak's LAG engine has often been confused with the Honda CVCC (Compound Vortex Controlled Combustion) engine [29]. Although the Honda CVCC engine also falls into the category of prechamber divided chamber engines, there exists a fundamental difference between two. In the Honda case, a turbulent flame emerges out of the prechamber and propagates without interruption into the cylinder and is considered as a torch cell engine design [29]. This in contrast to the LAG engine where combustion is extinguished by shear at the exit of the relatively smaller orifice. The torch cell design idea was conceived to simplify the LAG design by removing the need for auxiliary prechamber fueling. Both the LAG and CVCC engines were eventually aborted due to complex three-valve mechanism and lack of flexibility.

Jet igniters fall under the category of the divided chamber stratified charge concept with the notable difference being the much smaller orifices for connecting the main chamber and prechamber combustion cavities [10]. TJI is an advanced pre-chamber type ignition system for a standard SI engine. The pre-chamber igniter is illustrated in Figure 1-1. The concept incorporates elements studied based on several pre-chamber research [26–29] including:

1. Small pre-chamber volume (<5% of main combustion chamber volume at TDC) for minimizing crevice volume and heat loss
2. Multiple-orifice nozzle connecting pre-chamber to main chamber
3. Small orifice diameter
4. Separate fueling strategies for pre-chamber and main chamber.

To avoid jet impingement on the main chamber wall, the prechamber volume has to be kept minimal. Similar to homogeneous charge compression ignition (HCCI), with jet ignition chemical kinetics plays a larger role in determining combustion.

Oppenheim et al. [30,31] miniaturized the valve operated prechamber of Gussak and developed a pre-chamber system called the Pulsed Jet Combustor (PJC). PJC exhibited twice the burn rates of an SI system. It was observed that if the PJC orifice diameter was too small, the jet penetration and hence the velocity gradient increased such that it could no longer ignite the lean mixture. Maxson [32] showed that the PJC process consists of three stages: the jet, the plume and the puff. The first is the formation of a jet plume, a pure fluid mechanical process uncoupled from the exothermic effects of chemical reaction. The plume is the most active stage of the system where vigorous combustion of the entrained charge takes place within the large-scale vortex structures in the main chamber. Maxson described the puff as a turbulent cloud of products surrounded by a

flame front. The PJC assembly can be installed in place of a 14 mm sparkplug and its prechamber is 0.5 mm^3 in volume. Tests results were published for single orifice and triple orifice configurations. The minimum nozzle diameter at which PJC would operate satisfactorily was found to be 2.5 mm [32].

During the 1990s, a Hydrogen Assisted Jet Ignition (HAJI) system was developed by Watson et al. at the University of Melbourne [14,33,34]. During HAJI operation, hydrogen accounting for 2% of the main fuel energy, was injected into the prechamber forming a locally rich and inflammable mixture near the spark plug [33] or glow plug [34]. Compared to SI engines, HAJI equipped engines showed higher thermal efficiency with lower CO and NO_x emissions.

A further application of flame jet ignition has been in controlling the ignition timing of HCCI engines, with studies completed by Murase and Hanada at Kyushu university [35]. In this case, the mixture was leaner than the lean flammability limit, hence flame propagation from the jet was not observed and instead the mixture homogeneously ignited following the initial jet penetration.



Figure 1-1 Illustration of TJI with a single orifice nozzle as visualized from a RCM experiment [36].

Although Kyaw and Watson [37] recognized that gasoline is not an effective prechamber fuel due to its narrow flammability limits, in order to make the TJI technology feasible for passenger vehicle applications, Attard and Blaxill [26] investigated gasoline (both in liquid and vaporized form) injected as the prechamber fuel in several prechamber designs. The location of prechamber and its components within an optical engine used by Attard [25] is shown in Figure 1-2a with Figure 1-2b indicating the ranges of λ (inverse of equivalence ratio) possible for different prechamber fuels in comparison with a spark-ignited engine. It must be noted that the performance figures for the vaporized gasoline case were higher than the liquid fueled case due to the poor mixture preparation in the small prechamber. Figure 1-2c shows the high speed images obtained from an optical engine when using gasoline was used as a fuel[38]. Some of the recent developments in TJI are further documented in the Chapter 3.

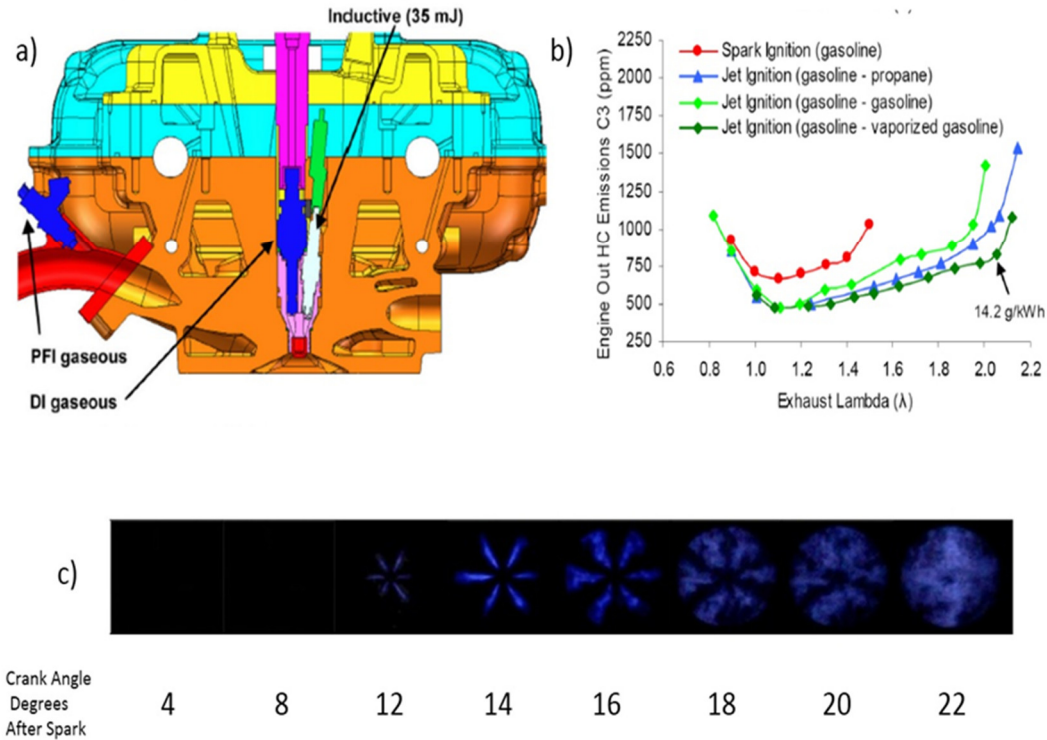


Figure 1-2 Plane of pre-chamber cavity and location of supporting hardware on a cylinder head
b) Unburned hydrocarbon emissions (UHC) with different pre-chamber fuel [27] c) Optical visualization of gasoline combustion ignited by turbulent jets issued from pre-chamber (as viewed from bottom of the piston) [38].

1.4 Knock in SI Engines

In cylinder combustion process within SI engines can proceed normally or abnormally. In the former case, the flame is initiated by a spark plug propagates with a normal velocity and consumes the entire pre-mixed charge. For the latter case, part of the charge undergoes spontaneous combustion resulting in abnormally high pressure rise rates. This non-uniform in cylinder pressure rise causes pressure waves or shock waves to propagate across the chamber, resulting in the chamber resonating at its natural frequency [39]. This event is termed knocking combustion in SI engines. Figure 1-3 compares a normal engine cycle with a knocking cycle. However, the upper

limit of this increase depends on the onset of knock. Knocking fundamentally limits SI engine efficiency as it determines the ceiling value of the compression ratio which in turn dictates the efficiency. It is now agreed that knocking is a result of autoignition of fuel air mixtures [40]. Autoignition is a chemical kinetic process and is determined by the chemical composition of the reacting mixture and thermodynamic condition inside the cylinder. There are other modes of abnormal combustion in engines such as low speed pre-ignition, however mode and occurrence of such abnormalities are different compared to a traditional knocking event in a normally aspirated engine. Knock intensity during engine testing is usually defined as the maximum amplitude of the fluctuating pressure signal. The engine is said to knock if the intensity reaches 20 kPa [6]. In-cylinder pressure also increases the severity of the knock [41], which is a limitation faced in modern downsized engines because for these engines turbocharging is employed to compensate for the loss of engine size, leading to higher pressures. Damage caused by knocking in SI engines includes piston crown melting, piston ring sticking, cylinder bore scuffing, piston ring-land cracking and cylinder head erosion [42]. The knock limit determines the engine's durability, fuel consumption, power density, noise and emission performance, gasket leakage and cylinder head erosion [39].

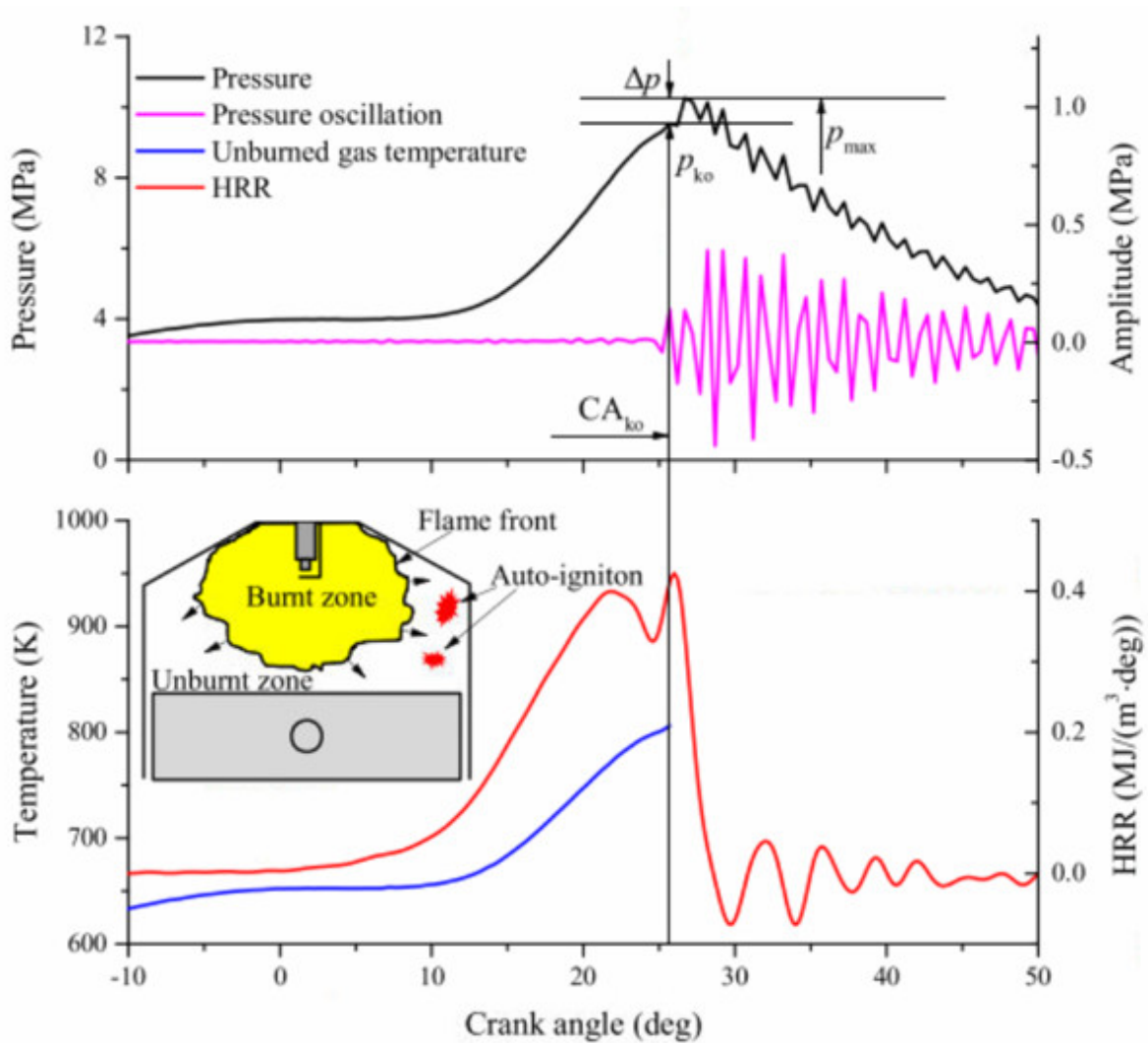


Figure 1-3 Combustion parameters - normal vs knocking cycle [39].

1.4.1 Knock and Fuel Chemistry

Gasoline fuels are a complex mixture of hundreds of hydrocarbons mostly spanning the C4-C10 range. Hydrocarbons present in a typical commercial grade gasoline are listed in Table 1.1 and these compounds make up more than 70% of the fuel by weight [7]. The major classes of components of gasoline are alkanes (paraffins), alkenes (olefins), cycloalkanes (naphthenes) and aromatics [1]. Octane number (ON) is associated with the knocking tendency of a fuel; the higher

the octane number the higher the knock resistance. Octane number also determines a parameter called knock limited spark advance (KLSA). If the engine is not run at its maximum load and efficiency due to knock, it is then said to be knock limited [6]. More knock resistant fuels can enable higher compression ratio and optimal spark timing even at higher loads, leading to better efficiency [7].

Having understood the importance of knock in SI engines, a standard testing methodology for identifying octane numbers of various fuels was put in place in 1922 by the corporate fuel research (CFR) committee [11]. Testing methodologies to determine two different octane numbers, the Research Octane Number (RON) and Motor Octane Number (MON), were detailed in the American Society for Testing and Materials (ASTM) documents in ASTM-D2699 [43] and ASTM-D2700 [44] respectively. The RON test is run at an engine speed of 600 RPM with intake temperature set at 52°C while the MON test is performed at 900 rpm and 149°C. A mixture of two pure components, iso-octane and n-heptane are used to establish a scale for octane number and are called the primary reference fuels (PRF). The octane number of a PRF mixture is determined by the volume percentage of iso-octane in the mixture. For example, a PRF mixture with 80% by volume of isooctane and the remaining (20% by vol.) n-heptane will have an octane number of 80. The ON of a given fuel is determined by the composition of PRF mixture that can produce the same knocking intensity under the fixed testing conditions [7].

For modern SI engines a fuel's knock/antiknock property is closely related to a parameter called sensitivity (S) and is defined as the difference between MON and RON [7]. Primary reference fuels (PRF) consist of a mixture of n-heptane and iso-octane and are said to possess zero sensitivity. It is evident that the PRFs only represent n-alkane and iso-alkane chemistry of a practical gasoline and hence as result they will have zero sensitivity. A practical gasoline will

match different PRF blends at different octane numbers. The actual antiknock quality of the fuel according to Kalgathi [7] is best described by the Octane Index (OI), where $OI = (1-K) RON + KMON = RON - KS$. In this equation K is an empirical constant that depends on the temperature and pressure history of the unburned mixture in the cylinder. For practical fuels the sensitivity is in the range of 9-13.

Amer et al [45] using a single cylinder engine study investigated the effect of fuel composition and inlet pressure on knock. They found at stoichiometric and boosted conditions reducing the compression ratio provided the highest potential for downsizing. Antiknock quality of the fuels enables higher IMEP, however the gain with increasing octane index (OI) decreases as the OI is further increased above ~100. It was found that there were fast diminishing returns on increasing RON above 100 as long as the sensitivity was 10 or greater [45]. For illustrating the effect of pressure over autoignition tendency, ignition delay times of n-heptane as a function of temperature for various pressure is shown in Figure 1-4.

The antiknock quality of a fuel depends upon its molecular structure [46]. Branched paraffins are known to have better antiknock quality than straight chain paraffins with equal number of carbon atoms (e.g., iso-octane vs n-octane) since knocking tendency increases with increasing carbon chain length [46]. Naphthene and aromatic components tends to have higher octane number but with increasing side chain length their reactivity and hence knocking tendency increases. [3] Addition of aromatics (such as Toluene) and olefins (such as 1hexene) increases the RON and the sensitivity of a base PRF mixture [47].

Table 1-1- Components present in a typical commercial grade gasoline (~98 RON) at greater than 1% by weight [7].

toluene	11.7
isopentane	11.43
m-xylene	6.93
n-butane	5.41
iso-octane	4.34
o-xylene	4.04
ethylbenzene	3.04
1,2,4-trimethylbenzene	2.69
p-xylene	2.58
2-methylbut-2-ene	2.3
2-methylpentane	2.07
n-pentane	2.02
isobutane	1.87
trans-pent-2-ene	1.7
m-ethyltoluene	1.65
2-methyl-1-ene	1.39
2-methylbut-1-ene	1.39
3-methylpentane	1.31
2,3,4-trimethylpentane	1.3
2-methylhexane	1.24
benzene	1

Heywood [11] presented a correlation for ignition delay time in order to further understand and predict knock behavior:

$$\tau = C_1 P^{-n} \exp\left(\frac{C_2}{T}\right)$$

In this equation C_1 , C_2 and n are fitted constants while P and T are pressure and temperature. The end gas reactions can be retarded by either decreasing the temperature or by chemical means, such as adding antiknock additives to the fuel or by dilution of the fuel air mixture. Autoignition chemistry of a fuel-air mixture is far more complex than can be described by a single relationship and more detailed mechanisms are explained in the next section.

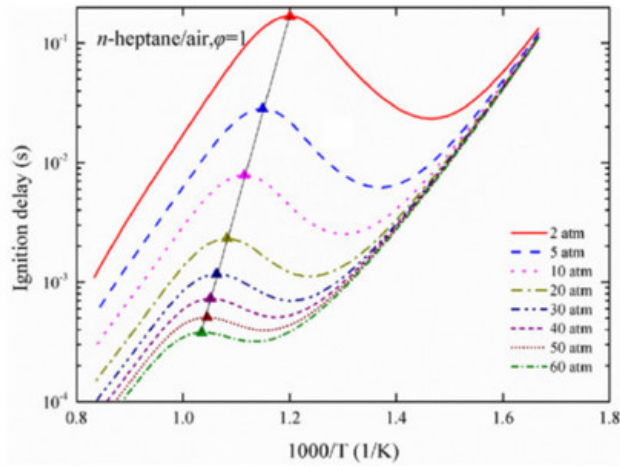


Figure 1-4 Ignition delay times of stoichiometric n-heptane-air mixtures at various pressures conditions [48].

1.4.2 Oxidation Chemistry of Hydrocarbon

A brief discussion regarding the low temperature oxidation chemistry for n-alkanes (R-H) is provided here since the chemistry is relevant for IC engine conditions. The foundation of modern hydrocarbon autoignition interpretation is based on the concept of free radicals and chain reactions

proposed by Semenov [49]. Free radicals have at least one unpaired electrons in the valence shell and hence are highly reactive. There exist several classes of elementary reactions through which free radicals are formed, propagated and removed in a reacting system. Such elementary reactions can be grouped as below,

Table 1-2- Types of elementary reactions and their meanings [50].

Primary Initiation	Radicals are produced from parent molecules
Chain Propagation	Number of radicals is unchanged
Chain Termination	Reduction or removal of radicals
Chain Branching	Increase in number of radicals
Degenerate Branching (Secondary Initiation)	Production of new radicals from stable intermediates

Unimolecular fuel decomposition reactions producing either two radicals or one alkyl radical R and one H atom serve as initiation reactions only at high temperatures, such as those encountered in shock tubes [51]. However, at low temperatures H atom abstraction from the parent molecule serves as an initiation step. Abstraction of the H-atom by an OH radical is largely responsible for radical pool generation, when compared to abstraction by an O₂ molecule since this process is highly endothermic and relatively slow [51]. H-atom abstraction is highly selective and can produce various isomers of R depending on the abstraction site with preference for more stable isomers[51]. In the case of iso-octane, primary, secondary or tertiary iso-octyl radicals are formed based on the abstraction sites [52]. At temperatures below 900K, the β -scission route for alkyl radicals becomes less important due to the high activation energies (27-40 kcal mol⁻¹) [51]. At low temperatures, the most important reaction is the addition of O₂ to the alkyl radical resulting in

the formation of RO₂. The peroxy radicals then undergo isomerization reactions through transition state rings resulting in the formation of hydro-peroxyl radicals (QOOH) [53]. In the case of n-heptane four RO₂ species can be formed by O₂ addition. There are 18 possible QOOH isomers produced by internal H-atom abstraction [51]. QOOH radicals continue to react with oxygen to form peroxy alkyl peroxide radicals (O₂QOOH). The O₂QOOH radicals tend to undergo internal isomerization producing ketohydroperoxide radicals [46]. This pathway eventually results in the formation of active OH radicals and other oxygenated radicals, hence accelerating the overall reaction rate. Therefore, the autoignition chemistry at these temperatures is primarily controlled by isomerization reactions of O₂QOOH and RO₂, along with the initial OH and parent fuel molecule reactions[54]. The mechanism of alkylperoxy and hydroperoxyalkyl radicals governs the low temperature chemistry and is very important for LTC engines [55] and understanding knocking in SI engines.

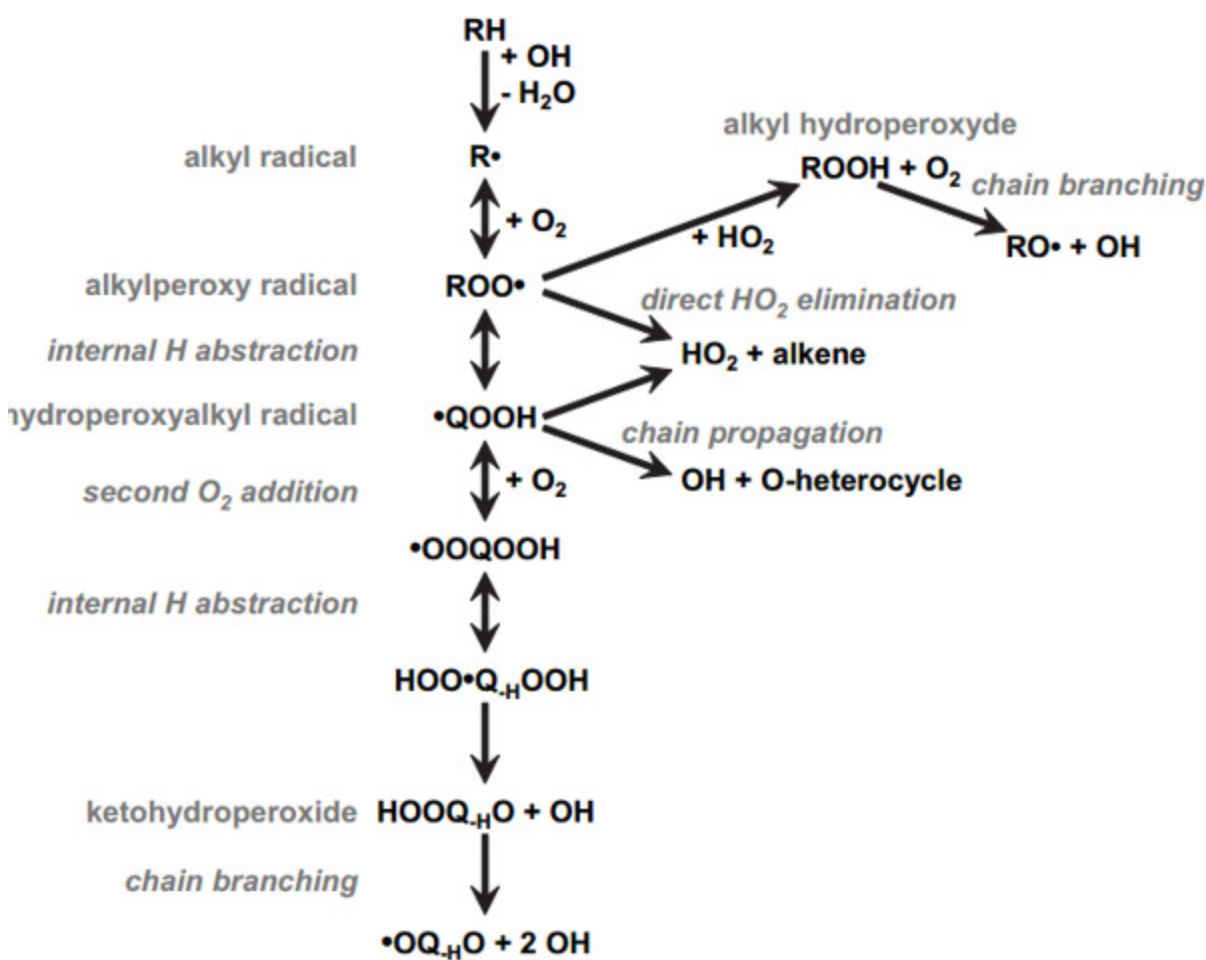


Figure 1-5 Possible pathways for low-temperature oxidation of hydrocarbons [51].

As temperature increases RO_2 dissociates into the conjugate olefin and HO_2 [51]. This pathway is highly pressure dependent and is quenched with increasing pressure [56]. HO_2 is a stable intermediate and its removal results in the formation of another unreactive intermediate H_2O_2 . The overall system reactivity is then decreased with the formation of HO_2 radicals favored in comparison to RO_2 chain propagation reactions. This decreased in reactivity manifests as the NTC region and is observed for many hydrocarbons. When the temperature increases to $\sim 1000K$, decomposition of H_2O_2 begins leading to the second stage ignition event [57].

It is possible to gain insights into octane number and octane sensitivity (OS) of fuel components by measuring their auto ignition times in a rapid compression machine (RCM). It has been that ignition delay times of high OS fuels are observed to decrease less rapidly with increasing pressure than ignition delay times of other fuels, making high OS fuels more resistant to knock and more desirable in turbocharged and high compression ratio engines. [58] Mittal et al. [59] suggested that autoignition phenomenon in modern engines takes place at temperatures between 775 and 900K, while the MON tests usually capture the chemical kinetics above 900K. As a general trend, fuels having higher sensitivity display lower reactivity at temperatures below 700K and higher reactivity in the NTC region. Singh et al. [60] concluded that ignition delay times at $T=750\text{K}$ and $P=25\text{bar}$ provide the best correlation with RON, and $T=825\text{K}$ and $P=25\text{bar}$ provide the best correlation with MON. An example of a relationship between ignition delay times and octane numbers is illustrated in Figure 1-6.

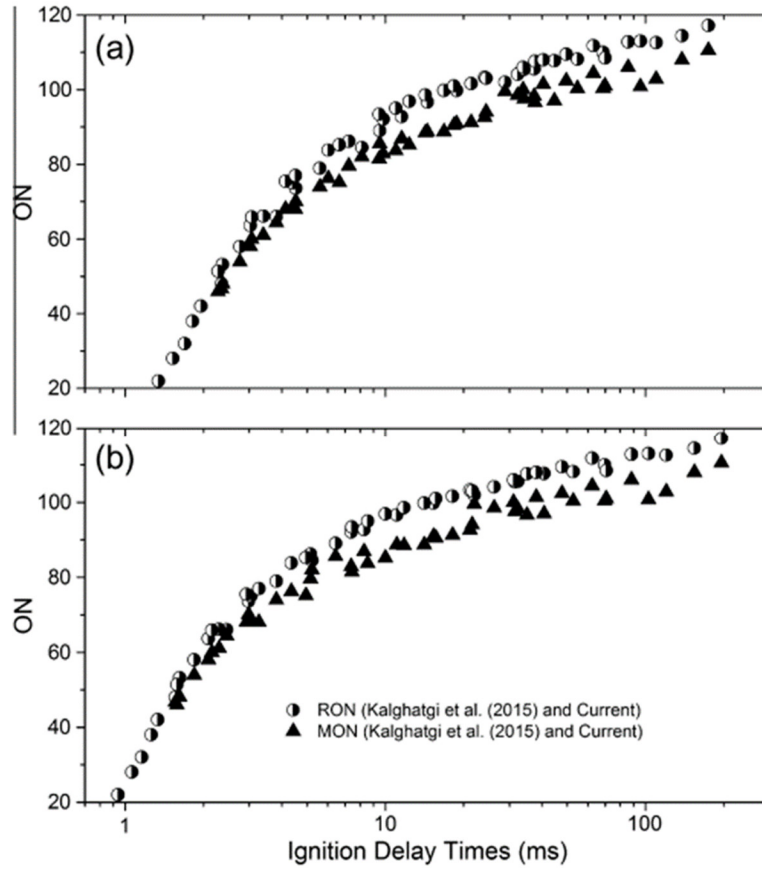


Figure 1-6 Ignition delay times and ON plotted for a) 835K and 20 bar b) 825K and 25 bar compressed conditions in a RCM for stoichiometric TPRF-air mixtures[61].

1.5 Cold EGR Dilution Strategy in SI Engines.

Using high octane fuel reduces knocking tendency but additional steps are required in petroleum refineries to improve the octane rating of the fuel. These steps include catalytic reforming, alkylation, isomerization etc. which increases cost and reduces conversion efficiencies [7]. Hence it is prudent to explore other strategies that can reduce knocking tendency while using a relatively lower octane fuel. One of the most effective strategies to avoid knock in SI engines is through dilution of the intake charge with cold EGR. The EGR technique was originally used in diesel engines to suppress thermal NO_x temperatures by limiting the combustion chamber temperature

[62]. In order to suppress knock the ignition delay times of the end gas mixture needs to increase so that the time available for deflagration is increased.

Inducting diluent such as EGR increases the total heat capacity [Figure 1-7] of the end-gas and reduces the temperature rise. Cold EGR is also an effective means to reduce NO_x and has been recently shown to help control particle soot emissions [63] in GDI engines. With respect to downsized engines, EGR is classified as either high pressure (HP-EGR) or low pressure (LP) EGR [64]. In the former case EGR is introduced before the inlet compressor, while in the latter case EGR is introduced after the compressor. Cold EGR increases inlet density and thus increases the volumetric efficiency of the engine. Lean burn combustion via air dilution is also an effective way to reduce NO_x but requires more costly lean NO_x aftertreatment since the three-way catalyst rapidly loses effectiveness with mixtures that vary from stoichiometric. However, when EGR is used as the diluent three way catalyst compatibility is retained since an overall stoichiometric composition can be maintained [65]. EGR is also an effective means to avoid fuel enrichment at high loads, which is particularly useful for modern downsized engines. Thermal loads for such engines become an issue at high loads and traditional fuel enrichment (excess fuel) is used to lower temperatures [66]. Grandin et al. [67] has demonstrated that cold EGR can be used as an effective replacement for enrichment at high loads since thermal loads are lowered by lower combustion temperatures.

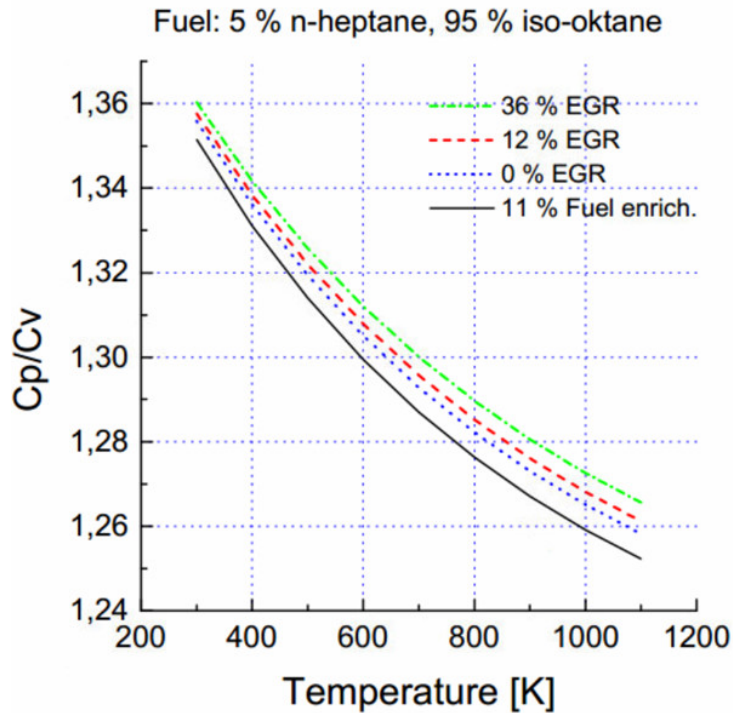


Figure 1-7 Ratio of specific heats as a function of the amount of dilution and temperature [62].

1.6 Effects of Dilution and Fuel Composition on Ignition Delay Times of Natural Gas-Air Mixtures

Nearly a dozen alternative fuels, either in production or under development, are suitable for use in alternative fuel vehicles and advanced technology vehicles [68]. Compressed natural gas (CNG) and liquefied natural gas (LNG) are considered alternative fuels under the Energy Policy Act of 1992 [68]. The U.S. Energy Information Administration estimates that as of January 1, 2015, there were about 2,355 trillion cubic feet (Tcf) of technically recoverable resources of dry natural gas in the United States. At the rate of U.S. dry natural gas consumption in 2015, the United States has enough natural gas to last about 86 years [69]. This is mainly possible due to advancements made in shale gas recovery, in which the U.S. has remained a forerunner. The abundance of shale gas

has led to a decrease in natural gas prices in the U.S and enabled a noticeable shift from coal to gas for electricity in recent years [7]. Using natural gas as a fuel in internal combustion engines provides energy security by reducing the dependence on foreign oil and has potential for lower emissions. This makes CNG and LNG attractive fuels for use in class 7 and 8 trucks requiring a greater range. Natural gas, when used as a transportation fuel, can help reduce CO₂ emissions due to the higher hydrogen to carbon ratio (H/C) of the fuel. The H/C ratio is increased from 1.8 to 3.7- 4.0, when changing the fuel from diesel to natural gas. Additionally, a high research octane number (around 130) [70] provides an increase in engine thermal efficiency by enabling higher compression ratios (CR) during spark ignition operation.

Methane, a surrogate for natural gas fuel, is considered for experiments using a TJI system in Chapters 3 and 4. More details about the practical implementation of natural gas fuel for TJI systems are covered in Chapter 3. The autoignition delay times of methane-air mixtures were not measured in the MSU RCM facility and hence a brief review covering ignition delay response of CH₄-air mixtures is given here and the effects of diluents and fuel composition on the ignition delay times of natural gas-air mixtures are discussed. Burke et al. [71] measured the ignition delay times of natural gas-air mixtures at 10 atm and 25 atm across various equivalence ratios in the temperature range of 900K to 1700K using an RCM and a shock tube. The recorded ignition delay times for 10 and 20 atm is illustrated in Figure 1-8. The authors concluded that the most promoting reaction for methane ignition was $\text{CH}_3 + \text{O}_2 \rightleftharpoons \text{CH}_2\text{O} + \text{OH}$ and the most inhibiting reactions were the recombination reactions leading to the formation of ethane. In a study by Gersen et al. [5], ignition delay times of CH₄ and CH₄-H₂ blends were measured in a rapid compression machine. In Gersen et al.'s [5] study CO was used as the diluent and delay times were measured for $\phi=0.5$ to 1.0 at pressures between 20 to 80 bar, and compressed

temperatures of 900-1000K. The authors observed that CO dilution did not alter the ignition delay times for up to 20% dilution levels.

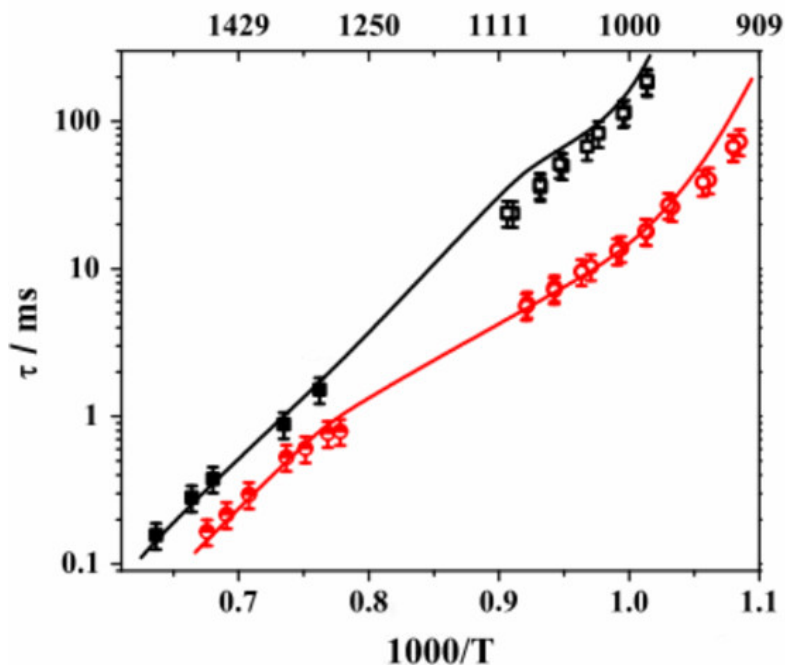
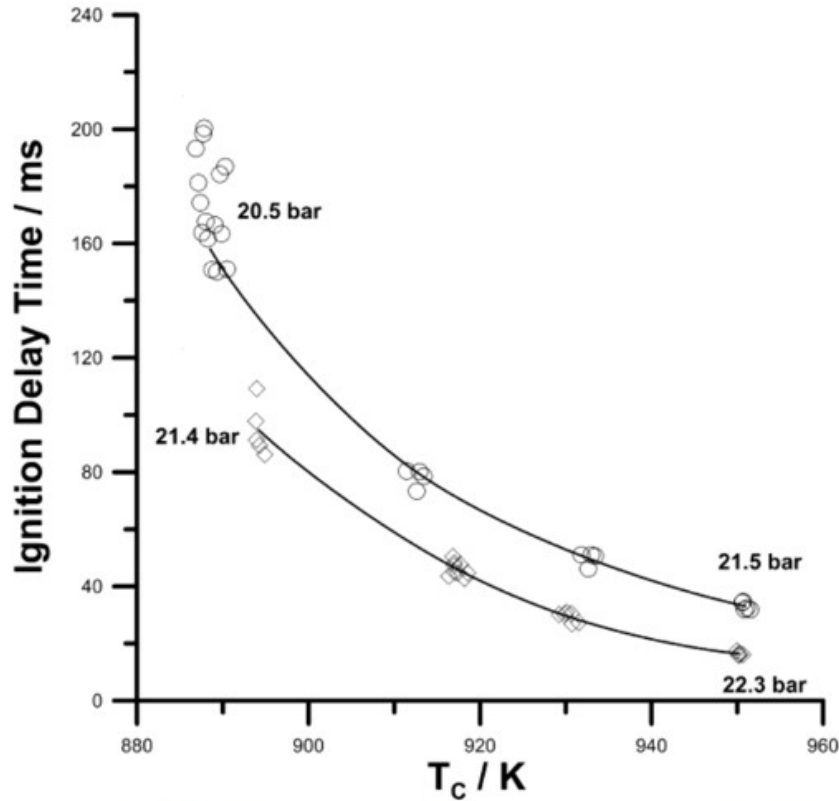


Figure 1-8 Ignition delay times of CH₄-air mixtures at 10 and 20 atm for stoichiometric conditions [71].

Natural gas is a blend of methane and other light hydrocarbons with the percentage of the individual components varying depending upon the source. Natural gas can be procured as a fossil fuel or can be obtained via a renewable route using biomass. The effect of fuel composition on ignition for different natural gas blends are discussed in several studies. In Figure 1-9, it can be seen that reactivity is increased when changing from pure methane to natural gas mixtures. In Chapter 3 and 4 only methane was used and hence increased reactivity should be expected if other natural gas components are present in the actual mixture. Methane does not show NTC behavior, as seen in Figure 1-8, unless blended with other alkanes like propane [72]. Heyene et al. [73] measured ignition delay times of natural gas for 850-925K

temperature range in order to validate a reaction mechanism for use in prechamber engines working in the autoignition mode. In a study by Healy et al. [74], NTC behavior was observed when 30% propane was substituted in the place of methane. In another study by the authors [75], 70%-methane and 30%-butane mixtures exhibited NTC behavior and the reactivity trends of the blend was more in line with that of pure butane. Yu et al. [72], studied methane and natural gas containing 89% methane, 9% ethane and 2% propane and the effect of CO, CO₂ and water dilution was also included in the study. Yu et al. [72] observed that the addition of CO did not impact the ignition delay times of NG-air mixtures and attributed this behavior to the chemical reactivity of CO since if CO was inert then the delay times would have increased. The addition of CO₂ (20% of fuel substituted with CO₂) did not affect the delay times. Similarly, H₂O present at 30% relative to fuel quantity did not affect ignition delay times. Ethanol is another alternative fuel and its presence in gasoline and gasoline-like fuels changes the ignition behavior of the fuel depending upon the amount of ethanol present. The compositional effect due to the presence of ethanol in gasoline will be explored in Chapter 8.



8.

Figure 1-9 Ignition delay times of stoichiometric natural-gas-air mixtures (diamonds) vs methane-air mixtures (circles) [72].

1.7 Relationship Between Fuel's Ignition Delay Times and Their Octane Numbers

Few studies have attempted to identify the link or relationship between octane numbers (ON) measured from a CFR engine and ignition delay times obtained from ideal reactor environments including RCMs. In the following studies, pressure and temperature conditions for which IDTs strongly correlates with RON and MON of fuel-air mixtures were proposed. Mehl et al. [76], completed a shock tube study in which they proposed a relationship between AKI (anti-knock index) and ignition delay time at conditions of 825K and 25 bar. Sarathy et al. [77] compared the ignition delay times of fuel-air mixtures from shock tube experiments and simulations with RON values. The authors observed a correlation between the two at 835K and 20 bar. Griffiths et al. [40] used an RCM to relate ignition delay times of PRF mixtures with varying RON values at a

compressed temperature of 900K. Here the compressed condition was chosen based on the argument that the end gas temperatures under knocking conditions for high RON fuels was found to be around 900K. Badra et al. [61] compared simulated ignition times for various TPRF mixtures and obtained correlations for RON and MON using fixed volume and variable volume simulations. In a recent study by Westbrook et al. [78] correlations between experimentally measured RON and MON values and simulated ignition delay times were made using pressure inputs derived from RON and MON test conditions. In a study by Singh et al. [60] it was observed that the simulated ignition delay times at $T=750\text{K}$ and $P=25$ bar provided the best correlation with RON while $T=825\text{K}$ and $P=25$ bar showed the best correlation with MON. These studies establish the fact that a link exists between ignition delay times measured in idealized reactors and ON measured from a CFR engine. This topic will be further explored and supported with experimental data from the MSU RCM facility in Chapter 8.

1.8 Research Questions and Objectives

In order to successfully implement an ultra-lean burn strategy using TJI, design consideration for the nozzles issuing the jets becomes crucial since proper jet characterization is required to overcome the poor ignition and flammability inherent to ultra-lean mixtures. Also, to understand the effect of CO_2 dilution on hydrocarbon-air mixtures in the context of knocking propensity, autoignition delay times, a fundamental chemical kinetic property, of these mixtures needs to be studied over a temperature and pressure range of interest. Finally, in order to understand the effect of fuel composition on autoignition delay times, the effect of substituting ethanol (biofuel) in gasoline surrogates for up to 40% by volume is studied. The work presented here attempts to address the research questions below and add to the knowledge regarding dilution and fuel composition effects that positively impact SI engine efficiency.

1. For a methane fueled TJI system, how does a single jet and/or converging jets compare with the burn durations and lean limit extension observed with diverging jets?
2. Performance metrics derived from main chamber pressure such as 0-10%, 10-90% burn durations, and the durations of the peak first and third derivative values of the pressure trace are compared for various TJI configurations. Can this information be used to evaluate and compare TJI performance in both the active and passive configuration?
3. Can the direct test chamber (DTC) charge preparation technique replace the traditional mixing tank-based charge preparation approach for ignition delay studies in an RCM?
4. What is the effect of CO₂ dilution on ignition delay times for full blend gasoline, and their simple and multicomponent surrogate-air mixtures?
5. Can CO₂ dilution provide any octane relaxation potential?
6. Ethanol is an octane booster that blends antagonistically with aromatics such as toluene and synergistically with alkanes. What are the resulting ignition delay times when ethanol is blended for up to 40% by volume to PRF (alkane only) and TRF (alkane aromatics) mixtures? What is the reason for the observed trends in terms of underlying fuel chemistry?
7. Is there a relationship between measured ignition delay times in the RCM and measured RON and MON values from a CFR engine?

1.9 Outline of the Dissertation

In this section a summary of the contents presented in the coming dissertation chapters are outlined. Chapter 2 provides an overview of the MSU RCM facility and modifications that were required to conduct TJI and autoignition experiments respectively. Chapter 3 focusses on comparing the burn

durations and lean limit extensions of an auxiliary injected TJI system with a single jet, dual diverging jets and dual converging jets. Chapter 4 extends on the work of Chapter 3 by analyzing the performance of TJI nozzles for both active (auxiliary-fueled) and passive (unfueled) prechamber configurations. Additional nozzle configurations are tested and new performance metrics from high speed images and pressure signal are derived and discussed. The suitability of these performance metrics for evaluating TJI configurations using the RCM is evaluated. In Chapter 5, the direct test charge (DTC) approach is introduced as a viable approach to test gasoline like fuels in a RCM and measure their ignition delay times. Using the DTC technique air-fuel mixtures of a required equivalence ratio are prepared directly in the RCM test chamber instead of using an external mixing tank. In addition, the effect of CO₂ dilution at 15% and 30% levels on ignition delay times of iso-octane mixtures is also studied. Chapter 6 adapts the experimental approach used in Chapter 5 for measuring ignition delays of full blend gasolines. In order to validate the DTC approach for full blend gasolines containing a spectrum of hydrocarbons, a GCMS study was performed and vaporization of high boiling point fuel components were confirmed. Ignition delay times of both CO₂ diluted, and undiluted fuel-air mixtures are measured and compared with a single component gasoline surrogate. In Chapter 7, the ignition delay times of multi-component gasoline surrogates are measured at both diluted and undiluted conditions. These surrogates were formulated to capture the reactivity of the gasolines studied in Chapter 6 and hence the ignition delay times were compared against the respective gasoline-air mixtures at both diluted and undiluted conditions. Additionally, advantages of CO₂ dilution in context to EGR dilution in SI engines is evaluated from the measured ignition delay times. In Chapter 8, the effect of blending ethanol with PRF-91 and TRF-91 surrogates, in terms of autoignition delay times, for up to 40 vol% of ethanol is studied. Kinetic analysis using chemkin-pro is performed for nine

different fuels. Also, the results are analyzed to identify any existing trends between the ignition delay times and the octane values of the resulting mixture.

Chapter 2 Experimental Setup

The experiments completed for this research were performed in a RCM which was designed, built and characterized at Michigan State University (MSU) [36,79–81]. Both TJI and autoignition studies reported in this work were completed using the same RCM with modifications to the cylinder head, ignition and fueling systems. Details regarding each configuration are explained in the respective chapters, while an overall overview is presented here as it applies to both configurations.

2.1 MSU Rapid Compression Machine

RCMs are traditionally used for chemical kinetic and ignition delay studies and can achieve engine relevant compressed conditions. By installing a spark plug and corresponding ignition hardware they can be modified for studying spark ignition processes in detail. A schematic of a cross-sectional view of the RCM is shown in Figure 2-1 while various components that makeup the RCM facility are shown in Figure 2-2.

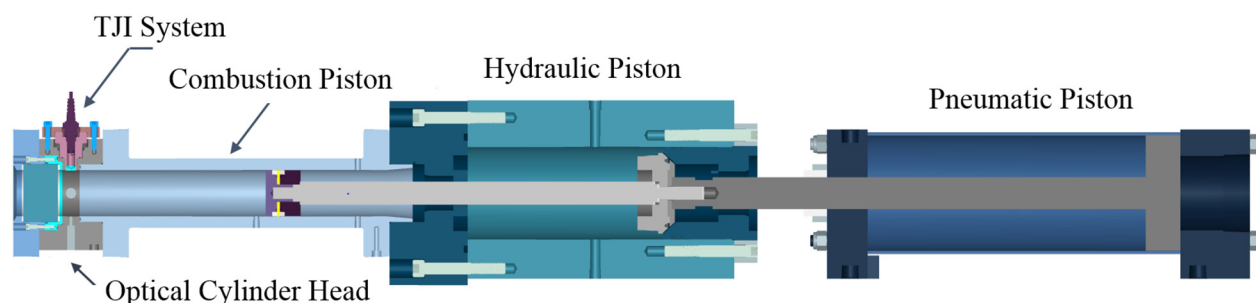


Figure 2-1 Cross section of various chambers within the RCM test facility showing the TJI system installed.

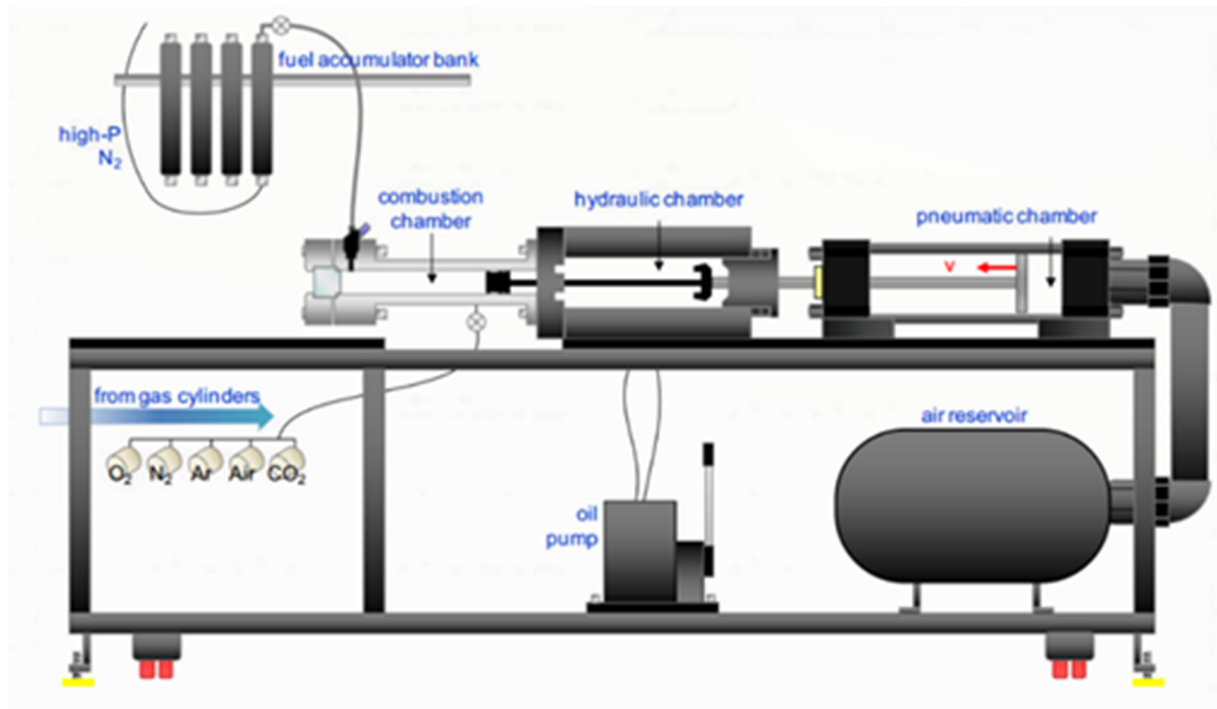


Figure 2-2 RCM test facility at MSU showing the autoignition setup.

The RCM consists of a combustion chamber in which a gas mixture is rapidly compressed by piston motion to engine relevant conditions. This piston is driven pneumatically and is decelerated and stopped hydraulically using a stopping ring and a groove mechanism [79]. The test section piston, hydraulic piston and pneumatic piston are interconnected along the same shaft as shown in the Figure 2-1. Prior to compression, the pistons are held in their initial position by pressurizing the hydraulic chamber. Before firing the RCM, the hydraulic pressure is greater than the pneumatic pressure and provides the holding force to lock the piston in its initial position. Compression is initiated by triggering a solenoid valve in the hydraulic section venting the hydraulic oil into a reservoir. With the hydraulic pressure relieved, the pneumatic pressure accelerates the piston forward. The entire compression process takes roughly 25ms. In the final stage the piston is held by the force of the driving air, which remains greater than the force of the compressed or burning

mixture and hence allows combustion to occur under constant volume conditions. National Instruments® hardware and LabVIEW® VIs are used for controlling and acquiring data from the RCM. The entire RCM assembly is shown in Figure 1. During this study the main chamber was instrumented with a piezoelectric pressure transducer (Kistler – 6125C) and charge amplifier (Kistler-type 5010B), for pressure measurement at 100 kHz sampling frequency. At the onset of compression, once the voltage level from the pressure transducer reaches 0.15V, which is well above the baseline voltage of the system, storage of pressure data is initiated. This voltage point also serves as a reference for timing the ignition and injection process. The RCM is equipped with heating bands that can be signaled and controlled through a LabVIEW® VI . Wall temperatures are measured using k-type thermocouples as shown in Figure 2-4. The wall temperature can be varied from 85°C to 175°C (current maximum stable RCM temperature) while the compression ratios varied from 6.8 to 17.1. A zoomed in view of the RCM's test section with the TJI set-up is shown in Figure 2-4 and the test section equipped with a straight gasoline direct injector for gasoline autoignition studies is illustrated in Figure 2-5. A detailed explanation of these configurations is provided in the next sections while additional details are given in Chapters 4 and 5, respectively.

2.2 TJI Experimental Configuration

For the TJI experiments heating bands were installed on the RCM and controlled using a LabVIEW® VI program to maintain the wall temperatures at 80° C. The spark plug used for these experiments was an NGK 8201 ER8EHIX with a gap of 0.7mm. The RCM head was equipped with a quartz optical window that enables optical access of the entire combustion chamber. As shown in Figure 2-3, a Photron SA-4 high speed color camera in conjunction with a Nikkor 50mm lens with aperture set at f/2.8 was used and images were captured at 10000 fps with a resolution

of 512 x 512. RCM combustion chamber with the TJI igniter installed is shown in Figure 2-4. The intake manifold was connected to the bottom of the combustion cylinder. Mixture stoichiometry was controlled by monitoring the partial pressures of the gases using an absolute pressure transducer which was installed in the intake manifold. For these tests compressed methane (surrogate for natural gas) with 99.9% purity obtained through supplier Airgas was used as the main and auxiliary fuel. Approximately three minutes [39] was allowed before firing as this was determined to enable adequate mixing time to obtain a homogeneous mixture. A production Bosch direct injector was used for the prechamber fueling. The GDI unit is connected to a high-pressure methane fuel line. Injector flow calibration was performed to determine the mass of fuel injected at different pulse widths. This mass value was used to determine a theoretical prechamber lambda value for different test conditions. Mass of fuel and air introduced during the charge preparation phase was calculated using the ideal gas equation while the mass of the auxiliary fuel was obtained from the injector flow calibration data. A flat piston was used for this study as turbulence is desired in the experiments.

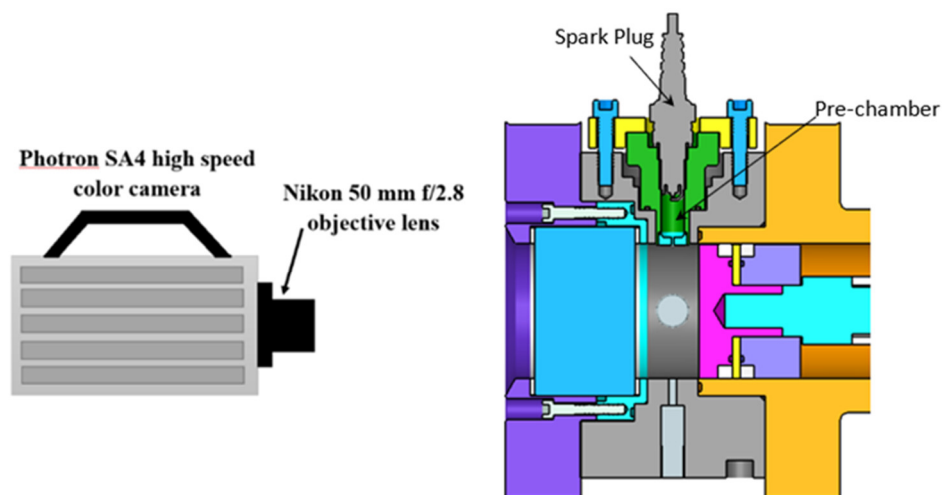


Figure 2-3 Optical imaging setup with high speed camera aligned in front of quartz window.



Figure 2-4 Enlarged view of RCM head fitted with optical window and TJI igniter.

2.2.1 Testing Protocol for TJI Experiments

1. Preheat the RCM wall temperatures to 80°C.
2. Use the TJI LabVIEW VI to set values for the timing of spark and auxiliary fuel injection.
3. Prior to each test vacuum the entire test section using a vacuum pump.
4. Prepare the test section air-fuel mixture by admitting dry-air and methane from compressed cylinders through ports installed in the intake manifold.
5. Pressurize the hydraulic chamber to 1000 psi by using the manual hydraulic pump thus filling the chamber with mineral oil.
6. Now pressurize the pneumatic section of the RCM to 140 psi by using the compressed air from the air compressor.
7. Setup the camera in trigger mode so that image acquisition begins with the onset of spark dwell signal.

8. After allowing sufficient mixing time fire the RCM using the LabVIEW VI. This activates a solenoid in the hydraulic reservoir and relieves the 1000psi pressure in the hydraulic chamber moving the pistons forward and starting data acquisition.
9. Save the pressure and image data.
10. Manually bring the piston back to the initial positions followed by vacuuming of the test chamber.

2.3 Experimental Configuration for Autoignition Studies

In order to carry out autoignition studies few important and notable changes were made in comparison to the previous TJI study. Mixture stoichiometry was controlled by varying the pulse width and number of pulses using a water-cooled direct injector as shown in Figure 2-5. During this study different compressed temperatures are attained by changing the wall temperatures in conjunction with the compression ratio (CR). The wall temperature was varied from 85°C to 175°C (current maximum stable RCM temperature) while the compression ratios varied from 6.8 to 17.1. The compression ratio change was effected by adjusting the stroke length achieved by adding or removing shims in the back of the hydraulic chamber. This changes the BDC volume but the TDC volume remains the same hence reducing CR. Also, shims can be added to the front of the hydraulic cylinder, this maintains the same stroke length but changes both the TDC and BDC volume reducing CR. In addition, a stepped metal window as shown in Figure 2-6, which contains a step on one of its faces, can be used to alter the TDC volume. The additional step, when introduced into the test chamber, will decrease the TDC (and BDC) volume thereby increasing the CR for a given stroke length. Different CR configurations for attaining different compressed conditions used in the current study is tabulated in Table 2-1. The RCM head can be equipped with

either a metal window or with a quartz window enabling optical access of the entire combustion chamber. For imaging a Photron SA4 color camera at 10,000 frames per second was used in conjunction with NIKOR 105mm lens for imaging the autoignition event. Additional details about the configuration are provided in Chapter 5.

Table 2-1 RCM conditions used for achieving the target compressed condition.

Compressed Temperature (K)	CR	TDC volume(cm ³)	Wall temperature range (°C)	Initial pressure range (bar)
650	6.8	70.4	90-130	0.89-2.03
700	9.6	47.9	90-125	0.66-1.39
750	13.9	31.9	85-125	0.49-1.00
800	13.9	31.9	110-150	0.49-1.00
850	17.1	31.9	110-160	0.39-0.84
900	17.1	31.9	145-175	0.39-0.85

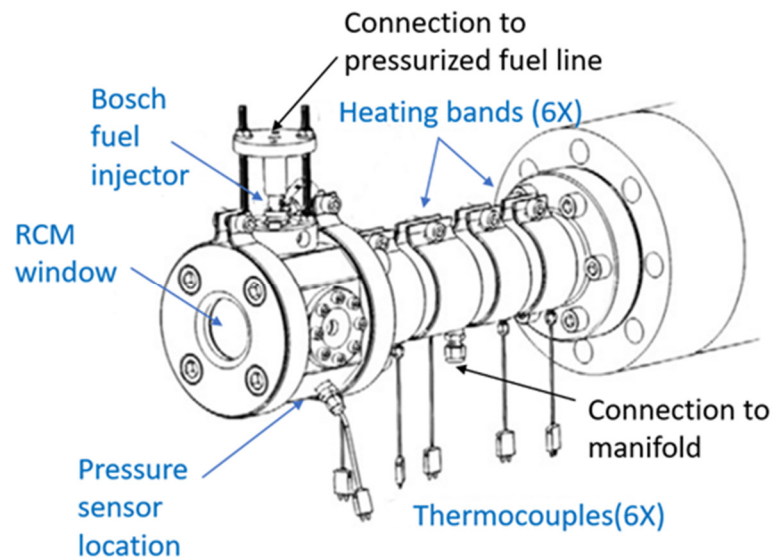


Figure 2-5 View of RCM combustion cylinder with component locations and connections for autoignition studies.

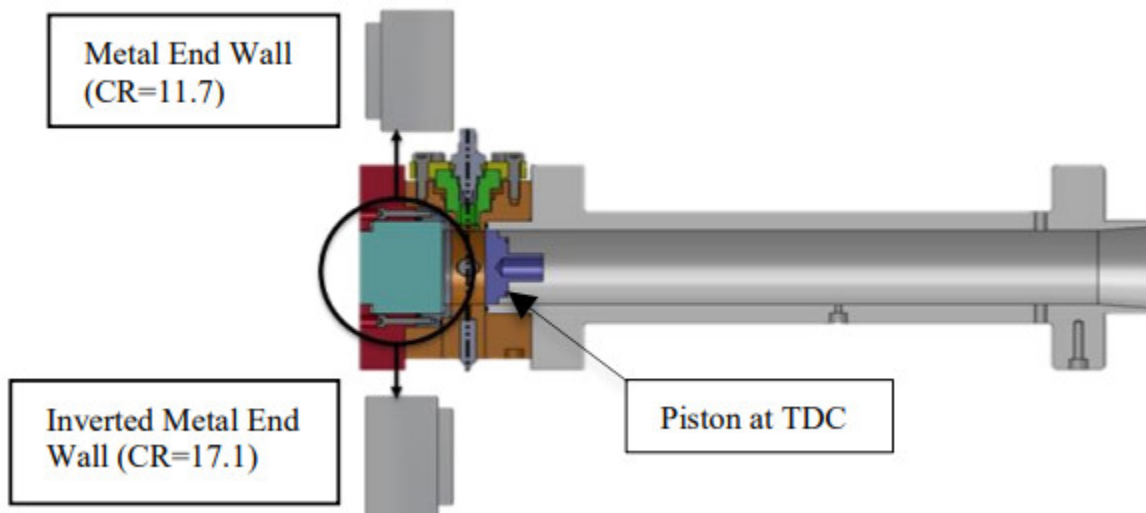


Figure 2-6 View of RCM with stepped metal window used for increasing or decreasing TDC volume.

2.3.1 Testing Protocol for Autoignition Experiments

1. Preheat the RCM wall temperatures between 80 to 170°C based on the target compressed temperatures and compression ratio.
2. Prior to each test vacuum the entire test section using a vacuum pump .
3. Prepare the test section by admitting dry-air or dry-air plus diluent from compressed cylinders through ports installed in the intake manifold
4. Close the manifold and use Labview VI to inject fuel into the RCM by sending pulses to the direct injector.
5. Pressurize the hydraulic chamber to 1000 psi by using the manual hydraulic pump and filling the chamber with mineral oil.
6. Now pressurize the pneumatic section of the RCM to 140 psi by using the compressed air from the air compressor.
7. Setup the camera in trigger mode so that image acquisition begins with the onset trigger signal.
8. After allowing sufficient mixing time fire the RCM using the LabVIEW VI. This activates a solenoid in the hydraulic reservoir and relieves the 1000psi pressure in the hydraulic chamber moving the pistons forward and starting data acquisition.
9. Save the pressure and image data.
10. Manually bring the piston back to the initial positions followed by vacuuming of the test chamber.

Chapter 3 Nozzle Design Evaluation for TJI Applications in Natural Gas Engines

3.1 Introduction

The purpose of the series of experiments described in this chapter was to design and optimize the nozzle type and nozzle area for an auxiliary fueled TJI system for implementation in heavy duty natural gas fueled applications. For this chapter, the focus is placed on comparing the combustion performance of nozzles with a single jet, dual diverging jets and dual converging jets in a rapid compression machine (RCM). Although comparison among single jet and diverging jets nozzles has been carried out in earlier studies, to the authors' knowledge a converging jet type nozzle has not been explored, thereby adding to the novelty of this work in this chapter. Upon entering the main chamber, the dual diverging jets penetrate the main chamber in opposite directions creating two jet tips, while the dual converging jets, after exiting the orifices, converge into a single location within the main chamber. Both of these configurations minimize jet-wall impingement compared to the single jet. The total cross-sectional area of the orifice(s) are maintained the same for all the nozzles while for the dual jet configurations, the angle between the nozzle holes are kept constant. High speed color images along with pressure records obtained from the experiments are further processed to extract derived quantities such as burn duration, flame edge and flame area. The test matrix for this study was based on the results obtained from earlier MSU studies [36,81,82].

3.2 Research Questions

The experiments were mainly carried out to determine the effect of nozzle geometry on the lean limit and burn rate and to answer the following questions

1. The single hole and converging nozzles offer a concentrated source of ignition energy. Is there a difference between the lean limit extension among these two designs?
2. How does a single jet and/or converging jets compare with the burn durations and lean limit extension observed with diverging jets?
3. Is there a correlation between burn rates and flame area information extracted from the jet ignition images?

3.3 Background and Literature Review

3.3.1 Natural Gas as Fuel for Heavy Duty Applications

Compressed natural gas (CNG) and liquefied natural gas (LNG) are considered alternative fuels under the Energy Policy Act of 1992 [68]. The U.S. Energy Information Administration estimates that as of January 1, 2015, there were about 2,355 trillion cubic feet (Tcf) of technically recoverable resources of dry natural gas in the United States. At the rate of U.S. dry natural gas consumption in 2015 the United States has enough natural gas to last about 86 years [69]. This is mainly possible due to advancements made in shale gas recovery, in which the U.S. has remained a forerunner. The abundance of shale gas has led to a decrease in natural gas prices in the U.S and enabled a noticeable shift from coal to gas for electricity in the recent years [7]. Using natural gas as a fuel in internal combustion engines provides energy security, by reducing the dependence on foreign oil and has potential for lower emissions. This makes CNG and LNG attractive fuels for use in class 7 and 8 trucks requiring a greater range. Natural gas when used as a transportation fuel can help reduce CO₂ emissions due to the higher hydrogen to carbon ratio (H/C) of the fuel. The H/C ratio is increased from 1.8 to 3.7- 4.0, when changing the fuel from diesel to natural gas.

Additionally, a high research octane number (around 130) [70] provides an increase in engine thermal efficiency by enabling higher compression ratios (CR) during spark ignition operation.

One strategy to implement natural gas fuel in existing engines is to convert a previously direct injected compression ignition (DICI) diesel engine to a premixed spark ignited (PMSI) engine. The most substantial mechanical change in this conversion is drastically lowering the compression ratio (around 10.5:1). DICI engines are more efficient than typical PMSI engines for two reasons, they operate at a higher mechanical compression ratio (~16:1) and they operate at high dilution levels, up to 100% extra air mass in the combustion chamber. Both of these features increase the engines thermal efficiency and lower its exhaust gas temperatures [83]. With Spark Ignition, unlike compression ignition, it becomes a challenge to ignite and maintain combustion as the air fuel mixture becomes increasingly dilute. The lower dilution levels lead to both higher average combustion temperatures and higher exhaust gas temperatures when making the same amount of power. The higher average combustion temperatures lead to higher NO_x emissions [84] and the higher exhaust gas temperatures limit how much power the engine can produce. Lean burn natural gas operation decreases exhaust gas temperature and reduces NO_x emissions while providing opportunity for increased thermal efficiency. HC and CO emissions can generally increase in a lean burn system due to incomplete combustion and lack of combustion stability mainly because of slower flame speeds and easier quenching of the flame near the combustion chamber walls and in the crevice region. HC tail-pipe emissions from a natural gas engine are mostly methane, hence referred to as methane-slip, which has a higher greenhouse gas potential compared to CO₂, thereby mitigating any advantage gained by the reduction in CO₂ emissions [85]. Hence proper implementation of a lean burn strategy is crucial for successful conversion from diesel to natural gas operation in terms of both environmental and economic impact.

In terms of fuel chemistry, the main constituent of natural gas is methane which has some oxidation characteristics that are different from other hydrocarbons. Because of its strong tetrahedral covalent bonding resulting from sp^3 hybridization between carbon and hydrogen atoms, abstraction of H atoms requires high activation energy and hence high ignition energy [86]. Also, the intermediate methyl radical (CH_3) formed through such abstraction has a strong tendency to recombine into stable ethane molecules making it a less reactive fuel exhibiting slower burn speeds compared to heavier alkanes. The above-mentioned issues are magnified at lean conditions due to slower flame speeds and therefore a high energy ignition device that can potentially produce a distributed ignition source is advantageous.

3.3.2 Ultra-Lean Burn Strategy for Natural Gas Engines using TJI

A prechamber system, such as a turbulent jet ignition (TJI) system [87,88], enables a sudden discharge of hot turbulent jets of combustion gases into a combustible mixture and is capable of initiating and sustaining deflagration at ultra-lean mixture conditions. By using TJI it is possible to address the requirement of higher ignition energy with thermally reacting jets acting as an ignition source. Distributed ignition is achieved due to the penetrating nature of the jet. The turbulent jets also act as a source of turbulent kinetic energy, thereby enhancing the flame speed during the jet penetration period. This causes much faster heat release rates which allow ignition timing advance to be reduced significantly. The reduced ignition advance combined with the higher dilution in the cylinder allow the compression ratio to be significantly increased, with CR higher than 13:1 possible [88]. The increased CR and the lower exhaust gas temperatures allow a TJI equipped PMSI lean burn engine to approach the thermal efficiency and the power output of the original diesel engine it was converted from without the need for complicated NO_x reduction systems such as EGR and UREA based SCR.

An auxiliary fueled prechamber ignition system can be used in an IC engine environment to provide lean limit extension with minimal cyclic variability and low emissions. Geometry and distribution of the prechamber orifices form an important criterion for performance of these systems since they are responsible for transferring and distributing the ignition energy into the main chamber charge. Generally, a prechamber ignition device can be classified as a jet ignition or a torch ignition system. A torch ignition system has a large diameter, generally greater than 6mm, and allows a flame front to emerge out of the prechamber without disturbance [89,90]. In a classical study performed by Boston et al. [91] it was shown that torch ignition systems enabled improved flame propagation compared to spark plugs in a combustion bomb under low turbulence conditions. Other categories of prechamber ignition systems use smaller nozzles to quench the flame entering the main chamber to various degree. With nozzles less than 1mm, the flame is completely quenched upon entry into the main chamber. This type of jet reignites in the main chamber after a relatively large ignition delay time and is used in the APIR [92] system. Comparatively, a partially quenched flame, as used in TJI, would have a high thermal energy and incomplete combustion products. The incomplete combustion products could trigger chain branching reactions that require less activation energy. For example, a third body reaction with a methane molecule requires 13.9×10^{15} cal/mol activation energy while a H radical attacking a CH_4 molecule only requires 6.6×10^8 cal/mol to trigger chain branching [93]. The under expanded hot jet also achieves higher velocity due to the smaller nozzle which increases the turbulent kinetic energy [94], thus promoting higher flame speeds relative to laminar conditions. The high turbulence created during the jet ignition process helps to either breakup the flame kernels at the ignition site or wrinkle them increasing the flame area, hence resulting in flame acceleration at certain conditions [95,96].

Also, the prechamber cavity can be either fueled separately (auxiliary fueled), using a valve or a specialized injector or non-fueled. Sometimes these configurations are referred to as scavenged and unscavenged prechambers with respect to natural gas applications, since the addition of gaseous fuel to the prechamber can help displace or scavenge the burned contents residing in the chamber from the previous cycle [97]. Unfueled prechamber igniters have wide spread use in large bore stationary natural gas engines [98,99]. In an unfueled prechamber configuration, no auxiliary prechamber fuel injection occurs and hence the lambda across both the chambers remains the same. In this operation mode, it is important to maintain the mainchamber lambda closer to ignitability limits of a standard spark plug configuration in order to initiate and sustain a deflagration even within the spark plug. Implementing an unfueled prechamber is simpler and has demonstrated reduced cyclic variability compared to standard spark plugs [100], however, a lean limit extension benefit compared to a spark plug is not realized [101]. By having auxiliary fuel injection in the prechamber a faster burn rate and better lean limit extensions can be achieved. In TJI, by having a slightly richer than stoichiometric mixture within the prechamber [87], faster flame propagation with a higher adiabatic flame temperature is ensured, resulting in a higher pressure build up within the prechamber (causing a higher pressure differential between the chambers) and hence a higher velocity for the exiting jet. Also, a slightly rich flame provides a higher distribution of active radicals when quenched, compared to a lean or a stoichiometric mixture [102]. Another design variable is volume of the prechamber, which for TJI is generally maintained at less than 5% of the clearance volume. Further details about different prechamber configurations and a comprehensive review about their history and applications can be found in reviews of prechamber systems compiled by Toulson et al. [22] and Alvarez et al. [103]. Other configurations of hot jets igniting

premixed charge are also studied for aviation applications [104] and mining safety [105] which expands the fundamental knowledge about these ignition systems.

3.3.3 Prechamber Ignition for Natural Gas Engines

Prechamber ignition devices have not been commercially implemented in automotive engine applications and this literature review covers some of the previous work performed with prechamber igniters using natural gas as a fuel. Kammerstatter et al. [106] studied natural gas combustion using an auxiliary fueled prechamber ignition system in a constant volume combustion chamber equipped with intake and exhaust valves. Their results revealed that larger nozzles had less auxiliary fueling requirement compared to smaller ones to achieve high ignition probability. Mastorakos et al. [107] used an optical vessel fitted with a quartz prechamber to study the chemical composition of the jet using CH^* and OH^* chemiluminescence records. They compared the chemical and physical aspects of the turbulent jets issued using ethylene and methane as prechamber fuels and concluded that methane fueled prechambers generally produced a weaker jet and exhibited higher quenching.

Kawabata et al. [108] did a high-speed visualization study of an auxiliary fueled prechamber combustion system with 4, 5 and 6 nozzles installed in a 150 mm bore cogeneration engine that had a swirl intake port. They observed that the turbulent jet tips were turning at the periphery of the combustion chamber due to the effect of the swirl. They also calculated the flame area using image processing, with the best performance obtained with 6 nozzles. By targeting jets into the valve recess area, emission reduction was achieved. When operated unfueled the prechamber performed like the conventional spark plug. The study, however, did not include any emission measurements. Olsen et al. [109] using a 356 mm bore engine found that significant NO_x is produced in the initial unburned fuel that comes out of the prechamber. In a different study [109],

they observed that NO_x can be reduced by controlling injection angle in the prechamber. Simpson et al. [110] tested fueled and unfueled prechamber configurations in a large bore engine and found that increasing the nozzle length/diameter ratio decreased the prechamber fuel loss to the main chamber. Duong et al. [111] performed optical diagnostics in a large bore (340 mm) genset natural gas engine. In the high-speed images, they found that chemiluminescence intensity closely followed the heat release rate analysis obtained from the pressure curves. The study concluded that variation in prechamber combustion did not correlate with variation in main chamber combustion, and hence the source of cyclic variation was due to main chamber parameters. Shah et al. [112] tested prechambers with 1.4, 2.4 and 3.7% of the clearance volume and found that the 3.7% prechamber offered a lean limit extension of up to λ 2.5 and exhibited the shortest burn duration but increased NO_x emissions. The 2.4% prechamber was found to have the best tradeoff between ignition and emission characteristics.

Baumgartner et al. [97] studied a fueled prechamber system in a single cylinder natural gas 0.5-liter engine with a bore and stroke of 92 mm x 75 mm which is closer to a passenger car engine dimensions. Prechamber fueling was achieved using a direct injector with an injection pressure of 9-bar and a prechamber that was 3.5% of the clearance volume with a 1.3mm diameter orifice. Spark timing was moved closed to TDC to achieve MBT. A reduction of 11 % in specific fuel consumption was achieved at λ 1.6. Toulson et al. [38,113] performed an optical study in a 0.4-liter single cylinder engine with propane and natural gas as fuels. Comparison was made between a spark ignition system and a turbulent jet ignition system containing six nozzles. It was observed that the performance of the spark plug deteriorated at λ 1.5 due to unreliable combustion initiation and propagation, while the TJI system exhibited great combustion stability even at λ 1.8.

3.4 Experimental Setup

Basic features of the RCM facility used for this study have been documented in Chapter 2. Figure 3-1 shows the exploded view of the prechamber assembly and further details of the TJI igniter installed in the top of the RCM optical head can be seen in Figure 2-4. When these components are assembled they form a closed prechamber cavity with the nozzle forming the connection between the prechamber and main chamber cavities. Different jet configurations, such as single or multiple jets can be tested by changing the nozzle. Also, the nozzle throat configurations can be altered if required. The prechamber was not equipped with a pressure sensor during this study. The test conditions and additional hardware information are provided in Table 3-1.

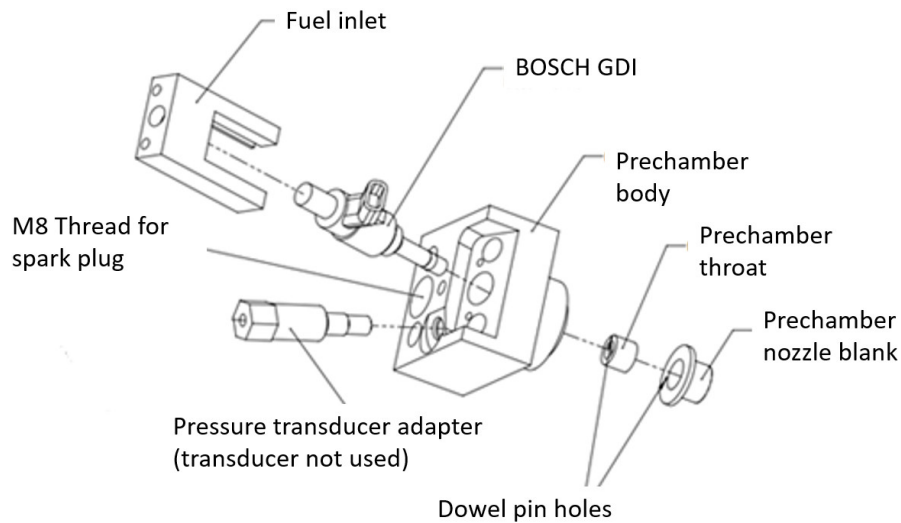


Figure 3-1 Exploded view of components used in the TJI igniter.

Table 3-1- RCM experimental set-up.

Bore	50.6 mm
Stroke	229 mm
Displacement volume	462 cc
Clearance volume	52.5 cc (without prechamber vol)
Prechamber volume	2.15 % of clearance volume
Initial pressure	1 bar (absolute)
Compression ratio	10:1 (prechamber volume not included)
Aux fuel injection pressure	250 psi (gauge)
Spark dwell time	5 ms
Spark discharge timing	18ms after TDC
Wall temperature	80 ° C
Compressed pressure (@ TDC)	16 bar (absolute)
Fuel injector	Bosch direct injector- Production
Mainchamber lambda range	1.8 to 3
Mainchamber fuel	Methane
Prechamber fuel	Methane
Prechamber lambda (theoretical)	0.8
Injector pulse width range	1 to 1.6 ms
Nozzle hole(s) diameters	2.26 mm x 1 & 1.57 mm x 2

3.5 Testing Methodology

For each nozzle configuration, tests were carried out starting from main chamber $\lambda=1.8$ until misfire was observed. Each test point was repeated three times and as mentioned earlier, prechamber fuel enrichment via auxiliary fuel injection was used for all test points. Auxiliary fuel

injection timing impacts the mixture distribution within the prechamber at the time of the spark. Early injection promotes a more homogeneous mixture in the prechamber compared to later injection. The auxiliary prechamber fuel was injected during the initial stages of compression for the current tests. The pulse width of the fuel injection was increased with increase in the main chamber lambda to maintain a similar theoretical prechamber lambda value across all tests.

The theoretical prechamber lambda value assumes that no auxiliary injected fuel leaves the prechamber [114]. During RCM operation, based on the compression pressure, some fuel might escape the prechamber and enter the main chamber after injection. Considering the above-mentioned scenario, it is likely that the actual lambda values could be higher than the theoretical lambda values reported here. Earlier studies indicate maintaining richer mixtures [101], around $\lambda=0.9$ [115], in the prechamber provides better combustion performance compared to lambda of 1 or higher. Hence for the tests conducted, a theoretical lambda in the range of 0.8 was targeted. This was achieved by modulating the injector signal pulse width for each lambda point. Considering the loss of some prechamber fuel into main chamber while injection it is possible that the actual prechamber lambda would be closer to 0.9-1.

3.6 Nozzle Configurations

The nozzle configurations used in this study are shown in Figure 3-2. In order to maintain the same exit cross sectional area as the 2.26 mm single hole nozzle, two holes with a diameter of 1.57 mm (nearest drill size) were machined into a diverging type and a converging type nozzle configuration. In an earlier in-house computational study performed by Thelen et al. [116], it was observed that TJI performance deteriorated with orifice size smaller than 1.5mm. Hence the choice of orifice diameters chosen for this study can be considered optimal. The two-orifice nozzles were

identical with respect to dimensions but they were inverted in the sense that one issues diverging-jets while the other is a converging-jets type. In practice, situations where two jets could converge spatially within the cylinder bore could occur in a system containing more than one prechamber [117,118]. Also with the converging jets type it would be possible to target the ignition energy into a single location and reduce over penetration or impingement. The angle between the holes was a constraint imposed by a component named the prechamber throat which can be located in the assembly found in Figure 3-1. As seen in the figure, the prechamber throat is located over the top of the nozzle orifices. The edge to edge distance of the lower opening in the prechamber throat placed a constraint on the maximum angle between the nozzle holes. A 35° angle was chosen between the nozzle holes so that the length at the diverging end of the holes, remains such that the nozzle holes do not get blocked.

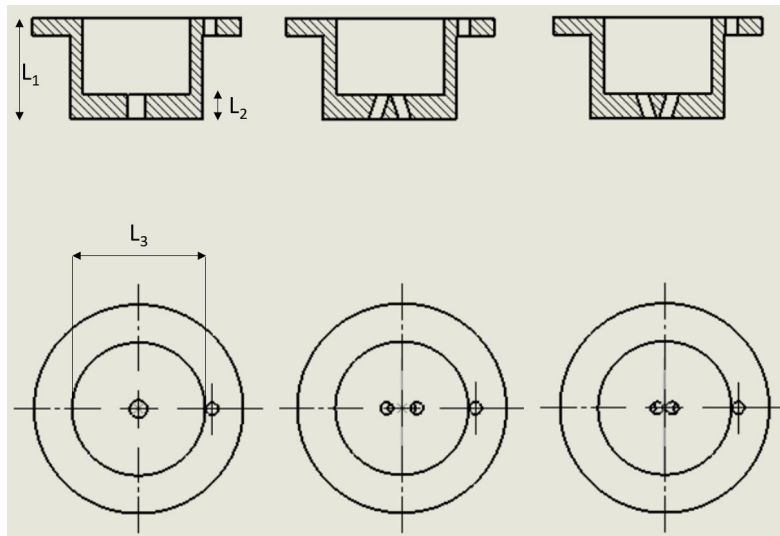


Figure 3-2 Sectional and bottom views of the nozzle configurations used in the TJI igniter with $L_1=13.2\text{mm}$, $L_2=3.2\text{mm}$ and $L_3=17.2\text{mm}$.

3.7 Results and Discussions

3.7.1 Main Chamber Pressure Analysis

A typical pressure trace obtained during RCM operation is shown in Figure 3-3. It can be observed that the entire compression process occurs within 25ms. Spark ignition was timed to occur after TDC so that combustion happens in a constant volume environment. A spark dwell time of 5ms was used in conjunction with a conventional inductive discharge ignition system operating using a 13.5 V power supply system. At the end of the dwell period spark discharge occurs and this instance is timed as 0 ms. The auxiliary fuel injection process and spark discharge are indicated in Figure 3-3. Auxiliary fuel injection was timed to occur early during the compression process so that sufficient mixing is ensured when the main-chamber charge enters the prechamber during the compression process. It has to be noted that the start of injection occurs against a back pressure of around 5 bar while the injection pressure (or fuel lines pressure) is 18 bar. This pressure difference will contribute to some of the injected gas leaving the prechamber and entering the main-chamber during the compression phase.

The 0-10% and 10-90% burn durations are calculated by defining the peak pressure as the 100% burn point and the pressure at the end of spark discharge as the 0% burn point. Times for 0%, 10% and 90% of the peak pressure rise are obtained from the graph and corresponding burn durations are calculated [119]. It is generally accepted that the 0-10% burn duration indicates the

effectiveness of the ignition device in initiating deflagration while the 10-90% burn duration indicates overall combustion performance [114].

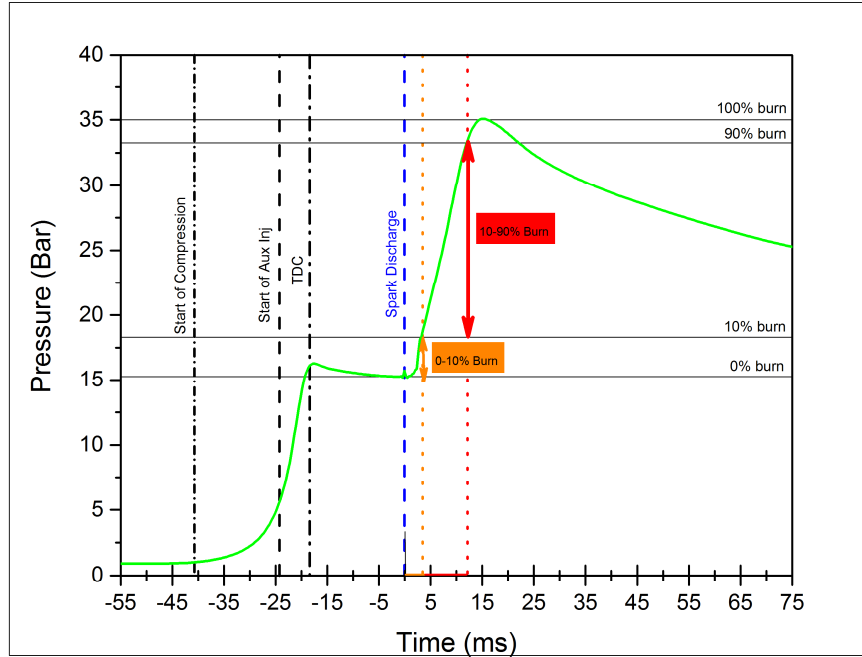


Figure 3-3 Sample pressure trace indicating derived pressure quantities and timing of various events during RCM operation.

The pressure traces collected from the test points for each nozzle configurations are plotted separately in Figures 3-4, 3-5 and 3-6. All lambda values shown in the plots are global lambda values which includes both the main and prechamber fuel. As mentioned earlier, each of the lambda test points were repeated thrice and they are plotted separately in the graphs. Variation among these traces for the same lambda point can be used to assess the combustion stability. In Figure 3-4, for the single jet nozzle at lambda 1.78, the variation among repetitions are very minimal. The variation becomes noticeable as we move from lambda 2.48 to 3.02. At lambda 3.10 combustion becomes very unstable with test #3 registering no pressure rise after the jet discharge period. The single jet nozzle hence achieves a lean limit of 3.02. The pressure records for diverging

jets are illustrated in Figure 3-5. The peak pressure was higher for lambda points 1.78 through 2.48, in comparison to the single hole nozzle. Also, the repeatability of the experiments has improved indicated by the overlapping nature of the pressure traces for each lambda point. This increase in performance and repeatability is expected with multi-hole nozzles as indicated in classical studies [117]. Combustion fails at $\lambda = 3.02$, slightly earlier compared to the single hole nozzle.

Similarly, the pressure data for converging jets are shown in Figure 3-6. The overall behavior was similar to the single jet type with a few notable differences. The variability for $\lambda=2.21$ was observed to be lower than with the single hole nozzle, however past this point higher variation is observed. The converging jets achieved a lean limit of $\lambda=3.02$, similar to the single jet. By comparing the pressure records of the nozzle configurations, it can be concluded that all three configurations can achieve a maximum lean limit of $\lambda=2.93$.

In Figure 3-7, the average pressure data for each lambda point, across all three nozzles is presented. Until $\lambda=2.48$, the diverging type nozzle exhibits faster burn and higher peak pressures. At $\lambda=2.75$ there was little difference among the three nozzles except that the single hole nozzle offers slightly higher pressure rise rate during the jet penetration phase. Although multiple jets are expected to offer better performance than a single jet, it is interesting to observe how similarly the single jet and converging jets perform. This underlines the importance of ensuring proper jet distribution when multiple jets are discharged into the combustion chamber.

In Figure 3-8, the mean 0-10% burn duration extracted from the pressure curves are presented. The calculated standard error is plotted as error bars. It can be observed that throughout the lambda range and across the jet configurations, the burn duration lies within the 2.5-3ms range. Also, the longest 0-10% duration is exhibited by the diverging jet at its lean limit, while the shortest duration

is exhibited by the single jet at $\lambda=2.48$. The data suggests that strong correlations between nozzle design and the 0-10% burn duration cannot be established. However, it appears that the single jet generally initiates combustion faster, except at $\lambda=1.8$. In an earlier study by Gentz et al. [120] it was found that varying the fuel pulse width, thereby varying the prechamber stoichiometry affected the 0-10% burn durations, but in this current study the prechamber stoichiometry remained constant across all of the lambda test points. Hence it is possible that 0-10% burn duration is more sensitive to prechamber mixture than the nozzle configuration. This will be confirmed with additional tests carried in the next chapter. Figure 3-9 shows that for the 10-90% burn durations, in contrast to the 0-10% burn durations, a clear trend can be established across different nozzle configurations. The diverging jets offer faster combustion performance consistently exhibiting at least a 3ms difference until lambda 2.48. However, the trend reverses at the lean limit where it is seen that the diverging jets are slowest. Also, the burn durations across all nozzle configurations converges at lambda 2.75. This may be due to the fact that as the lean limit is approached, the burn duration is limited by ignition energy and not by ignition distribution. Also, the single jet and converging jets are slightly faster at their lean limits, when compared to the diverging jets. When comparing the single jet and converging jets, the later consistently performs better which is attributable to the increased concentration in ignition energy coupled with reduced wall impingement.

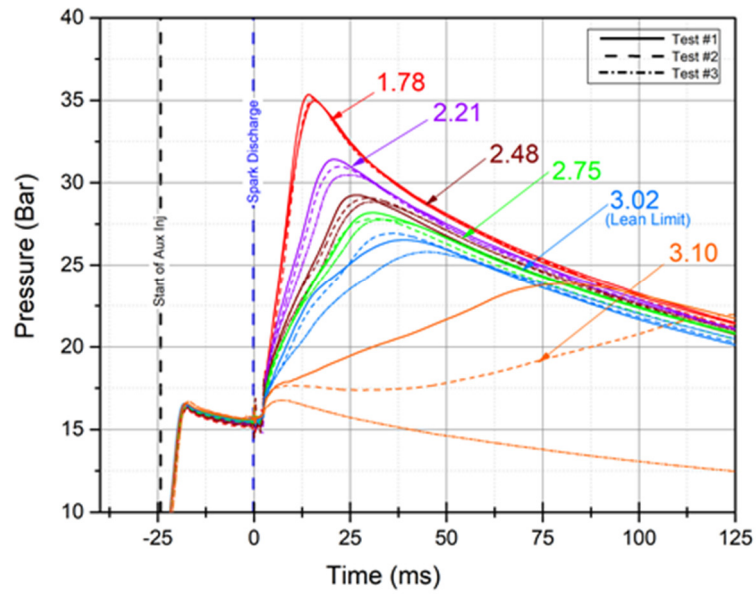


Figure 3-4 Experimental pressure traces for single jet nozzle configuration.

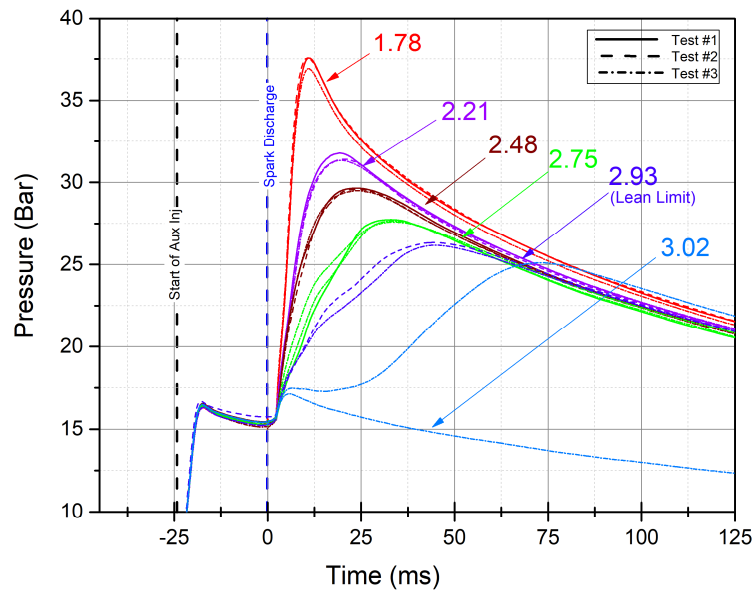


Figure 3-5 Experimental pressure traces for diverging jets nozzle configuration.

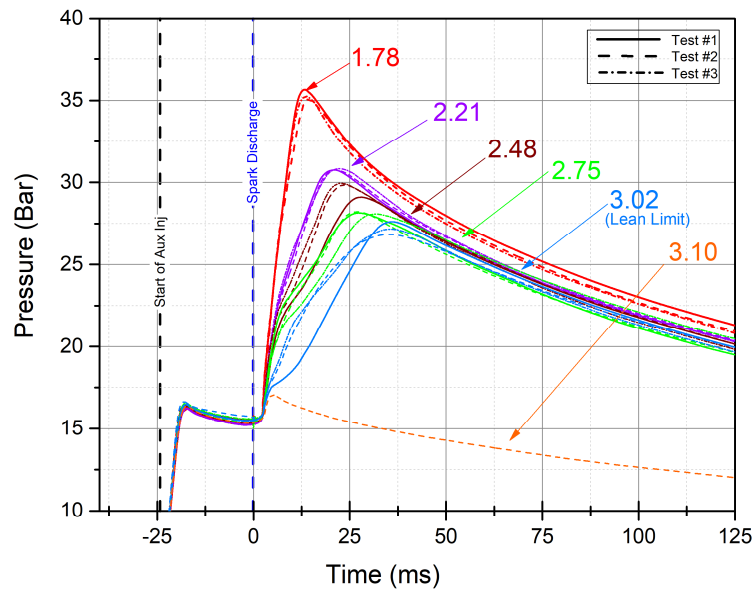


Figure 3-6 Experimental pressure traces for converging jets nozzle configuration.

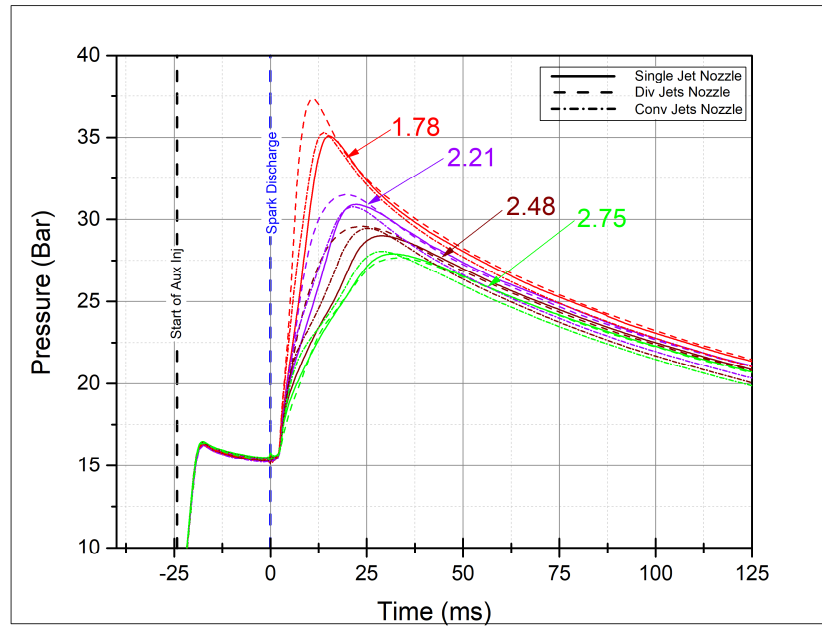


Figure 3-7 Average experimental pressure trace for single jet, dual diverging and dual converging jets nozzle configurations.

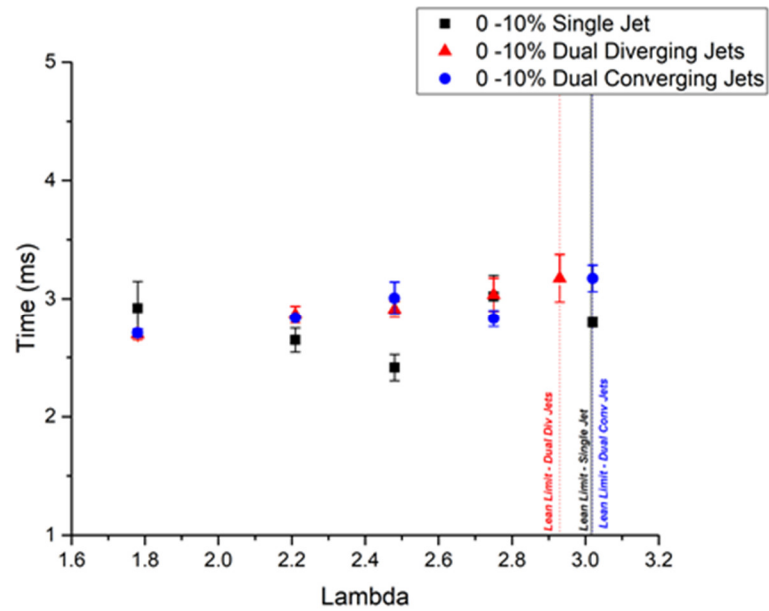


Figure 3-8 0-10% mean burn durations for single jet, dual diverging and dual converging jets nozzle configurations.

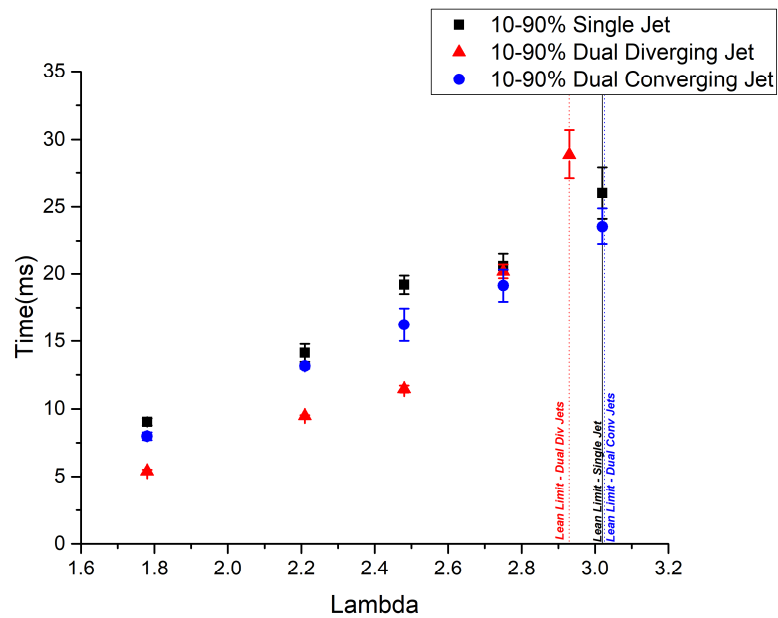


Figure 3-9 10-90% mean burn durations for single jet, dual diverging and dual converging jets nozzle configurations.

3.7.2 High Speed Image Analysis

In this section the acquired high speed images are analyzed and differences observed in the burn durations are explained by comparing the flame propagation pattern resulting from different jet configurations. Figure 3-10 illustrates the jet penetration and flame propagation in the main chamber at different instances during the combustion pressure rise. It can be observed that the pressure rise rate is faster between 2-4ms, after ignition, as indicated by the rate of change in pressure curve. This period corresponds to the phase during which the jet penetration is active. Past this period combustion can be seen to proceed at a constant rate as the jet discharge and the associated mixing stops. Maximum luminosity is observed as peak pressure is approached and the chemiluminescence color changes from shades of purple to bright yellow.

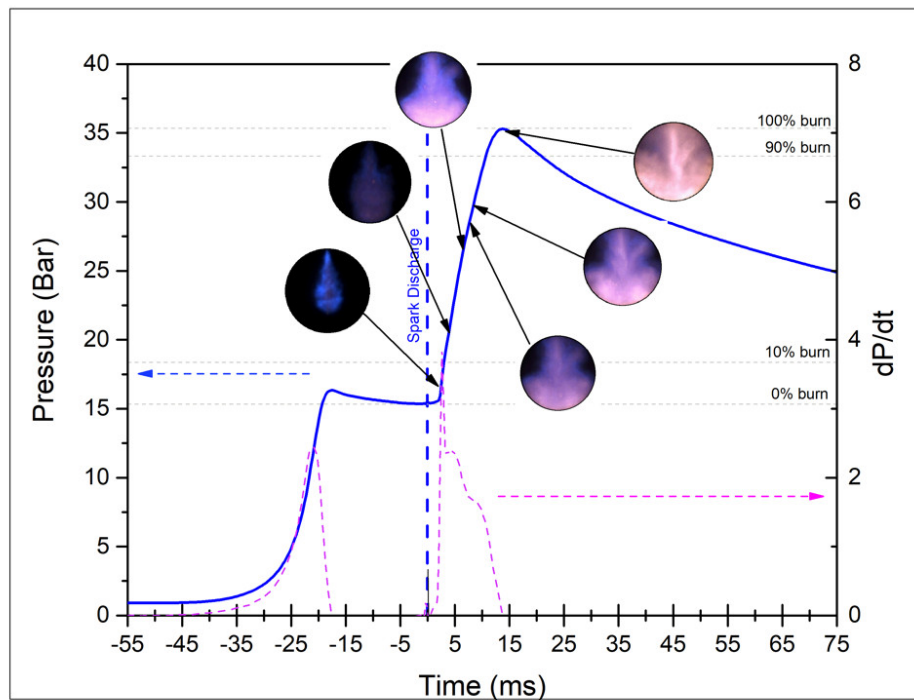


Figure 3-10 RCM experiment pressure trace (blue) and rate of pressure change (pink) overlaid with high speed images at respective time interval.

Images comparing the different jet configurations for $\lambda=1.78$ are shown in Figure 3-11. As mentioned earlier, the entire 50 mm bore is being visualized in these images. The images contained within the orange dashed border are enhanced for better clarity using ImageJ software [121]. The amount of enhancement applied across all the images is the same, hence the luminosity differences correspond purely to differences in combustion. Lambda 1.78 is chosen for this comparison since the decrease in luminosity is greater as the mixture was further diluted. Any further enhancement to already darker images resulted in image processing artifacts. Nevertheless, when comparing the images across the lambda points, the jet visual qualities were similar and provided insight into the combustion characteristics. From Figure 3-11, it can be observed that the body of the penetrating jet consists of a yellow inner core and reacting purple outer region. After the initial jet, the second set of images at 3.6ms becomes darker, but then the luminosity starts to increase in the subsequent frames. With respect to jet impingement it can be observed that the single jet reaches the wall first at 2.6ms. Wall impingement is considered detrimental for jet ignition processes [122] as both loss of thermal and turbulent energy will occur. It must be noted that for the diverging jets case the choice of the jet angle, which was a constraint imposed by the throat, appears to be near-optimal for the combustion chamber geometry. The reason being that a further increase in angle would result in earlier wall impingement or a reduction in angle would result in two jets converging along the inner sites reducing the jet distribution.

It is interesting to note that the converging jets appears similar to a single jet with no indication of the presence of two separate jets. However, when compared to the single jet the converging jet exhibits lower penetration/impingent at 2.6 ms and the jet tip/jet head appears bulkier. This could affect the 0-10% durations but as observed in Figure 3-8, that is not the case. Also at 3.6 ms, the single jet exhibits increased combustion at the stagnation zone, whereas for the converging jets the

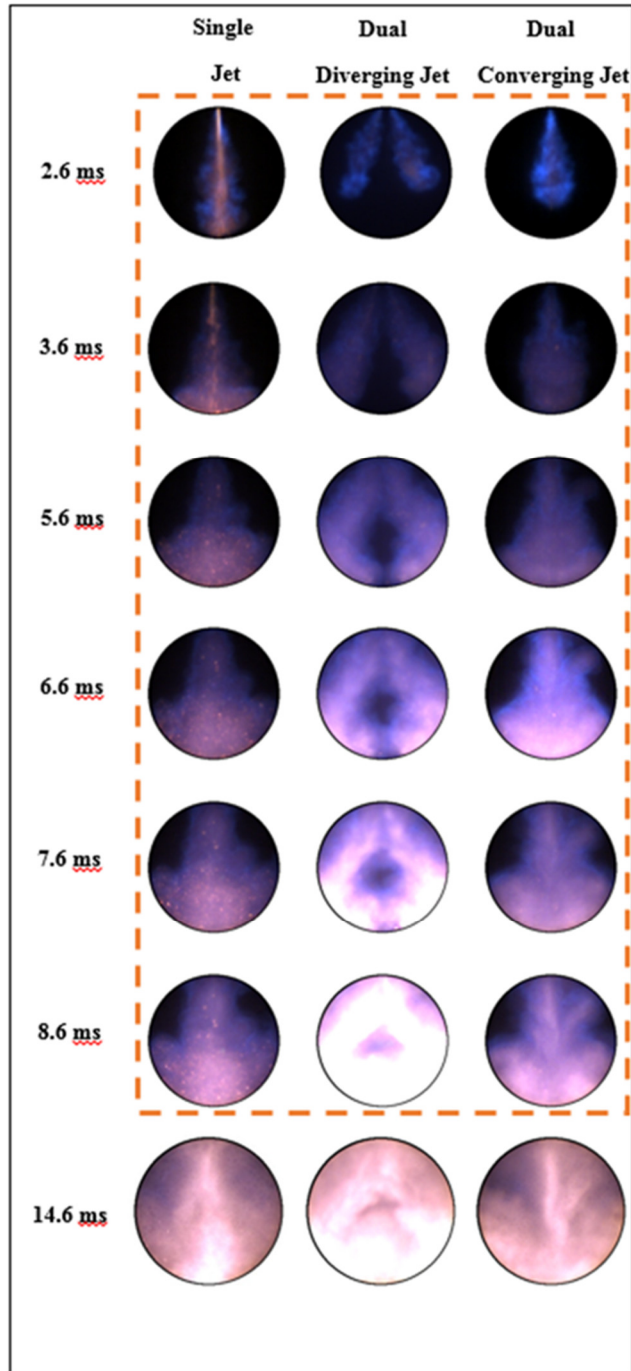


Figure 3-11- Montage comparing high speed images for single jet, dual diverging and dual converging jets nozzle configurations. Images within the orange dashed border are enhanced (equally) for better clarity.

bulk combustion occurs slightly above the wall. This could be considered beneficial in terms of reduction in heat loss from the jets to the wall. Also at 3.6ms the converging jets have increased flame surface area in comparison to single jet. At 6.6ms the single jet's reaction site is seen to be confined within the lower half of the combustion chamber, while the converging jets exhibits reaction in the top right regions. The tail growing on the top right region suggests that the jet penetrating towards the right end of the chamber could be stronger compared to the left jet. This is possible since, in a dual jet configuration jet asymmetry is always present, the asymmetry being driven by the prechamber flame propagation pattern, which is also subject to cycle to cycle variability [115]. Such an asymmetric penetration pattern is also observed for the diverging jet configuration.

Comparing the visual images, it is evident that the diverging jets offer better distribution and consume the bulk charge more quickly. After 7.6ms, which roughly lies close to its 90% burn point the reaction zones of the diverging jets exhibit higher luminosity relative to the other jet configurations. At 14.6ms, which corresponds to a time after the peak pressure is reached, the diverging jet configuration has less unburned zones as seen in the image. In the following section the images presented in Figure 3-11 are further processed for better visualization and to obtain quantitative information

3.7.3 Image Analysis Methodology - Flame Area and Edge

The montage presented in Figure 3-11 is a two-dimensional representation of a three-dimensional flame, and hence any analysis performed needs to be considered as approximate to a certain degree. In this section the high-speed images are further processed to extract the flame edges to aid in better visualization and comparison of flame growth. Also, the area enclosed by the flame is calculated quantitatively to compare the growth of the luminous region across the jet

configurations. For this purpose, an image processing algorithm for flame edge detection and for calculating the flame luminous area was written in MATLAB®. The code works by initially converting the original color image into a grayscale image. This grayscale image is used to detect intensity difference within the image and a global threshold value for the intensity is then decided. Using this threshold value, the grey scale image is converted into a binary image where 0 represents black and 1 represents white. A Sobel edge detection algorithm is applied on top of the binary image for extracting the flame edge. The program also counts the number of pixels that have a value of 1 in the binary image. The final sum of the pixels when multiplied with the area per pixel gives the flame area. This step is repeated frame by frame thereby extracting flame edge and area information from each image.

In Figure 3-12, contour plots containing the flame edges of different jet configurations are compared at subsequent times by overlaying them onto a single frame. Also, the color image obtained at 2.6ms is overlaid within the contour for assessing the robustness of the edge extraction technique. This comparison enables better visualization of the flame propagation pattern versus time, across the jet configurations. It can be observed that the diverging jets have a distinct flame propagation pattern when compared to the other two configurations. The diverging jets consume the charge in a fairly symmetric pattern across the right and left portion of the combustion chamber. The flame reaches the top wall rather quickly in comparison, exhibiting faster consumption along the outer edges of the jets. However, along the inner sides of the jets, the flame growth is more pronounced at the jet tips/jet head region leaving a pocket of unburned region closer to the center of the chamber. At 8.6ms, unburned zones are present in the center of the chamber and on the top right and left corners.

Observing the single jet and the converging jets, although similar in appearance, they exhibit notable differences with respect to their flame propagation pattern. For instance, comparing the overlaid edge contours it can be seen that the flame propagation pattern along the bottom region of the jets is different. The single jet exhibits stronger influence on jet impingement throughout the combustion duration, with flame edges emerging from the stagnation zone and from the counter rotating vortices produced to the sides of the stagnation zone. In contrast the converging jets show better radial growth throughout the jet head region and exhibit a less impingement driven flame propagation pattern. It has to be noted that the resultant momentum direction of the jets plays an important role in the observed flame propagation pattern seen here. For the single jet, the resultant jet direction was vertical, hence the observed wall impingement, whereas for the converging jets the resulting jet direction was towards the sides due to the angle of the jet issuance explaining the increased radial growth. There could also be differences with respect to kinetic energy due to jets impinging on each other which requires further investigation. In chapter 4 the extracted edges will be used to extract additional information regarding jet penetration vs time.

In Figure 3-13, a comparison of normalized flame area (flame area/piston area) versus time is provided for the jet configurations. The flame area was obtained for the experiments shown in Figure 3-11, using the image processing techniques mentioned earlier. The dual diverging jets exhibit superior flame growth and approach the normalized flame area of one indicating that the entire chamber is luminous at that point. For the other two jet configurations, around 80% of the chamber appears luminous towards the end of combustion. This is also reflected in the pressure traces through the peak pressure, which is higher for the diverging jet by 3 bar at $\lambda=1.78$. It can be clearly observed that after the 10% burn point, the converging jets have a higher flame area in

comparison to the single jet, and therefore consume more charge. However, as they approach 90% burn duration, both the converging and single jet configurations have similar flame area. This is due to the fact that during this time window, the converging jets show increased radial growth (relative to the single jet) which was due to a combination of reduced wall impingement and direction of the resultant momentum of the converging jets.

The mean 10% and 90% burn duration times obtained earlier from the pressure curves are also plotted on top of the curves for their respective jet configurations. It can be observed that the 90% burn point is located approximately in the same location as the 90% flame area however the 10% burn point does not follow the same pattern. This could be due to the fact that for the jet ignition process, the ignition source is distributed in the combustion chamber unlike a spark ignition source. The entire jet area might not correlate with the early pressure release because the flame area, during this stage, is an addition of both burned prechamber contents and burning main chamber charge. Isolating the burned main chamber charge responsible for 10% pressure rise in the main chamber is not possible with the current image processing methodology.

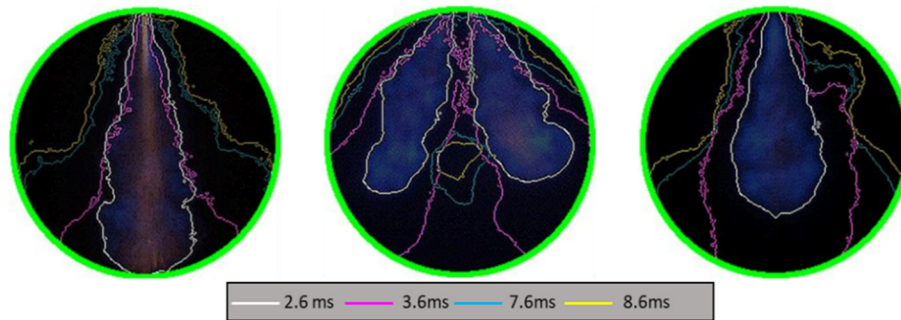


Figure 3-12- Comparison for flame propagation pattern through extracted flame edges for single jet, dual diverging jets and dual converging jets nozzle configurations at lambda 1.78.

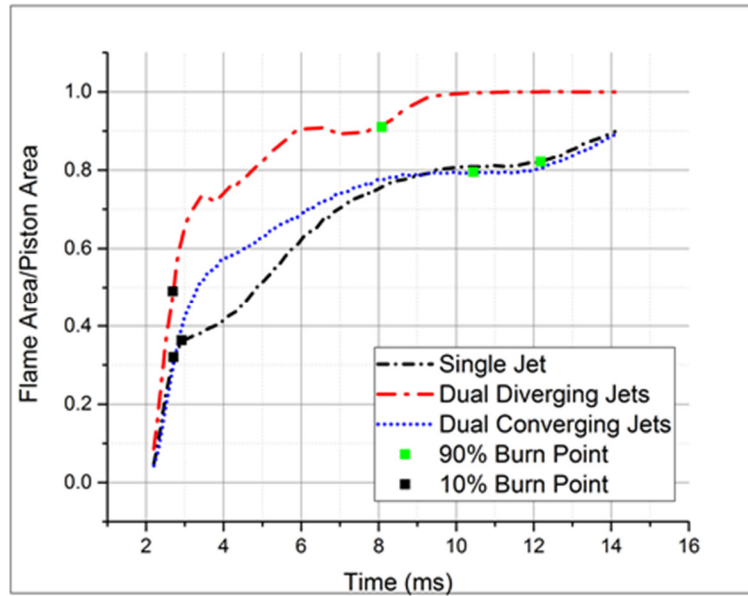


Figure 3-13- Comparison of normalized flame area across jet configurations for lambda 1.78.

3.8 Chapter Summary

In order to compare the lean limit extension and burn rate performance for different jet types, three different jet configurations were tested in this chapter. Raw pressure traces and high-speed color images were processed with suitable assumptions to analyze the performance of different jet configurations in an auxiliary fueled TJI system using methane as both the primary and auxiliary fuel. These derived quantities enabled better assessment of macro behavior of the turbulent jets across the configurations tested. It was observed that the dual diverging jets offered overall superior combustion performance and would be well suited for natural gas engine applications where a reasonable lean limit extension, for NO_x reduction, together with faster and more complete combustion, for targeting higher efficiency and low HC emissions, are required. The converging jets configuration appeared visually similar to a jet issued from a single orifice. However, compared to the single jet there are some notable differences in the flame propagation pattern. In

comparison to the single jet, jet-wall impingement is reduced and radial growth of the flame is more pronounced during the earlier stages of combustion. This resulted in a slightly better burn rate profile compared to the single jet. The single jet and converging jets provide a slightly higher lean limit extension compared to the dual diverging jets, however the difference is minimal. It is safe to conclude that all three nozzle configurations offered similar lean limit extension. Between the dual converging and dual diverging jets, it can be concluded that the effectiveness of the multiple jets system is reduced substantially when jets converge into a single location due to a reduction in the reaction area and possible reduction in the main chamber turbulence generation. Hence part or complete interference between jets should be avoided through nozzle design. For applications where a single jet ignition site is desired and over-penetration/wall impingement is a concern, the converging jet configuration is preferred over a single jet as it provide a slightly better burn rate profile and a similar lean limit extension. For the current study, when using converging jets, the main ignition location occurred slightly above the wall hence providing concentrated ignition energy with reduced heat losses. Results and insights obtained here are used in chapter 4 to compare passive TJI operation and other performance parameters.

Chapter 4 Performance Metrics for Fueled and Unfueled Turbulent Jet Igniters in a Rapid Compression Machine

4.1 Introduction

This chapter extends on the work of the previous chapter, by analyzing the performance of TJI nozzles for both active (auxiliary-fueled) and passive (unfueled) prechamber configurations. The results from the passive configurations are expected to support stationary power generation applications. Stoichiometry in the main chamber is varied from $\lambda=1.0$ until the lean limit ($\lambda\sim 3.0$). Results from a new smaller single hole nozzle ($\varnothing=1.85\text{mm}$) is included to understand the effect of increased quenching in comparison to a 2.26 mm single hole nozzle. Also, in order to compare the performance of TJI with standard spark plug operation, a no-nozzle configuration, consisting of a single 3.81 mm hole is tested. The new and existing results from the previous chapter are analyzed with new performance metrics such as flame area and time dependent visible hot-jet penetration distance obtained from the optical images. Also, the 1st and 3rd derivatives values and their respective durations, extracted from the pressure signal, are compared for different nozzles and TJI operation strategy. The usability of these derived quantities for assessing the performance of TJI configurations in the passive and active mode are discussed.

4.2 Research Questions

1) In the previous chapter, high speed images helped visualize the jet shapes and their interaction in the main chamber environment and explained the trends observed in the burn duration calculations. Would measuring the jet penetration offer important insights, such as the effect of compressed pressure on jet penetration distance?

- 2) 0-10% burn durations did not show any trends in the previous chapter with respect to nozzle design, when λ in the prechamber was maintained constant. Will there be any sensitivity in the 0-10% burn durations if the λ in the PC is varied?
- 3) In the TJI configuration, two distinct peak pressure rise rates were observed during the combustion process. One during the jet ignition phase and other during the main chamber combustion phase. Can this data be used to analyze performance of the nozzles?
- 4) In this chapter, 'Jet ignition duration' is defined as the elapsed time between the 3rd derivative peaks (obtained from the pressure trace) located at the start of jet issuance and at the end of jet issuance. Can this data be used to analyze performance of the nozzles in the active and passive configurations?

4.3 Background and Literature Review

Several recent studies TJI have been completed using constant volume combustion (CVC) vessels, while these studies provide more practical access for imaging both the main chamber and prechamber combustion processes, they are limited to lower test pressures and temperatures. Additionally, the majority of these studies have used gaseous fuels (natural gas) which eliminates concerns regarding complex spray penetration within the prechamber [123] which will exist if liquid fuels such as gasoline is used. In studies conducted by Mastorokas et al. [124] and Allison et al. [125], flame propagation within a fueled prechamber was experimentally studied using an optically accessible quartz prechamber at atmospheric conditions. Fuels studied included ethylene and methane for nozzle diameters of 3mm and 6mm [124]. Jet penetration length was calculated from the OH* chemiluminescence optical data. For the 6mm nozzle the existence of a cylindrical reaction zone surrounded by unburned prechamber fuel-air mixture was observed within the

emerging jet from both the experiments and LES simulations. The methane jet flame was found to be weaker than the ethylene jets due to lower flame speeds, higher curvature induced quenching and turbulent stretch. Allison et al. [125] further extended the study to include 1.5 mm nozzle and also explored the effects of ignition location within the pre-chamber. With methane as the fuel, flame quenching occurred for both 1.5 mm and 3 mm nozzles. LES results indicated that a recirculation zone within the orifice can further reduce the effective diameter of the orifices and enhances quenching tendencies. Kammerstatter et al. [126] studied natural gas combustion using an auxiliary fueled prechamber ignition system in a constant volume combustion chamber equipped with intake and exhaust valves. Using high OH* chemiluminescence data the authors extracted jet penetration length and reacting area information. Their results revealed that larger nozzles had less auxiliary fueling requirement compared to smaller ones to achieve high ignition probability. Biswas et al. [127], using a CVC with dimensions resembling a large bore engine, explored the effect of spark discharge location within the prechamber using methane as the fuel. It was concluded that for spark plug positions nearest to the nozzle, the emerging jets had lower Reynolds number in the range of 2500 and 8000 resulting in laminar flame initiation. In another CVC study by Biswas et al. [128], a global Damköhler number was defined for the jet ignition process in order to remove parametric dependency thereby making the results from the CVC experiments applicable for practical applications. Biswas et al. [6] determined that the limiting Damköhler number, for which ignition probability is nearly zero, was 140 for CH₄/air and 40 for H₂/air.

In idealized reactors such as RCMs, higher initial pressures more relevant to practical combustors can be achieved since the compression process leads to higher pressures at TDC. In a computational study by Thelen et al. [129], for the same RCM configuration used in this study, it

was found that a 1.5mm orifice diameter produced the fastest 0-10% and 10-90% burn durations compared to 2.0 mm and 3.0 mm diameter orifices. The prechamber internal volume was 1 cubic centimeter (cc) which represented 2% of the main chamber clearance volume. The study used propane as a fuel at $\lambda=1.27$. The turbulent kinetic energy was found to influence only the initial phase of the combustion. Recently Gentz et al. [81] used iso-octane as both the pre and main chamber fuel [81] and used up to 3rd order pressure derivatives to identify inflection points for separating jet ignition and jet ignition induced auto-ignition processes in the RCM. Gholamisheeri et al. [130], for the same RCM configuration, studied a non-auxiliary injected prechamber (5% of the clearance volume) with methane for nozzles between 2.0-3.0 mm in diameter. Jet penetration distance and velocity was measured using the high-speed images. Results revealed a reduction in hot jet penetration speed with an increase in equivalence ratio. Also, a reduction in jet penetration speed was observed with decreasing orifice exit area.

4.4 Testing Strategy

Detailed explanation of the experimental setup and test methodology is provided in the chapter 3. Table 4-1 provides updated RCM test conditions and the test strategy corresponding to the prechamber operation is explained below.

Pre-chambers operated without auxiliary fuel injection are also referred as passive prechambers. Such configurations are typically used in stationary power generation applications and are already in production [98,99]. Usually a lean limit extension and stable operation when compared to spark plug operation is achieved [100]. In order to evaluate suitability of the nozzles under passive configuration all nozzles were tested for $\lambda=1.0$ to 1.5 and performance metrics were evaluated for a passive operation strategy. Each test point was repeated twice for this test strategy.

When operating in passive mode, at higher dilution levels, the stability of the TJI system is compromised due to poor ignitability and flame speed/flammability limits of the main chamber mixture. In order to increase combustion stability and further increase the lean limit tolerance, TJI is operated in the active mode in which natural gas is injected via the direct injector located within the pre-chamber. Mixture stratification achieved within the prechamber avoids misfires and promotes stable kernel formation within the spark electrodes. Prechamber fueling starts from main chamber $\lambda=1.8$ and is maintained until the lean limit. The pre-chamber lambda was maintained at 0.8 based on the optimal lambda value chosen from a prechamber lambda sweep study that will be discussed in the later sections. Each test point was repeated thrice in this operating strategy. Table 4-2 outlines the pre-chamber fueling strategy based on the global lambda.

Table 4-1- Overview of RCM experimental setup and initial conditions.

Bore	50.6 mm
Stroke	229 mm
Displacement volume	462 cc
Clearance volume	52.5 cc (without prechamber vol)
Prechamber volume	2.15 % of clearance volume
Initial pressure	1 bar
Compression ratio	10:1 (prechamber volume not included)
Aux fuel injection pressure	250 psi (gauge)
Spark dwell time	5 ms
Spark discharge timing	18 ms after TDC
Wall temperature	80 ° C
Compressed pressure (@ TDC)	16 bar and 30 bar
Initial Pressure (@ BDC)	1.0 and 1.3 bar
Fuel injector	Bosch - Production
Mainchamber lambda range	1 to 3
Mainchamber fuel	Methane
Prechamber fuel	Methane
Prechamber lambda(theoretical)	0.75 – 1.25
Injector pulse width range	1 to 1.6 ms
Nozzle hole(s) diameter	1.85 mm x 1, 2.26 mm x 1 & 1.57 mm x 2, 3.81 x 1 mm

Table 4-2- Prechamber fueling strategy.

Global Lambda	M/C Lambda	P/C Aux Fuel
1	1.00	Off
1.25	1.25	Off
1.5	1.50	Off
1.78	1.80	On (P/C $\lambda \sim 0.8$)
2.21	2.30	On (P/C $\lambda \sim 0.8$)
2.48	2.60	On (P/C $\lambda \sim 0.8$)
2.75	2.90	On (P/C $\lambda \sim 0.8$)
2.93	3.10	On (P/C $\lambda \sim 0.8$)
3.02	3.20	On (P/C $\lambda \sim 0.8$)

4.5 TJI Nozzle Descriptions

In Figure 4-1, the cross sections of the nozzles considered for this study are illustrated. The two-hole nozzles, namely the diverging jets and converging jets nozzles, and a single hole nozzle with a nozzle diameter of 2.26 mm were introduced in chapter 3. This enabled the comparison of the effect of nozzle distribution and the number of nozzles for the same cross-sectional area. Also, in order to compare the effect of orifice diameters, for the single hole nozzles, a smaller hole nozzle (1.85mm) is added to the test matrix. For this smaller hole nozzle, designing an equivalent cross-sectional area two-hole nozzle would result in a nozzle diameter smaller than 1.5mm and hence such a nozzle was not tested. In this chapter the 1.85 mm single jet nozzle will be referred to as the small hole nozzle and the 2.26 mm single jet will be referred to as the large hole nozzle. The largest nozzle has a diameter of 3.81 mm and is referred to as the no-nozzle design and is assumed to be that of ignition via standard spark plug and hence enables comparison of the passive TJI configuration to that of a standard spark plug. This assumption avoids change in the clearance volume if the prechamber is replaced with a spark plug. Here the nozzle diameter equals the diameter of the throat section in the prechamber and no restriction to the flow is provided. The throat section and its internal cavity volume is illustrated in Figure 4-2.

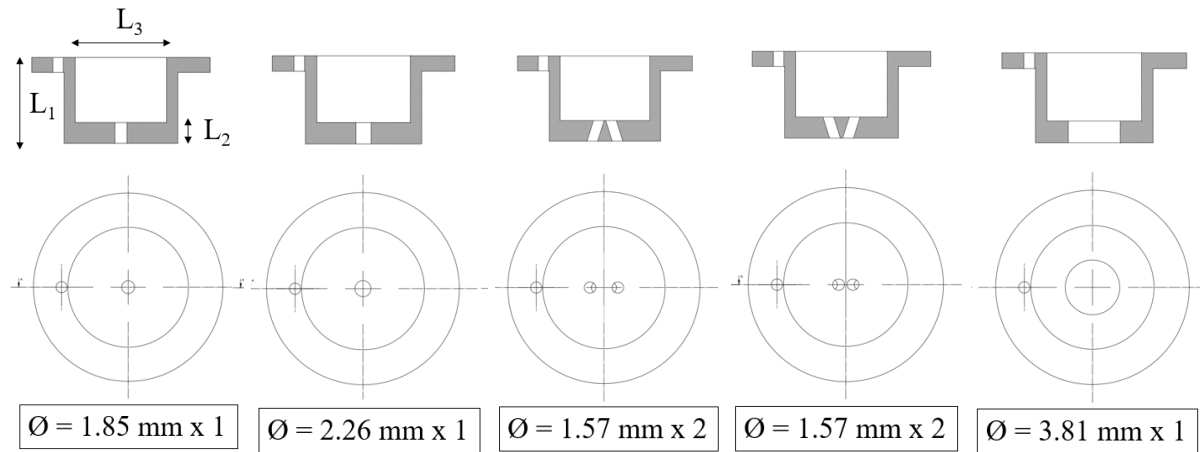


Figure 4-1 Sectional and bottom views of nozzle configurations used in the TJI igniter for this study with $L_1=13.16\text{mm}$, $L_2=3.175\text{mm}$ and $L_3=17.22\text{mm}$.

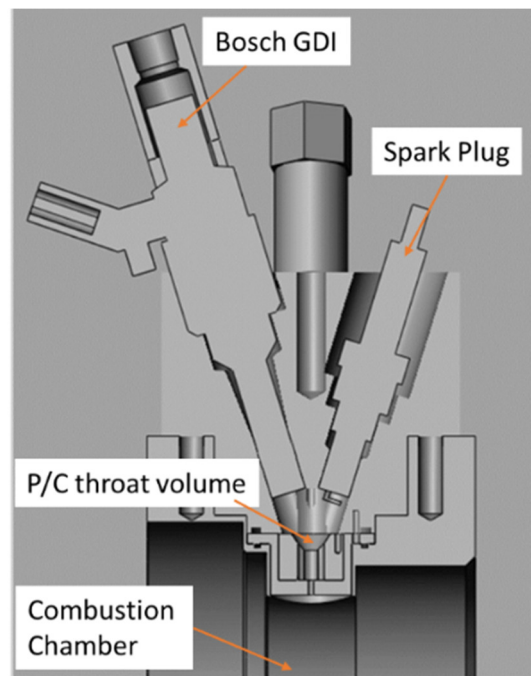


Figure 4-2 Cross sectional view of the TJI igniter installed in RCM head.

4.6 Results and Discussions

4.6.1 Passive TJI images

To illustrate the TJI process when operating in the passive prechamber configuration, high speed images for the $\lambda=1.5$ test case are shown in Figure 4-3. The leaner case allows the jet to penetrate for a longer time before strong main chamber ignition occurs and hence observation of jet structures can be performed for a longer duration relative to the $\lambda=1.0$ and 1.25 cases. At $\lambda=1.5$, large variations were observed in the pressure curves and hence the test case corresponding to the faster burning test is shown in the images. Here the images are enhanced by adjusting contrast and brightness using ImageJ software [131]. The images are presented with 0 ms occurring at spark discharge and hence jet penetration time is influenced by the flame propagation event within the pre-chamber. Among the single hole nozzles, the smaller hole nozzle jet shows stronger penetration and faster radial growth compared to the large hole nozzle jet. With the multi hole nozzles, the converging jets visually appear as a single jet. However, the converging jet shows stronger radial growth and wall impingement is significantly reduced compared to the larger hole nozzle. The diverging jets have better penetration and area coverage compared to the other jet configurations. For the no-nozzle test cases, jet like physics are visible during the initial stages of penetration. Roughly 5 mm away from the prechamber exit, a spherical flame structure is formed, and this strongly resembles the spherical flame formed during the later stages of the spark ignition process. In contrast to the single source jets, the ignition happens at the top portion of the combustion chamber and growth is more pronounced in the top regions. The no-nozzle case exhibits very slow flame propagation speed compared to the jet ignition cases mainly due to the reduced penetration and lower turbulence generated within the main chamber. Cold jets of unburned mixture are discharged from the orifices prior to the appearance of hot jets. Other than

increasing the turbulence intensity they also create a local charge stratification in the main chamber in the active configuration. In the main chamber, the turbulence intensity rises initially because of the cold jets and later due to the hot jets [94,129]. Turbulence enhances mixing and this enables wrinkling of the flame surface thereby increasing its surface area allowing for increasing consumption in the unburned zone [132]. The jet configurations also affect the turbulence levels due to difference in velocity of the issued jets.

4.6.2 Active TJI images

For the active configuration, when additional fuel is injected directly into the prechamber, discussions related to large, diverging and converging jets were made in chapter 3. It was concluded that the diverging jets offered better burn rates. In comparison to the single jets, the converging jet offered faster burn rates and reduced wall impingement. Similar overall trends were observed as in the passive configuration discussed above. The main difference between the active and passive configurations was the behavior of the small hole nozzle in comparison to the large hole. With auxiliary fuel injection, the jets have similar penetration and area growth. From Figure 4-4, it can be seen that most of the combustion process, up to 8.6 ms, appears similar for both the single hole nozzles. This is in contrast to the passive configuration where the smaller hole nozzle had earlier penetration compared to the large hole nozzle. Between 2.6 ms and 3.6 ms the smaller hole nozzle achieves faster penetration compared to the large hole nozzle. This is due to the fact that with smaller hole nozzles the pressure buildup in the prechamber is higher due to more of the contents being burned before mass starts to leave the prechamber. For the small hole nozzle test case, existence of this higher delta pressure could be the reason for the faster penetration.


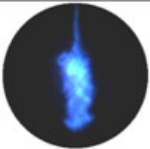
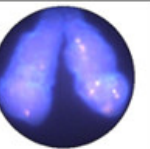
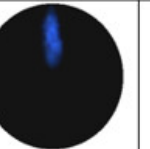
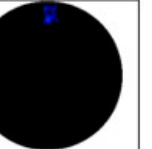


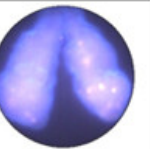
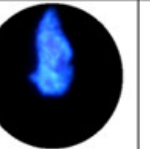
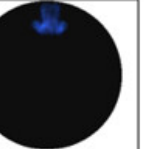
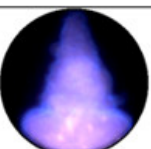
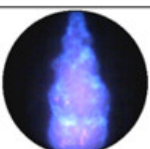
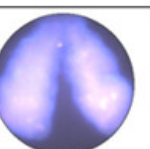
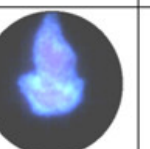
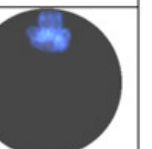
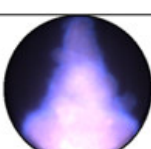
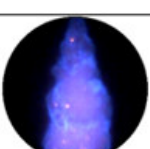
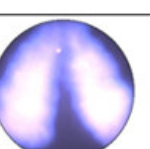
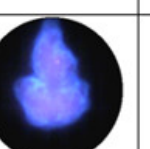


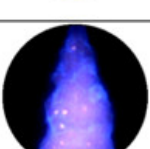
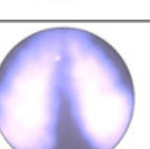
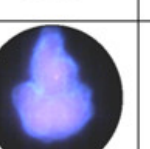

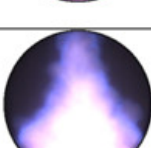
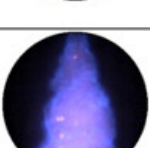
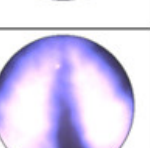
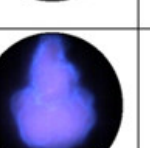
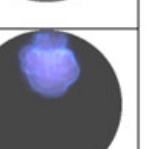
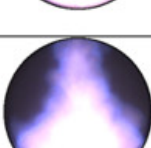
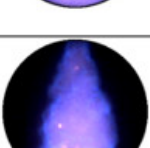
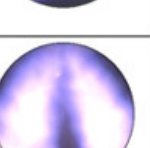
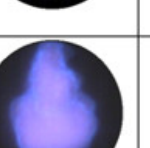
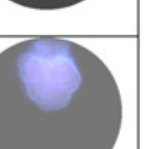
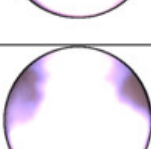
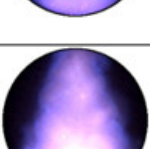
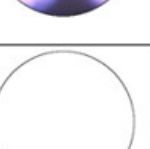

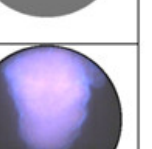
Time after spark	Small Hole	Large Hole	Diverging	Converging	No Nozzle
4.3 ms					
4.6 ms					
4.9 ms					
5.2 ms					
5.5 ms					
5.8 ms					
6.1 ms					
8.1 ms					

Figure 4-3 High speed images showing mainchamber combustion in passive TJI mode for all five nozzles at $\lambda=1.5$. Images are enhanced for better visualization.

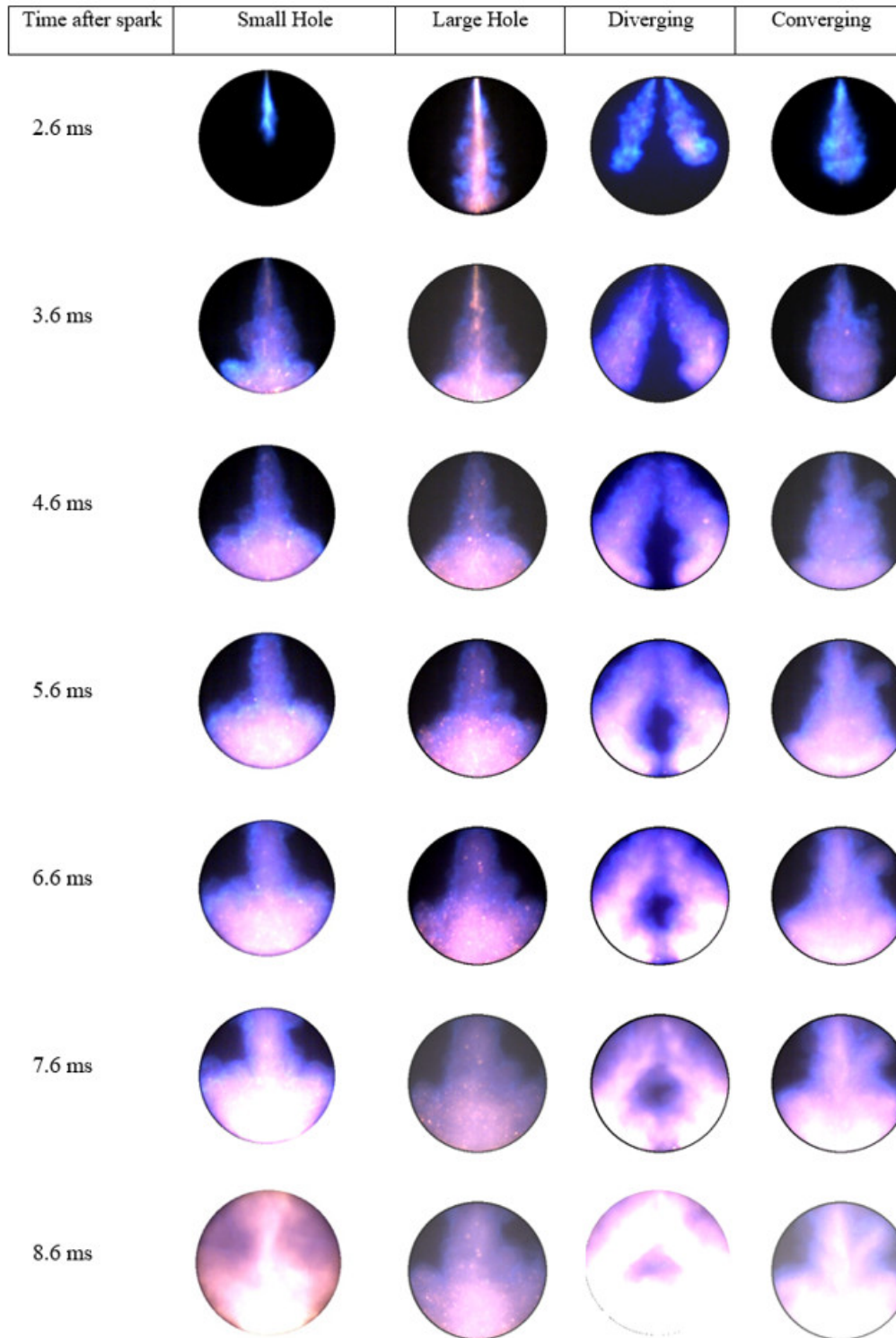


Figure 4-4 High speed images showing combustion in active TJI mode for global $\lambda=1.78$. Images are enhanced for better visualization.

4.6.3 Flame Area Analysis

An image processing algorithm developed using MATLAB® was used to carry out flame area study for the TJI system. A detailed description of the MATLAB® code used here is provided in chapter 3. For $\lambda = 1.78$ it was noted that the 90% burn duration time matched the 90% flame area, but the 10% burn point did not correlate well with the flame area due to the nature of the TJI ignition process, therefore, the flame area correlation is not repeated in this chapter. The flame area calculation plot for a global $\lambda=1.78$ for all 4 nozzles tested in the active configuration is shown in Figure 4-5. The standard error is shown as error bands in these plots. At $\lambda=1.78$, the small hole nozzle exhibits similar growth to the converging jets. This correlates with the 10-90% burn durations, shown in later sections, where the small hole and converging jets have similar durations. The large hole nozzle exhibits the slowest growth as observed in the 10-90% values. For leaner cases, past $\lambda=1.78$, the images had little luminosity and extracting pixel information was more difficult. Additionally, the flame area plot for the nozzles at $\lambda = 1.5$ is shown in Figure 4-6. In Figure 4-6, it can be seen that the smaller hole nozzle has more area coverage compared to the larger hole nozzle, although this was not easily observed in the high-speed images. The higher area coverage of the small nozzle should also indicate faster burn durations which is verified in the later sections of this work. It can be seen that the diverging jets and small hole nozzle show very large variations at the leanest passive case. This variation in flame area is expected to be visible in the pressure traces which will be shown and discussed in coming sections. Flame area calculations were not performed for the passive mode cases at $\lambda = 1$ and 1.25 due to the tendency of the images to get saturated which introduced large uncertainties in the later stages of the combustion process. This is illustrated in Figure 4-7 for the large hole nozzle at $\lambda = 1$ where it can be seen that edge

details of the flame are lost due to emission intensity. Reducing the aperture for these conditions obscured the observation of the initial jet.

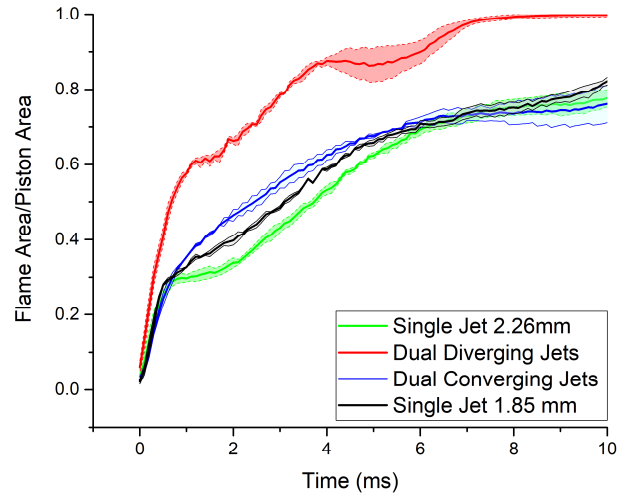


Figure 4-5 Comparison of normalized flame area in active TJI mode for all nozzle configurations at $\lambda=1.78$.

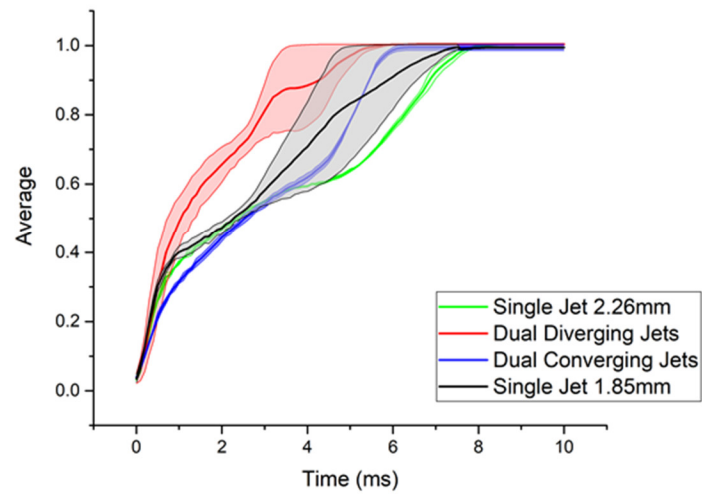


Figure 4-6 Comparison of normalized flame area in passive TJI mode for all nozzle configurations at $\lambda=1.5$.

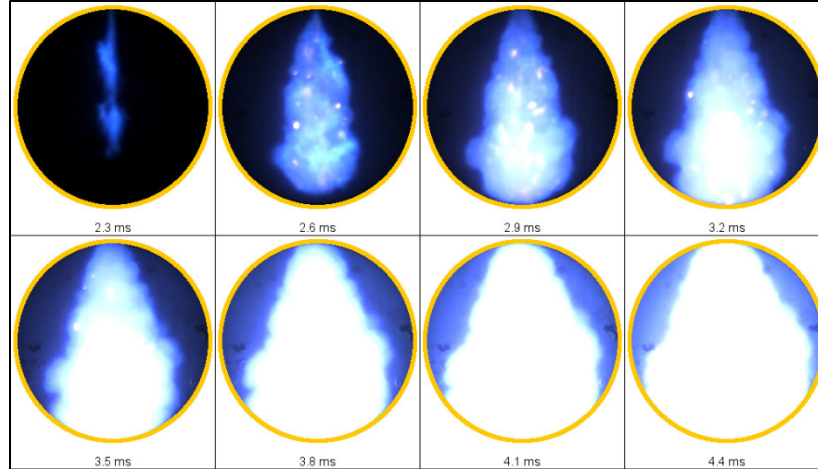


Figure 4-7 High speed images showing jet penetration and main chamber combustion for the large hole nozzle configuration at $\lambda = 1.00$.

4.6.4 Jet Penetration Analysis

An edge detection code using MATLAB® was used to identify the leading edge of the flame from the high-speed image as illustrated in Chapter 3. The jet penetration length was extracted by measuring the distance from the mid-point of the nozzle exit to the leading edge of the flame along the jet axis for each frame until wall impingement was observed. The jets exhibited strong axial growth for the time duration of this measurement. Radial growth was only pronounced when the jets reached the vicinity of the walls. Hence these measurements offer sufficient resolution capturing the trends in jet penetration. The measured jet penetration distance is normalized by the value D , where D equals 52 mm (the diameter of the bore) in the case of single jets and the dual converging jets. For the case of the diverging jets, $D = 47\text{mm}$ was used which represents the axial distance between mid-point of nozzle exit to the combustion chamber wall. The jet velocity was not calculated from the penetration data since the frame speed of 10000 fps used was not sufficient to obtain enough velocity data points in order to capture trends. Hence only the jet penetration is measured and shown in this section. The time scale on the x-axis starts at the instance the jet first appears in the main-chamber and is not based on the start of the spark event in the prechamber as

in previous sections. For leaner cases, past $\lambda=1.78$, the images had little luminosity and extracting pixel information was more difficult. Hence edge extraction was not performed for test points leaner than $\lambda=1.78$.

In Figures 4-8, 4-9 and 4-10 the nozzle designs are separately compared in terms of jet penetration length, and comparison is made for both passive and active configurations. For the single hole designs a solid trend cannot be observed due to the fast penetration. The faster penetration is also represented in Figure 4-7 with the large hole nozzle at $\lambda=1$. Hence, a higher frame rate is required for the single hole nozzles due to early impingement. In the case of the diverging nozzle a better trend emerges and it can be seen that both $\lambda=1.0$ and $\lambda=1.8$ remain fastest with minimal difference between them. It should be noted that the jet penetration for $\lambda=1$ is mainly due to the main chamber mixture flame propagation speed since the jets quickly reignite in the main chamber before reaching the walls. However, for the $\lambda=1.8$ condition the jet velocity is responsible for the penetration speed since the reignition in the main chamber is delayed due to high dilution. Also, it is interesting to see that both $\lambda=1.25$ and $\lambda=1.5$ attain the same penetration speed in the middle of the jet penetration phase. Although, the converging hole nozzle looks visually similar to the single hole nozzles, it has a slower penetration speed in comparison as can be seen in Figure 4-10. The observation is similar to that of the diverging hole nozzles at $\lambda=1$ and $\lambda=1.8$, which show the fastest penetration whereas $\lambda=1.5$ shows the slowest jet penetration speed. For the converging hole nozzle, the difference in penetration distance versus time between the $\lambda=1.25$ and 1.5 test points, is greater in comparison to the single hole nozzles.

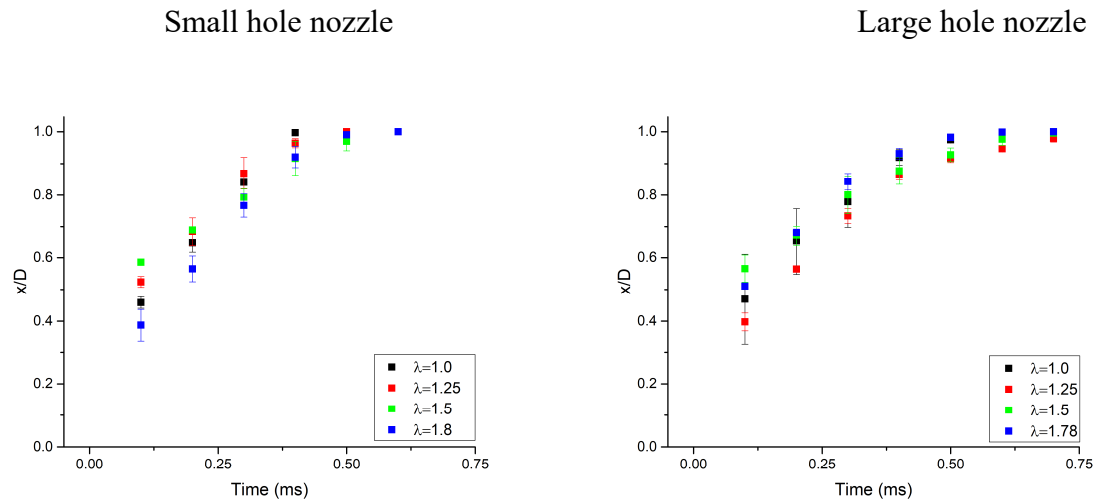


Figure 4-8 Normalized jet penetration values for the small hole nozzle (left) and the large hole nozzle (right) for active and passive TJI systems.

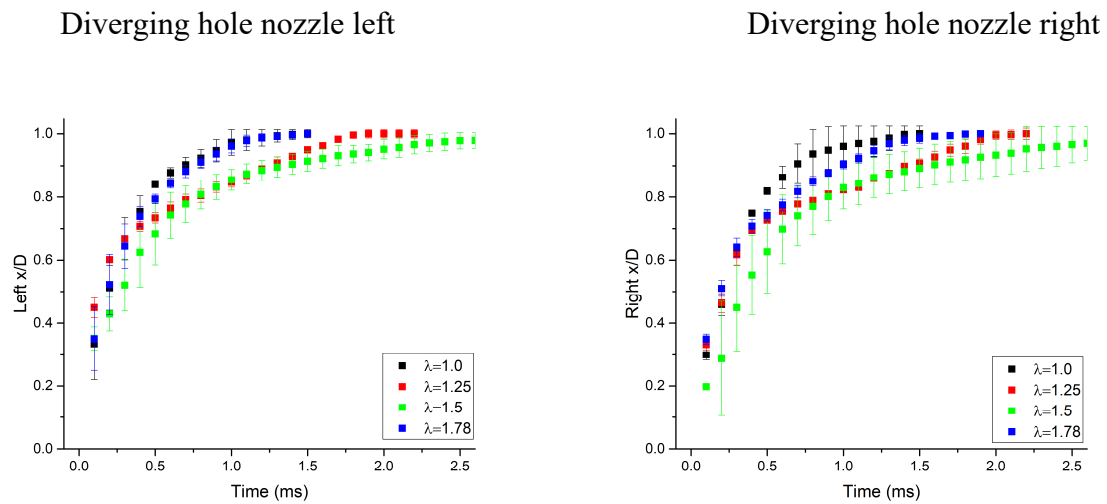


Figure 4-9 Normalized jet penetration values for the diverging nozzles with the left plot corresponding to the left hole and the right plot corresponding to the right hole for the active and passive TJI systems.

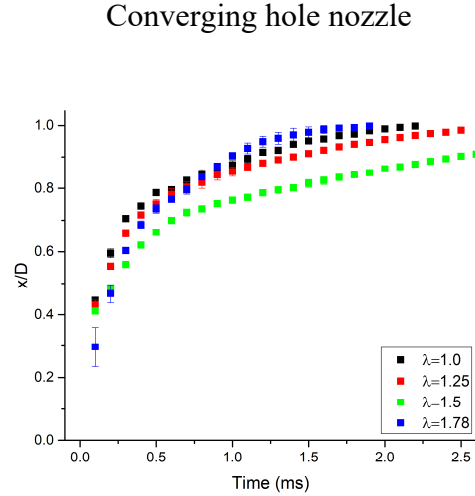


Figure 4-10 Normalized jet penetration values for the converging nozzle for active and passive TJI systems.

4.6.5 Prechamber Lambda Sweep

The effect of varying prechamber lambda values on jet penetration is illustrated in Figure 4-11. For these experiments the main chamber lambda was kept constant at $\lambda=1.8$, but the prechamber lambda was varied by changing the pulse width of the injector. The experiments were only conducted for the diverging jets configuration. From the jet penetration measurements, it is clear that the penetration is fastest when the prechamber is at $\lambda=0.8$. It can be observed that for $\lambda=0.75$ the jet penetration is similar to that at $\lambda=1.0$. In terms of penetration, no clear advantage is observed if the prechamber mixture gets richer than $\lambda=0.8$. The penetration speed is important for TJI design since faster penetration can help burn the end gas mixture first in an IC engine and could potentially enable knock mitigation [133]. From the plots it is clear that both $\lambda=1.10$ and $\lambda=1.25$ offer slower penetration compared to the other lambdas. Therefore, it is clear that $\lambda=0.8$ in the prechamber is optimal for active TJI operation and is a suitable lambda value for evaluating various prechamber designs.

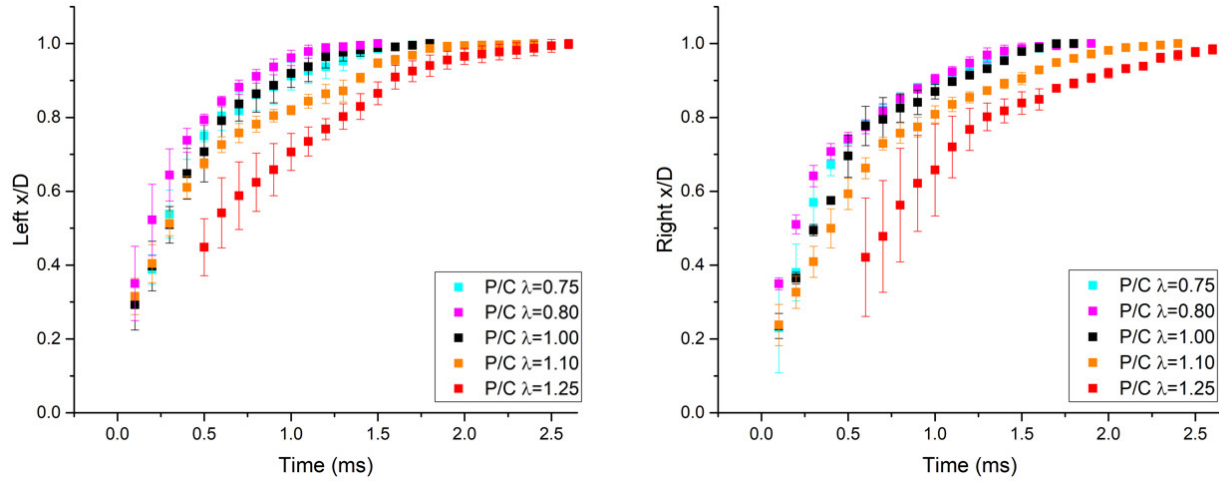


Figure 4-11 Normalized jet penetration curves for the diverging nozzle showing the effect of varying pre-chamber λ for a fixed mainchamber $\lambda=1.8$.

4.6.6 Effect of Initial Pressure on Jet Penetration

The current set of experiments were done to understand the effect of initial pressure on jet penetration. From a fundamental perspective it is known that the laminar flame speed of the fuel-air mixture decreases with increasing pressure for most lower hydrocarbons [134]. Also, an increase in initial pressure of fuel-air mixture leads to a decrease in flame thickness. This in turn leads to a decrease in quenching distance [125]. In Figure 4-12, the penetration distance for the left and right jets for the dual diverging nozzle design is measured for an initial pressure of 1 bar and 1.3 bar. These initial pressures resulted in a compressed pressure of 16 bar and 21 bar respectively. It is clear that the lower initial pressure results in higher penetration speeds. Also, in order to check the prechamber λ sensitivity with increasing pressure, the higher-pressure case was tested for two prechamber λ s ($\lambda=0.8$ and 1.1). In comparison with the lower pressure runs the higher initial pressure resulted in reduced pre-chamber λ sensitivity, which indicates that with increasing pressure jet penetration displays a different range of λ sensitivity. This shows the implications on jet penetration for naturally aspirated vs. boosted

engines, where for the later, higher compressed pressures are expected during the combustion event.

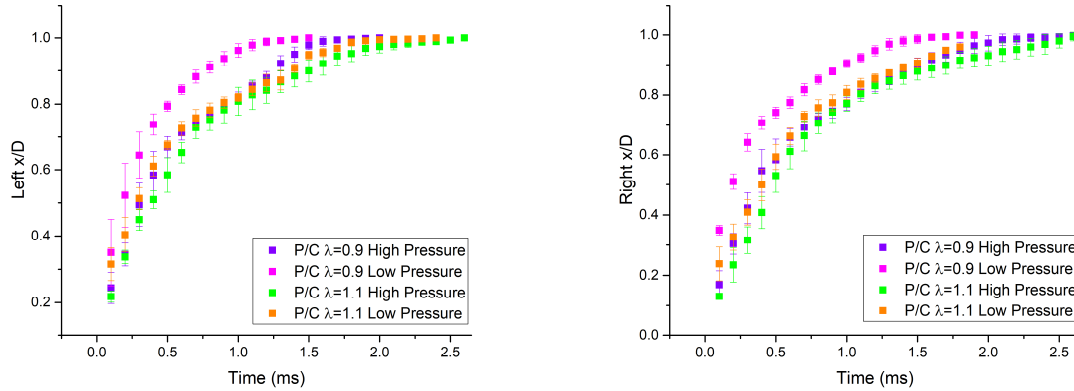


Figure 4-12 Normalized jet penetration curves for the diverging nozzle showing the effect of varying prechamber λ and increasing mainchamber pressure for a fixed mainchamber λ of 1.8.

4.6.7 Main Chamber Pressure Analysis

A detailed description of the RCM events as described by the pressure history and the definition of extracted burn durations are provided in chapter 3. The pressure curves corresponding to all the nozzles tested under passive conditions for $\lambda=1$ are shown in Figure 4-13. It can be observed that the single hole nozzles have very similar burn profiles at stoichiometric conditions. However, the diverging jets and converging jets (2-hole nozzles) offer faster burn durations compared to the other nozzle types. The diverging jets offers the fastest pressure rise and the no-nozzle case has the slowest burn duration. A similar trend is seen for $\lambda=1.25$ but with a slightly increased variation as shown in Figure 4-14. It can be concluded that no sensitivity to nozzle diameter is observed for the single hole nozzles in the 1-1.25 lambda range. At $\lambda=1.5$ higher variation is observed across all nozzle types as shown in Figure 4-15. The pressure curves of all the nozzles start to overlap at $\lambda=1.5$ with the fastest average phasing shown by the diverging jets and the slowest phasing by the no-nozzle case. In Figures 4-13 to 4-15, we can see that the as the mixture gets leaner the no-

nozzle case pressure rise falls much faster compared to the TJI configurations. This highlights the benefit of operating lean with TJI even in the passive mode. In the high-speed images (Figure 4-3), it was shown that the small hole nozzle had the highest penetration and flame area compared to the single jet and the pressure data reflects the same if average phasing is considered. This is in contrast with the λ 1.0 and 1.25 cases. The variation in these pressure traces is also reflected in the burn area plots shown in Figure 4-6.

In Figure 4-16, the averaged main chamber pressure traces for up to $\lambda=2.48$ for the auxiliary injected cases are shown for all 4 nozzles. The global λ values include the prechamber fuel in the overall λ calculation. The no-nozzle configuration is not considered for the auxiliary injection strategy. It can be observed that the diverging nozzle produces a higher and faster pressure rise and is more repeatable as the global λ increases. The small hole nozzle pressure curves overlap with the average pressure curves for the converging nozzle. The differences in combustion phasing in terms of burn rates will be further discussed in the burn rate section below. A representative set of pressure traces showing a complete λ sweep can be seen in Figure 4-17 for the small nozzle configuration. Repeatability, and thus combustion stability, decreases as we move away from the stoichiometric condition, with increased variability observed for the $\lambda=1.5$ case in the passive configuration. Auxiliary injection begins at $\lambda=1.78$ and it can be seen in Figure 4-16 that these test cases are as repeatable as the stoichiometric condition. For the non-auxiliary injection case, $\lambda=1.25$ can be considered to be an acceptable limit due to repeatability. Unlike a conventional IC engine combustion environment, in the RCM the jet penetration is the major source of turbulence. With no additional in-cylinder charge motion in the RCM, the improved stability at $\lambda=1.78$ is purely due to turbulent, thermal and chemical benefits provided by the TJI system. As we further dilute the main chamber mixture, the repeatability of the main chamber

pressure reduces. For this study, lean limit for a nozzle is defined as the lambda value before which combustion of the main chamber charge is no longer observed [135]. Past the lean limit there is a small initial pressure rise in the main chamber, which is mainly due to the prechamber combustion process [81]. The small nozzle exhibits a lean limit of $\lambda = 2.93$. This lean limit value is similar to that of the diverging nozzle case and is slightly lower than the 3.02 limit observed in the chapter 3 for large hole and converging nozzle configuration. It is possible that the reduction in lean limit for the small hole nozzle is due to the higher heat losses experienced by the jet as it passes through the smaller orifice or it may be due to the relatively higher level of wall impingement. Also, in the passive prechamber configuration (Figure 4-15) it was observed that the repeatability of the diverging nozzle and small hole nozzle was less compared to the others for the leanest case. This coupled with the lower lean limits in the active mode most likely indicates that the heat loss due to the jet distribution or excessive quenching decreases the lean limit but does not necessarily affect the burn rates. The pressure records for global lambda leaner than 2.48 for the other three nozzles can be found in chapter 3.

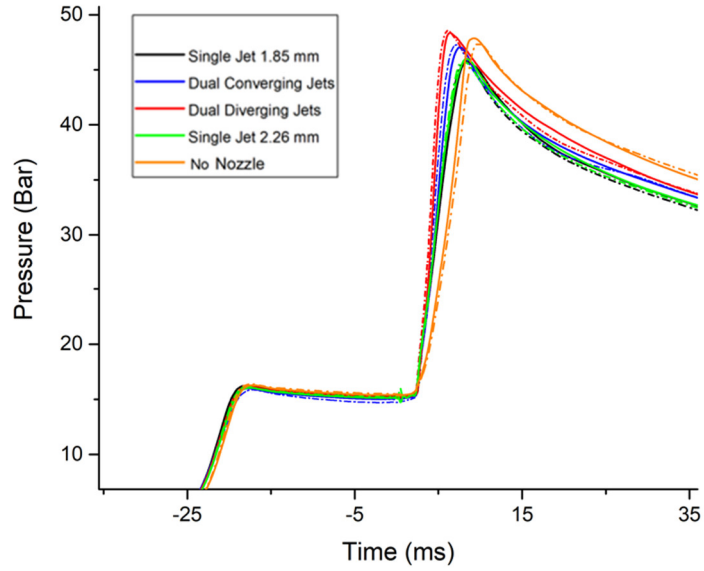


Figure 4-13 Main chamber pressure for TJI nozzles in the passive configuration at $\lambda=1$. The x-axis 0 ms corresponds to the spark discharge event.

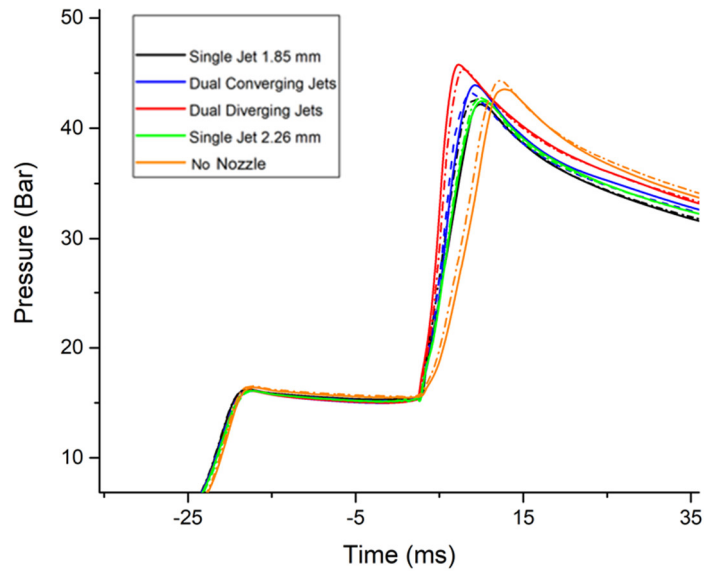


Figure 4-14 Main chamber pressure for TJI nozzles in the passive configuration at $\lambda=1.25$. The x-axis 0 ms corresponds to the spark discharge event.

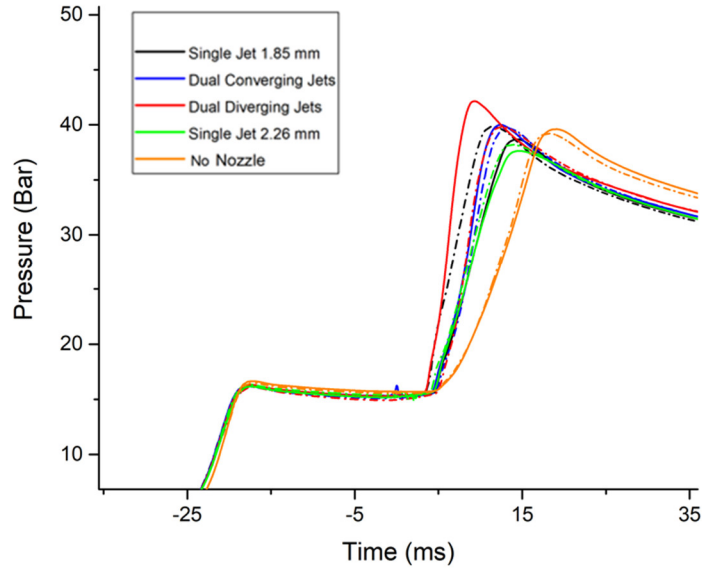


Figure 4-15 Main chamber pressure for TJI nozzles in the passive configuration at $\lambda=1.5$. The x-axis 0 ms corresponds to the spark discharge event.

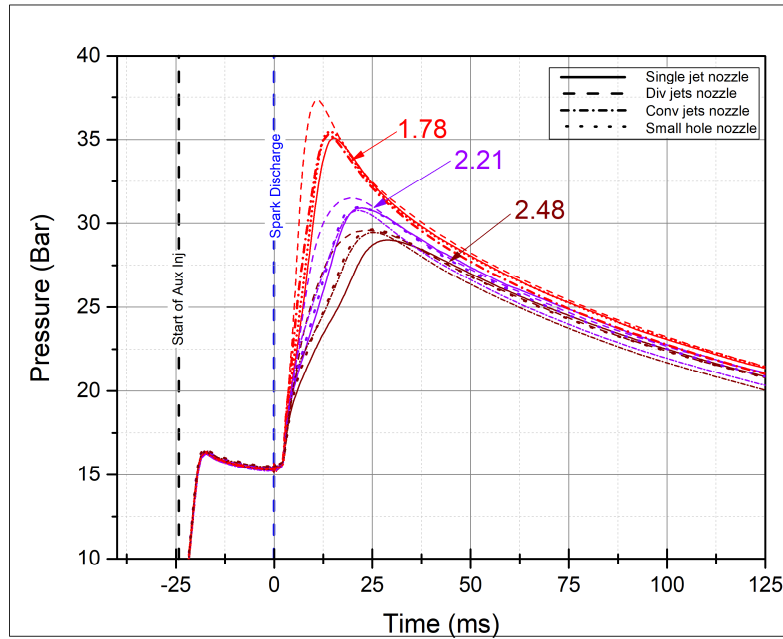


Figure 4-16 Comparison of averaged main chamber pressure curves in the active TJI mode for up to a global lambda value of 2.48.

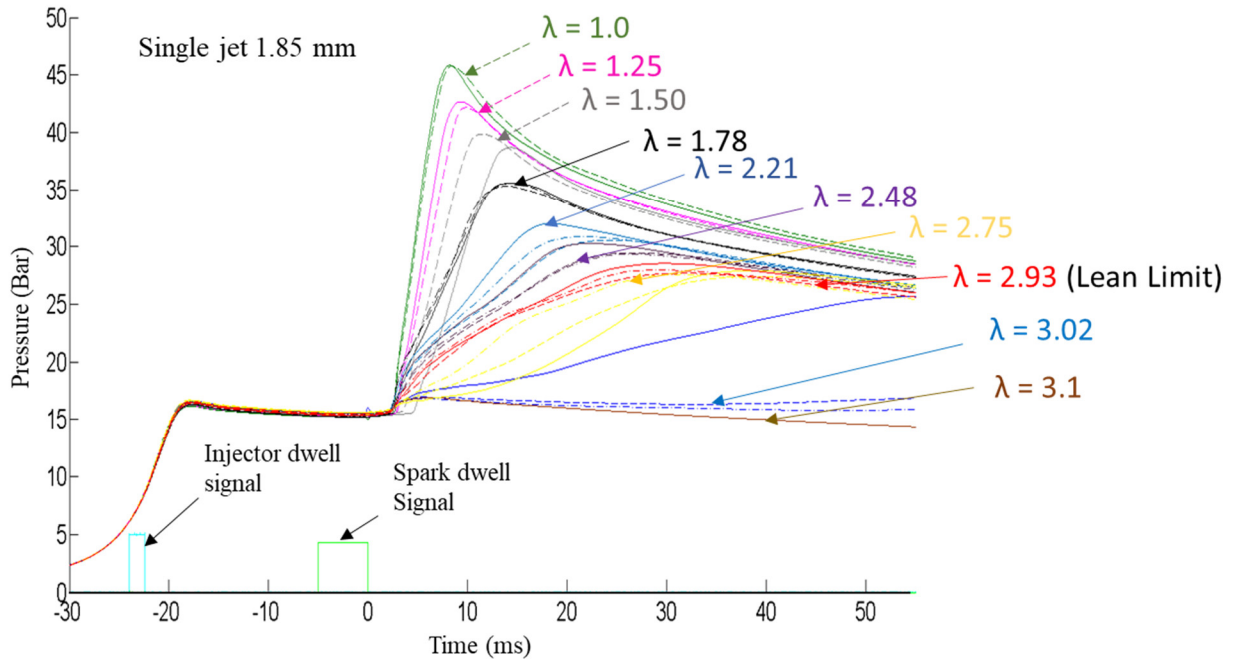


Figure 4-17 Pressure for the small hole nozzle showing prechamber operation mode changing from passive to active (past $\lambda=1.5$) until lean limit is achieved.

4.6.8 Burn Rate Data

The pressure records for global lambda leaner than 2.48 for the other three nozzles can be found in a previous publication in chapter 3 of this thesis. The pressure records in the main chamber were further used to extract burn durations as illustrated in the RCM events section. The burn durations in the passive and active TJI mode are presented separately and usability of these performance metrics for future RCM experiments will be discussed. The 0-10% burn duration indicates the effectiveness of an ignition device to initiate combustion [136]. The average burn duration 0-10% for passive TJI operation is shown in Figure 4-18. At $\lambda=1.0$ and $\lambda=1.25$, all of the nozzles exhibited a very similar burn rate. At $\lambda=1.5$, a high deviation can be noted and based on the average values, the smaller hole nozzle and dual diverging jet nozzle offer the faster initiation. Although strong trends regarding performance of the individual nozzles cannot be determined from Figure 4-18, a trend of increasing 0-10% duration with increasing lambda can be observed overall.

In Figure 4-19 a comparison of 10-90% for all nozzles in passive TJI operation is shown. Compared to the 0-10% plots, performance trends can be observed in the 10-90% burn duration plot. The dual diverging jets consistently offer shorter combustion durations followed by the converging jets configuration. Both the single hole nozzles exhibit similar but longer burn durations throughout the lambda range. In chapter 3, for the active TJI configuration, it was found that the 10-90% burn duration values converged as the nozzles approached their respective lean limits, with the diverging jet configuration the slowest. However, such an observation was not noted for the passive configuration, possibly indicating that the lean limit for the passive configuration is not reached at $\lambda = 1.5$.

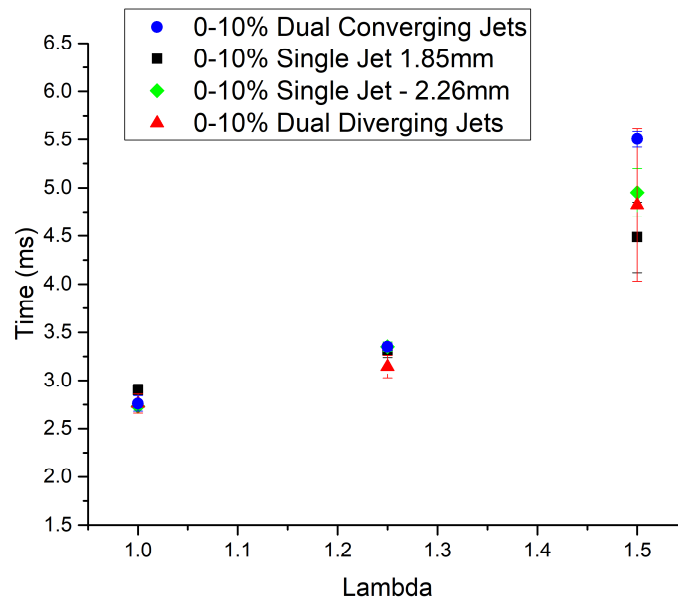


Figure 4-18 0-10% burn duration comparison for the passive TJI (no auxiliary injection) test points.

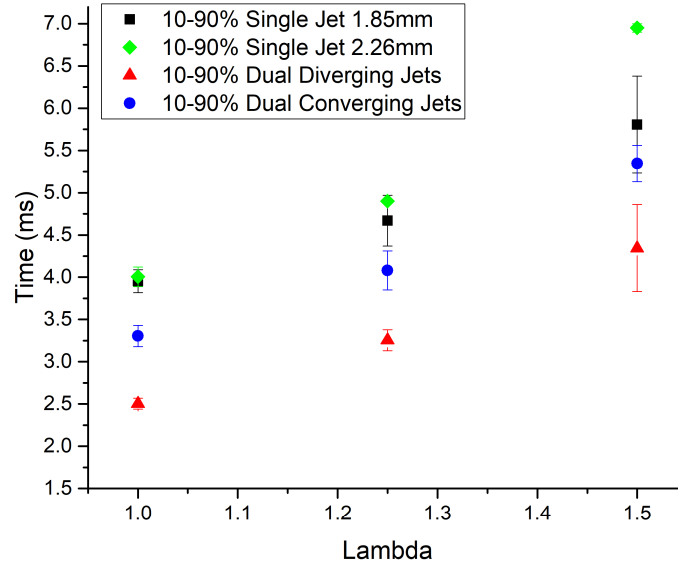


Figure 4-19 10-90% burn duration comparison for the passive TJI test points.

In Figure 4-20 the 0-10% burn duration for the auxiliary fuel injected test points are shown. It can be seen that similar times are observed for all the nozzles, independent of global lambda, with the large nozzle showing the shortest duration at $\lambda=2.5$. At $\lambda=2.72$, the 0-10% burn durations appear to converge. The smaller hole nozzle is slower than the diverging jets configuration in initiating combustion at the lean limit. Unlike the 0-10% burn duration plot for the passive TJI test points, the 0-10% burn durations show no sensitivity to the global lambda values. This indicates that the 0-10% burn duration is a strong function of the prechamber lambda, since the lambda values within the prechamber were held constant in the active configuration but were variable in the passive configuration.

The 10-90% burn duration for the active TJI configuration for the large hole and two-hole nozzle configuration were previously discussed in chapter 3. Figure 4-21 shows the burn duration plot updated with the smaller nozzle and interesting trends can be observed. In chapter 3 it was

observed that the dual diverging jets offered the fastest burn rate until global $\lambda=2.5$ was reached after which the burn rates of all nozzles converged, however the diverging jet was the slowest at its lean limit. It can be seen that the smaller single hole nozzle performs similarly to the converging nozzle, however the large single hole nozzle has the longest burn duration. This difference between the two single hole nozzles may be due to the increased heat losses that occur as the jet passes through the smaller orifice, which leads to the jet having a lower thermal energy. However, the smaller hole nozzle has comparable burn durations to the converging jet case despite exhibiting higher impingement (hence loss of thermal and turbulent energy) as observed in the initial images. There could be two explanations for this behavior. First, the pressure rise in the pre-chamber is higher for the smaller hole case due to the larger restriction, promoting higher levels

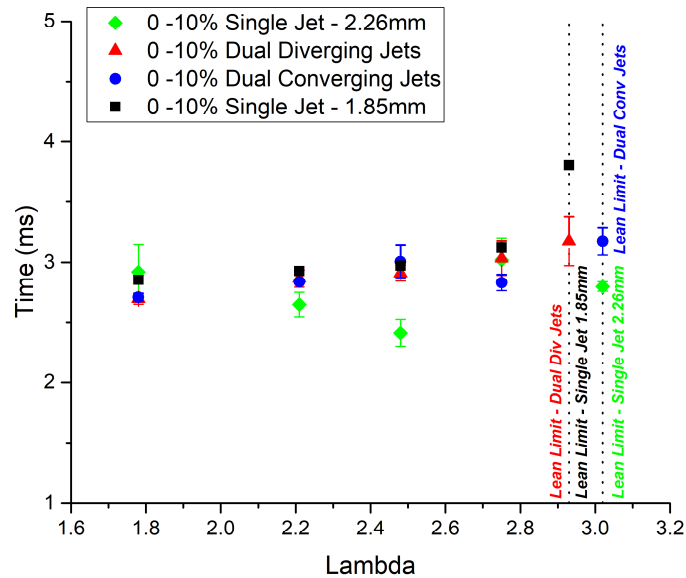


Figure 4-20: 0-10% burn duration comparison for the active TJI configuration.

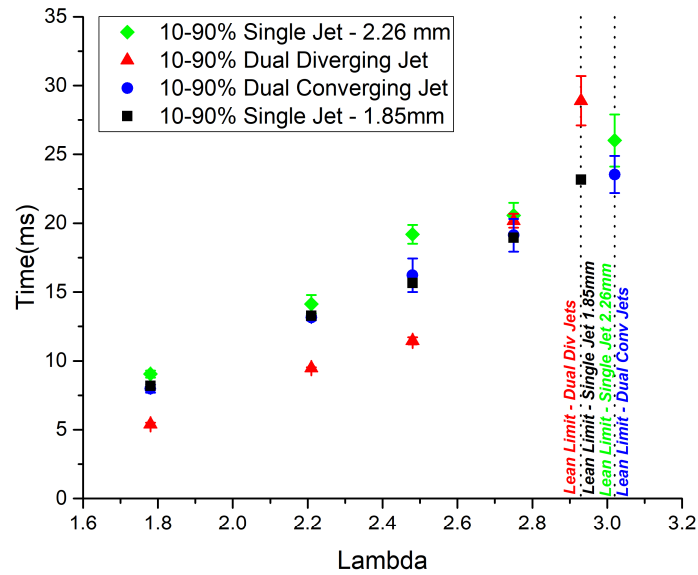


Figure 4-21 10-90% burn duration comparison for the active TJI configuration.

of turbulence in the main chamber and second, the converging jets may have reduced turbulent kinetic energy levels due to the cross impinging nature of the jets. A CFD study may shed more light on the latter observation. The smaller hole nozzle also has a shorter burn duration at the lean limit. Based on the 10-90% burn duration data, the converging jet and smaller single hole nozzle have similar performance and indicating a potential tradeoff between loss of kinetic energy and thermal energy.

The burn duration data was analyzed for a prechamber lambda sweep, where the prechamber lambda was varied for a fixed mainchamber lambda value of 1.78. In the previous section, for the passive configuration, it was found that the 0-10% burn duration did not exhibit any sensitivity to the nozzle type, and in case of the active TJI configuration no sensitivity was observed for the nozzle type and global lambda values. In an earlier study by Gentz et al. [81], the 0-10% burn duration data exhibited sensitivity towards prechamber lambda. In Figure 4-22, the 0-10% burn

durations are plotted with the x-axis representing the pre-chamber lambda. It can be observed that there is a minimum in the 0-10% burn duration at $\lambda=0.8$, and hence this value was used in the rest of active TJI test cases. This value is also consistent with previous research on the optimal prechamber lambda value [13,137]. It should be noted that for prechamber lambda values in the range of 0.75 to 1.0 the difference in 0-10% duration is less than 10% and this range represents the tolerance that can be maintained with respect to prechamber lambda for optimum ignition initiation. It can be concluded that the 0-10% burn duration is not a very relevant performance metric for constant lambda within the pre-chamber irrespective of the nozzle type and main chamber lambda.

In Figure 4-23, the 10-90% burn duration is compared in terms of the prechamber lambda. As observed in the 0-10% burn duration data, $\lambda=0.8$ has the shortest average combustion duration and for the lambda range of 0.75 to 1.0 the difference in burn duration is less than 5%. Figures 4-22 and 4-23 indicate that it is essential to maintain a slightly rich lambda in the prechamber for natural gas applications. Considering the potential loss of prechamber auxiliary fuel to the main chamber during the injection event [138], it is possible that the actual prechamber lambda could be closer to 0.9 compared to a theoretical value of 0.8. Details on the calculation of the theoretical lambda value can be found in chapter 3. At $\lambda=0.9$ the fastest laminar flame speed is achieved for hydrocarbon mixtures because of higher adiabatic flame temperature [139]. In addition to high thermal energy, pre-mixed flames from richer mixtures tend to produce higher unburned active radicals with quenching. Since the prechamber fuel does not contribute much to power output, excess auxiliary fueling should be avoided for improved efficiency and reduced prechamber sourced emissions [140].

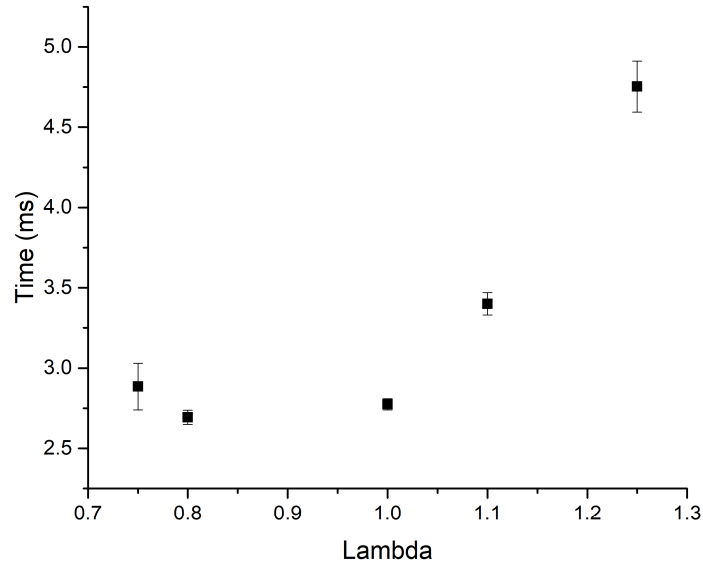


Figure 4-22 0-10% burn duration comparison for the dual diverging nozzle in the active TJI configuration for fixed main chamber lambda and varying prechamber lambda. The x-axis indicates the prechamber lambda value.

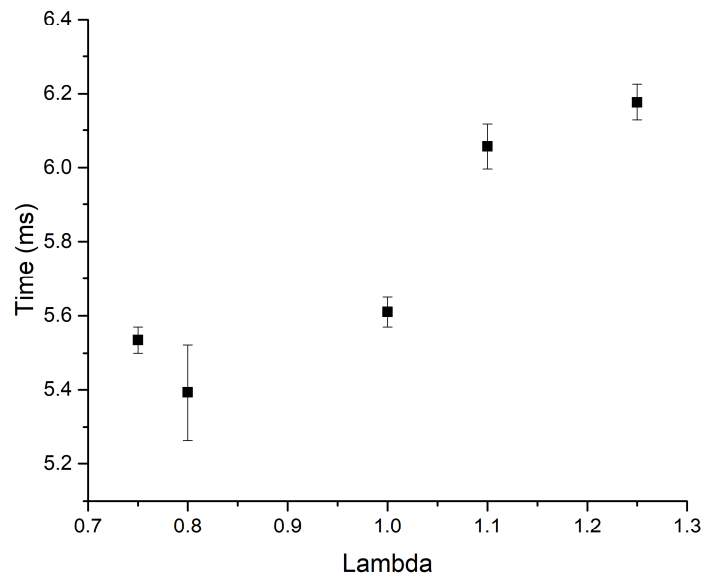


Figure 4-23 10-90% burn duration comparison for the dual diverging nozzle in the active TJI configuration for fixed main chamber lambda and varying prechamber lambda. The x-axis indicates the prechamber lambda value.

4.6.9 Characteristic Times

The 1st and 3rd derivatives of the main chamber pressure curves were used to characterize the main chamber ignition phase and the jet ignition phase. The direction of flow is from the pre-chamber to the main chamber after spark ignition. During this phase the issued jet penetrates and consumes the unburned main chamber charge and this phase is labelled the jet ignition phase. Once strong ignition initiates in the main chamber, the direction of flow reverses from the main chamber to the prechamber due to the higher pressure in the main chamber [141]. During this stage, combustion is mainly controlled by the resultant flow from the jet ignition process and the flame area and mixture properties of the main chamber since the hot jets are no longer issued from the pre-chamber. This 2nd phase is labelled the main chamber combustion phase. These two phases can be identified in the pressure traces by a change in slope observed when transitioning from the jet ignition to the main chamber combustion phase. This transition can be identified by locating the 3rd derivative peaks after the spark discharge event as indicated in Figure 4-24. The pressure curves are also used to extract maximum dP/dt (1st derivative) values due to the jet ignition phase and the main chamber combustion phase and are labelled as 1st dP/dt and 2nd dP/dt . In a constant volume environment, the dP/dt values are proportional to the heat release rate and hence offer key insights with respect to combustion phases.

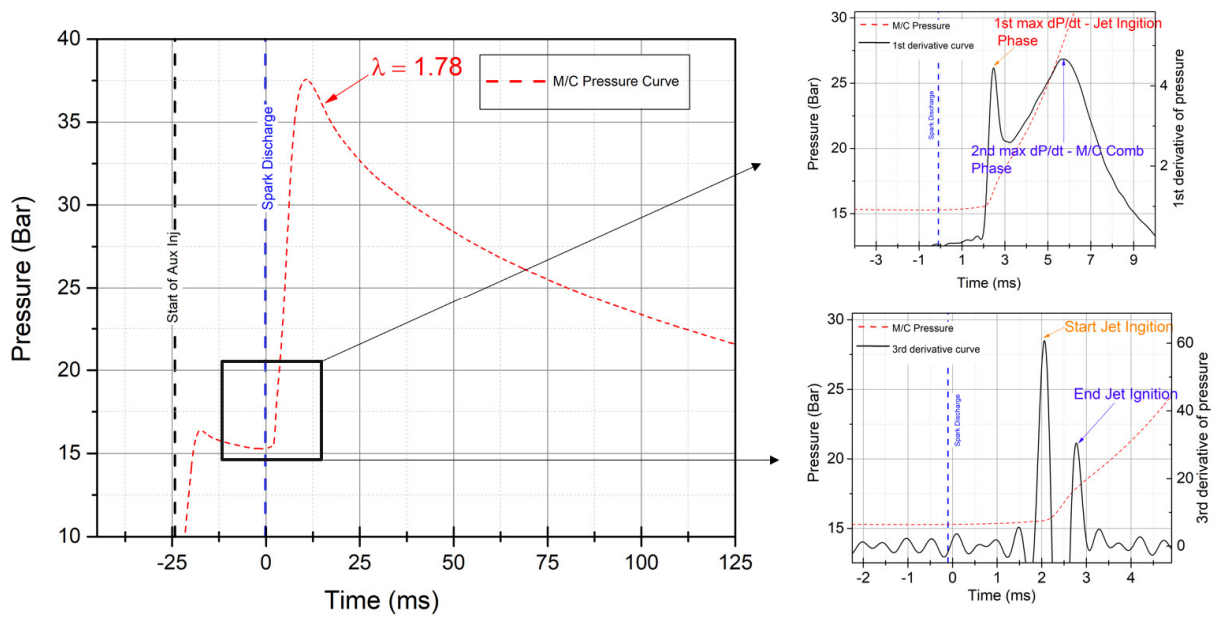


Figure 4-24 Pressure and derivatives of the pressure curves illustrating inflection points during the jet ignition phase and the main chamber combustion phase for the diverging nozzle in active TJI mode.

The 1st dP/dt value refers to the maximum dP/dt value during the jet ignition phase. The jet ignition phase is the time duration between the 3rd derivative peaks as indicated in Figure 4-24. During this phase, flow happens from the prechamber to the main chamber. In Figure 4-25, for the passive TJI configuration, it can be observed that the small hole nozzle exhibits the highest pressure rise rate in comparison to the diverging jets. The converging and large hole nozzle shows minimum but similar dP/dt values at $\lambda=1$. At $\lambda=1.25$, only the small hole nozzle shows the largest values, with the other nozzles showing similar average values. For a fixed equivalence ratio, although the absolute value of the dP/dt is changing based on the nozzle type, the elapsed duration from spark (x-axis) does not vary to the same degree for different nozzle types until $\lambda=1.25$. At $\lambda=1.5$ high variation is observed which is in line with the variation in the pressure curves and it can be observed that the single jets shows the highest pressure rise rate during the jet ignition phase. Also, in general it can be observed that the pressure rise rate reduces for all nozzles with decreasing main

chamber lambda. As the global lambda decreases the elapsed time duration from spark to the appearance of the 1st dP/dt is also increasing. Higher reduction in pressure rise rate is observed when moving from $\lambda = 1.25$ to 1.5 in comparison to 1.0 to 1.25. The small hole nozzle recorded the highest average value across all lambda values but also shows the highest variation with respect to time from spark. It is interesting to see that the diverging jets which have the highest penetration area and fastest burn duration do not have the strongest ignition during the jet ignition phase. It is possible that the higher pressure build-up within the prechamber due to smaller nozzle diameter is the reason for the stronger jet ignition phase. As a general trend, it can be concluded that the small hole nozzle and the diverging jets exhibited consistently higher values of dP/dt during the jet ignition phase. From Figure 4-25 it can be seen that the no-nozzle type exhibits a weak 1st dP/dt value indicating that the configuration resembles a jet ignition process during the initial stage of ignition. The pressure rise rate value changes from 2.5 to 1 as the main chamber lambda decreases, whereas the small hole nozzle showed a range of 10 to 3.5. This indicates a weak dependence of pressure rise rate with main chamber lambda for the no-nozzle configuration. Based on this observation, a dP/dt value below 2.5 is labelled as a weak jet ignition event. For a traditional spark ignition process no such observation can be expected and the ignition process should contain a single dP/dt value unless abnormal combustion events are present in the cycle.

In Figure 4-26, the 2nd dP/dt values during the main chamber ignition phase, which occurs past the jet ignition phase, are shown. At $\lambda = 1$, both the single hole nozzles exhibit similar dP/dt values which occur in a similar time frame. This is consistent with the observation from the pressure traces and the 10-90% burn duration plots where similarity was observed for both the single hole cases. The trend reverses from the 1st dP/dt values, with the small hole nozzle exhibiting the lowest dP/dt values, which are similar to that of the large hole nozzle. The major determining factor for a

lower peak heat release for the single hole nozzles may be due to heat losses that occur in the main chamber resulting from the higher jet impingent in comparison to the dual holes nozzles. For the 2nd dP/dt a consistent trend can be observed, with the dual diverging jets showing the highest pressure rise rates throughout the lambda range. The converging jets show the second highest pressure rise rate and this observation is in line with the 10-90% burn duration plots. It is interesting to see that these observations are not in line with the data trends observed in the jet ignition dP/dt plot shown in Figure 4-25. It can be observed that the dP/dt values reduce with increasing lambda values and hence indicate a similar lambda sensitivity as the first pressure derivative. With respect to elapsed time from the spark, the difference is minimal over the lambda range of 1 to 1.25. In comparison to the first dP/dt value it can be observed that the values of the pressure derivatives are higher for the main chamber combustion phase. There is a 50% increase in the dP/dt value in comparison to the jet ignition phase for the dual diverging jets at $\lambda = 1$. This indicates that for TJI operating in the passive configuration, the main chamber combustion phase is the strongest indicator of the burn duration and that the jet ignition phase pressure rise rate values do not necessarily indicate the combustion performance. The main chamber peak pressure occurs after the jet issuance period has ended as shown in Figure 4-24 and hence indicates that the jet distribution and main chamber heat losses primarily affect the main chamber combustion and not the jet issuance pressure rise rate. In general, the main chamber dP/dt trends of the dual hole nozzles and single hole nozzles follow the trends of the 10-90% burn duration, where it was observed that the dual hole nozzles had shorter burn durations compared to the single hole nozzles. However, the large hole nozzle had longer burn durations compared to the small single nozzle, a trend that was not seen in the second dP/dt plots. For the no-nozzle configuration the second dP/dt values, although they occur after longer duration, are of similar magnitude to the single hole

nozzles. This behavior is in contrast to the first dP/dt values where smaller values were recorded for no-nozzle configuration. This behavior may indicate that there is a trade-off occurring between the turbulence and penetration effect benefits from TJI operation, which may be partially due to the increased heat loss for the single hole configurations. For practical IC engine operation NVH can be partially determined from the pressure rise rates, and for the non-auxiliary cases (passive TJI) it is clear that shorter 10-90% burn durations correspond to higher pressure rise rates with the highest recorded at stoichiometric conditions.

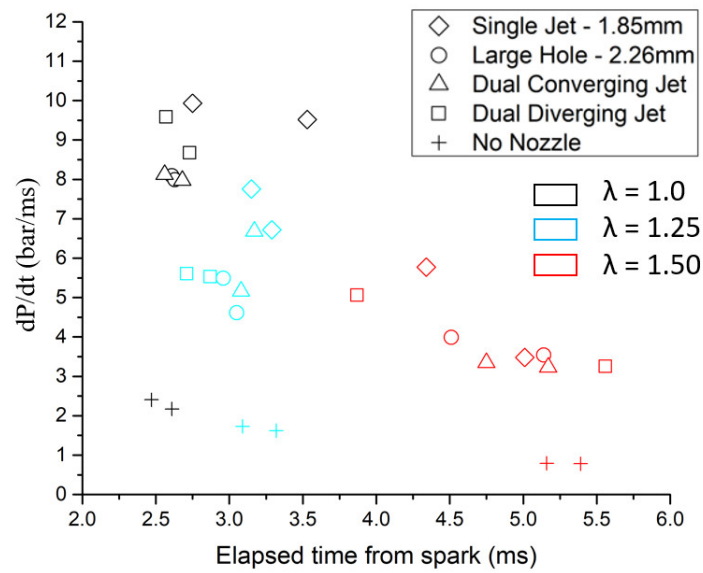


Figure 4-25 The maximum values for the 1st derivative of pressure during the jet ignition phase (1st dP/dt) for the passive TJI mode.

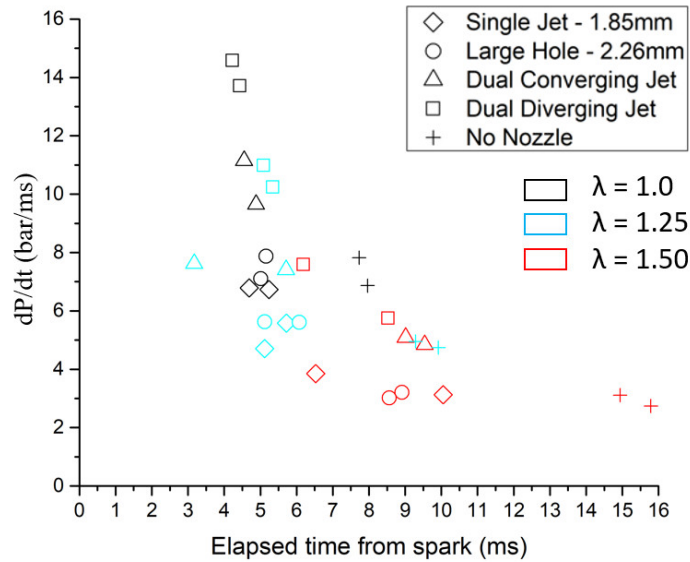


Figure 4-26 The maximum values for the 1st derivative of pressure during the main chamber combustion phase (2nd dP/dt) for the passive TJI mode.

The 1st and 2nd dP/dt values were extracted for the active TJI configuration and the observed trends are discussed below. From Figure 4-27, It can be observed that the large hole nozzle shows the highest pressure rise rate values throughout the lambda range although this difference is only pronounced up to $\lambda=2.21$. Past $\lambda=1.78$ the dP/dt values are located in a narrow region and do not exhibit strong dependence on nozzle type. The small hole nozzle type shows higher variation from the time of the jet ignition phase until $\lambda=2.21$. The reason for this may be due to higher heat loss and increased impingement for the small hole nozzle.

For mixtures leaner than $\lambda=2.21$ the majority of the pressure rise rate values fall below the value of 2.5, which is similar to the dP/dt values observed for the no nozzle case and are therefore labelled as weak jet ignition. Although data is presented in the plots, detailed observations were not made for mixtures past $\lambda=2.21$ due to weak jet ignition. It can be observed that the time during which the jet ignition phase dP/dt occurs does not strongly depend upon the global lambda. This

is in contrast with the passive TJI configuration where a lambda dependence was observed for the elapsed time from the spark. The maximum pressure rise rate at $\lambda = 1.78$ reaches 6.5 which is similar to $\lambda = 1.25$ for the passive configuration. This shows that even though the pre-chamber is maintained near stoichiometric conditions, for changing global lambda the pressure rise rate at jet ignition is strongly influenced by the main-chamber lambda. The main chamber lambda strongly controls the dP/dt during jet ignition phase. Unlike the passive TJI configuration the 1st dP/dt duration lies in a very narrow range, between 2.2 and 4 ms. Also, unlike the passive TJI configuration the large hole nozzle exhibits higher dP/dt values in the active mode. This shows that nozzle diameter plays an important criterion in initiating combustion and the diameter requirement changes from the active to passive configuration. For the passive configurations the small hole nozzle achieved higher dP/dt values. It is observed in Figure 4-27 that there are few cases for the large hole nozzle at $\lambda = 2.93$ that are above the weak ignition region, which could be due to the presence of rich regions around the hot jet from the initial unburnt fuel-air mixture coming out of the pre-chamber. This may become more pronounced for the leaner cases since more fuel is injected into the pre-chamber to keep the same prechamber lambda.

For the 2nd dP/dt value a clear peak was not visible for all nozzle types at $\lambda = 1.78$ as shown in Figure 4-28. No visible peaks were observed for most nozzles past $\lambda = 1.78$ and in the case of the converging jet nozzle no peaks were detected for any of the test points with the active TJI configuration. Only the diverging jet had an identifiable peak at $\lambda = 2.21$. At $\lambda = 1.78$ both the single hole nozzles showed similar absolute values, with the small hole nozzle recording larger variation in time. Similar variation was observed with the small hole nozzle for the passive TJI configuration. Only the diverging jets show a strong ignition event, which indicates that the main chamber combustion continues to be strongly influenced by the configuration of the nozzle even

after the jet ceases to exit the prechamber. This shows the importance of the pre-chamber nozzle design for both the jet penetration phase and the main chamber combustion phase. In other words the nozzle design continues to affect the main chamber combustion phase even after the cessation of the jet.

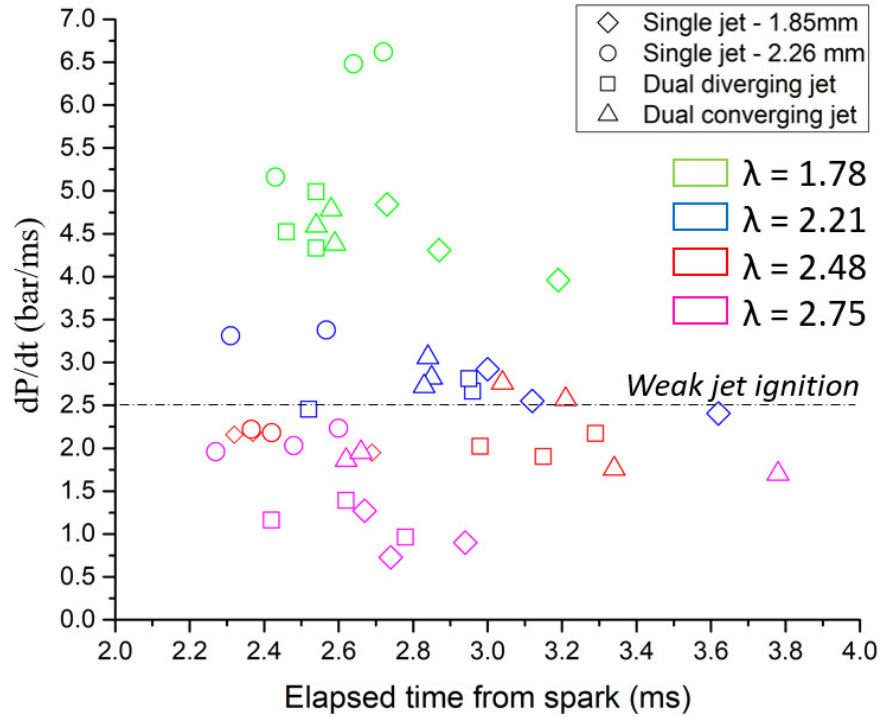


Figure 4-27 The maximum values for the 1st derivative of pressure during the jet ignition phase (1st dP/dt) for the active TJI mode.

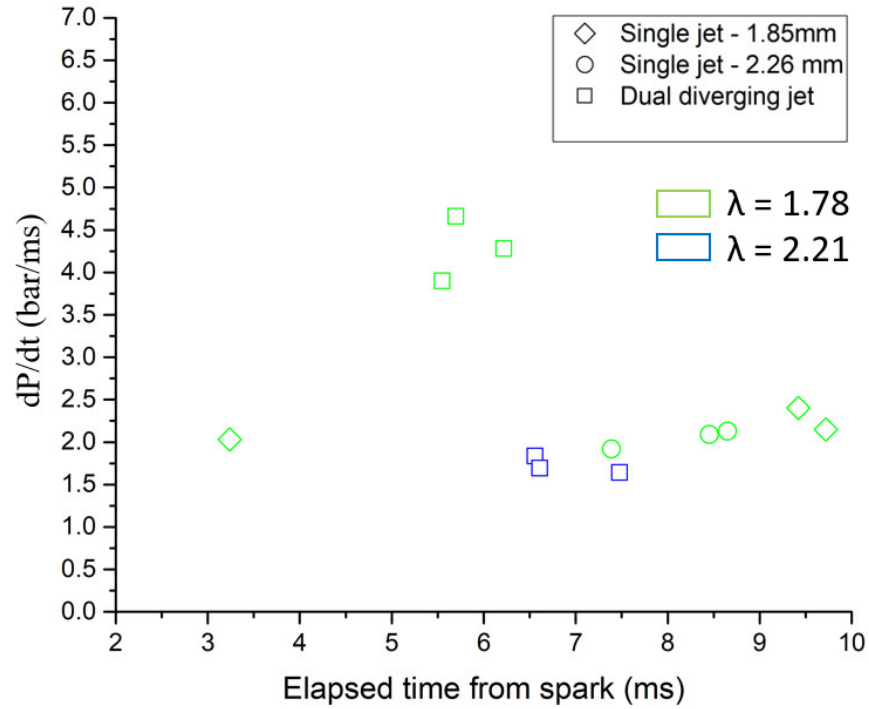


Figure 4-28 The maximum values for the 1st derivative of pressure during the main chamber combustion phase (2nd dP/dt) for the active TJI mode.

The pressure rise rate analysis was also completed for the prechamber lambda sweep runs. For these test cases the main chamber lambda was held constant and hence the maximum dP/dt during the jet ignition phase was affected only by the prechamber lambda. From Figure 4-29 it can be observed that for the 1st dP/dt value, from lambda 0.75 to 1.0, very similar durations and very similar dP/dt values are recorded. However, as the mixture becomes leaner the pressure rise rate values reduce and the duration increases. The dP/dt values at $\lambda=1.1$ and $\lambda=1.25$ are very similar but the duration increases with dilution. This trend suggests that the jet-ignition dP/dt is strongly controlled by the main chamber lambda for a fixed nozzle design

Figure 4-30 shows the main chamber combustion phase and a similar trend can be observed for the dP/dt values with respect to time at the maximum 2nd dP/dt . The dP/dt values lie in a narrow

range with the highest value recorded for prechamber $\lambda=0.8$. This shows that the maximum dP/dt due to main chamber combustion is only a function of main chamber λ and the pre-chamber λ only controls the combustion phasing. Based on Figure 4-29 and 4-30 it can be concluded that the pressure rise rate during the jet ignition phase and the main chamber combustion phase do not show any λ sensitivity in the range of 0.75 to 1.0.

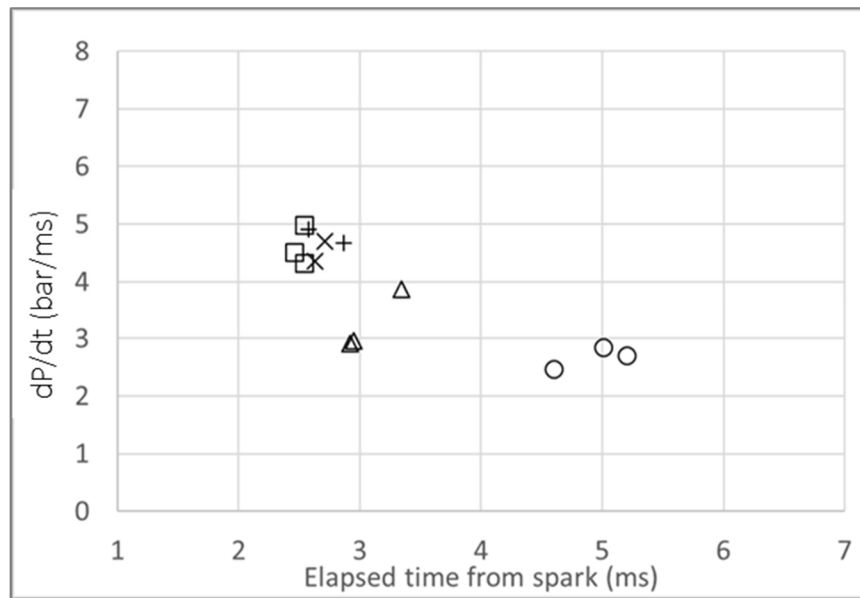


Figure 4-29 Maximum values for 1st derivative of the pressure during the jet ignition phase (1st dP/dt) for a prechamber λ sweep study in the active TJI mode.

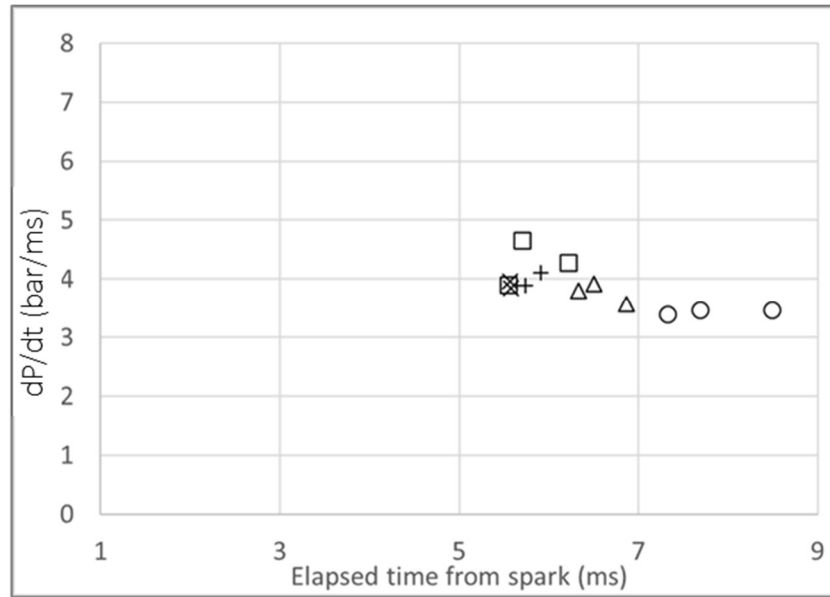


Figure 4-30 The maximum values for the 1st derivative of pressure during the main chamber combustion phase (2nd dP/dt) for a prechamber lambda sweep study in the active TJI mode.

The elapsed time duration between the 3rd derivative peaks, as illustrated in Figure 4-24, is the jet ignition duration. The jet ignition duration measurements remove the effect of spark timing and the time required for flame propagation within the pre-chamber. In Figure 4-31, for the jet duration in the passive TJI mode, it can be seen that the diverging jets have the shortest duration indicating quicker flow reversal. A trend of increasing jet duration with increasing lambda is observed only past $\lambda=1.25$. Although the duration is increasing, it can be seen that the maximum pressure rise rate due to jet ignition is reducing with increasing lambda in Figure 4-25. The increasing jet duration is mainly due to the delay in strong main chamber ignition which delays the flow reversal process from main chamber to prechamber.

In Figure 4-32, the jet duration time comparison is extended for the lambda sweep study. The jet duration does not change significantly until $\lambda=1.1$, but at $\lambda=1.25$ the jet duration increases, and the variability increases as well. This shows that since the prechamber is not effective in initiating a strong ignition sooner in the main chamber the jet duration increases hence delaying the flow

reversal event. It can be concluded that lambda sensitivity is not observed for the jet ignition duration in the lambda 0.75-1.1 range which is a wider lambda range in comparison to 1st and 2nd dP/dt measurements. Identifying the third derivative peak for the end of jet ignition is difficult past $\lambda = 1.8$ so the jet ignition duration plot is not included for the auxiliary injection case.

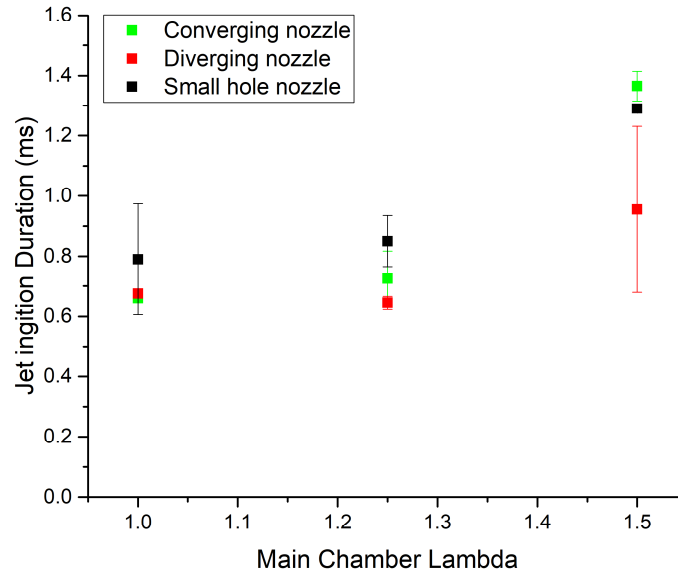


Figure 4-31 Jet ignition duration measurements for the passive TJI mode.

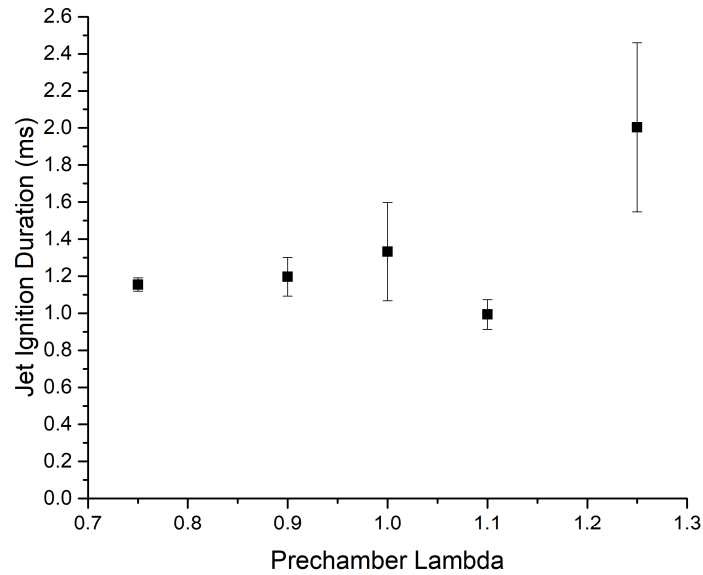


Figure 4-32 Jet ignition duration measurements for the active TJI mode – prechamber lambda sweep study.

4.7 Chapter Summary

In this chapter the high-speed images and pressure traces were used to extract secondary quantities and their usefulness as TJI performance indicating parameters was evaluated. High-speed images are an important input for the development of TJI systems since jet shapes and their interaction in the main chamber environment explain the trends observed in the burn duration calculations. The flame area plots are useful in assessing the completeness of the combustion and variation in flame propagation pattern from test to test. The jet penetration analysis offered several key insights that were not immediately apparent from the high-speed images. The fastest penetration was observed at prechamber $\lambda=0.8$, which correlated well with shorter burn durations for the active configuration at a global $\lambda=1.78$. For the diverging jets, the jet penetration with respect to time was similar for the passive configuration at $\lambda=1$ and the active configuration at $\lambda=1.78$. The jet penetration plots also indicated a reduction in penetration speed with increasing main chamber initial pressure. At

higher main chamber pressure, the jet penetration speed showed less sensitivity to the prechamber λ . When analyzing the 0-10% burn duration plots, the data did not show any comparable trends among the nozzles in both active and passive configuration. However, the duration increased with increasing dilution for the passive configuration indicating that the 0-10% burn duration is a strong function of the prechamber λ . This was confirmed in the prechamber λ sweep study where the nozzle type and main chamber λ were held constant. The 0-10% burn duration is indicative of whether an optimum air-fuel ratio is achieved within the prechamber. Based on the pressure records and burn duration, it was seen that in the passive configuration, the single hole nozzles (1.85mm and 2.26mm) performed in a similar fashion. However, in the active mode the performance of the converging jets and the 1.85mm single hole nozzle were identical. This indicates that TJI nozzle performance is also dependent upon the prechamber fueling strategy and hence that nozzle designs should be evaluated separately for both active and passive configurations. The nozzle design affects both the jet ignition phase and the main chamber combustion phase. In the TJI configuration, two distinct pressure rise rates were observed during the combustion process. One during the jet ignition phase and one during the main chamber combustion phase. Test points with high pressure rise rates during the jet ignition phase did not necessarily correlate with high pressure rise rates during the main chamber combustion phase. Nozzle design continued to affect the main chamber combustion pressure rise rates even past the jet ignition phase. Hence, the main chamber pressure rise rates were found to be a function of both main chamber λ and nozzle design. The jet ignition duration, measured by locating the inflection points of the 3rd derivative of pressure, is a strong function of main chamber λ and nozzle type in the passive mode. In the active mode, the jet duration exhibited a weak sensitivity to the pre-chamber λ indicating that the change in main chamber λ and nozzle design

would show a stronger dependence. Overall the diverging jets offered better performance in both the active and passive configuration followed by the converging jets configuration.

Chapter 5 Impact of CO₂ Dilution on Ignition Delay Times of Iso-Octane at 15% and 30% Dilution Levels in a Rapid Compression Machine

5.1 Introduction

The main objectives of the experiments described in this chapter are to study the effect of CO₂ dilution, at 15% and 30% dilution levels, on autoignition delay times of iso-octane in the low to intermediate temperature range and also to evaluate the direct test chamber (DTC) charge preparation approach which was used for introducing the iso-octane directly into the RCM test chamber via a direct injector. Experiments were conducted over a temperature range of 650K-900K at 20 bar and 10 bar compressed conditions for equivalence ratios (Φ) 0.6, 0.8, 1.0 and 1.3 in a RCM. CO₂ dilution by mass was introduced at 0%, 15% and 30% levels with the O₂:N₂ mole ratio fixed at 1:3.76 (air equivalent) emulating the exhaust gas recirculation (EGR) substitution in spark ignition (SI) engines. The results using this approach are compared with other RCM data available in the literature at undiluted $\Phi = 1.0$ and 20 bar compressed pressure and show good agreement. Although some ignition delay data for CO₂ diluted mixtures of iso-octane (or alkanes) are available, an exclusive study accounting for the presence of CO₂ at low and high dilution levels is not available. The experiments conducted in this chapter add to the database by including test points at 15% and 30% by mass of CO₂ substituted for air. Since the temperature range in this study includes the NTC region the effect of CO₂ dilution in the NTC region is analyzed in detail. In addition, the validity of the DTC approach will be scrutinized for use in chapter 6 where full blend gasoline fuels are studied.

5.2 Research Questions

1. Is the direct test chamber (DTC) approach a viable replacement for a traditional mixing tank based charge preparation technique for full blend gasoline fuels and its single and multi-component surrogates?
2. What is the effect of CO₂ dilution on ignition delay time of alkane-air mixtures and is the effect consistent at all conditions?
3. Can CO₂ dilution provide any octane relaxation potential?

5.3 Background and Literature Review

Knocking in a SI engine is a result of auto ignition of fuel-air mixtures in the end gas regions of an engine. Dilution of the intake charge with an inert gas such as CO₂ alters the auto ignition propensity of the end gas thereby delaying knock or reducing its intensity. A cooled exhaust gas recirculation (EGR) system, in which EGR temperature is reduced with an EGR cooler, is an effective method to avoid abnormal combustion. Cooled EGR systems have already been introduced in mass-produced naturally aspirated (NA) gasoline engines [10]. Cooled EGR involves introducing CO₂ and N₂ into the combustion chamber with or without water vapor, depending upon whether the water has condensed during the process. As the amount of dilution increases, the initial mole fraction of the reactants decreases, and hence the build-up of the radical pool leading to autoignition increases in duration. This increases the delay required for autoignition of fuel-air mixtures [142]. This results in extending the end-gas ignition delay time in SI engines and decreasing the auto-ignition heat release rate. CO₂ dilution has further applications in ignition timing control for low temperature combustion technologies exploiting flameless combustion in homogeneous mixtures [55].

In early work by Quader et al. [143], a first explanation was provided for the now experimentally established fact that CO₂ dilution reduced NO_x emission, because CO₂ is largely inert and lowers compressed and combustion temperatures due to higher specific heat capacity, thereby inhibiting thermal NO_x formation. Hence with cold EGR strategy it is possible to operate at higher compression ratios due to reduced knocking tendency and at the same time reduce NO_x emissions due to lower combustion temperatures. Kumana et al. [144] investigated the effect of knock suppression by cooled EGR in a turbo charged SI engine. EGR was emulated by using a mixture of N₂+CO₂ and was injected upstream along with the intake. Up to an 8% EGR ratio was used and they found that NO_x emissions were reduced with no negative impact on the exhaust emissions. For every 1% EGR ratio increase about a 1 deg CA spark advance was possible.

At high load condition, gasoline engines are often operated fuel rich to reduce exhaust gas temperature and NO_x emissions. Cairns et al. [66] completed a comparison for a boosted SI engine operating at high load with excess fuel, excess air and cooled EGR charge dilution. It was concluded that cooled EGR was a more effective suppressant of knock than excess air. Grandin et al. [145] demonstrated the potential to replace fuel enrichment for high load knock control using cooled EGR using a 2.3-liter PFI turbocharged engine. It was concluded that EGR dilution helped control the mass burn rate with reduced temperature rise rate and enabled inhibition of knock. In another work [146], Grandin et al. compared excess air with EGR for charge dilution and concluded that EGR provided more stable burn together with NO_x reduction. Recently Hyundai [147] and Toyota [148], in their latest generation of naturally aspirated engines designed for hybrid electric vehicles, used EGR as one of the key technologies that enable 40% brake thermal efficiency.

For our current study we aim to understand the decrease in knocking tendency with CO₂ addition by studying its effect on total ignition delay times of iso-octane for up to 30% dilution levels. Several studies have discussed the auto ignition behavior of paraffins, the main constituents of commercial gasolines. The primary reference fuels, n-heptane and iso-octane are the benchmarks of a very reactive straight chain molecular structure (ON=0) and a less reactive, highly branched structure (ON=100). Most practical gasoline fuels have octane numbers higher than 85, and hence iso-octane is the principal component in the PRF surrogates and strongly dictates the surrogate's combustion chemistry. Also, when iso-octane is added to relatively less reactive compounds, such as toluene, the reactivity of the blend tends more towards iso-octane since the blend's reaction pathway is dominated by reactive intermediates formed by iso-octane decomposition [149]. Several fundamental combustion experiments have been conducted for iso-octane, including ignition delay time and pyrolysis measurements in shock tubes [150], and rapid compression machines (RCM) [151–155]. As a result, several comprehensive chemical kinetic models for iso-octane combustion such as by Curran et al. [54] and Mehl et al. [156] are available for kinetic modelling. In recent years additions to the above mechanisms are considered at low and intermediate temperatures and at lean conditions. Atef et al. [53] recently added alternative isomerization pathways for peroxy-alkyl hydroperoxide radicals, which has further improved low temperature reactivity predictions. Due to the availability of several published ignition delay datasets and a well validated reaction mechanism, iso-octane was chosen as the fuel for this study. In recent work, Goldsborough et al. [157] published a compilation of ignition delay data from different RCM facilities at 20 bar compressed pressure for iso-octane. This comparison was made to get an understanding regarding influence of facility effects in measured ignition delay time. In

the current study we additionally intend to assess the performance of the direct test charge (DTC) approach by comparing our data with other RCM data reported in [157].

Few studies have explicitly examined the effects of CO₂ dilution on alkanes. In a recent work by Tingas et al. [142], the authors explored the dilution effects of CO₂ and water separately on NO_x emissions and ignition delay times in methane mixtures. They performed adiabatic and isochoric autoignition simulations at 800 K, $\Phi=0.8$ and 30 bar conditions with CO₂, H₂O and Ar as diluents. The study included data on 15% and 30% CO₂ dilution levels by mole fraction. They concluded that the CO₂ impact on reactions is mostly thermal in nature and that the CO₂ acts predominantly as a thermal buffer, while for H₂O dilution they showed that water not only acts a thermal buffer but also enhances reactivity through the reaction $\text{H}_2\text{O}_2 + \text{H}_2\text{O} \rightarrow \text{OH} + \text{OH} + \text{H}_2\text{O}$. Because of the chemical nature of this case, sometimes ignition delay can be shortened by H₂O addition, however, this effect was never observed with CO₂. The final mass fraction values of NO and CO were both reduced through dilution addition. The study did not include the NTC region since methane does not exhibit NTC behavior [158]. He et al. [152] studied the ignition delay times of iso-octane mixtures with trace amounts of H₂O and CO₂ (0.5, 2.0 and 3% by mol) for 5-20 atm at high temperatures of 943-1027 K. This study also did not include the NTC region since iso-octane does not show NTC behavior over this temperature range. For these small amounts CO₂ dilution there was no chemical effect, however the H₂O dilution did decrease the ignition delay by small amounts. Di et al. [151] explored the effects of several buffer gases on iso-octane which included Ar, N₂, and a mixture of CO₂ and Ar. They did not explore the dilution effects in context with EGR substitution due to a fixed buffergas:O₂ ratio at 1:3.76. Experiments covered 600-800K range at 20bar and $\Phi=1$. Their observations indicated that the effects of the buffer gases on the first-stage ignition delay were very small, but the changing heat capacity of the buffer gas changed the final

delay time during two-stage ignition. The higher heat capacity of CO_2 increased the total ignition delay time in comparison to N_2 . Di et al. also noticed the effect of the higher collision efficiency of CO_2 on ignition delay times compared to N_2 (CO_2 is 3.8 times higher than that of N_2). Higher collision efficiency reduces ignition delay times. When a single stage ignition event was observed, which occurs at temperatures lower than the NTC region (700 K for isooctane), experimental data and model predictions showed no influence of buffer gas composition on delay times.

5.4 Experimental Setup

Basic features of the RCM facility used for this study have been documented in Chapter 2. In this study compressed gas temperatures were altered by modifying the compression ratio of the RCM as explained in Chapter 2. A more traditional approach for achieving different compressed temperatures by using fixed CR is to replace or substitute the non-reactive portion of the charge, N_2 , with a buffer gas consisting of N_2 , CO_2 , Ar [153]. Here different compressed temperatures are achieved due to change in specific heat of the mixture made by altering buffer gas composition. Usage of buffer gas can alter ignition delay times of the mixture mainly due to changing heat loss characteristics or change in third body efficiencies. In a study by Davidson and Hanson [143], auto ignition of isooctane using Ar and N_2 as the buffer gas was modeled, and results showed up to 50% difference in the ignition delay times depending on the reaction mechanisms used. In an experimental study completed by Shen et al. [159] it was shown that ignition delay times for isooctane mixtures, using Ar as the diluent, showed 20% shorter ignition delay durations when compared to using N_2 . Würmel et al. [158] compared the effect of Ar as a buffer gas in a shock tube and an RCM. Ar was shown to enable ignition in the shock tube at certain conditions, but in the RCM a retarding effect was observed. This was primarily due to post-compression heat loss governed by the different thermal diffusivities of the buffer gases. In a computational study of

auto-ignition times of iso-octane, n-heptane, and n-butanol performed by Wagnon and Wooldridge [160], it was found that fuels that exhibit negative temperature coefficient (NTC) behavior may show significantly higher buffer gas effects during two stage ignition, with a factor of two or more impact on total ignition times. The above studies illustrate that buffer gases can affect delay times based on the test conditions. Although the effect of buffer gases on ignition delay times are eliminated in the current study, changing heat loss characteristics due to changing TDC volume and wall temperature should be still considered and included in numerical simulations. There are other studies, such as by Chen et al. [161], that have used and reported a similar strategy to achieve different compressed conditions by changing CR, as was employed here.

Table 2-1 presents the CR and wall temperatures required for achieving various compressed temperatures. The demand for higher initial pressures reduces as we increase the compression ratio. This is important since our mixture preparation methodology relies upon mixing within the combustion chamber and hence lower initial pressures helps in further lowering the partial pressure requirement for liquid fuels. The lowest values for initial pressure and temperature shown are for 10 bar compressed condition for an equivalence ratio of 0.6 at 0% CO₂ dilution while the maximum values are for the 20 bar compressed condition with an equivalence ratio of 1.3 at 30%

CO₂ dilution. Both the increase in fuel concentration and increase in CO₂ dilution will decrease the total specific heat capacity of the mixture. Hence to achieve similar compressed temperature targets across test points a 10°C increase in wall temperature is provided when there is an increase in equivalence ratio at a given dilution or when there is an increase in dilution at a given equivalence ratio. For the current study heating bands were installed on the RCM and controlled using a LabVIEW® VI program to maintain the wall temperatures at the targeted temperatures. Temperatures inputs were obtained through k-type thermocouples.

5.5 Data Interpretation

5.5.1 Ignition Delay Definition

The primary data extracted from the RCM pressure trace is illustrated in Figure 5-1. End of compression (EOC) is designated as the time when the dP/dt values becomes negative past the start of compression. Here ignition delay time is defined as the the elapsed time duration from EOC to maximum pressure rise rate due to ignition activity. All of the ignition delay data were extracted from the filtered pressure trace (Butterworth filter with 5000Hz cutoff) for easy interpretation of the inflection points. The reported ignition delay times in this work are capped between 100ms on the higher end and 3ms for the lower limit. The higher limit was set based on the study of Mittal et al. [162] who reported that above 100ms the adiabatic core assumption starts losing its validity. Due to this reason the data set obtained at 10 bar compressed condition is not exhaustive enough to observe trends and only limited information is provided in this study. The lower limit for ignition delay times were set to 3ms [163] to avoid influence of pre-compression reactions. The achieved compressed pressures are within ± 0.5 bar from the target pressures and hence no pressure scaling is used when reporting the ignition delay times.

5.5.2 Measurement of Compressed Temperatures

Direct measurement of reactant gas temperatures is not possible in the rapid compression machine. Direct measurements of core temperature with thermocouples can affect core homogeneity and hence is not usually recommended. Due to high pressure conditions prevalent within the reaction cylinder usage of non-intrusive absorption techniques also becomes difficult. For the autoignition studies the compressed pressure is measured directly from this data while the compressed

temperature is calculated using the widely used adiabatic core hypothesis (Equation 1), which uses mixtures variable specific heats, initial conditions and final compressed pressure as inputs.

$$\ln \frac{P_c}{P_i} = \int_{T_i}^{T_c} \frac{\gamma}{\gamma-1} \frac{dT}{T} \quad 5.1$$

In the current and the coming chapters, equivalence ratio ϕ is used instead of λ . This is done to be consistent with the general community guidelines where equivalence ratios are used when reporting ignition delay times measured in an RCM. Equivalence ratio is equivalent to inverse of the λ value. For calculating equivalence ratio values of air-fuel ratio (AFR) were used for no dilution runs and when CO₂ was present the oxygen-fuel ratio (OFR) values were used as shown in Equations 2 and 3 below,

$$\phi = \frac{(AFR)_{stoich}}{(AFR)_{current}} \quad 5.2$$

$$\phi = \frac{(OFR)_{stoich}}{(OFR)_{current}} \quad 5.3$$

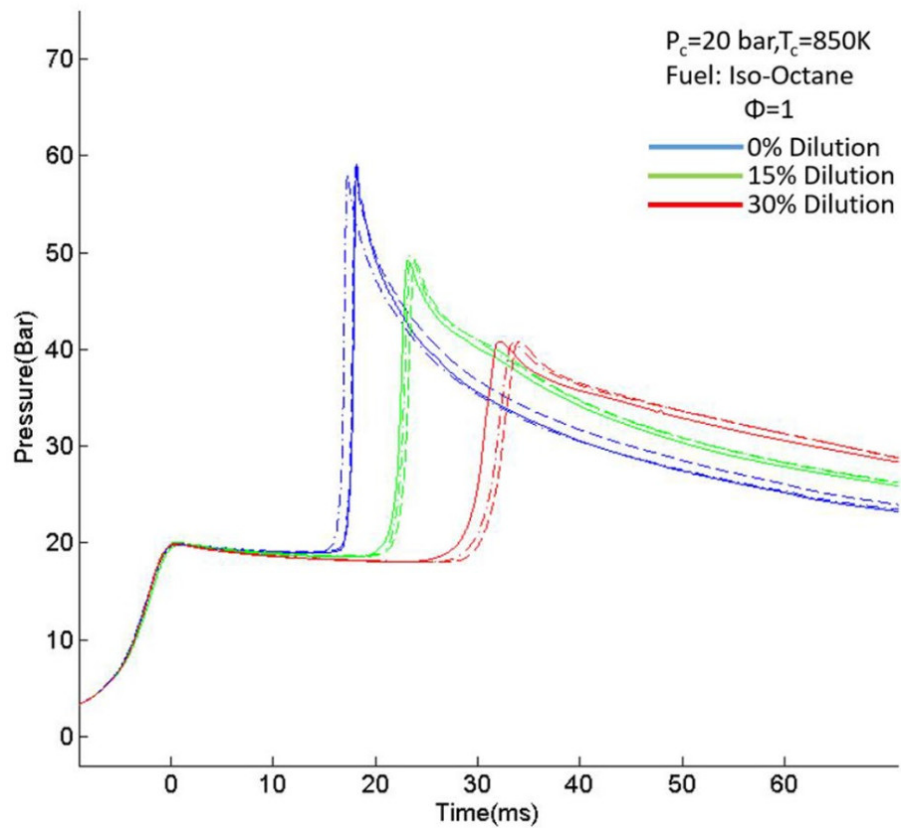
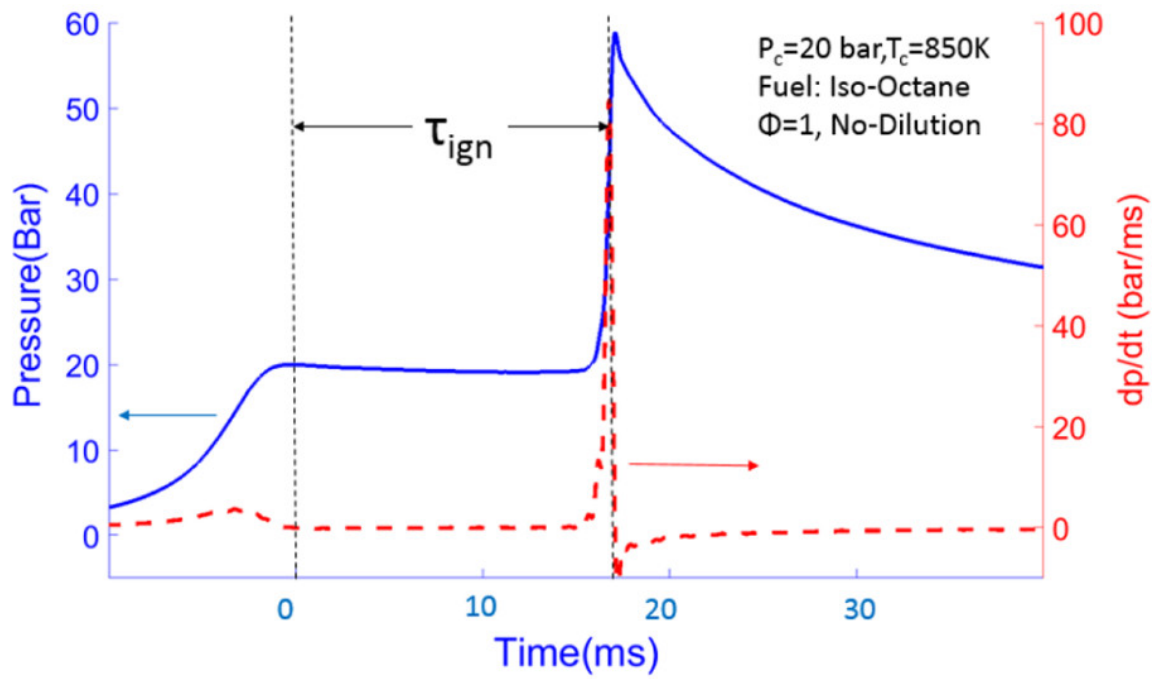


Figure 5-1 Sample pressure and dp/dt curve (top) illustrating ignition delay definition and pressure traces showing experimental repeatability for various dilution levels (bottom).

5.6 Direct Test Charge Approach

Direct test charge (DTC) was initially developed by Allen et al. [164] for studying non-volatile synthetic jet fuels in the RCM. A brief description of the direct test charge approach is presented here and a more detailed explanation and validation can be found in [164]. The DTC approach involves introducing volatile or non-volatile fuels directly into the RCM test chamber instead of relying upon a traditional mixing tank technique. This enables quick preparation of different equivalence ratio mixtures within the RCM test chamber and reduces risks associated with traditional techniques such as thermal decomposition of the fuel and condensation in the lines connecting them mixing vessel to the test chamber. Since initial pressure within RCM is between 0.4-2 bar, partial pressure requirement of the fuel and the wall temperature required for complete evaporation are lowered. Fuel is precisely metered into the RCM using a production water cooled 7-hole GDI injector manufactured by Bosch. A hydraulic accumulator pressurized to 30 bar was used to pressurize the fuel line.

5.6.1 Fuel Calibration

The fuel injector was calibrated by pulsing the injector 10 times into the RCM test chamber maintained at 100 °C in vacuum. The injector was commanded with LabVIEW by sending TTL signal pulses to a custom-made driver box. The pressure rise, measured using an absolute pressure sensor, after fuel injection was used to calculate the mass injected using the ideal gas law. This procedure was performed for a 0.5ms to 1.0ms pulse width range. Each test was repeated 5 times and the partial pressure recorded across the tests displayed a negligible standard deviation in the range of 1E-4. This highlights the repeatability of the injectors even for very small number of injections in the pulse width range. The resulting linear fit from the injector calibration procedure is shown in Figure 5-2.

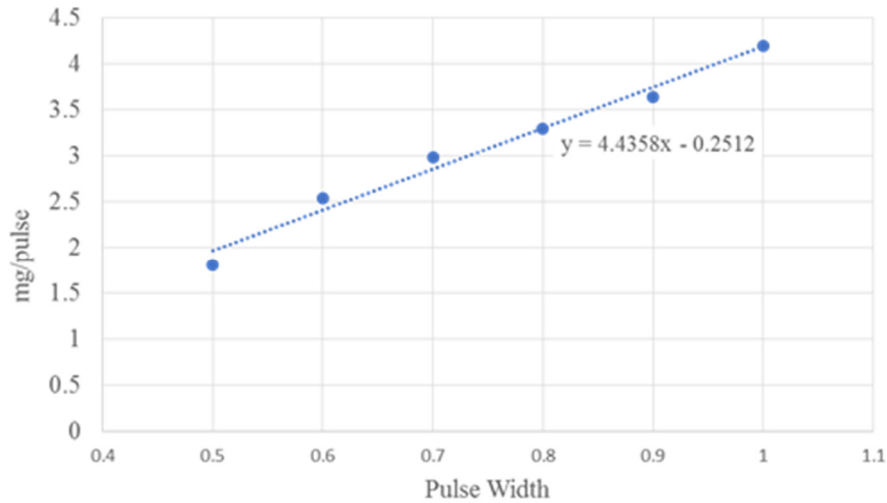


Figure 5-2 Fuel injector calibration curve showing pulse width vs mass injected information.

5.6.2 Mixture Preparation

Prior to each test the entire test section was emptied using a vacuum pump. The test section is then filled with dry air or premixed CO_2 , O_2 and N_2 mixtures via a manifold while monitoring the pressure using an absolute pressure transducer installed in the intake manifold. Since no mixing tanks were used in this study dry air and CO_2 , O_2 , N_2 custom premixed bottles were obtained from Airgas® to ensure homogenous and consistent oxidizer mixtures. The premixed custom mixture gas has 15% dilution level and 30% before fueling hence after addition of fuel the overall CO_2 dilution level in the mixture goes down with increasing equivalence ratio up to 1% for when 15% mixture and up to 2% when 30% dilution bottle is used. Based on the dilution level required corresponding premixed-gas is filed into the RCM to target pressure. Now the manifold is closed, and fuel is admitted into the chamber using the GDI injector as explained in DTC approach. Mixture stoichiometry was controlled by varying the pulse width and number of pulses in the

injector. Approximately three minutes [164] was allowed before firing to enable adequate mixing time to obtain a homogeneous mixture.

5.7 Results and discussions

5.7.1 Validation with Other RCM Data

In order to validate the results of our current study, we have adapted the data obtained from recent work of Goldsborough et al. [157] and overlaid it with data obtained from our current study. As seen in Figure 5-3, the NTC region appears around 700-850K for isooctane at 20 bar for air levels of dilution. This region is well captured by our tests and a reasonable agreement is obtained over the temperature range. At 850K and 900K our data has slightly shorter ignition delay times, which is likely due to the fact that for these temperatures the wall temperatures used during our study was higher, as seen in Table 2-1, in the 130-170°C range and most of the reported work shown in Figure 5-3 uses varying buffer gas composition in order to achieve higher compressed gas temperature. This may have resulted in lower heat losses in our RCM experiments and hence shortened the total delay time. As mentioned in [157], this highlights the

challenges associated with comparing experimental results when only compressed temperatures are used as a basis for comparison.

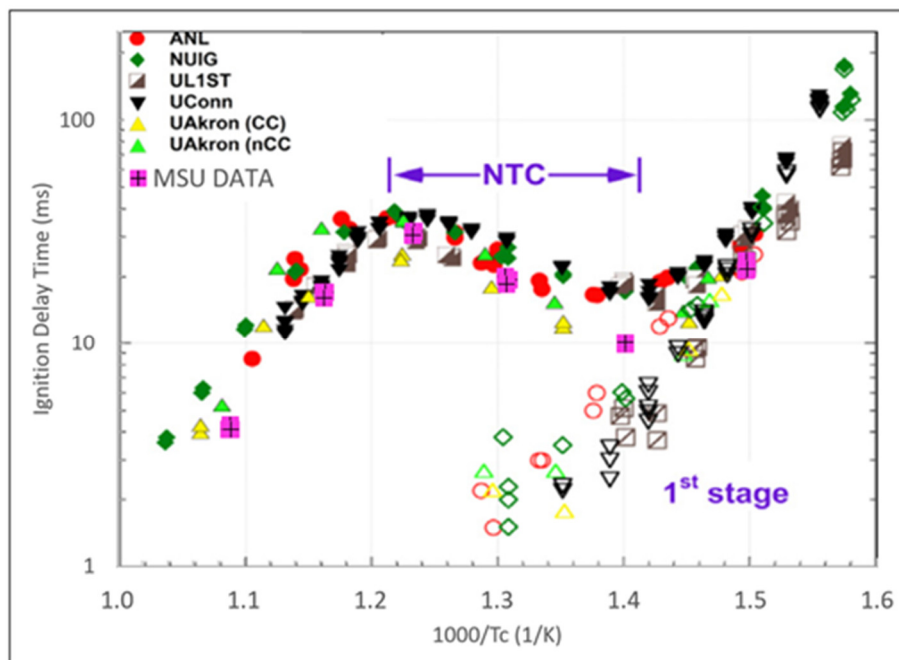


Figure 5-3 Results comparing several RCM ignition delay data for iso octane as reported in [157] overlaid with total ignition times from our current study at 20 ± 0.6 bar compressed pressure.

5.7.2 Effect of Equivalence Ratio

The effect of equivalence ratio on ignition delay is investigated for all different dilution levels in Figure 5-4. The data points were connected with straight lines in order to improve visualization and all three data points taken to ensure repeatability at each point are shown. The data shows a trend of decreasing ignition delay times with increasing equivalence ratio for the conditions investigated. The increase in reactivity with increasing equivalence ratio is due to the effect of maintaining a fixed N_2/O_2 ratio but varying the fuel concentration levels. An opposite trend where lean mixtures become more reactive is observed when the equivalence ratio is varied while the fuel concentration is held constant [28]. The higher reactivity is a byproduct of the increase in

oxygen concentration leading to lower dilution levels. The same equivalence ratio effect is observed over the entire temperature range and for all dilution levels, which consistent with other published hydrocarbon data [15,22,23].

5.7.3 NTC Region Analysis

In Figure 5-4, for the equivalence ratios reported here, the NTC region can be seen between $T_c=700-850K$ with exception of $\Phi=0.6$ where the NTC region can be observed as early as 650K. This is in line with the fact that as the mixture gets leaner the NTC region is shifts to lower temperatures and is more pronounced [139,131,133]. A similar trend can be observed for increases in CO_2 dilution levels at fixed equivalence ratios. From the figures it can be observed that the slope of the connected lines does not show much change across equivalence ratios. However, this is not true for the lines connected between the 650K-700K range. In this range, the NTC region shift, with changing equivalence ratio and dilution levels, can be observed more clearly. The connecting lines get flatter (or tend towards a more positive slope) as the dilution level increases across all equivalence ratios. At the 30% dilution level this trend is more noticeable, with the $\phi=0.6$ case entering the NTC region earlier, as indicated by a shift from a negative to a positive slope. Similarly, for the richer cases at 30% dilution, although they still exhibit a negative slope, the connecting lines are relatively flat compared to the lower dilution condition. This shows the tendency of the NTC region to shift towards lower temperatures as dilution increases. At 650K for the 0% dilution condition, it can be observed that the ignition delay times of all the curves have converged irrespective of the equivalence ratio. However, as dilution increases, differences starts to appear as the equivalence ratio changes.

At 800K the maximum ignition delay is observed, and this fact does not change with equivalence ratio or dilution levels. Past 850K there is a sharp decrease in ignition delay times, signaling the

departure to high temperature reactions pathways. It can be observed that the NTC trend does not shift with increasing dilution levels which clearly indicates that CO₂ acts purely as a thermal buffer and it does not interfere with reaction pathways that were mentioned earlier. In other words, no chemical activity of CO₂ is observed in our current study.

5.7.4 Delta Ignition Delay Times

Increase in ignition delay times with increasing dilution levels is shown in Figure 5-5 as a difference in ms from the 0% dilution case. The data in the figure is at 800K compressed temperature, where the maximum delay times were observed. For 30% dilution, more than twice the increase in differential ignition delay times were observed when compared to 15% dilution. The trend holds irrespective of the mixture being lean or rich. This shows that higher dilution levels can enable better knock mitigation control under the same thermodynamic conditions as undiluted or mild dilution cases. This can manifest as spark advance or increase in compression ratio in a SI engine thereby increasing thermodynamic efficiency. Increase in dilution levels can increase burn durations leading to emission issues, but to counteract this other flame speed enhancement techniques such increase in turbulence levels or ignition enhancement devices like turbulent jet ignition can be used [165]. Similar bar charts for other temperature points are presented in the appendix section.

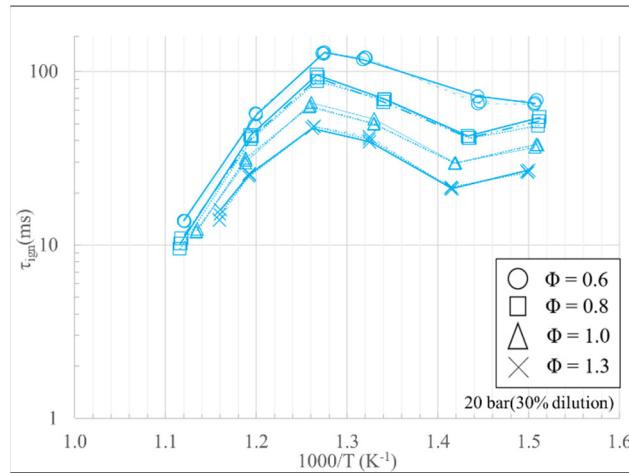
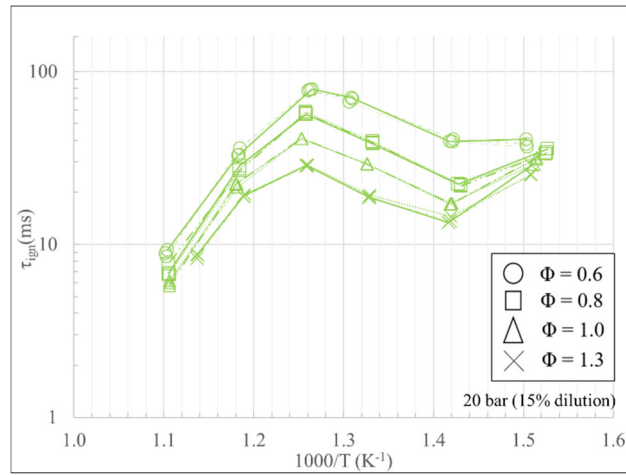
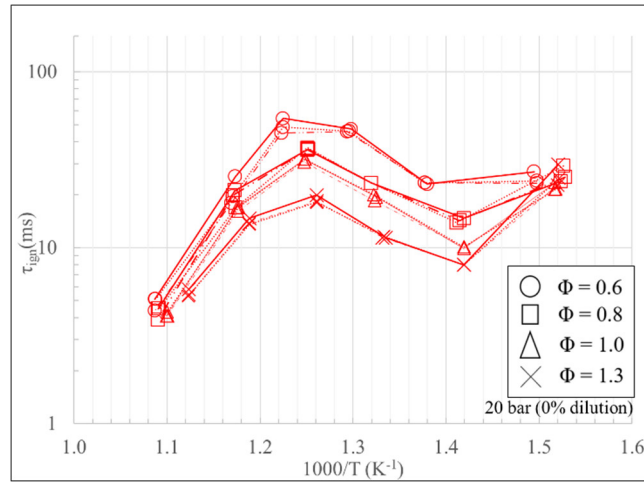


Figure 5-4 Ignition delay times shown in Arrhenius form for $\Phi=0.6, 0.8, 1.0$ and 1.3 for 0%(upper), 15%(middle) and 30%(lower) CO_2 dilution levels at compressed pressure of 20 ± 0.5 bar.

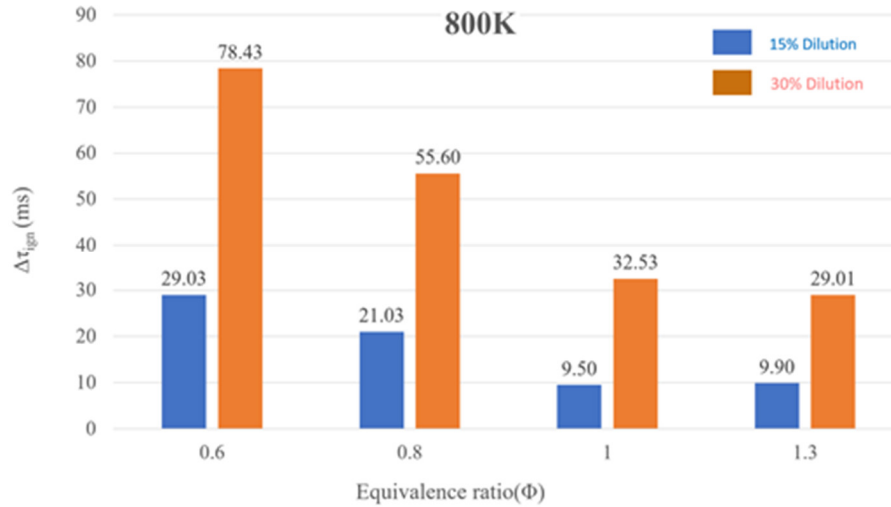


Figure 5-5 Bar charts showing average increase in ignition delay times with increasing dilution using 0% dilution delay times as baseline @ $T_c=800K$.

5.7.5 Effect of CO₂ Dilution at Fixed Equivalence Ratio

The 20 bar ignition delay data is presented in Figure 5-6 (a to d) with fixed equivalence ratios but varying CO₂ dilution levels. One striking feature across all the plots is that the NTC region remains fixed as we maintain the equivalence ratio but increase the CO₂ dilution. This indicates that for the temperature range studied here, at a given equivalence ratio, increasing the dilution does not shift the NTC region or modify its trend. Also compared to the fixed dilution plots presented earlier in Figure 5-4, the slope of the line between 650K and 700K is similar across the equivalence ratios except for the $\phi=1.3$ case, where the ignition delay data converges at 600K irrespective of the dilution levels. In terms of total ignition delay time, the 15% dilution level times were closer to the 0% dilution case in comparison to the 30% dilution cases, although this trend is less pronounced due to the nature of the log plots. Also, from the figures it can be observed that for the 30% dilution level the maximum compressed temperature attained was less than 900K. This is due to the fact that the maximum stable wall temperature that can be maintained in the RCM was

175°C. The diluted and undiluted test points were conducted at this fixed wall temperature since further increased in temperature were not possible. Since CO₂ addition increases the specific heat of the mixture, the compressed temperature values dropped from target as the dilution increased.

5.7.6 Pressure Dependence of NTC Region

When comparing the 10 bar and 20 bar data for 0% dilution (Figure 5-7) level the shift in NTC delay with pressure level can be clearly observed. The observation holds for both the $\Phi=1.0$ and 1.3 data presented here. The observation is in line with other studies where it has been shown that for alkanes the NTC region is observed to shift to higher temperatures with increasing pressure [166]. At 20 bar the NTC region is less pronounced for $\Phi=1.3$ when compared to $\Phi=1.0$, which is again a known trend observed for alkanes with increasing equivalence ratio [160]. These observed trends further confirm the validity of the approach used in this study. The data sets corresponding to the dilution runs were not included in the plots since several recorded delay times were above 100ms at the 10 bar condition. As an illustration, Figure 5-8 compares the ignition delay times for the 10 bar compressed pressure for both the dilution and non-dilution cases. At $\Phi = 1.3$ ignition delay times above 200 ms (within NTC region) were recorded with CO₂ dilution, while a minimum delay time of 35ms was noted for the no dilution condition. Also, high amount of variability were observed as the ignition delay time increased beyond 100ms as seen at $T=833K$ ($1000/T(K)=1.3$).

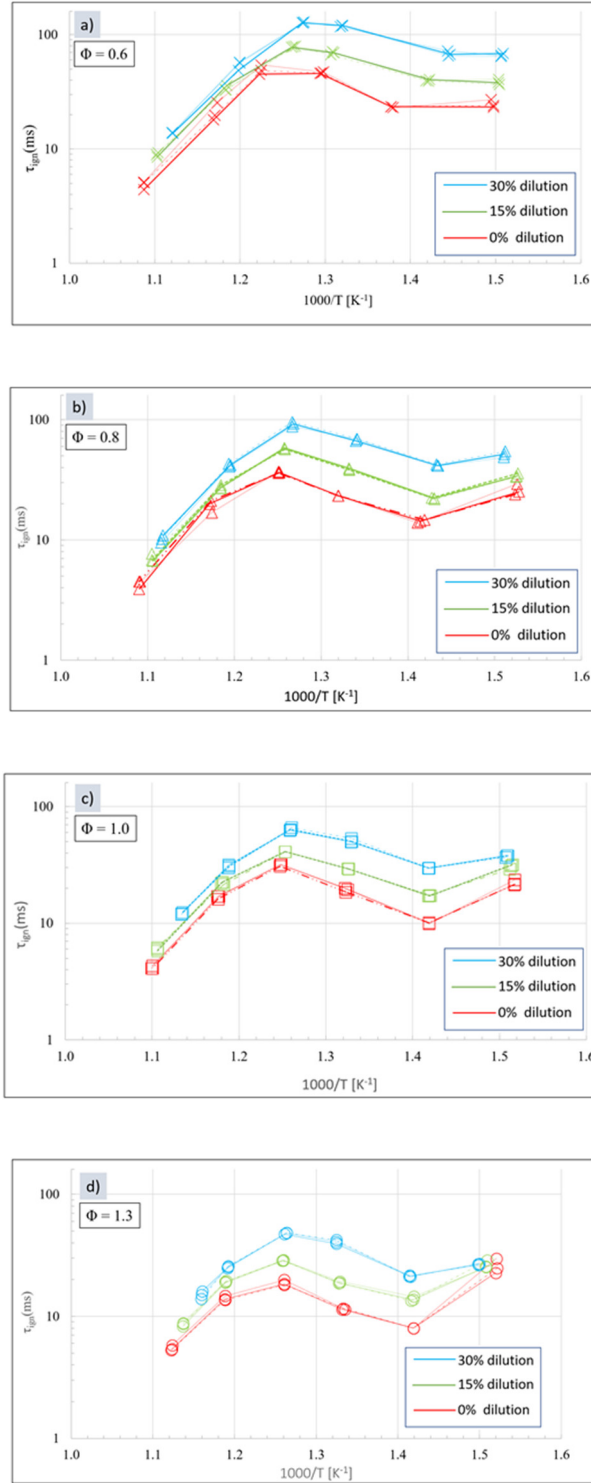


Figure 5-6 Ignition delay times shown in Arrhenius form for 0%,15%, and 30% CO₂ dilution levels for $\Phi=0.6$ (8a), $\Phi=0.8$ (8b), $\Phi=1.0$ (8c) and $\Phi=1.3$ (8d) at compressed pressure of 20 ± 0.5 bar.

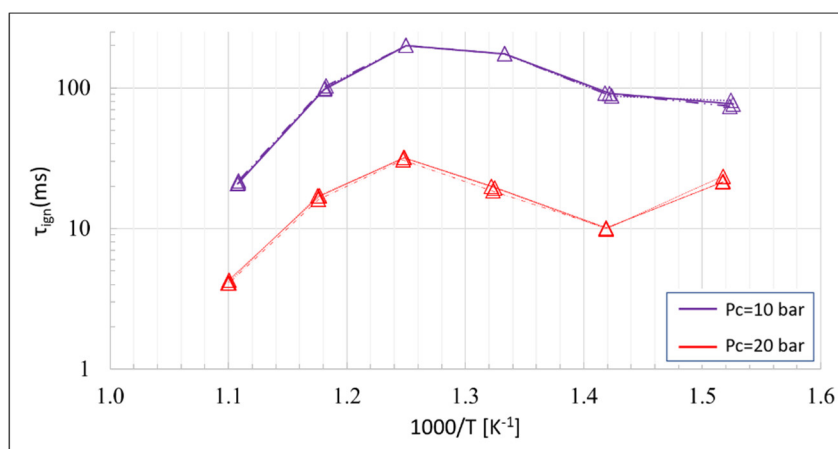
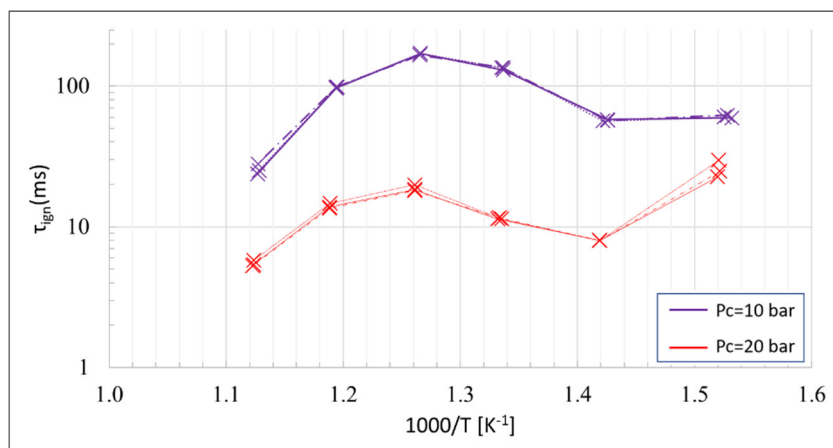


Figure 5-7 Ignition delay times at $\Phi=1.3$ (top) and $\Phi=1.0$ (bottom) comparing the effect of pressure on ignition delay times for 10 ± 0.5 bar vs 20 ± 0.5 bar.

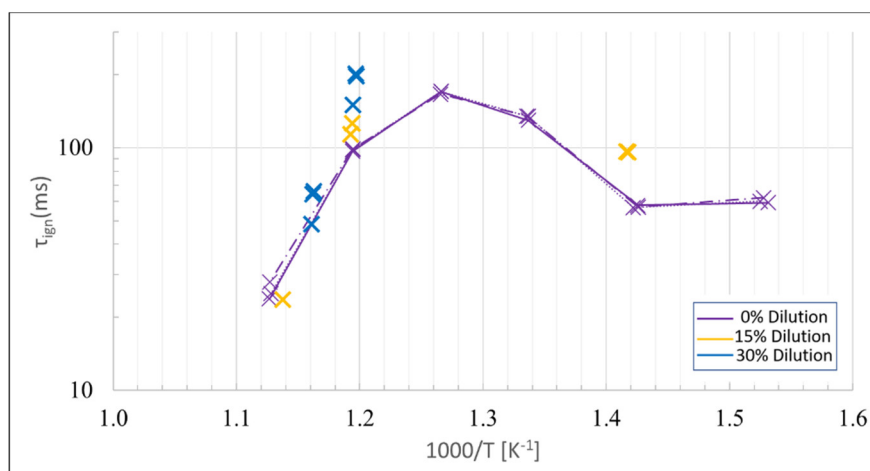


Figure 5-8 Ignition delay times at $\Phi=1.3$ for 10 ± 0.5 bar comparing the effect of dilution. Connecting lines not shown for the dilution cases due to long ignition times in the NTC region.

5.7.7 Image Analysis

For this work a Photron SA4 color camera at 10,000 frames per second was used in conjunction with NIKOR 105mm lens for imaging the autoignition event. Although the primary purpose of this study was not optical imaging, a few images for observation purposes were recorded and are presented in Figure 5-8. The images represent two undiluted tests at $\Phi=1.0$ and 0.5 at 700K and 20 bar compressed conditions (CR 9.6). The first three images in each of these frames were enhanced to better observe the features and each subsequent frame is 0.1 ms apart. The first luminous image in each of these experiments roughly occurred at 0.3ms before the peak pressure rise rate and hence the observed events are very close to their ignition delay times.

For $\Phi=1.0$ (Figure 5-9 – top row) the auto ignition event is initiated in the top portion of the combustion chamber. The auto ignition front can be seen accelerating downwards in the subsequent frames. In the last frame the main autoignition event can be seen and the luminosity of this event saturates the camera sensor obscuring further observations. For the $\Phi=0.5$ (Figure 5- 9 bottom row) test point, in the second frame, a hot spot centered on what appears to be a particle is visible. The applied image enhancement makes this hot spot appear redder. The size of the spot does not grow when moving from the second to the third frame. However, the luminosity of the hot spot increases revealing a yellow core surrounded by a blue front suggesting a weak deflagration. In the same frame the main auto ignition can be seen developing in the upper right regions. The location of this zone indicates that hot spot does not initiate this main event. Although

only limited optical data is shown the trends seems to be similar to images obtained from other studies [155].

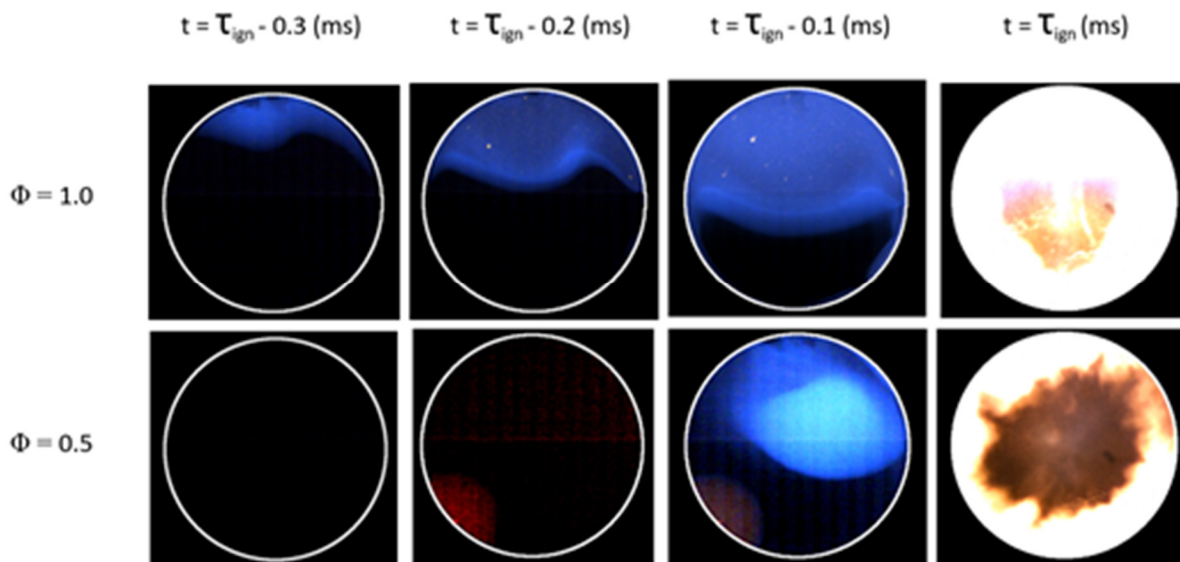


Figure 5-9 High speed images illustrating autoignition events at $\Phi=1.0$ (top row) and $\Phi=0.5$ (bottom row). First frame corresponds to ~ 0.3 ms before total ignition delay time and each frame is spaced 0.1ms apart.

5.7 Chapter Summary

In this chapter the application of the DTC approach for a known gasoline surrogate (iso-octane) was first demonstrated. Using the DTC approach in conjunction with premixed gas bottles eliminated the need for using a mixing tank and enabled faster preparation of the charge. Changes in compressed conditions were achieved by using different compression ratios rather than varying the buffer gas composition as is done in most previous studies. The data acquired for iso-octane using the current methodology is in line with other RCM data [157] and the trends observed with respect to changes in temperature and pressure is in accordance with other published hydrocarbon data. The approach used in this study is a viable approach for studying full boiling range gasoline

fuels and multicomponent gasoline surrogate fuels which will be shown in Chapter 6. For the full boiling range fuels, a gas chromatography and mass spectrometry (GCMS) study was carried out as an additional validation for identifying potential issues such as preferential evaporation or thermal cracking. No chemical activity due to CO₂ substitution, for up to 30% by mass, was observed in our study. This indicates that CO₂ acts as a thermal buffer for the conditions investigated here. This is in line with observations from other related studies [167]. Also at fixed equivalence ratio, the NTC region temperature range is not altered with increasing CO₂ dilution levels. At a compressed pressure of 20 bar, up to a factor of three increase in differential ignition delay times were observed at 30% CO₂ dilution levels in comparison to 15% dilution levels. A similar response for real gasoline blends is expected and will be discussed in the next chapter.

Chapter 6 Impact of CO₂ Dilution on Ignition Delay Times of Full Blend Gasolines in a Rapid Compression Machine

6.1 Introduction

Unlike air-dilution, EGR dilution can be implemented in current SI engines due to strategy compatibility with existing three-way catalyst systems. Hence it is prudent to test the benefits of cold EGR in context to current practical fuels such as gasoline. In this chapter autoignition delay times of two full blend gasoline fuels (high and low RON) were explored using the RCM. Benefits of using cold EGR were detailed in chapters 1 and 5. The work reported in the current chapter continues the testing methodology adopted in chapter 5 and extends the results for full blend gasoline fuels. The full blend gasoline fuels were admitted directly into the combustion chamber for mixture preparation using the direct test chamber (DTC) approach. Unlike a single component fuel such as iso-octane, full-blend gasolines are a complex mixture of several hundred hydrocarbons. In order to assess the application of the DTC approach with these fuels, a GCMS study was undertaken and the results are reported in this chapter. EGR was simulated using CO₂ dilution at 0%, 15% and 30% by volume levels and maintaining a fixed O₂:N₂ mole ratio of 1:3.76. Experiments were conducted over the temperature range of 650K-900K and at 10bar and 20 bar compressed pressure conditions for equivalence ratios of (Φ) 0.6-1.3.

6.2 Research Questions

Currently there is a lack of ignition delay times of full blend gasolines and their surrogates with CO₂ dilution in the low to intermediate temperature range available in the literature. The majority of the experimental studies on dilution in SI engines focus on dilution in the context of EGR substitution as the gamma effect of EGR dilution lowers compressed temperatures [145]. This effect is a primary driver in reducing combustion temperatures (NO_x reduction) and together with the dilution effect reduces knocking (autoignition) tendency. The main motivation and the novelty of this study was in isolating the dilution effect by maintaining the same compressed temperatures for all the tested dilution levels. The main constituents of EGR are N₂, H₂O and CO₂. The inertness of N₂ is a well-established fact, with thermal NO_x pathways most relevant at high temperatures. H₂O has been shown to retard combustion in certain conditions, while also promoting ignition at other engine relevant conditions [152,168]. Hence H₂O is not considered an inert constituent of EGR. Ignition delay times of full blend gasolines with CO₂ dilution in the low to intermediate temperature range is currently lacking and this work provides a first set of data on such a comparison. Since the temperature range in this study includes the NTC region the effect of CO₂ dilution in the NTC region will also be analyzed in detail. Additionally, the work reported in this chapter is the first to use the novel DTC approach for mixture preparation of full blend gasolines in the combustion chamber. The research questions below are sought to be answered,

1. Can the DTC approach be successfully implemented for mixture preparation with full blend gasoline fuels?
2. Can a single component surrogate iso-octane adequately capture the ignition delay trends of the full blend gasoline over the temperature range for both diluted and undiluted conditions?
3. Are the effects of CO₂ dilution for the full blend gasolines comparable to those found with the CO₂-iso-octane-air mixtures from Chapter 5?
4. Can CO₂ dilution provide any octane relaxation potential?

6.3 Literature Review

Autoignition delay times of iso-octane (primary component of PRF) and its response to CO₂ dilution was studied in Chapter 5. In comparison to ignition delay studies on simple and multi-component gasoline surrogates, studies on full blend gasolines in the low to intermediate temperature range has been limited with most of the recent work done at KAUST [169–171] on full blend FACE fuels. Some of these works and the ignition delay trends observed are discussed below. The initial work of Kukadapu et al [172] provided the first ignition delay data on full blend gasoline (RD 387) at low to intermediate temperature. The work covered $\phi=0.3-1.0$ at compressed pressures of 20 and 40 bar over the 665K-950K temperature range. The performance of chosen surrogates was also tested using 0D simulations. It was observed that the pressure rise after the first stage of ignition (when observed) reduced with increasing compressed temperature. The NTC response of the gasoline was noticed to be flatter and also shifted to higher temperatures with increase in pressure. In a study by Javed et al. [169] ignition delay times of FACE I and FACE J fuels with an anti-knock index (AKI) of 70 and low octane sensitivity were compared. The two

gasolines, despite of large differences in their compositions, exhibited similar reactivity due to similar octane ratings. By comparing the results with low-temperature ignition delay data from other studies it was shown that octane and compositional differences have negligible effect on low temperature reactivity of low octane, low sensitivity gasolines.

Lee et al. [173] recently measured the ignition delay times of two oxygenated full blend gasolines from Haltermann (RON=91) and Coryton (RON=97.5), at 650K-1250K and at 10-40 bar pressures using both an RCM and a shock tube. Other than formulating suitable surrogates they also focused on understanding the dependence of ignition delay times on RON/MON and fuel formulation. The study showed that the effect of octane number (and fuel composition) on autoignition delay times were more pronounced in the NTC (or intermediate temperature) region. Three surrogates with up to eight components were used for comparison. The authors also observed that for the lower sensitivity (due to more paraffins) Haltermann gasoline, both two stage ignition and the NTC behavior were more pronounced [14]. Irrespective of the fuel type the NTC region was observed to be less pronounced at 40 bar pressure. The authors also observed that at temperatures above 900K, ignition delay times became independent of RON/MON. Also, dependence of ignition delay times on the type of fuel was higher at 20 bar compared to the 10 bar and 40 bar experiments [14].

Chung et al. [174] studied a 95 RON gasoline, along with a few surrogates at temperatures between 650-1000K using a RCM. Their research indicated that the octane number of the fuel determines the occurrence of two-stage ignition. Gauthier et al. [168] measured RD387 ignition delay times in a shock tube at temperatures between 850 to 1280K and at pressures of 15-60 atm. Ignition delay times were compared with two ternary mixtures containing iso-octane, n-heptane and toluene. In addition, the study analyzed the effect of EGR (CO_2 , H_2O , O_2 , N_2) for 10% and 20 %

EGR substitution. There was an increase in delay times with increased EGR loading at $\phi=1.0$ but at $\phi=0.5$ the presence of EGR components did not affect the ignition delay times.

Studies explicitly examining the effect of CO_2 dilution on gasoline-air mixtures are nonexistent, but several studies have been completed on alkanes, a major hydrocarbon type found in gasoline and its surrogates. He et al. [152] studied the ignition delay times of iso-octane mixtures with trace amounts of H_2O and CO_2 (0.5, 2.0 and 3% by mol) for pressures of 5-20 atm and at high temperatures of 943-1027 K in a RCM. This study did not include the NTC region since iso-octane does not show NTC behavior over this temperature range. For these small amounts of CO_2 dilution there was no chemical effect, however the H_2O dilution did decrease the ignition delay by small amounts. Di et al. [151] explored the effects of several buffer gases on iso-octane which included Argon(Ar), N_2 , and a mixture of CO_2 and Ar in a RCM. However they did not explore the dilution effects in context with EGR substitution due to a fixed buffergas: O_2 ratio at 1:3.76. Experiments covered the 600-800K range at 20bar and $\Phi=1$. Their observations indicated that the effects of the buffer gases on the first-stage ignition delay were very small, but the changing heat capacity of the buffer gas changed the final delay time during two-stage ignition. The higher heat capacity of CO_2 increased the total ignition delay time in comparison to N_2 . Di et al. also noticed the effect of the higher collision efficiency of CO_2 on ignition delay times compared to N_2 (CO_2 is 3.8 times higher than that of N_2). Higher collision efficiency reduces ignition delay times. When a single stage ignition event was observed, which occurs at temperatures lower than the NTC region (700 K for isooctane), experimental data and model predictions showed no influence of buffer gas composition on delay times.

$\text{OH} + \text{CO} \rightleftharpoons \text{H} + \text{CO}_2$ is a known reaction pathway through which CO_2 participates in chemical reactions and slows down the combustion process by competing for H radicals [175]. In recent

work by Tingas et al. [167], the authors explored the dilution effects of CO₂ and water separately on NO_x emissions and ignition delay times in methane mixtures. They performed adiabatic and isochoric autoignition simulations at 800 K, $\Phi=0.8$ and 30 bar conditions with CO₂, H₂O and Ar as diluents. The study included data on 15% and 30% CO₂ dilution levels by mole fraction. They concluded that the CO₂ impact on reactions is mostly thermal in nature and that the CO₂ acts predominantly as a thermal buffer, while for H₂O dilution they showed that water not only acts a thermal buffer but also enhances reactivity through the reaction $\text{H}_2\text{O}_2 + \text{H}_2\text{O} \rightarrow \text{OH} + \text{OH} + \text{H}_2\text{O}$ [167]. Because of the chemical nature, sometimes ignition delay can be shortened with H₂O addition, however, this effect was never observed with CO₂. The final mass fraction values of NO and CO were both reduced through dilution addition. The study did not include the NTC region since methane does not exhibit NTC behavior [158].

6.4 Experimental Methodology

6.4.1 Mixture Preparation

The mixture preparation methodology is very similar to the steps followed in Chapter 5. Based on the dilution level required, the RCM was filled to the target pressure with the appropriate premixed-gas was and the gas manifold was closed. The fuel was then metered into the test chamber using a production water cooled 7-hole GDI injector manufactured by Bosch. A hydraulic accumulator pressurized to 30 bar was used to pressurize the fuel line. In contrast to chapter 5, fuel flow calibration was performed gravimetrically in the pulse width range of 0.5 to 1.0ms. The pulse width range was chosen so that multiple injections could be used for a given equivalence ratio during the mixture preparation process, reducing variability between tests [164]. At each pulse width the injector was pulsed 100 times into a graduated cylinder. The weight of the cylinder

before and after fuel injection event is measured with a calibrated scale with readouts showing two significant digits. The results were used to obtain the final calibration curve for each fuel and its injectors. Mixture stoichiometry was controlled within the test chamber by varying the pulse width and number of injector pulses.

6.4.2 Fuel Characterization and Handling

Two full blend fuels, characterized and referred to as low RON and high RON fuels, were considered for testing. The fuel properties such as RON, molecular weight of the fuel etc. are proprietary information. Each of the fuels were stored in a separate fuel accumulator, with separate fuel delivery lines and separate calibrated fuel injectors. The fuels used were of unknown composition with only distinction being the RON characterization. Since the molecular weight of the fuels were unknown AFR stoichiometric value of 14.6 for gasoline [11] was used for all the fuels when calculating the stoichiometry. Stoichiometry was calculated using Eq 5.1 and 5.2. Gasoline molecular weight can vary from ~85 to 110, higher RON gasoline is expected to have higher molecular weight due to the presence of heavier molecules [7]. This could introduce differences between the estimated equivalence ratio and actual equivalence ratio, hence some deviation is to be expected.

6.4.3 GCMS Study

Verification of mass loading of the direct injectors used for DTC approach was completed by Allen et al. [164] and hence was not repeated for this study. As a first step towards validation, ignition delay data obtained for iso-octane-air mixtures prepared using the DTC approach was compared with data from other facilities, as described in chapter 5. As iso-octane is a single component fuel, determination of its vapor pressure for given initial conditions is straight forward. For the case of

full blend gasolines containing numerous components spanning a range of boiling points, further validation is required before using the DTC approach. The purpose of this current GCMS study is to confirm evaporation of fuel blend components (without thermal decomposition or condensation) and determine the appropriate duration for complete evaporation and mixing of the fuel prior to testing. The GCMS gas-phase sampling study is very similar to what was reported in [164] except for several key differences as follows. The GCMS samples were drawn from the RCM at wall temperatures of 80°C, 100°C and 120°C. Gas phase samples were extracted at 2 minutes and at 10 minutes after fuel injection using a 10ml gas tight syringe equipped with a stopcock. After extraction, the gas phase sample was bubbled through a HPLC grade chloroform solvent. This chloroform solvent was premixed with known concentrations of stable labeled internal standards which were used as references for obtaining concentration values of the C4-C10 n-alkanes present in the sample. Before the sampling procedure, the RCM was pressurized to 1 bar and fuel corresponding to $\phi=1.4$ was injected. This is richer than the maximum equivalence ratio target ($\phi = 1.3$) for our tests and the 1 bar pressure was chosen to avoid a pressure differential between the solvent (stored at 1 bar) and hence avoid the formation of spray when inserting or removing the gas tight syringe through the septum. This procedure was repeated three times at each test condition and the GCMS results obtained for the gasoline fuels are shown in Figure 6-1 and 6-2. The results suggest that, within the experimental error, a wall temperature as low of 80°C is adequate and 2 minutes of mixture preparation time is enough to achieve a homogeneous mixture. The intent of this study is to determine the evaporation duration of gasoline, and hence only the normalized concentration of the major species were compared at different wall temperatures. Apart from the n-alkanes(C4-C10), this study did not reveal the actual composition of various components present in the gasoline.

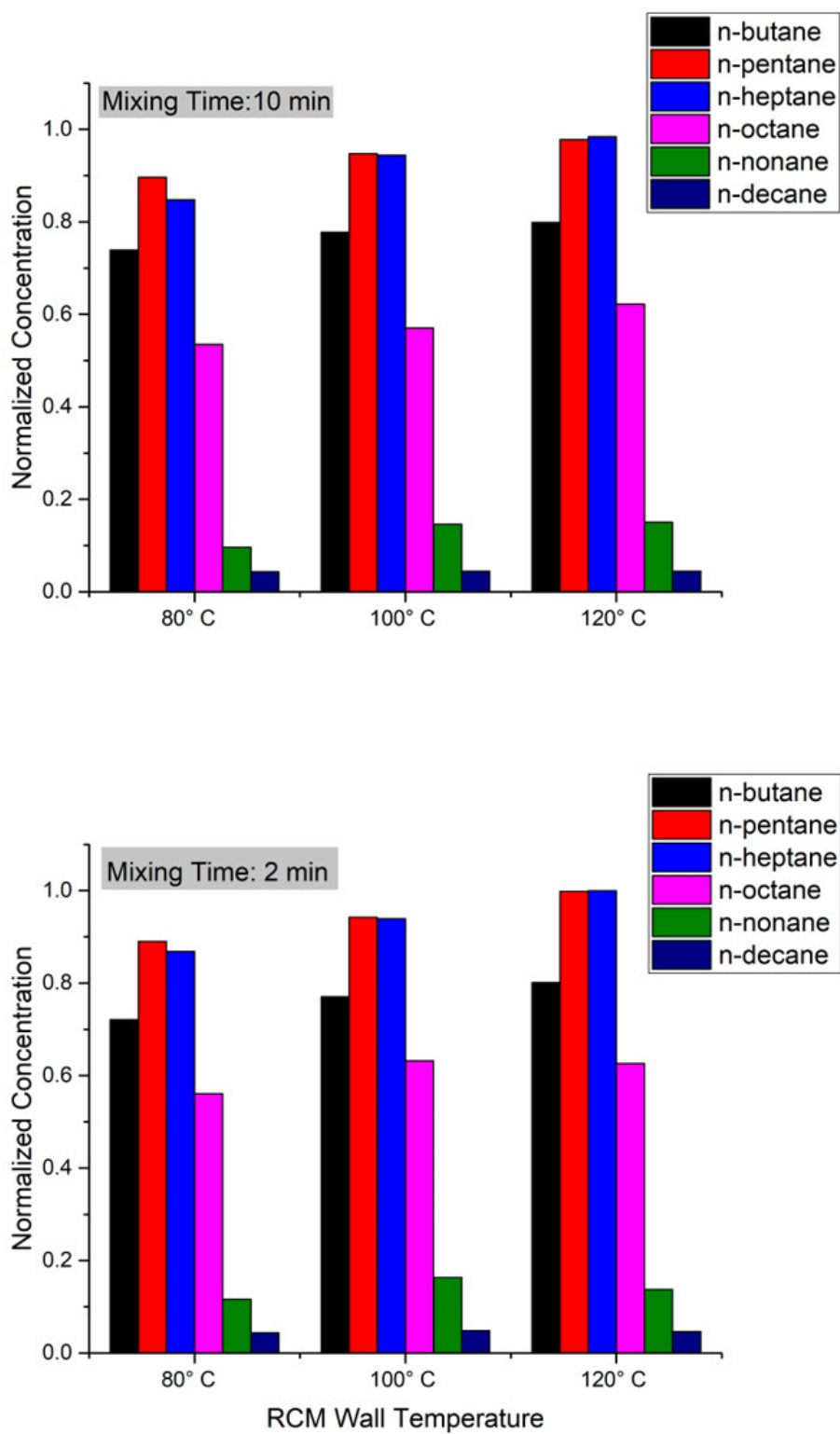


Figure 6-1 Results from GCMS analysis showing normalized concentration values of n-alkanes in the gas phase sample of low RON fuel.

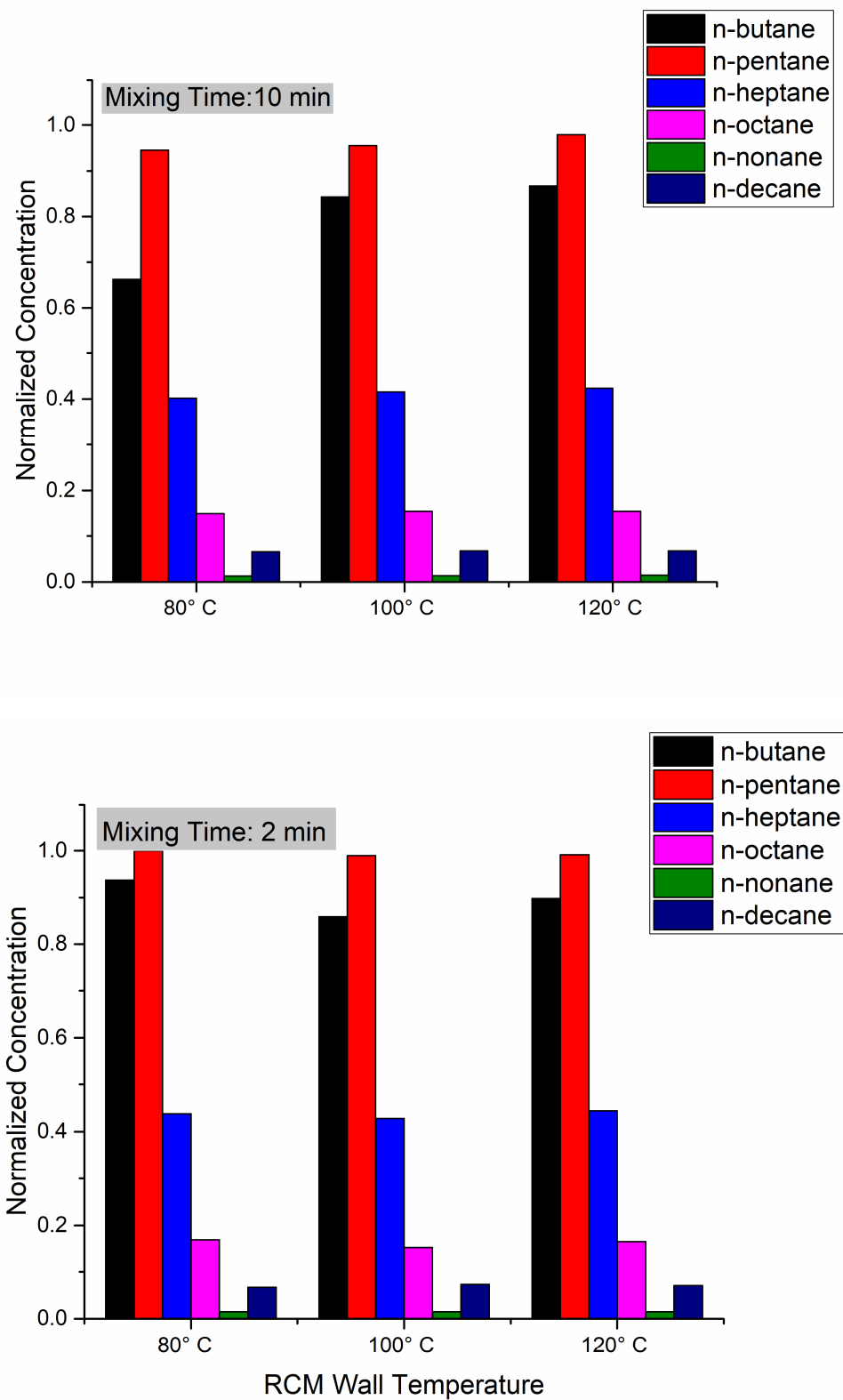


Figure 6-2 GCMS results showing normalized concentration values of n-alkanes measured in the gas phase sample of the high RON fuel.

6.5 Results and Discussions

6.5.1 Effect of Equivalence Ratio and Pressure

The effect of equivalence ratio on ignition delay times (IDTs) is investigated for all dilution levels in Figure 6-3. The data points were connected with straight lines in order to improve visualization and a minimum of two data points taken to ensure repeatability at each point are shown. In Figure 6-3, for the high RON fuel (left column), the NTC region is observed between 750 and 800K at the 20 bar compressed pressure condition. At undiluted conditions past 850K, the EOC was not discernible at 20 bar pressures and hence the ignition delay data could not be recorded. At 10 bar, the NTC region starts early at 700K and is more pronounced. This trend can be observed to hold as the dilution level increases except that the delay times are now retarded. In general, a trend of increasing reactivity with increasing equivalence ratio can be noted. The increase in reactivity with increasing equivalence ratio is due to the effect of maintaining a fixed N_2/O_2 ratio but varying the fuel concentration levels. An opposite trend where lean mixtures become more reactive will be observed if the equivalence ratio is varied while the fuel concentration is held constant. In such a scenario, the higher reactivity is a byproduct of the increase in oxygen concentration leading to lower dilution levels [77,176]. Also, it can be observed that the NTC region shifts to higher temperatures with increasing pressures. The reason for this shift is due to the pressure dependence of the ceiling temperature which controls H_2O_2 decomposition [172]. For 0% dilution, and at 20 bar conditions, the $\phi=1.0$ and $\phi=1.3$ curves exhibit very similar ignition delay times at lower temperatures. Similar behavior can also be observed for temperatures above 850K for the dilution cases at both 10 bar and 20 bar conditions. The difference between $\phi=0.6$ and $\phi=1.0$ curves are much more pronounced compared to the difference between stoichiometric and the richer condition, indicating that for rich of stoichiometric conditions the mixture reactivity is very similar.

It is also interesting to note that the profile of the $\phi=0.6$ at 20 bar looks very similar to the richest condition at 10 bar for all dilution levels.

For the low RON fuel (Figure 6-3 – right column) at 20 bar and at temperatures below 700K, the ignition delay times are independent of equivalence ratio and this trend holds for all dilution levels and at 10 bar compressed pressure conditions. The lines connecting the data between 650 and 700K at 10 bar show crossover and this can be attributed to a possible shift in NTC region with changing equivalence ratio. The NTC region moves to lower temperatures with decreasing equivalence ratio and this is more pronounced at $\phi=0.6$ and at the 10 bar condition for this temperature range. Hence a possible reason for this overlap is the shifting curvature due to the changing NTC region not being captured due to the lack of resolution in the data points, since data was only taken at 50K intervals. In future studies it is recommended that a minimum of a 25 K (or less) temperature interval be maintained to appropriately capture this region. Here the NTC region, can be observed between 750 and 850K irrespective of the compressed pressure. Compared to the higher RON fuel, with the lower RON fuel the NTC region seems to lie in a narrow range and is more pronounced. The shift in the NTC region with pressure is not apparent here and possible causes are lack of resolution combined with the narrow NTC region. In terms of reactivity at lower temperatures, the lower RON fuel exhibits a clear difference at $\phi=0.6$, while the richer cases exhibit minimal difference. As a general trend, it can be concluded that at $\phi=1.0$ and $\phi=1.3$, differences in reactivity is minimal at temperatures below 700K and above 800 K irrespective of the pressure and fuels studied here.

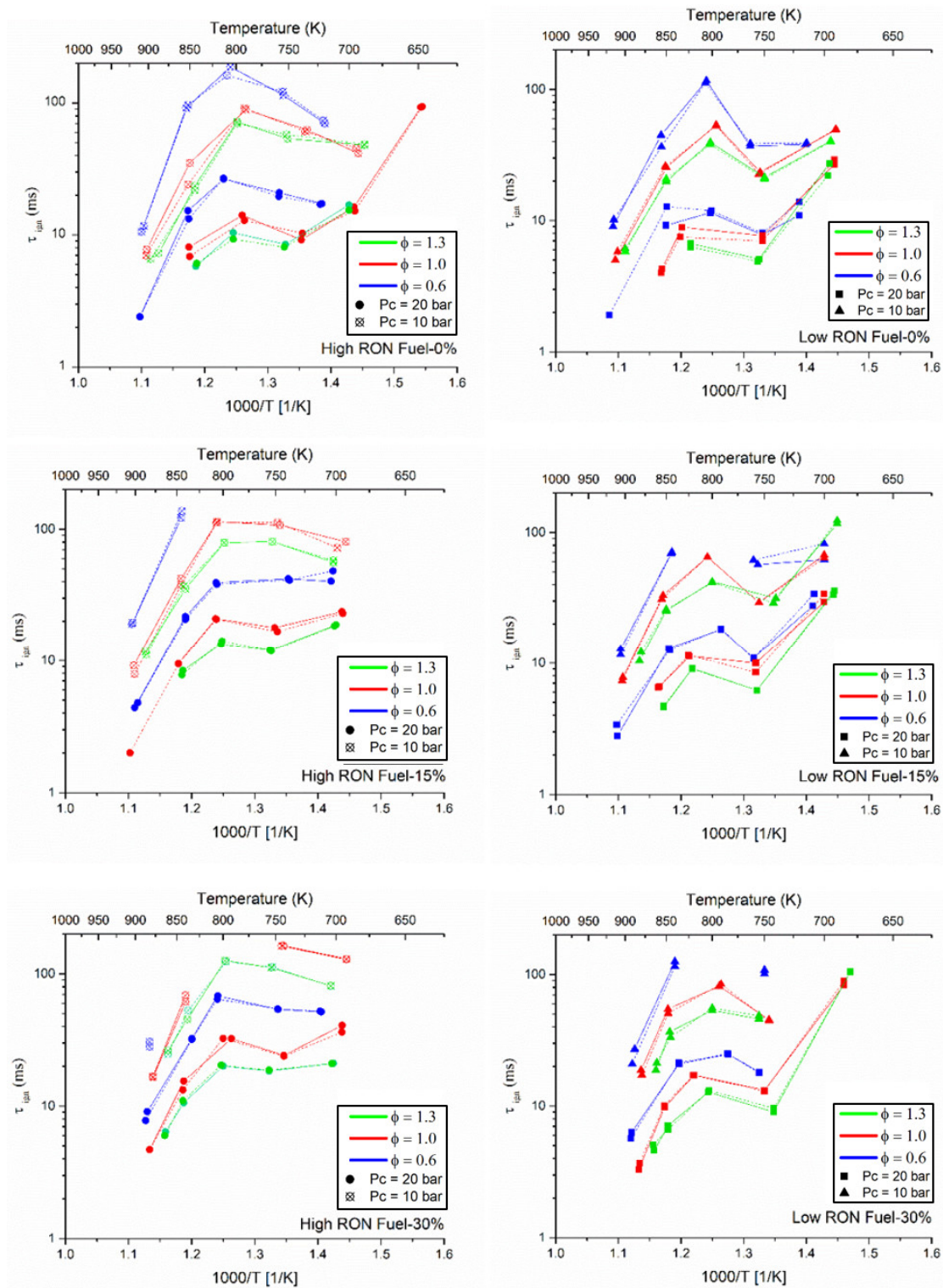


Figure 6-3 Ignition delay times shown in Arrhenius form for high RON fuel (left column) and low RON fuel (right column) for 0% (upper), 15% (middle) and 30% (lower) CO₂ dilution levels at a compressed pressure of 20±0.5 and 10±0.5 bar. Line type indicates different experimental sets.

6.5.2 Effect of CO₂ dilution and comparison with surrogate (iso-octane)

Figures 6-4 and 6-5 show ignition delay times for the high RON (green) and Low RON (red) fuels respectively, with 0%, 15% and 30% CO₂ dilution at equivalence ratios of 0.6, 1.0 and 1.3, at 20 bar (left) and 10 bar (right) compressed conditions. For the high RON fuel, at 20 bar conditions, the effect of CO₂ dilution is more pronounced within the NTC region. At lower temperatures, the reactivity of diluted and undiluted mixtures are similar at $\phi=1.3$ but with decreasing ϕ differences emerge. This reactivity trend is similar to equivalence ratio effect observed in Figure 6 and is line with results from previous work by the authors on iso-octane [177]. At higher temperatures the response to CO₂ dilution is even less noticeable and this can be clearly observed for the 10-bar data. It can be noted that the addition of diluent (CO₂) does not interfere with the NTC trends observed with the gasoline-air mixtures, with this observation consistent with previous chapter. Based on observations from current chapter and chapter 5, it can be stated that the CO₂ dilution only increased the delay times. The reactivity trend of the undiluted fuel-air mixture is preserved throughout the temperature range. This denotes that no significant chemical reactivity due to CO₂ addition is present since any such chemical activity would easily influence the NTC trend.

As a preliminary step, the ignition delay times for the full blend gasolines have been compared to previous results for iso-octane reported in chapter 5. Development of suitable surrogates is key for accelerating numerical simulations aimed towards developing high efficiency IC engines. Currently surrogates with 4 or more components (multicomponent) are preferred for capturing the ignition delay trends of gasoline observed in the low and intermediate temperature range [1]. For higher temperatures, as encountered in shock tubes, PRF mixtures are sufficient for capturing the reactivity of gasoline due to the fuel molecular structure becoming less important at higher temperatures [1]. Iso-octane is widely considered a single component gasoline surrogate and this

preliminary comparison is expected to aid in comparing the performance of multicomponent surrogates, which are tested in the next chapter. Only the trends for the 20 bar data is discussed here since iso-octane was much less reactive at 10 bar conditions and data points for comparison was limited. Compared to the high RON fuel, as expected, iso-octane shows longer ignition delay throughout the temperature range studied here. This indicates that the high RON fuel is of lower ON than iso-octane. Iso-octane's response to CO₂ dilution is also more pronounced than for the high RON fuel.

The NTC region is very poorly captured by the iso-octane, however the trend in the ignition delay times is matched at 800K and for higher temperatures. The NTC region is observed for fuels such as gasoline due to the shift in reaction pathways from the low to intermediate temperature range. In the case of iso-octane, the iso-octyl radicals are converted to alkylperoxy radicals through addition reactions with molecular oxygen. At low temperatures, followed by subsequent O₂ addition and series of isomerization reactions, ketohydroperoxide (containing carbonyl group) and OH radicals are formed. Additional OH radicals are formed by decomposition of ketohydroperoxides, thus leading to exponential growth in the OH radical leading to ignition [178]. At intermediate temperatures (NTC region), HO₂ production pathways dominate, and a slowing down of the chemistry occurs, which can be observed as the NTC region. In the NTC region, concerted elimination reactions (with HO₂ being eliminated) forming alkenes and HO₂ from RO₂, R+O₂ or QOOH is favored over subsequent O₂ addition [179]. HO₂ is primarily converted to H₂O₂ which later decomposes to two OH radicals via chain branching leading to the final stage ignition. At $\phi=0.6$ the NTC region is not very pronounced for the full blend fuels and similar effect is observed for the iso-octane as well. Within the NTC region, both the high RON fuel and iso-octane show peak IDTs at 800K. But the IDTs are an order of magnitudes different between the fuel and

the surrogate with differences decreasing with increases in temperatures. Additionally, the NTC curve appears different for the iso-octane in comparison to the high RON fuel. For the high RON fuel, the NTC region is less pronounced and plateaus in the 750K - 800K range. The NTC region starts at 700K for the iso-octane and 750K for the high RON fuel. Due to this difference, the 20 bar data for $\phi=1.3$ and 1.0, shows ignition delay times that are similar between the iso-octane and the full blend fuel at 750K and 700K.

At 20 bar conditions and for 800K target compressed temperatures, the first stage ignition occurred very close to EOC. Hence the test target temperature was shifted to higher values as can be seen in Figure 6-5. At 800K for $\phi=1.3$, the ignition delay times for the 0% dilution and 15% dilution cases are similar. This may be due to the flat NTC profile exhibited by the 15% dilution case and the lack of test data resolution in the region. The observations made previously for the high RON fuel regarding response to CO₂ dilution hold for the low RON fuel as well. The IDTs of the low RON fuel and iso-octane show a significant mismatch throughout the temperature range. However, the trend is somewhat improved in the temperature range of 750-900K for $\phi=1.3$, 1.0 and 0.6. Similar to the high RON fuel, with the low RON fuel the NTC region starts at lower temperature and is more pronounced for the iso-octane compared to the low RON fuel. The differences in the NTC response of the fuels can be linked to the octane sensitivity [180]. Compared to full blend gasolines which possess inherent sensitivity in the range of 7 to 11 [60], the isooctane (and PRFs) possess no sensitivity due to their paraffinic nature. Here sensitivity is defined as the difference between the RON and MON rating of the fuel. HO₂ production is favored more for fuels with higher paraffin content (or lower sensitivity) compared to a higher sensitivity fuel. This is the reason for the enhanced NTC behavior of the iso-octane compared to the full blend gasoline [178]. Fuels possessing high octane sensitivity show reduced to no NTC behavior due the electron

delocalization phenomenon that occurs for fuel components such as alkenes, alcohols and aromatics [58]. Such components tend to produce stable intermediates through reaction with H_2O_2 and remain unreactive until high temperature capable of breaking O-O bonds are achieved [58]. Since the full blend gasoline is a mixture of such components, the NTC region is less pronounced compared to iso-octane. The results from Figure 6-4 and 6-5 clearly show that a single component surrogate is a rather poor choice for capturing gasoline reactivity in the low and intermediate temperature range. It is expected that at temperatures higher than 900K the differences would further reduce for both diluted and undiluted cases due to the fuels' compositional differences having a less pronounced effect at higher temperatures due to a shift towards high temperature reaction pathways [46].

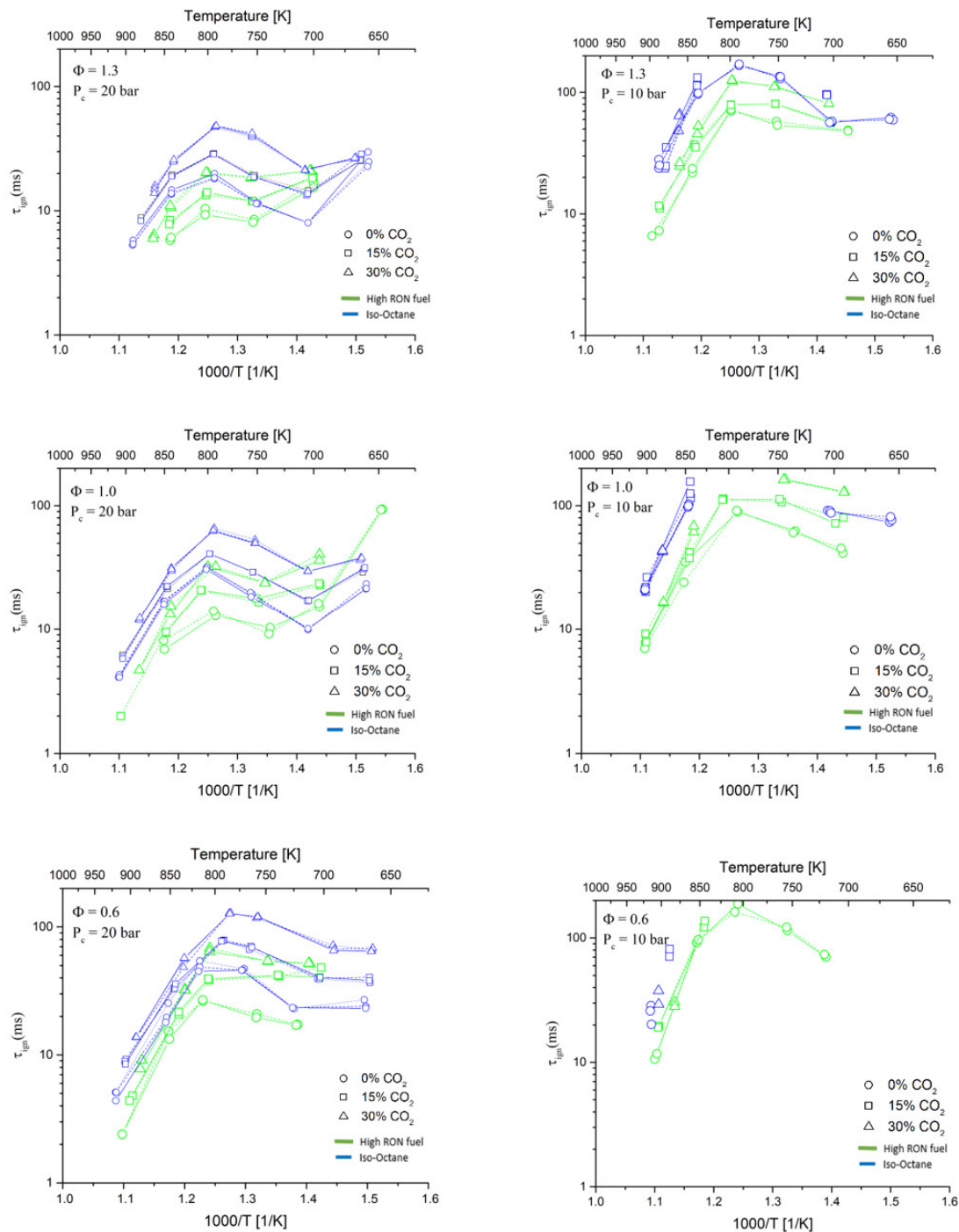


Figure 6-4 Ignition delay times of high RON fuel (green) and surrogate (iso-octane) shown in Arrhenius form for 0% (circles), 15% (squares) and 30% (triangles) CO₂ dilution levels for $\Phi=0.6$, $\Phi=1.0$ and $\Phi=1.3$ at a compressed pressure of 20 ± 0.5 bar (column) and 10 ± 0.5 (left column) bar. Line type indicates different experimental sets.

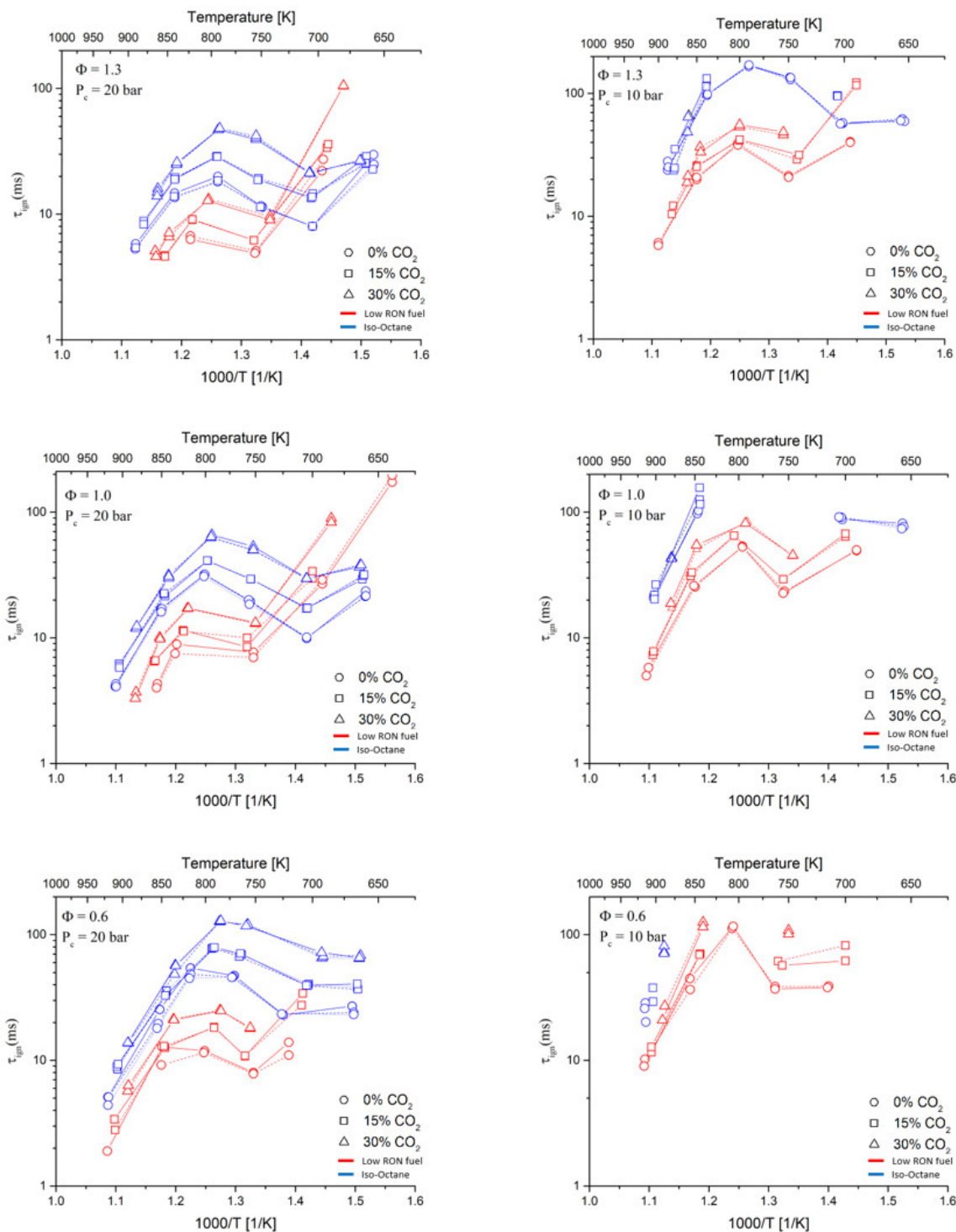


Figure 6-5 Ignition delay times of low RON fuel (red) and surrogate (iso-octane) shown in Arrhenius form for 0% (circles), 15% (squares) and 30% (triangles) CO₂ dilution levels for $\Phi=0.6$, $\Phi=1.0$ and $\Phi=1.3$ at a compressed pressure of 20 ± 0.5 bar (right column) and 10 ± 0.5 bar (left column) bar. Line type indicates different experimental sets.

6.5.3 Effect of Octane Number

Figure 6-6 shows a comparison between the IDTs of high RON versus low RON fuels for all dilution levels and equivalence ratios at both 10 and 20 bar compressed conditions. For these fuels, at the 20 bar conditions and at $\phi=0.6$, the NTC region for the high RON fuel starts at a relatively lower temperature ($T=700\text{K}$) compared to the low RON fuel which shows NTC behavior between 750K - 850K . For temperatures above 700K (including the NTC region and the high temperature region) the 30% dilution curve of the low RON fuel overlaps with the 0% dilution curve of the high RON fuel. For all the equivalence ratios studied here, except at the lowest temperature ($T\sim 675\text{K}$), the lower RON fuel at the 30% dilution level overlaps with the 15% or the 0% dilution curve of the higher RON fuel. It can be observed that the lower RON fuel shows a very pronounced NTC region while the higher RON fuel exhibits a flatter NTC curve. The lower RON fuel also exhibits a shorter NTC region. It is possible that the lower RON fuel shows a more pronounced NTC behavior due to the high amount of paraffinic components expected in this fuel when compared to the higher RON fuel which is expected to have higher amount of aromatics [7]. High amounts of n-alkanes in fuels tends to produce large amounts of H_2O_2 , OH and HO_2 , leading to the fuel displaying a more pronounced NTC behavior [181]. Within the NTC region, the higher RON fuel responds to dilution more prominently compared to the lower RON fuel, showing that the effect of dilution also depends on the octane rating of the base fuel. A similar trend was observed in the earlier comparison between the fuels and iso-octane, where iso-octane had a higher RON compared to the full blend fuels. This indicates that the retardation effect of CO_2 scales with increasing RON values. Interestingly it can be seen that the lower RON fuel is less reactive at 650K compared to the higher RON fuel at 20 bar conditions. For temperatures above 800K , at a given dilution level, irrespective of the octane number the ignition delay times are very similar at

the 0% and 15% dilution levels. However, for temperatures lower than 800K, the 30% dilution data from the high RON fuel does show a discernable difference. For $T > 800\text{K}$, the impact of dilution is less pronounced, and it can be expected that at temperatures higher than 900K this difference should become negligible. At 850K and higher temperatures, the lower RON fuel is observed to be more reactive compared to the high-octane fuel. At 10 bar conditions, for the high RON fuel, the entire data set lies within the NTC region. A similar overlap between the high RON fuel's no dilution level and the low RON fuel highest dilution point is seen for temperatures greater than 750K. However, this trend is not strongly evident due to the differing NTC profiles of the fuels. At 850 K and 900 K the reactivity is independent of dilution levels or octane numbers. The reason for this is that at high temperatures $\text{H}_2\text{O}_2 \rightarrow \text{OH} + \text{OH} (+\text{M})$ and $\text{H} + \text{O}_2 \rightarrow \text{OH} + \text{O}$ reactions control the chain branching process for a wide range of practical fuels and surrogates. Hence the ignition delay times at these temperatures were not found to be octane sensitive [170]. Overall as a general trend it can be seen that with 30% CO_2 substitution the lower RON fuel matches the higher RON ignition delay times at 0% dilution and sometimes up to 15% dilution. This shows the octane relaxation potential of CO_2 dilution when used in SI engine operation. High levels of CO_2 dilution can impact combustion stability, under such circumstances ignition enhancement techniques such as turbulent jet ignition (TJI) can be used[182].

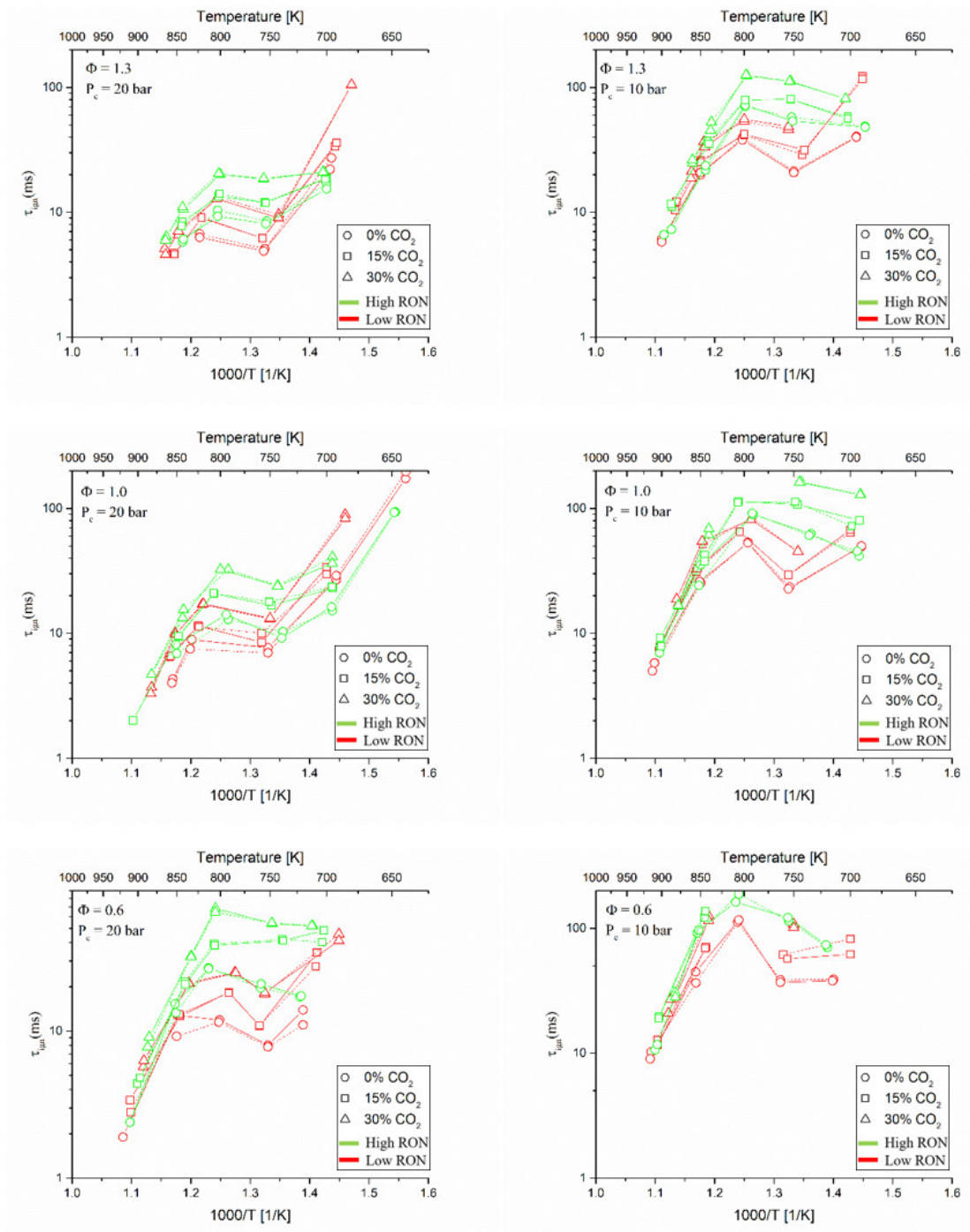


Figure 6-6 Ignition delay times of low RON fuel (red) and high RON fuel (green) shown in Arrhenius form for 0% (circles), 15% (squares) and 30% (triangles) CO₂ dilution levels for $\Phi=0.6$, $\Phi=1$ and $\Phi=1.3$ at a compressed pressure of 20 ± 0.5 bar (right column) and 10 ± 0.5 bar (left column) bar. Line type indicates different experimental sets.

6.6 Chapter Summary

In this chapter, experimental methodology developed for testing iso-octane-air mixtures in chapter 5 was successfully applied for testing full boiling range gasoline fuels in the RCM. Additionally, GCMS tests were carried out to ensure complete vaporization of the injected gasoline. Ignition delay times of two full blend gasolines were measured using an RCM for a range of equivalence ratios and CO₂ dilution levels, over a 650-900K temperature range and at 10 and 20 bar compressed pressures. Major observations are summarized below,

- 1) The DTC approach was successfully applied for preparing gasoline-oxidizer mixtures within the RCM test chamber. GCMS results indicated complete vaporization and mixing for wall temperatures around 80°C and mixing time of 2 minutes.
- 2) CO₂ dilution retarded the ignition delay times of gasoline-oxidizer mixtures for the temperature range studied here. The retardation effect was more pronounced within the NTC region when compared to low and high temperatures. Even at 30% dilution levels the reactivity trend of the undiluted fuel-air mixture was preserved indicating no significant chemical reactivity from CO₂ addition.
- 3) Response to dilution was more pronounced (higher retarding effect) with increasing RON values. This effect was observed for the full blend fuels and for the surrogate(iso-octane). The retardation effect of CO₂ scales with increasing RON values.
- 4) The single component surrogate (iso-octane) failed to capture the reactivity trends of both the gasolines for the conditions studied here. Multicomponent fuels will be explored in a future study with focus on capturing the reactivity in the NTC region for both diluted and undiluted mixtures.

- 5) At 20 bar conditions, the ignition delay times of the 30% CO₂ substituted low RON fuel mixtures overlapped with undiluted delay times of the high-RON fuels. This shows that CO₂ substitution can provide octane relief for use in modern downsized SI engines.

Chapter 7 Impact of CO₂ Dilution on Ignition Delay Times of Multicomponent Gasoline Surrogates in a Rapid Compression Machine

7.1 Introduction

In this chapter autoignition delay times of two multi-component surrogates with characteristics similar to that of the full blend gasoline fuels (high and low RON) studied in chapter 6 were investigated in an RCM. The reactivity of the multicomponent surrogates were compared to that of the gasoline-air mixtures at both diluted and undiluted conditions. EGR was simulated using CO₂ dilution at 0%, 15% and 30% by volume levels and maintaining a fixed O₂:N₂ mole ratio of 1:3.76. Experiments were conducted over the temperature range of 650K-900K and at 10bar and 20 bar compressed pressure conditions for equivalence ratios of ($\Phi =$) 0.6-1.3. The surrogates were admitted directly into the combustion chamber for mixture preparation using the direct test charge (DTC) approach.

7.2 Research Questions

The following research questions are sought to be addressed in this chapter,

1. Can the multi-component surrogates capture the ignition delay trends of the full blend gasoline over the intermediate temperature range at both diluted and undiluted conditions, in comparison to the iso-octane surrogate?
2. Are the effects of CO₂ dilution for the multi-component surrogates comparable to those found with the CO₂-gasoline-air mixtures from chapter 6?

3. Does the CO₂ dilution exhibit similar sensitivity to RON numbers as observed with the CO₂-gasoline-air mixtures in chapter 6?
4. What is effect of CO₂ dilution on first stage ignition delay times, for compressed conditions where two stage ignition behavior is observed?

7.3 Literature Review

Based on author's knowledge, no ignition delay time data exists for multicomponent gasoline surrogates with CO₂ dilution at the low to intermediate temperature range in the literature.

Studies on full blend gasolines in the low to intermediate temperature range have been scarce with most of the recent work done at KAUST [169–171,181] on full blend FACE fuels. Most of these studies also focused on developing a suitable surrogate with minimum number of components to emulate target properties of the full blend fuels. Some of these studies and the ignition delay trends observed are discussed below. The initial work of Kukadapu et al.

[52,172,183] provided the first ignition delay data on full blend gasoline (RD 387) at low to intermediate temperature. The work covered $\phi=0.3-1.0$ at compressed pressures of 20 and 40 bar over the 665K-950K temperature range. A three-component surrogate consisting of n-heptane, iso-octane and toluene (TPRF) and a four-component surrogate containing an additional olefin (2-pentene) component was compared with the reactivity of RD387. It was found that the 4-component surrogate was able to better capture the gasoline's reactivity under RCM conditions.

In a study by Javed et al. [169] ignition delay times of FACE I and FACE J fuels with an anti-knock index (AKI) of 70 and low octane sensitivity were compared. The two gasolines, despite large differences in their compositions, exhibited similar reactivity due to similar octane ratings. Performance of a PRF surrogate matching the octane numbers and two multicomponent

surrogates containing up to 7 components were tested using chemical kinetic simulations [169]. The multicomponent surrogates captured the reactivity in the low temperature and NTC region better in comparison to the PRF surrogate.

Lee et al. [173] recently measured the ignition delay times of two oxygenated full blend gasolines from Haltermann (RON=91) and Coryton (RON=97.5), at 650K-1250K and at 10-40 bar pressures using both an RCM and a shock tube. In this study three surrogates were formulated which included a TPRF mixture, a quaternary surrogate (TPRF+Ethanol) and an 8-component surrogate. The authors concluded that only complex surrogates can adequately capture the reactivity trends of high sensitivity gasoline. Other than formulating suitable surrogates they also focused on understanding the dependence of ignition delay times on RON/MON and fuel formulation. The study showed that the effect of octane number (and fuel composition) on autoignition delay times were more pronounced in the NTC (or intermediate temperature) region. The authors also observed that for the lower sensitivity (due to more paraffins) Haltermann gasoline, both two stage ignition and the NTC behavior were more pronounced [173]. Irrespective of the fuel type the NTC region was observed to be less pronounced at 40 bar pressure. The authors also observed that at temperatures above 900K, ignition delay times became independent of RON/MON. Also, dependence of ignition delay times on the type of fuel was higher at 20 bar compared to the 10 bar and 40 bar experiments [173].

Chung et al. [174] studied a 95 RON gasoline, along with a few surrogates at temperatures between 650-1000K using a RCM. Their results indicated that both octane number and chemical structure of the gasoline determines the occurrence of two-stage ignition. The surrogates tested included iso-octane, TPRF and two 7-component surrogates. The authors concluded that up to

20% cyclic alkenes are required in the surrogates in order to capture both the first and final stage ignition delay times of the target gasoline. Gauthier et al. [168] measured RD387 ignition delay times in a shock tube at temperatures between 850 to 1280K and at pressures of 15-60 atm and compared ignition delay times with two TPRF mixtures. Since the study did not cover the NTC region, the reactivity of the surrogates matched the gasoline well since complex surrogates are not required to match high temperature reactivity. In addition, the study analyzed the effect of EGR (CO₂, H₂O, O₂, N₂) for 10% and 20 % EGR substitution. There was an increase in delay times with increased EGR loading at $\phi=1.0$ but at $\phi=0.5$ the presence of EGR components did not affect the ignition delay times. A more comprehensive list on ignition delay time studies conducted over several simple and complex gasoline surrogates is available in [1].

7.4 Test Data Interpretation

Testing methodology and mixture preparation techniques carried out in this chapter have already been described in chapters 5 and 6. The primary data extracted from the RCM pressure trace with definitions are illustrated in Figure 7-1. End of compression (EOC) is designated as the time when the dP/dt values becomes negative after the start of compression. Here τ_1 is defined as the first stage ignition delay (if observed) which is the elapsed time duration from EOC to maximum pressure rise rate due to first stage ignition activity. τ_2 is measured from the end of τ_1 period until dP/dt becomes maximum due to the main ignition event. $\tau_1 + \tau_2$ is the total ignition time.

Repeatability and the influence of CO₂ dilution on the pressure curves are shown in Figure 7-2. The achieved compressed pressures are within ± 0.5 bar from the target pressures and hence no pressure scaling is used when reporting the ignition delay times. Test conditions registering

ignition delay times greater than 100ms are generally not included unless it helps in visualizing the trend of the delay times.

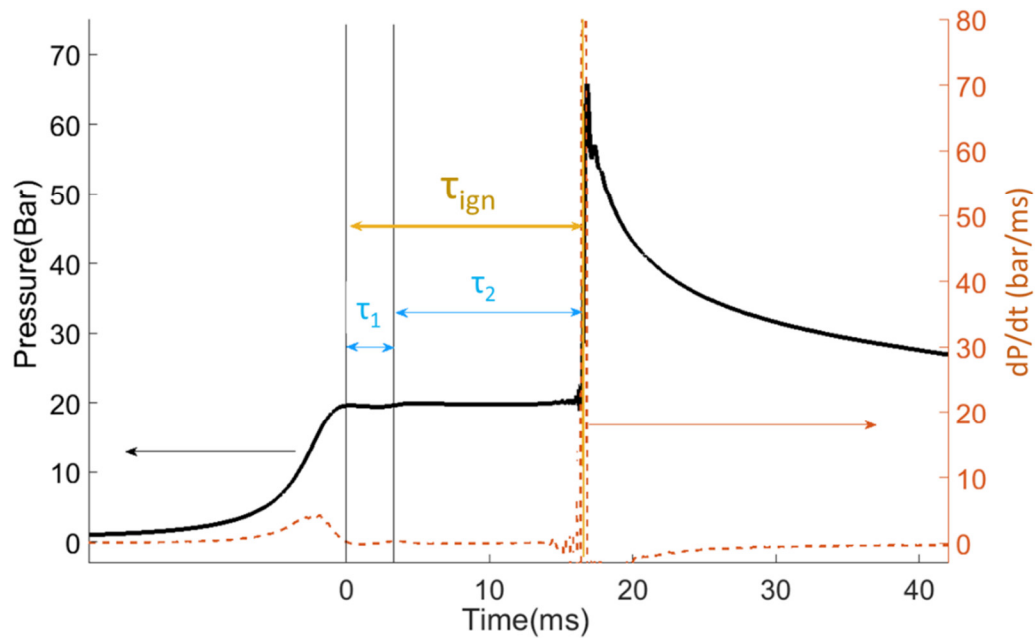


Figure 7-1 Sample pressure and dP/dt curve illustrating durations of ignition events.

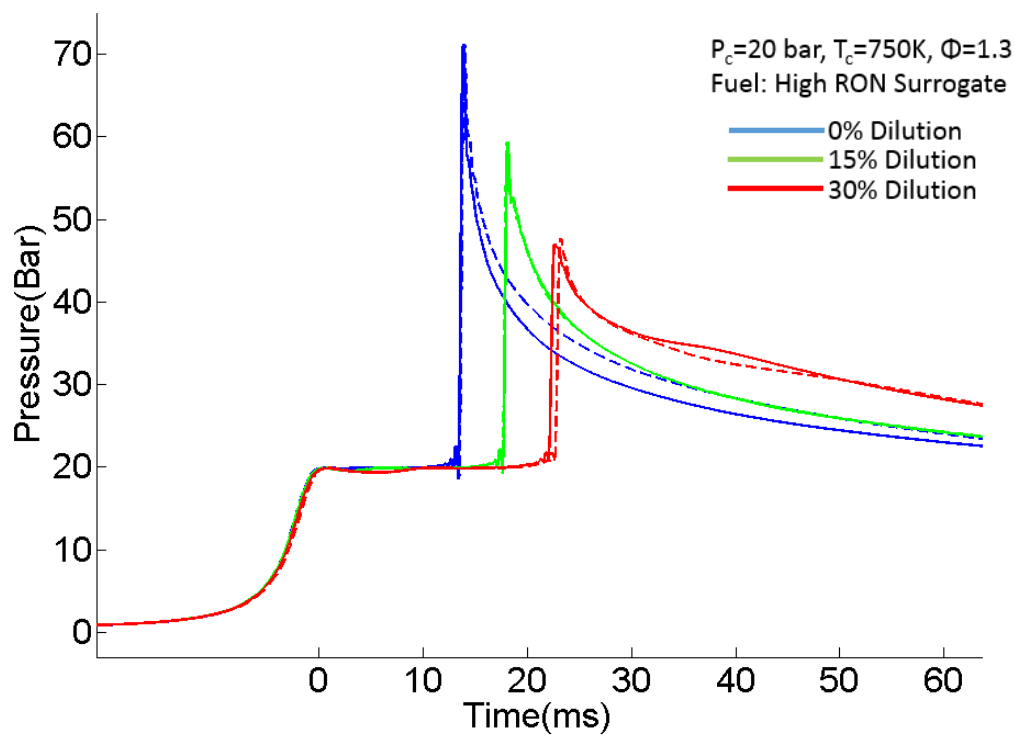


Figure 7-2 Pressure traces showing repeatability and influence of CO₂ dilution. Line type indicates different experimental sets.

7.5 Surrogate Formulation

A major challenge associated with the formulation of a suitable surrogate is in determining its composition so that it mimics the relevant properties of interest (or combustion property targets [184]) of the real fuel, while keeping the number of components small in order to reduce the modelling complexity. High and Low RON fuel surrogates were developed by FCA US LLC, and they, including the corresponding target fuels, were supplied to MSU for testing and validation. Information on the details of the fuel surrogates development process, including their compositions and target properties/application, are the proprietary of FCA US LLC, and may be published by FCA in the near future.

7.6 Results and Discussions

7.6.1 Effect of Equivalence Ratio and Pressure

The effect of equivalence ratio on ignition delay times (IDTs) is investigated for all dilution levels in Figure 7-3. The data points were connected with straight lines in order to improve visualization and a minimum of two data points taken to ensure repeatability at each point are shown. At 20 bar and undiluted conditions, for the high RON surrogate, only one test point could be taken at 900K due to difficulty identifying the EOC. In general, a trend of increasing reactivity with increasing equivalence ratio can be noted. Also, reactivity increases with increasing pressure. These trends can be observed even as the dilution level increases except that the delay times are now retarded in the presence of a diluent. At 0% dilution level, it can be observed that the NTC region shifts to higher temperatures with increasing pressures. The reason for this shift is due to the pressure dependence of the ceiling temperature which controls H_2O_2 decomposition [52]. The shift in the NTC region with pressure cannot be observed at diluted conditions due to test points exhibiting delay times greater than 100ms within the NTC region. The NTC peak can be observed at 800K for both pressures. At 20 bar conditions, for $\phi=1.0$ and $\phi=1.3$, the IDTs are very similar ignition delay times at lower temperatures. The difference between $\phi=0.6$ and $\phi=1.0$ curves are much more pronounced compared to the difference between stoichiometric and the richer condition, indicating that for rich and stoichiometric conditions the mixture reactivity is very similar. It should be noted that the trends observed here were also applicable to the gasoline fuels studied in chapter 6.

For the low RON fuel, pre-compression heat release was noted at temperatures above 800K at undiluted conditions for $\phi = 1.3$. As noticed for the high RON surrogate, the reactivity at $\phi = 1.0$ and $\phi = 1.3$, are very similar in comparison to $\phi = 0.6$. At 10 bar conditions, the lines connecting the data between 650 and 700K shows crossover and this can be attributed to a shift in NTC region with changing equivalence ratio. The NTC region moves to lower temperatures with decreasing equivalence ratio and this behavior is more pronounced at the 10 bar conditions. Hence a possible reason for overlap of the curves is due to the changing NTC region not being captured due to the lack of resolution in the data points, since data was only taken at 50K intervals. In future studies it is recommended that a minimum of a 25 K (or lower) temperature interval be maintained to appropriately capture this region. Here it can be seen that the NTC region shifts to lower temperatures and that the low temperature data has a change in slope at the 10 bar compressed conditions. The slope of the line changes from negative to positive in the 700-750K range. As observed in chapter 6, the reactivity of the surrogate fuels and gasoline are very similar at $\phi = 1.0$ and $\phi = 1.3$, particularly in the low temperature region, as shown in Figure 7-3. As a general trend, it can be concluded that at $\phi = 1.0$ and $\phi = 1.3$, differences in reactivity is minimal at temperatures below 700K ($1000/T \sim 1.42$) and above 850K ($1000/T \sim 1.18$) irrespective of the pressure for gasoline and surrogate fuels studied here, as shown in Figure 7-3. The profile at $\phi = 0.6$ and 20 bar looks very similar to the richest condition at 10 bar for all dilution levels.

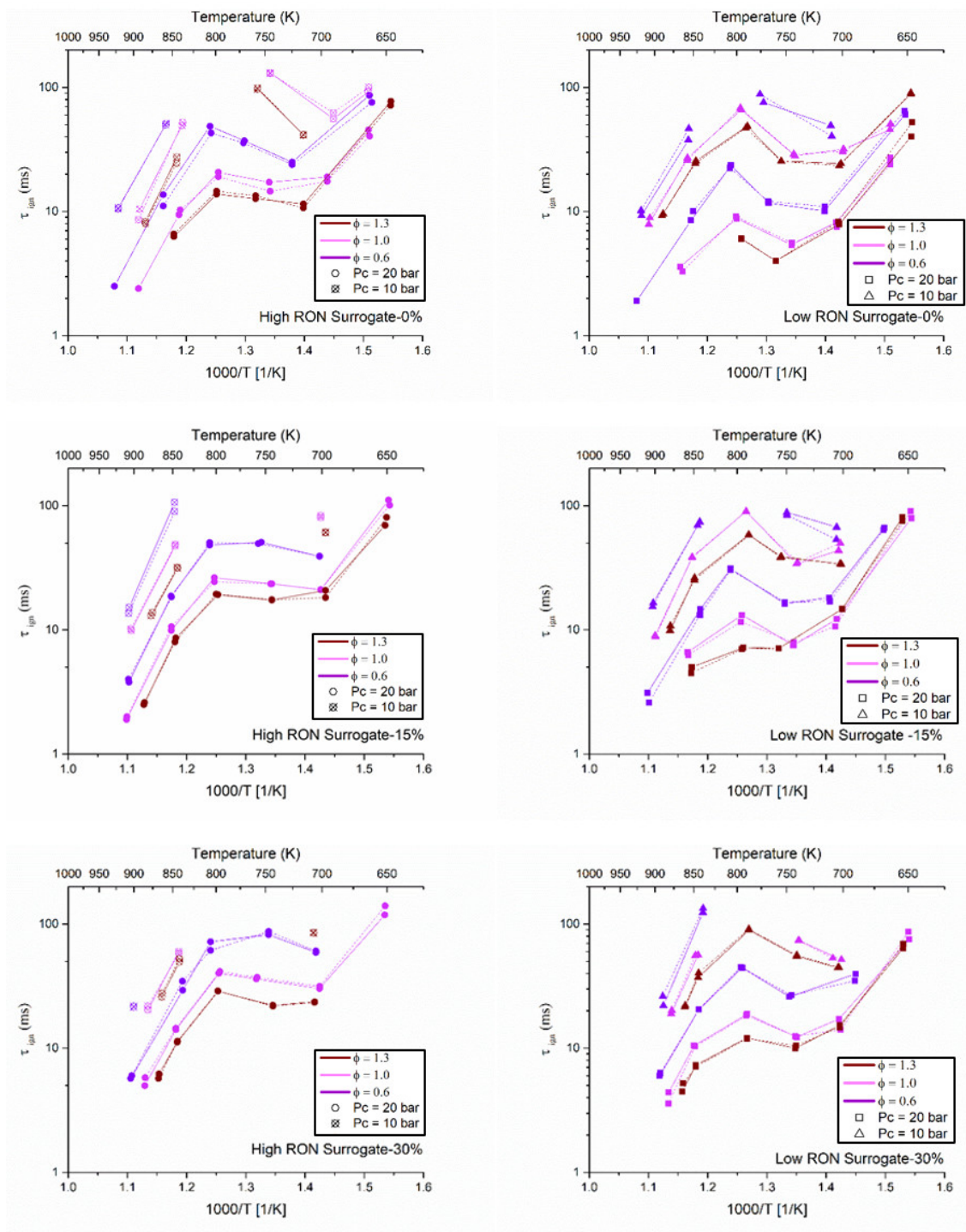


Figure 7-3 Ignition delay times shown in Arrhenius form for high RON surrogate (left column) and low RON surrogate (right column) for 0% (upper), 15% (middle) and 30% (lower) CO₂ dilution levels at a compressed pressure of 20±0.5 and 10±0.5 bar. Line type indicates different experimental sets.

7.6.2 Performance of Surrogates and Effect of Dilution

In chapter 6, as a preliminary step, iso-octane was used as a surrogate for both low RON & high RON gasoline due to the lack of information on the gasoline properties. Iso-octane mixtures generally exhibited longer ignition delay times relative to the gasolines for the temperature range studied here, as can be seen in Figure 7-4. This indicated that the high RON fuel is of lower ON than iso-octane. Iso-octane's response to CO₂ dilution was also more pronounced compared to both the fuels, due to pure paraffinic nature of the former. As a result, significant difference between the IDTs of the fuels and iso-octane was observed throughout the temperature range. Also, the NTC region of the iso-octane was also more pronounced compared to the fuels due to the iso-octane possessing no sensitivity. Here sensitivity is defined as the difference between the RON and MON rating of the fuel. HO₂ production is favored more for fuels with higher paraffin content (or lower sensitivity) compared to a higher sensitivity fuel. This was the reason for the enhanced NTC behavior of the iso-octane compared to the full blend gasoline [178]. Fuels possessing high octane sensitivity show reduced to no NTC behavior due the electron delocalization phenomenon that occurs for fuel components such as alkenes, alcohols and aromatics [58]. Such components tend to produce stable intermediates through reaction with H₂O₂ and remain unreactive until high temperature capable of breaking O-O bonds are achieved [58].

Figures 7-5 and 7-6 show ignition delay times for the high RON and Low RON fuels and surrogates respectively, with 0%, 15% and 30% CO₂ dilution at equivalence ratios of 0.6, 1.0 and 1.3, at 20 bar (Left) and 10 bar (right) compressed pressure conditions. In Figure 7-5, it can be seen that for the 0% and 15% dilution levels, the ignition delay times (when observed) are both similar at 650K. This shows that the impact of dilution is not pronounced at low temperatures. The NTC region for the surrogate starts at lower temperatures when compared to the original fuel. The surrogate is less reactive than the original fuel at all dilution levels although the response to CO₂ dilution is similar. At stoichiometric and rich conditions, except for the shift in delay times, the surrogate captures the delay trends of the fuel at 750K and 800K. The surrogate is observed to match the ignition delay times at lower and higher temperatures outside of the NTC region. At $\phi=0.6$, within the NTC region, the difference between the IDTs of gasoline and the surrogate fuel are within a factor of two. It can be seen that the performance of the surrogates in the NTC region improves as the mixture gets richer, which is mainly due the differences in the NTC region trend. It can be generally noted that the addition of CO₂ does not interfere with any of the NTC trends observed with the gasoline or its surrogate. This observation is in line with trends observed in chapter 5 and 6. CO₂ dilution only increases the delay times while preserving the reactivity trend of the original fuel throughout the temperature range. At the 10 bar conditions, the surrogate is less reactive and has longer delay times (>100ms) and also shows a different NTC curve as observed by the slope of the line connecting the 700K and 750K points. The surrogates and fuels show very good agreement past 800K irrespective of the pressure.

At both the 20 bar and 10 bar conditions, the NTC region is well captured by the surrogate as seen in Figure 7-6. The reactivity of the fuel is well represented in the NTC region, although at lower temperatures the surrogate is more reactive compared to the fuel. It should be noted that at 20 bar conditions; the surrogates were tested at 800K while the fuel was tested at higher temperatures as can be seen in Figure 7-6. This was due to the occurrence of first stage ignition activity during the compression stroke with the surrogate and hence the test target temperature was shifted. At 800K for $\phi=1.3$, the ignition delay times for the 0% dilution and 15% dilution cases are similar. This may be due to the flat NTC profile exhibited by the 15% dilution case and the lack of test data resolution in this region. Past 800K the agreement between the surrogate and the fuel improves. In terms of dilution response, the surrogate matches the dilution response of the low RON fuel very well. At $\phi=0.6$, the gasoline fuel is more reactive than the surrogate. When compared to the fuel, the surrogate exhibits NTC behavior at a relatively lower temperature of 700K. At the 10 bar conditions good agreement can be seen for temperatures higher/lower than 750K, however within the NTC region the surrogate is less reactive and shows a pronounced response to the increase in dilution. Similar to observations made at the 20-bar condition, the surrogate's NTC behavior can be observed at lower temperatures (700K).

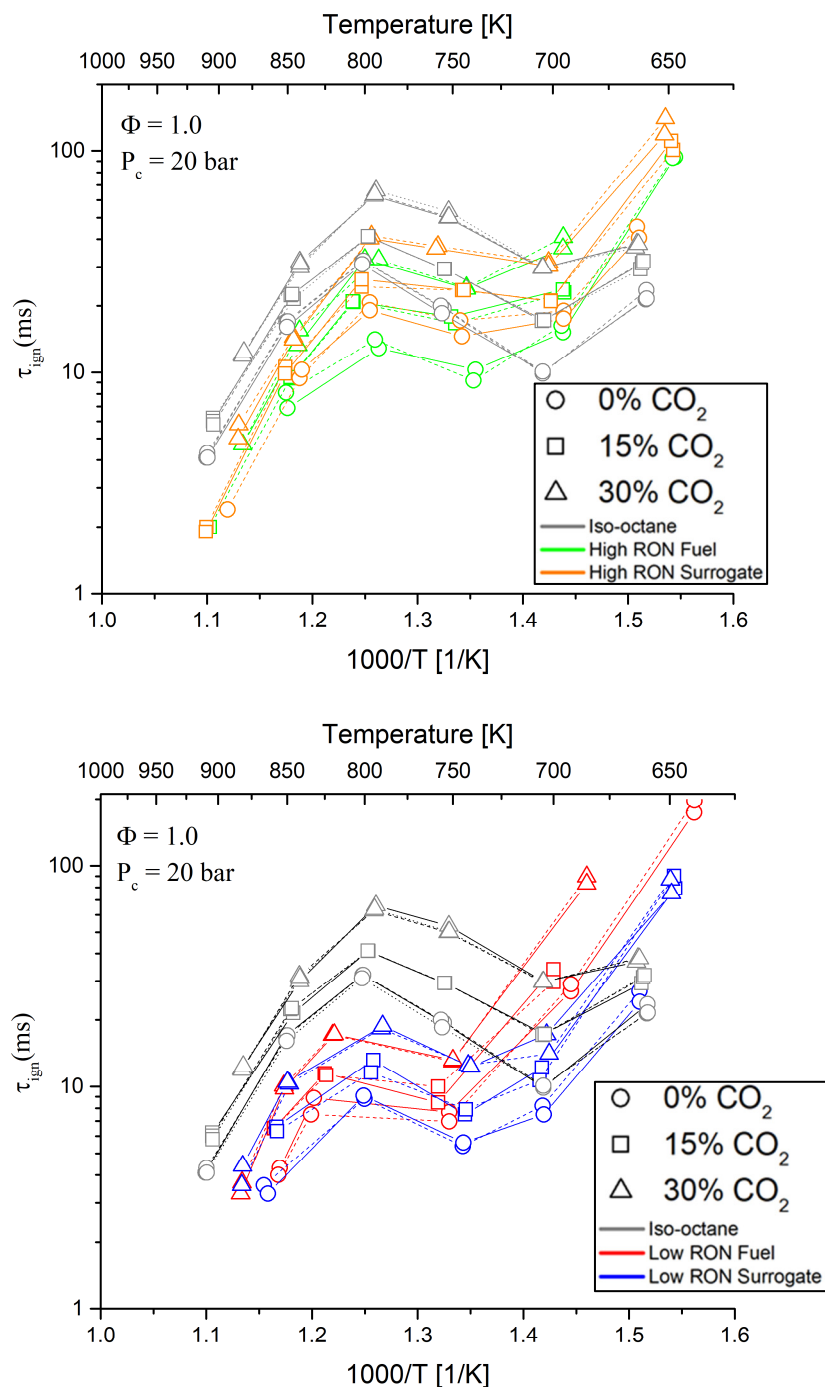


Figure 7-4 Ignition delay times of fuels and their surrogates, iso-octane and multicomponent, (high RON-top, low RON-bottom) shown in Arrhenius form for 0% (circles), 15% (squares) and 30% (triangles) CO_2 dilution levels for $\Phi=0.6$, $\Phi=1.0$ and $\Phi=1.3$ at compressed pressure of 20 ± 0.5 bar (right column) and 10 ± 0.5 (left column) bar. Line type indicates different experimental sets.

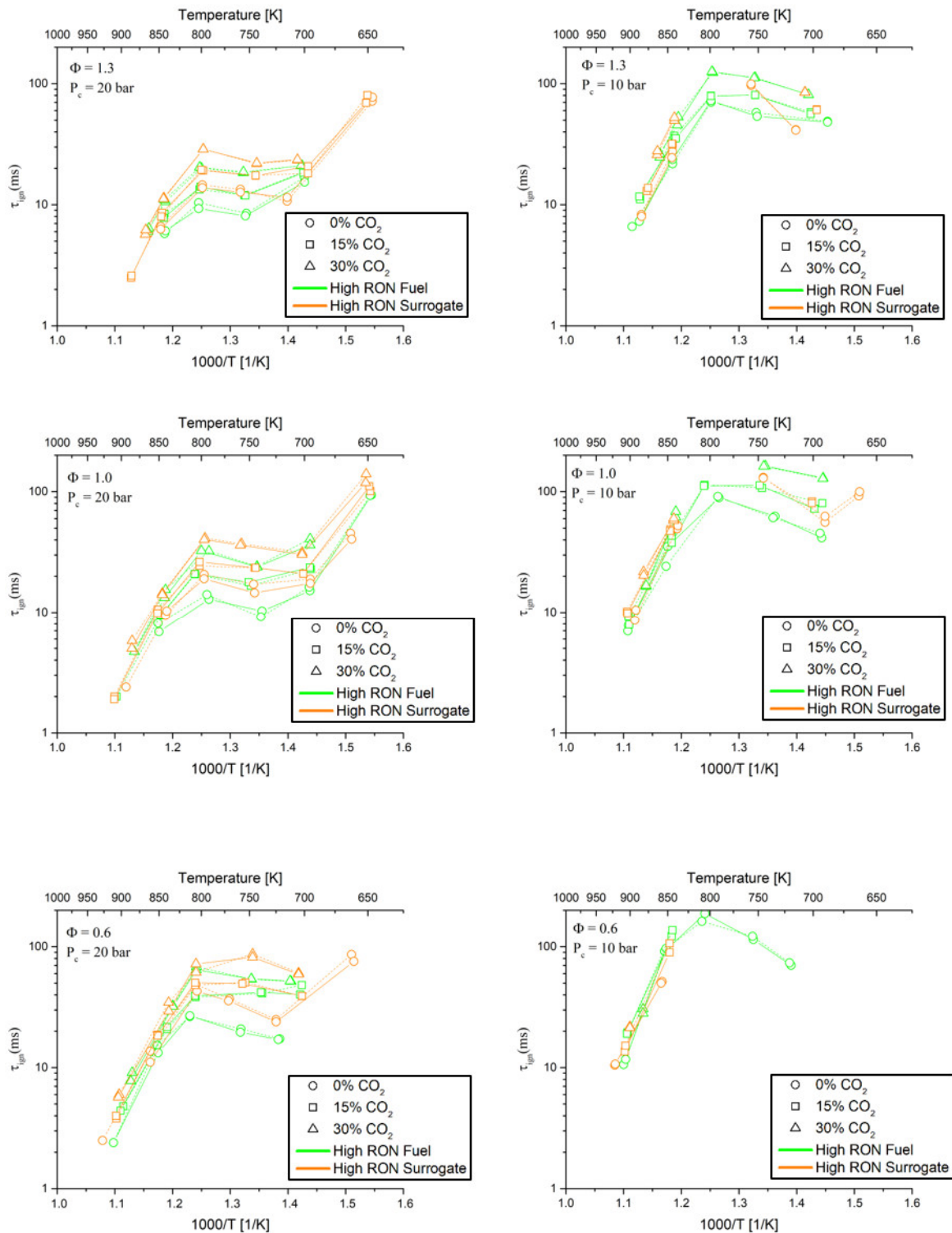


Figure 7-5 Ignition delay times of high RON fuel (green) and its surrogate (orange) shown in Arrhenius form for 0% (circles), 15% (squares) and 30% (triangles) CO_2 dilution levels for $\Phi=0.6$, $\Phi=1.0$ and $\Phi=1.3$ at compressed pressure of 20 ± 0.5 bar (right column) and 10 ± 0.5 bar (left column) bar. Line type indicates different experimental sets.

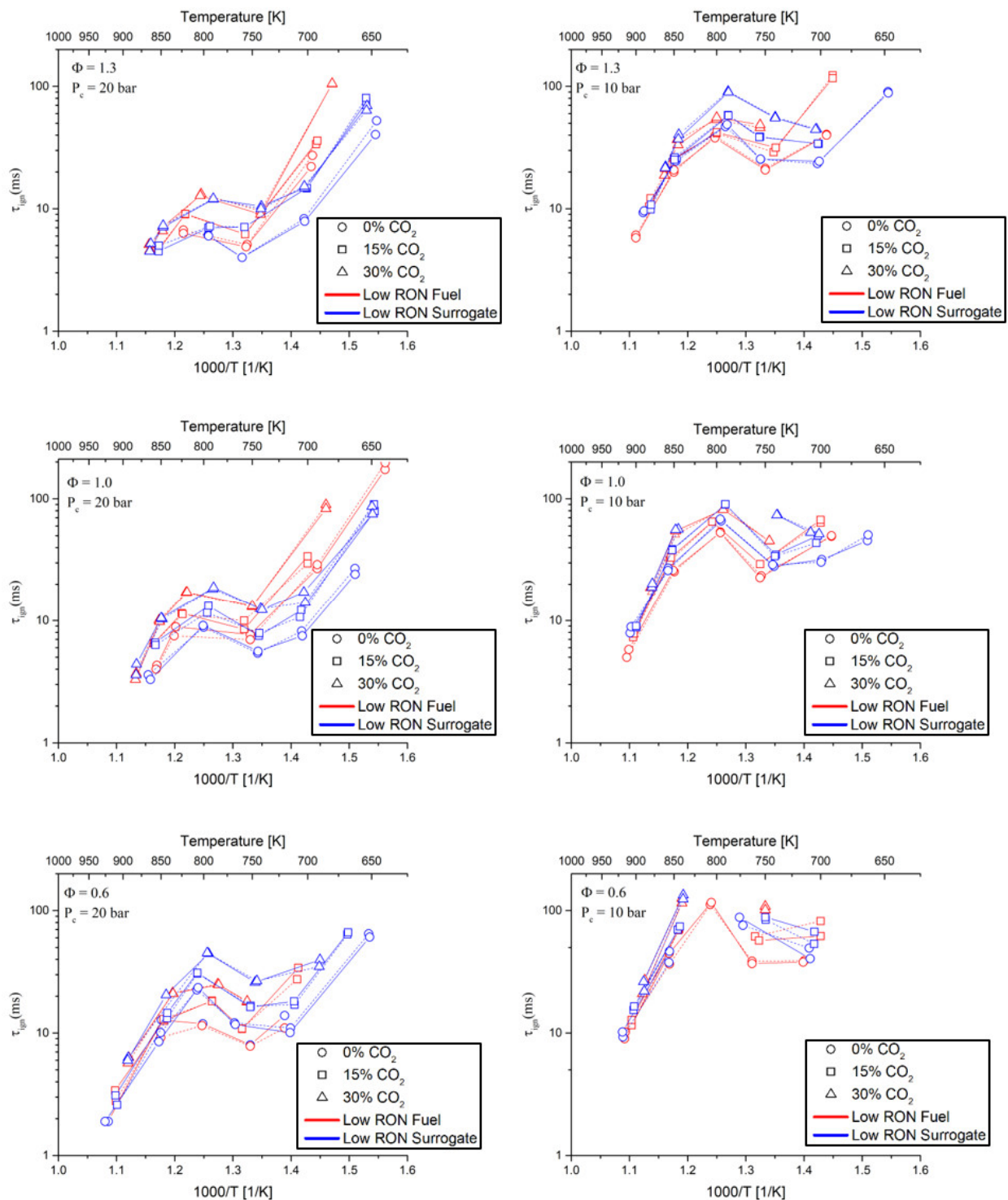


Figure 7-6 Ignition delay times of low RON fuel (red) and its surrogate (blue) shown in Arrhenius form for 0% (circles), 15% (squares) and 30% (triangles) CO_2 dilution levels for $\Phi = 0.6$, $\Phi = 1.0$ and $\Phi = 1.3$ at compressed pressure of 20 ± 0.5 bar (right column) and 10 ± 0.5 bar (left column). Line type indicates different experimental sets.

7.6.3 Effect of Octane Numbers

Figure 7-7 shows a comparison between the IDTs of the high RON and low RON surrogates for all dilution levels and equivalence ratios at both 10 and 20 bar compressed conditions. NTC region of both the surrogates occurs within the same temperature range of 700K – 850K. This NTC region is similar to that of the high RON gasoline (chapter 6) and that of iso-octane (chapter 5) at 20 bar compressed conditions. Also, the NTC region is roughly the same for the 20 bar and 10 bar compressed conditions for these surrogates. It can be observed that the lower RON surrogate shows a very pronounced NTC region while the higher RON fuel exhibits a flatter NTC curve.

The lower RON surrogate is less reactive than its high RON counterpart throughout the temperature range for both the compressed conditions. For both the fuel and the surrogate strong octane dependence was noted in the NTC region and this trend is in line with other studies [173]. At 10 bar compressed conditions, a comparison between the two surrogates is only possible at higher temperatures outside the NTC region. This is due to much lower reactivity of the high RON surrogate in the NTC region, with IDTs greater than 100ms. For temperatures greater than 800K, at 10 bar conditions, the reactivity levels are very similar between both the surrogates irrespective of the dilution levels. For 20 bar conditions and at 900K, the ignition delay times of both the surrogates at the corresponding dilution levels are very similar. The reason for this is that at high temperatures the $\text{H}_2\text{O}_2 \rightarrow \text{OH} + \text{OH} (+\text{M})$ and $\text{H} + \text{O}_2 \rightarrow \text{OH} + \text{O}$ reactions control the chain branching process for a wide range of practical fuels and surrogates. Hence the ignition delay times at these temperatures were not found to be octane sensitive [170].

Both the surrogates respond to CO_2 dilution in a very similar way. The retardation effect of CO_2 scaling with increasing RON number, observed for the full blend gasolines (chapter 6) was not

observed with the multicomponent surrogates. This is evident in the bar charts shown in Figure 7-8, where the ratio of the IDTs at diluted and undiluted conditions are shown for temperatures within the NTC region at $\Phi=1.0$. The higher RON gasoline shows higher retardation effect in comparison to its lower RON counterpart. However, in the case of the surrogates, both exhibit a similar CO₂ retardation effect. This suggests that in addition to octane number, the fuel composition can also have an impact on the retardation impact of CO₂. Overall as a general trend it can be seen that, at 20 bar conditions and with 30% CO₂ substitution, the lower RON surrogate matches the higher RON ignition delay times at 0% dilution. With this same trend observed for the gasolines as well (chapter 6), this shows the octane relaxation potential of CO₂ dilution when used in SI engine operation. High levels of CO₂ dilution can impact combustion stability, under such circumstances ignition enhancement techniques such as turbulent jet ignition (TJI) can be used [182].

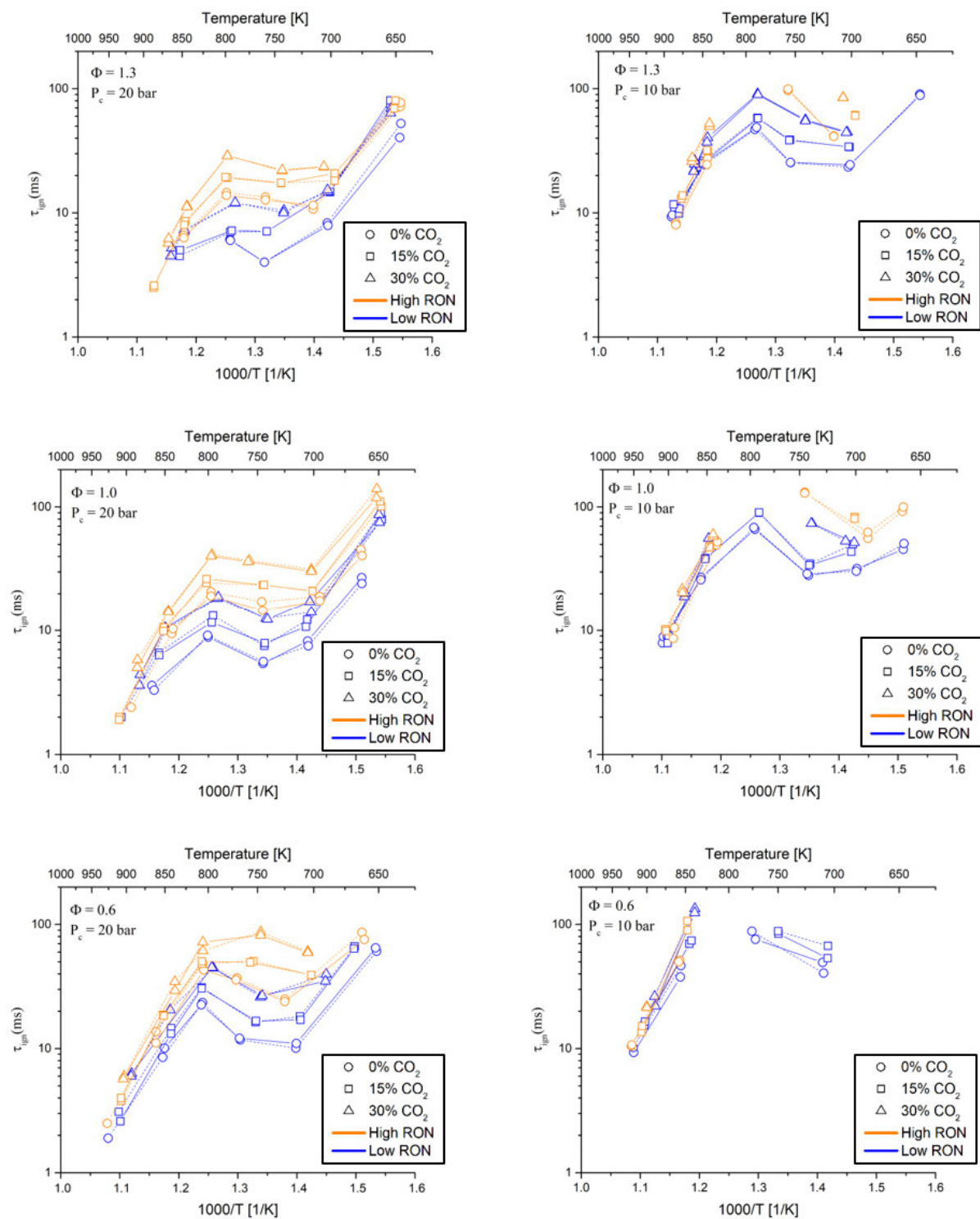


Figure 7-7 Ignition delay times of low RON surrogate (orange) and high RON surrogate (blue) shown in Arrhenius form for 0% (circles), 15% (squares) and 30% (triangles) CO₂ dilution levels for $\Phi=0.6$, $\Phi=1$ and $\Phi=1.3$ at compressed pressure of 20 ± 0.5 bar (right column) and 10 ± 0.5 (left column) bar. Line type indicates different experimental sets.

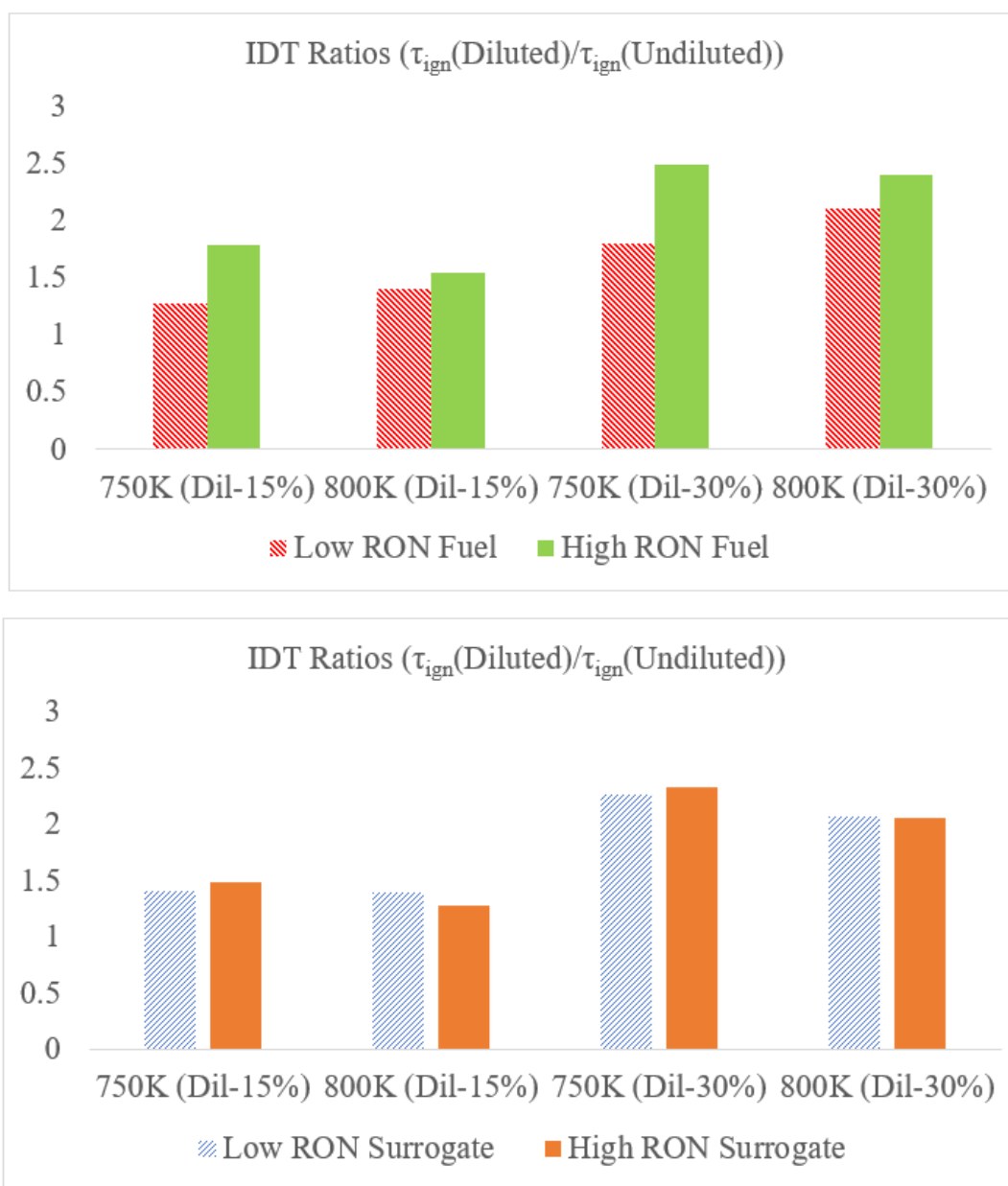


Figure 7-8 Average diluted ignition delay times of the high RON and low RON gasoline (top) and corresponding surrogates (bottom) normalized with their respective undiluted delay times for $\Phi=1$ at $P_c = 20 \pm 0.5$ with T_c chosen within the NTC region. X axis labels indicates compressed temperatures.

7.6.4 Impact of Dilution on First Stage Delay Times

The low to intermediate temperature range is of interest for low temperature combustion (LTC) engines. The evolution of low temperature heat release (LTHR) plays a critical role in the operation of such engines [185], where CA10 is related to the onset and magnitude of LTHR. Occurrence of low temperature chemistry is manifested either through a single stage or two stage ignition process related to phenomena such as cool flames and NTC behavior [57]. The effect of CO₂ dilution on the first stage heat release was analyzed by using the pressure traces from diluted and undiluted runs. In order to make this analysis more comprehensive, the first stage delay data from the full blend gasoline and iso-octane (single component surrogate) were included for comparison. In Figure 7-9(top), the first stage heat release at 750K, if observed, is plotted for all three equivalence ratios and dilution levels. First stage heat release was observed for all the fuels studied here within the temperature range of 700-800K at 20 bar compressed conditions. At 800K the first stage heat release moved closer to the EOC, hence exhibiting very short first stage delay times. Also, at lower temperatures, the pressure rise due to the first stage delay was very closer to the final stage making the identification of inflection points difficult. Also, weaker first stage heat release at leaner conditions and high dilution levels made recording the first stage delay more difficult at these conditions. Hence a common compressed temperature of 750K at 20 bar compressed pressure was chosen to observe the trends in first stage delay at undiluted and diluted conditions.

For the low RON fuel at 750K, the first stage heat release could not be discerned since the heat release occurred close to the final stage, hence was not included in the figure. Also, the high RON surrogate & iso-octane exhibited a weak first stage release at $\phi=0.6$ hence a clear pressure rise from the first stage delay was not observed. It was observed from the pressure traces that the

CO₂ dilution other than prolonging the first stage also made the pressure rise due to first stage event lower. The effect of equivalence ratio on the first stage delay can be observed in these plots. The most pronounced response to equivalence ratio is exhibited by the high RON gasoline. Comparatively, the surrogates including iso-octane shows relatively less dependence on equivalence ratio. The total ignition delay times corresponding to the data shown in first stage delay plots are included in Figure 7-9(bottom). It can be seen that both the first stage and total delay times show a trend of extended delay time with increasing dilution. With the ability to alter the first stage and total ignition delay times, CO₂ dilution is a viable option for ignition timing control in LTC strategies [55]. The general trend of similar reactivity between $\phi=1.0$ and $\phi=1.3$ observed with total delay times is not seen for the first stage delay times.

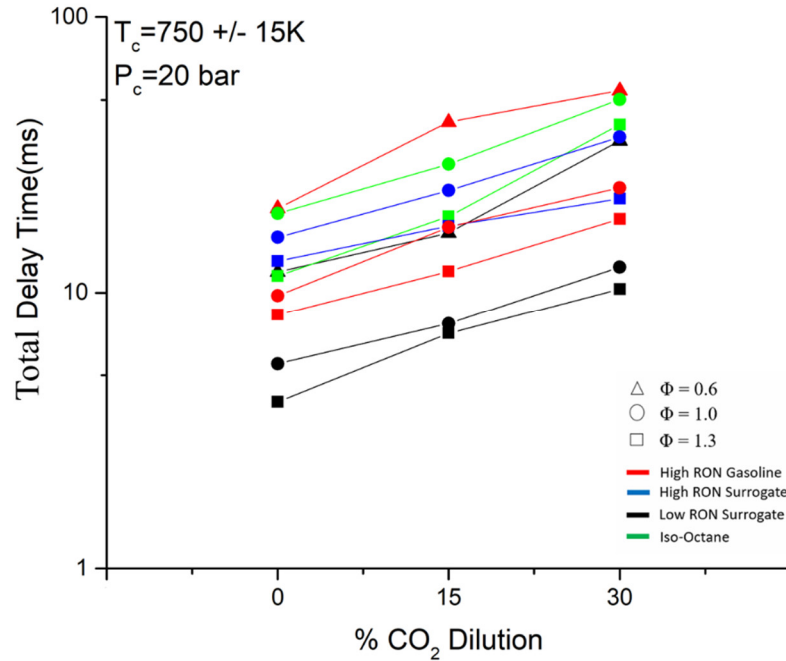
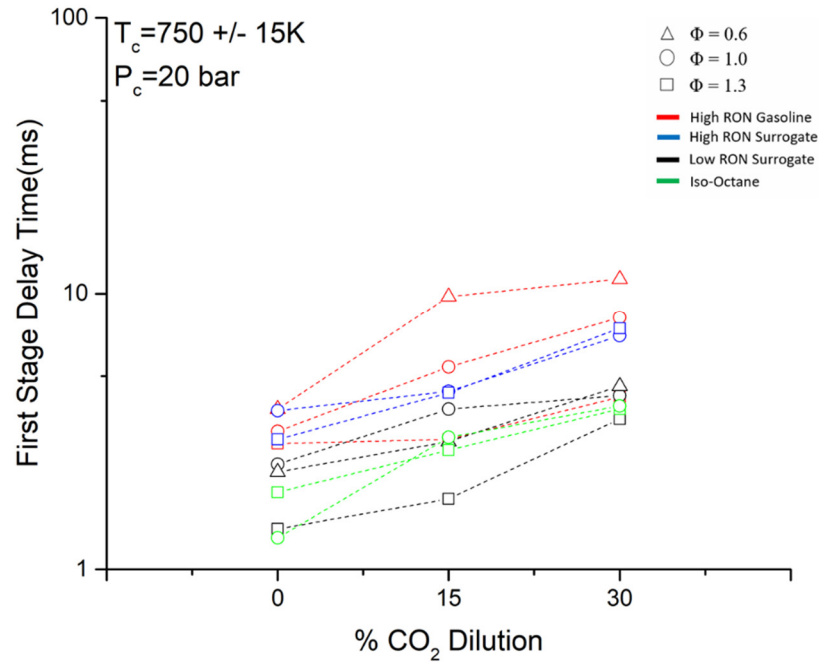


Figure 7-9 Averaged first stage delay times (top) and total delay times (bottom) of fuel and surrogates at $T_c=750K$ and $P_c=20 \text{ bar}$ for various equivalence ratios.

7.7 Chapter Summary

In this chapter ignition delay times of two multi-component surrogates (high RON and low RON) were measured using a RCM for a range of equivalence ratios and CO₂ dilution levels, over a 650-900K temperature range and at 10 and 20 bar compressed pressures. The recorded autoignition times and trends were compared with the corresponding the respective full blend gasoline fuel and isooctane. Major observations from this chapter are summarized below,

- 1) The reactivity of the multicomponent surrogates relative to the base fuels were compared at both diluted and undiluted conditions. Better agreement compared to the iso-octane surrogate was observed.
- 2) CO₂ dilution did not introduce any additional chemical activity and resulted in retardation of the undiluted delay times. The retardation effect was more pronounced in the NTC region with the shape of the NTC curve remaining unaffected.
- 3) With respect to first stage ignition activity, CO₂ dilution extended the first stage heat release of the fuel and reduced its pressure rise when compared to undiluted conditions.
- 4) For the full blend fuels, the retardation effect of CO₂ was more pronounced with increasing RON. However, this trend was not observed in this study with the multicomponent surrogates.
- 5) Test points were captured at 50K intervals, this resulted in a lack of resolution while observing NTC trends and a temperature interval of 25K is recommended for future work.

- 6) At 20 bar conditions, the ignition delay times of the 30% CO₂ substituted low RON surrogate overlapped with undiluted delay times of the high-RON surrogate, indicating octane relief potential.

Chapter 8 Effect of Ethanol Substitution on Ignition Delay Times and Ron Values for PRF and TRF Blends for Up To 40% by Volume

8.1 Introduction

In the previous chapters it was observed that the RON difference across the gasoline blends and surrogates manifested in terms of difference in the reactivity within the NTC region. This showed that there is a fundamental link between IDTs measured in the RCM and the octane numbers measured from a CFR engine. This link was not explored in detail in the previous chapters due to lack of RON values of the tested fuels and the data measured at the intervals of 50K did not provide enough resolution. In this chapter, ignition delay times for six different gasoline surrogates, with known RON and MON values, were measured in the RCM facility. The chosen surrogates were PRF and TRF mixtures containing ethanol for up to 40 % by volume. The chosen fuels possessed sensitivity (defined as the difference between RON and MON) and hence resembled practical gasoline fuels. Blending behavior of ethanol with gasoline surrogates is highly non-linear with respect to resulting octane numbers and is a topic of current research interest. This blending behavior arises due to binary interactions of ethanol with components present in the surrogates. The RCM tests in this chapter specifically focused on the intermediate temperature region where gasoline like fuels exhibit NTC behavior. Kinetic analysis was performed for the tested blends in order to understand the source of reactivity in the tested temperature range.

The objective of this chapter is twofold,

- 1) identify a link between IDTs and the fuels octane numbers (ON) in the NTC region using test data obtained from the MSU RCM facility
- 2) understand the blending behavior of ethanol with gasolines surrogates using kinetic analysis

8.2 Background and Literature Review

The current methodology for measuring RON (600 RPM and 52°C intake) and MON (900 RPM and 149°C) in a CFR engine is time consuming and does not truly represent the modern engine operating conditions [6]. Estimation of RON and MON values from sources other than a CFR engine have been previously attempted. Westbrook et al. [78] proposed chemical kinetic analysis as an alternate for traditional RON, MON testing methods in order to save effort and cost. The prerequisite for this technique was the availability of well validated reaction mechanisms. An alternate methodology for evaluating the ON values would be to use a linear or non-linear blending laws. In a work by Knop et al. [186] a simple linear mole blending law to predict octane numbers of TPRF fuel mixtures was derived. Morgan et al, [187] conducted 20 experiments measuring RON and MON for various TRF mixtures. Using their inhouse data and other RON and MON measurements from Andrae et al. [188] and Kalghatgi et al. [189] they calibrated a non-linear fitting algorithm. Badra et al. [61] collected data points for TRF blends containing varying volume percentage (10% to 80%) of toluene. Using their correlation, they found that the predicted ON values had uncertainties lower than that of experimental measurements. However, such laws do not predict correct octane number if oxygenates such as ethanol is used. Hence a

simple methodology for identifying the absolute or relative octane numbers, when new fuel components are introduced in a TRF blend, does not exist.

A brief description on gasoline surrogates and effects of each fuel component in determining the ignition behavior of the final blend is provided here. An ideal gasoline surrogate fuel blend must contain enough variety of fuel components representing the important classes of hydrocarbons present in the actual fuel, and at the same time be simple enough and focus on only a limited number of each class of these fuel compounds [1]. Actual gasoline contains a mixture of n, iso and cyclo paraffins, olefins, aromatics and oxygenates. Strong low temperature reactivity of fuel components (e.g. paraffins) correlates well with a lack of fuel sensitivity [58]. The degenerate chain branching kinetics, in which O_2 addition to R radicals followed by internal isomerization leading to ignition, are responsible for low temperature heat release (LTHR) in paraffins [46]. The temperature limits for LTHR occurrence is determined by the lowest temperature during which the molecular oxygen addition reactions can take place. Conversely, the lack of LTHR identifies high sensitivity values for a given fuel component. The specific mechanisms that prevents or limits the low temperature reactivity differs depending upon the class of hydrocarbon. For 1-alcohols such as ethanol, Westbrook et al. [58] describes that due to the smaller size of the molecule, radical isomerization reactions are not supported at low temperatures. Similarly, for alkylated benzene such as toluene, low temperature reactions begin in their side chain termed as benzylic C-H bonds. The reaction sequences at low temperature starts by abstraction of the benzylic H atom and is then followed by additional reactions involving O_2 , HO_2 or OH [53]. Further reactions involving the side chain leads to production of stable structures (within the side chain) and does not allow for the occurrence of cool flame phenomenon [58]. The term ‘cool flame’ also describes the LTHR phenomenon.

Higher sensitivity fuels show higher reactivity in the intermediate temperature range due to a lack of NTC behavior [76]. In blended fuels, the radical pool produced by the alkanes are scavenged by aromatic and alcohol components thus inhibiting LTHR [58]. Due to this, high sensitivity fuels display longer ignition delay times at lower temperatures. With increasing alcohol and aromatic components, the high temperature pathways of these fuels interfere with the NTC behavior of paraffins and accelerate IDTs of the overall mixture [60]. Also, at higher temperatures all surrogates exhibit similar high temperature reactivity due to a shift in reaction pathways favoring unimolecular decomposition and β -scission reactions [46]. Hence within the NTC region it becomes difficult to predict the reactivity of blends possessing varying levels of sensitivity. The NTC region is typically where knock is observed in SI engines [60] and hence this study will provide valuable insight into the behavior of the tested blends in the NTC region.

8.3 Research Questions

1. LTHR is sensitivity controlled and high temperature heat release (HTHR) is temperature controlled. Will the reactivity trends in the intermediate temperature region shows any relation to the RON and MON values of the tested gasoline surrogate blends?
2. The tested fuels contain various levels of sensitivity (~4 to 13). Will the low sensitivity fuels' pronounced NTC behavior interfere with the identification of a RON, MON vs. IDT relation?
3. Can the kinetic analysis provide insights on the source of a blend's reactivity in the tested range and provide an explanation for the antagonistic or synergistic blending nature of ethanol with toluene or alkanes?

8.4 Methodology

The gasoline surrogates chosen for this study are shown in Table 1. The PRF surrogates only represent the n-alkane and iso-alkane fraction of the fuel components present in gasoline.

Toluene reference fuels (TRF) additionally contains toluene, an aromatic component present in concentrations up to 30% in commercial gasoline, and hence is a more appropriate surrogate [1].

Toluene is an octane booster and hence is present in large quantities as shown in Table 1.1 .

Ethanol is commercially blended at up to 10 % volume levels in the USA and this blending level could potentially increase in the future. In this study PRF and TRF blends containing ethanol up to 40 % by volume are studied. The oxygenated TRF and PRF mixtures will be referred to as PRFE and TRFE in order to indicate the presence of ethanol in the blends. The three (PRFE) and four component (TRFE) surrogates used in this study possess sensitivity similar to practical gasolines. The surrogates used in this study do not contain other classes of hydrocarbons such as cycloparaffins (e.g. cyclohexane) and olefins (e.g., hexene).

Ethanol blends synergistically with alkanes and antagonistically with aromatics [190] and the blending laws should accurately predict such behaviors. Without the use of a CFR engine it could be possible to predict the RON and MON values using blending laws as illustrated in [61,186,189], however the accuracy of predictions will depend upon the blend laws considered. Hence in order to remove the dependency of the estimated RON and MON on the accuracy of blending laws, the octane numbers of the tested fuels were extracted directly from [191]. The surrogate blend composition was determined based on the study by Foong et al. [191] in which RON and MON ratings of these fuels were measured using ASTM standard tests in a CFR engine. Hence no blending laws have been applied for estimating the octane values. Foong et al. [191] used PRF91 and three different TRF91 blends with a final RON of 91 in order to resemble

Australian gasoline. The digits ‘91’ indicates the RON number of the base mixture when no ethanol is present in the mixture. Among the fuels studied in [191] only PRF91 and TRF91-45 is analyzed in this work to understand the blending nature of ethanol for up to 40% by volume with surrogate mixtures containing only alkanes and alkanes together with a high level of aromatics. For ‘TRF91-45’ the last two digits indicating the vol% of the toluene in the blend. It must be noted that TRF91-45 blend is referred to as just TRF91 in this work for brevity. Foong et al. [191] also studied TRF91-15 and TRF91-30 mixtures, with same base fuel RON but these are not included in the experimental test matrix in the current work. Uncertainties for RON and MON values are ± 0.7 and ± 0.9 ON respectively as reported in [191]. Based on this uncertainty, it can be considered that all three PRF mixtures in Table 1 have similar MON, while the PRF91E20 and TRF91E40 forms an identical RON pair. Also, PRF91E20 and TRF91E10 as well as PRF91E20 and TRF91E40 pairs exhibits similar sensitivity. Hence the chosen fuel matrix allows for grouping and comparison of surrogates based on their specific octane related properties.

Table 8-1- RON, MON and sensitivity values of the surrogate blends used in this study.

	PRF91- 10	PRF91-E20	PRF91- E40	TRF91- E10	TRF91- E20	TRF91- E40
RON	98.7	103.8	108	96	100.2	104.6
MON	94.3	95.3	94.5	87.2	89.1	90.9
Sensitivity	4.4	8.5	13.5	8.8	11.1	13.7

8.5 RCM Test Conditions

For the RON and MON test conditions, the temperature vs pressure trajectory is shown in figure 1.1. It can be observed that for a fixed pressure, the RON and MON test conditions lie at a specific temperature. In this work the RCM experiments are performed in the region between the RON and MON trajectory at 21 bar. Since the fuels chosen for this study have RON numbers higher than 90, the compressed pressure of 21 bar is chosen to avoid ignition delay times greater than 100ms in the RCM. In chapter 5, for iso-octane-air mixtures at 10 bar compressed pressures, ignition delay times higher than 100ms were observed. Such long delay times introduce non-ideal temperature distributions within the combustion chamber and hence should be avoided for accurate estimation of compressed temperatures [154]. Within the RON and MON trajectory, the constant pressure line at 21 bar overlaps the RON curve at 720K and the MON curve at 855 K. Since the chosen pressure and temperature intersects the RON and MON trajectory, a correlation among fuels with the same MON and RON number, if existing, will be attempted. The chosen pressure value spans a temperature range of 720K to 855K and this range lies in the intermediate temperature region for gasoline fuels. In this temperature range practical gasoline fuels displays NTC behavior for the given pressure.

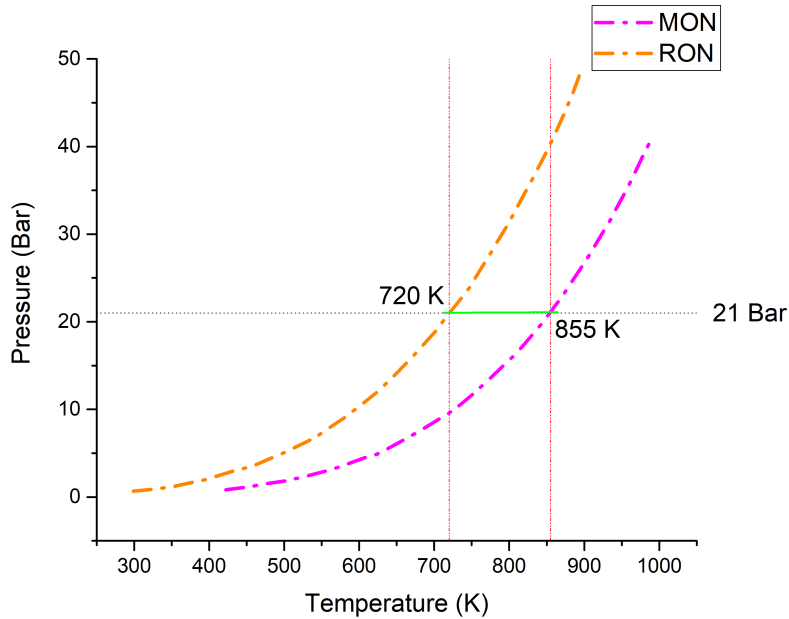


Figure 8-1 RON and MON trajectory extracted from [192] with the green line indicating the test conditions covered in this study.

In order to achieve this temperature range without the use of buffer gases such as Argon and CO₂, the compressed temperatures are modified by using a combination of wall temperature and different compression ratios (CR 9.6 and CR13). Buffer gases influence the overall ignition delays if two stage ignition is observed [151] and hence are not preferred in this study since in the temperature range studied for the fuels would exhibit NTC behavior and could potentially influence the RON and MON correlation. Strong NTC behavior is not expected for the TRFE fuels and PRFE40, since they contain significant toluene and alcohol content and hence higher sensitivity. Strong NTC behavior is observed for fuels with low to zero sensitivity [54]. CR9.6 is used for the temperature range of 720-770K and CR13 is used to reach higher temperatures of up to 850K. The change in CR is achieved by changing the clearance volume without altering the stroke length. Hence two different heat loss scenarios exist during the test conditions based on the CR.

The ignition delay times measured from the test conditions and non-adiabatic simulations are based on the time delay between the EOC and the maximum pressure rise rate during the main ignition event. This is illustrated in figure 5.1 while the CV simulations are based on a delta 400K temperature rise during the main ignition event.

8.6 Surrogate Composition

The surrogate blends used in this study are prepared based on the volume % and the compositions are provided in figure 8.2. Although the blends are prepared on volumetric basis, mole fraction values are also included in figure 8.2 since the reactivity of the resulting blends scales strongly with mole % of the components. Ethanol is known to synergistically blend with alkanes, i.e. resulting octane numbers are higher than the individual components in the blends and antagonistically with aromatics such as toluene []. The resulting effect of such behavior will be studied in terms of autoignition delay times in this work. It can be seen from figure 8.2, as the amount of toluene in the blend increases in order to maintain the same level of RON the amount of n-heptane is increased, and the iso-octane fraction is significantly reduced. Among the test fuels PRFE10 contains the highest amount of paraffinic content and is expected to show the highest NTC response. Among PRFE40 and TRFE40, the former has the highest amount of alkanes and hence is expected to have a lower reactivity in the NTC region. TRFE40 has a higher % of octane boosters and hence is another fuel of interest.

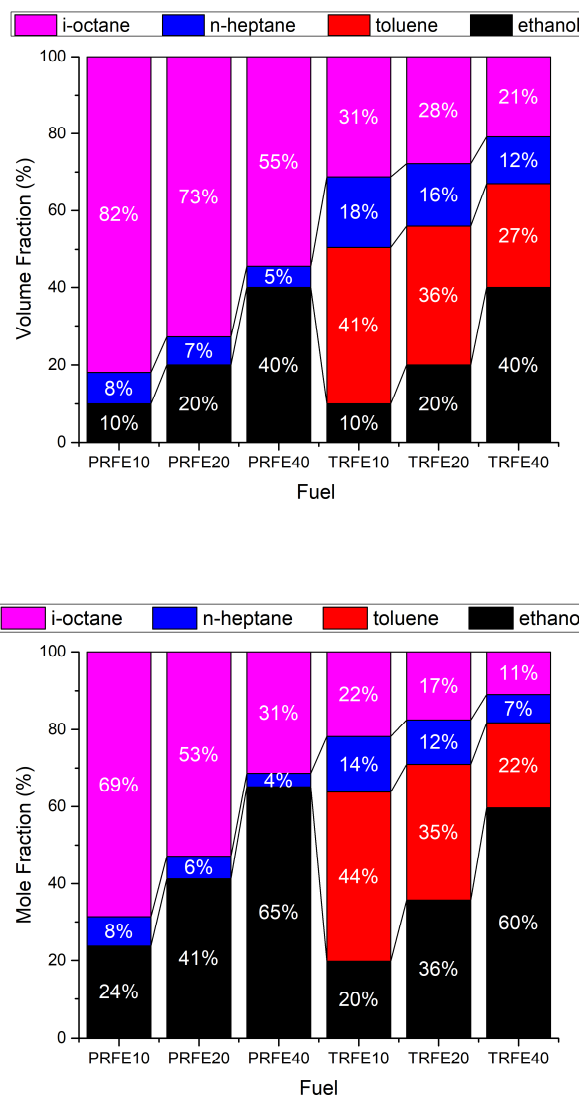


Figure 8-2 Volume fraction (top) and mole fractions (bottom) of various fuel components present in the PRFE mixtures and the TRFE mixtures tested in this study.

8.7 Simulations

In this study CHEMKIN-PRO simulations are performed in order to identify how fuel composition impacts the ignition delay times. The LLNL gasoline mechanism [193] consisting of 5935 reactions and 1387 species is used to simulate the autoignition process using CHEMKIN-PRO software. Fixed volume homogeneous reactor simulations are performed for a

total of nine fuels including the six fuels tested in the RCM. Non-adiabatic variable volume simulations are performed by importing the volume profile derived from the pressure data of non-reactive tests in the RCM. These non-reactive pressure profiles include the effects of the compression process and associated heat loss after the compression process in the numerical simulations. For achieving this, non-reactive tests are conducted in the RCM to obtain the pressure data. The non-reactive test cases are performed under the exact same set of conditions as the normal tests except that the oxygen portion of the mixture is replaced with nitrogen. Since the specific heat ratio of nitrogen and air are very similar, the heat losses are very well approximated, and the chemistry is frozen in these tests. The non-reactive tests are also useful to check if precompression reactions happen during compression process. This is very important if the fuel surrogate contains substantial amount of highly reactive components such as n-heptane. The obtained non-reactive pressure history is imported into CHEMKIN-PRO as a variable volume profile. Details on this conversion can be found in [79]. In figure 8.3, sample pressure outputs from the RCM experiments and from the simulations is shown. The compression ratio for this sample case was maintained at CR13.8 and TRFE40 was used as the fuel with a compressed temperature of 736K. It can be seen that the variable volume simulations accurately captures the compression and the heat losses past TDC. In addition to the variable volume simulations, constant volume simulations are also performed for 9 different fuels.

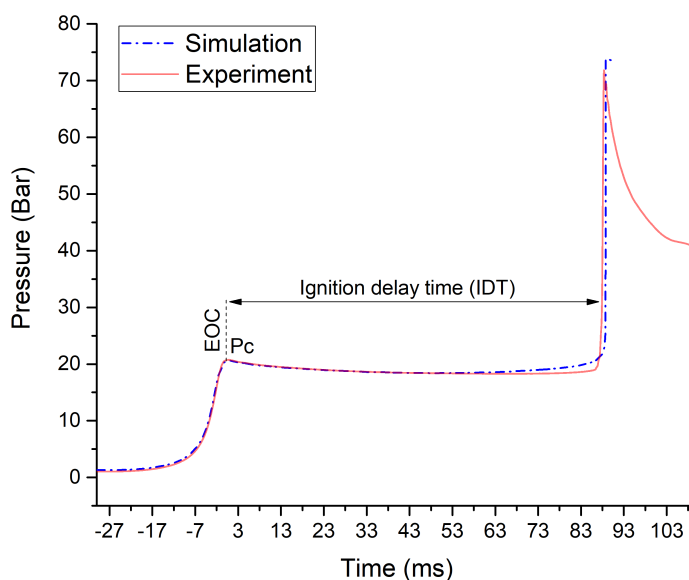


Figure 8-3 Comparison of pressure from RCM experiment and CHEMKIN-PRO simulation for TRFE40-air mixture at stoichiometric conditions for $P_c=21$ bar and $T_c=736$ K

8.8 Results and Discussions

8.8.1 RCM Experiments

From figure 8.4, it can be observed that for the PRFE40 blend no NTC behavior is observed and the test data shows largely Arrhenius behavior which is representative of the high volume of ethanol present in the mixture. There is a slight shift in Arrhenius behavior at 800K but this could be attributed to the change in compression ratio. The higher compression ratio has a smaller clearance volume which leads to higher heat losses that can slightly increase the ignition delay times. The ignition delay trend is captured by the simulations; however, the IDTs are under predicted by the constant volume (C-V) simulations. For the variable volume (non-adiabatic) simulations, the predictions improve but the mechanism remains more reactive at the lower temperatures. It is possible that the reaction mechanism is under predicting the effect of large

fractions of ethanol in the resulting blend. Lee et al. [173] proposed that the discrepancies in the prediction may be due to the deficiency in the ethanol chemistry or the cross reactivity of ethanol with the alkanes and toluene.

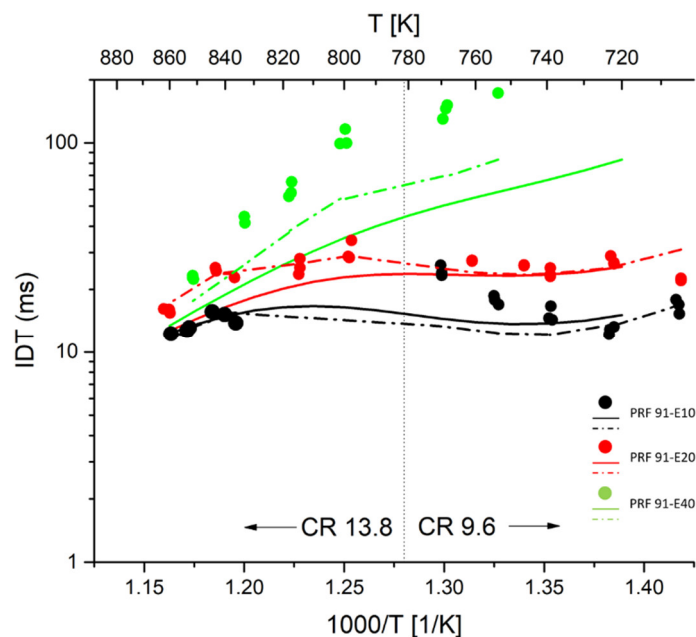


Figure 8-4 Comparison of total ignition delay times from RCM experiments (filled circles), variable volume (dashed line) and constant volume (solid line) numerical simulations for PRF91 with varying ethanol % by volume.

For the PRFE20 blend, the constant volume simulations captures the IDTs of the test data very well for CR9.6 compression ratio. However, at the CR13.8 conditions the C-V simulation under predicts the reactivity. However, for the variable volume simulations, with heat loss effects included, the predictions match the test data. Based on this observation it can be concluded that if the C-V simulations captures the IDT trends well, then the accuracy of the prediction can be improved by conducting variable volume simulations. Test data is not available for PRFE10 at 800 and 820K due to first stage heat release occurring before the end of compression. For PRFE10, predictions at low temperature and high temperatures are well captured by the

simulations, however, the fuel exhibits very strong NTC behavior due its high paraffinic content and this behavior is not captured by the simulations. For PRF mixtures a longer period between the timing of the first peak production of HO_2 radicals and the final ignition results in increasing concentration of HO_2 and H_2O_2 radicals. This makes the system unreactive leading to strong NTC behavior [51]. This is a more unreactive pathway to produce OH compared to paraffinic isomerization mechanisms [46]. Overall, it can be observed that for lower volumes of ethanol the NTC behavior of the fuel is over predicted by simulations and at higher ethanol volumes the reactivity is underpredicted by the mechanism.

Similar to the observations made for the PRFE40 blends, the TRFE40 delay times as shown in figure 8.5, are under predicted by the simulations but the deviation is lower in comparison. The TRFE40 blend shows Arrhenius like behavior in the tested region. For blends with lower ethanol volume fraction the IDTs are over predicted except at high temperatures. However, the numerical predictions fall within 20% of the test data values in comparison to the variable volume simulations. For the TRFE10 and TRFE20 fuels the experimental data shows enhanced NTC behavior in comparison to the predictions. This is similar to the observation made with the PRFE10 fuels. Overall, for the numerical predictions using the LLNL mechanism it can be concluded that predictions deviate when NTC behavior is observed in the test data. At 40% ethanol levels, the fuel shows largely Arrhenius behavior since the fuel is 60% ethanol by mole fraction and the simulations over predict the reactivity here. Longer delay times at CR13.8 could also be due to the fact that the heat losses are more since the increase in compression ratio is achieved by the reduction in clearance volume. Hence facility effects could play a role here which cannot be accounted for completely in the variable volume simulations [157].

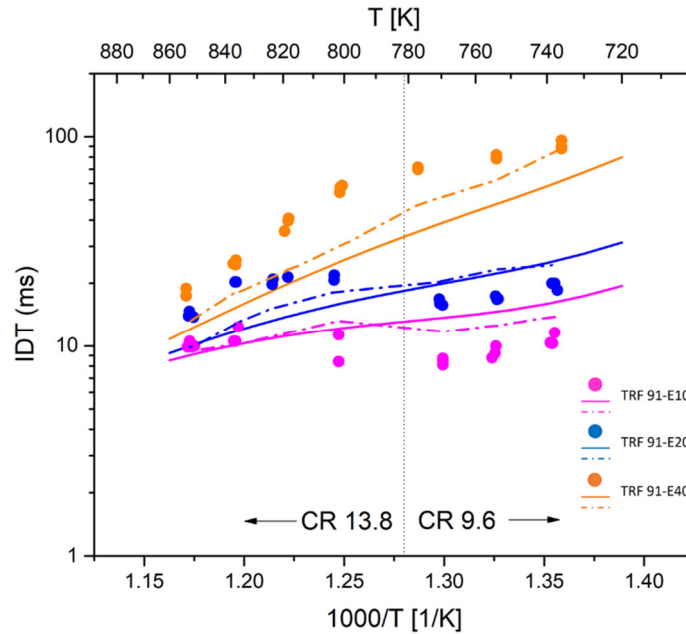


Figure 8-5 Comparison of total ignition delay times from RCM experiments (filled circles), variable volume (dashed line) and constant volume (solid line) numerical simulations for TRF91 with varying ethanol % by volume.

In figure 8.6, the experimental average IDT values are plotted and connected with straight lines to improve visualization. Around 740K the reactivity trends, as indicated by the IDTs, match the reactivity trends as dictated by the fuel's RON values. For reducing knocking phenomenon in SI engines higher sensitivity fuels are preferred [7]. The TRFE40 and PRFE40 have similar sensitivity values (~ 13.6) but the RON values dictate the reactivity of these fuels as seen from the IDT values, hence higher sensitivity and higher RON fuels are preferred for knock mitigation. The test conditions chosen for this study lie on the NTC region where high paraffinic fuels are supposed to be less reactive but we can see that the higher sensitivity fuels still maintain higher autoignition resistance throughout the range. It can be concluded for the tested fuels in the MSU RCM facility, that the fuel blends' reactivity at 740K and 21 bar resembles their relative RON numbers. At 740K the reactivity of the PRF surrogates (with high RON) are predicted to be lower than their TRF counterparts in the c-v simulations as illustrated in figure

8.7 and hence the simulations do not show a similar RON-IDT trend to the experiments. Since RON captures the low temperature reactivity, it is expected that longer delay times be recorded for PRFE10 at 720K, however the c-v simulations predict lower reactivity. For the simulations, a similar region where reactivity corresponds to relative RON values, is located at approximately 790K. This region cannot be verified for the experimental data due to the lack of test points at 800K for the PRFE10 blend. However, it is expected that in this region, PRFE10 (RON 98.7), due its NTC behavior, would have exhibited longer delay times in comparison to the TRF91E20 (RON 100.2) blend. PRFs with higher sensitivity showed much lower reactivity in the NTC region and this corresponds to their higher MON values. Although TRF91E10 have a higher % volumes of toluene and ethanol their RON and MON values are lower than PRFE10. This is due to the antagonistic blending nature of ethanol with toluene. A dependence for MON values vs IDT was not found in the tested range. Mittal et al. [59] suggested that MON tests capture chemical kinetics occurring above 900K and the limited range could be a possible reason for lack of correlation. For e.g. PRF91E10 and PRF91E40 have very similar MON values and but are spaced apart at 850K. Judging by the slope of the curves, since Arrhenius behaviour is expected at high temperatures, a possible crossover might occur at the higher temperatures.

CHEMKIN-PRO simulations predict similar reactivity between PRFE10 and TRF15E10. This is applicable because the fuel is only 15% toluene leading to fewer antagonistic blending effects. The c-v simulations also predict crossover between TRFE20 and PRFE10 as observed in the experiments. TRFE20 has a higher RON value but a lower MON value in comparison to PRFE10. This crossover is also captured in the testing except that the initial and final crossover happens at lower temperatures. The test data also shows that PRFE20 remains the least reactive compared to all other fuels containing less than 40% ethanol. However, at the lowest temperature

the delay times of TRFE20 and PRFE20 are similar and this is captured as a crossover points in the simulations.

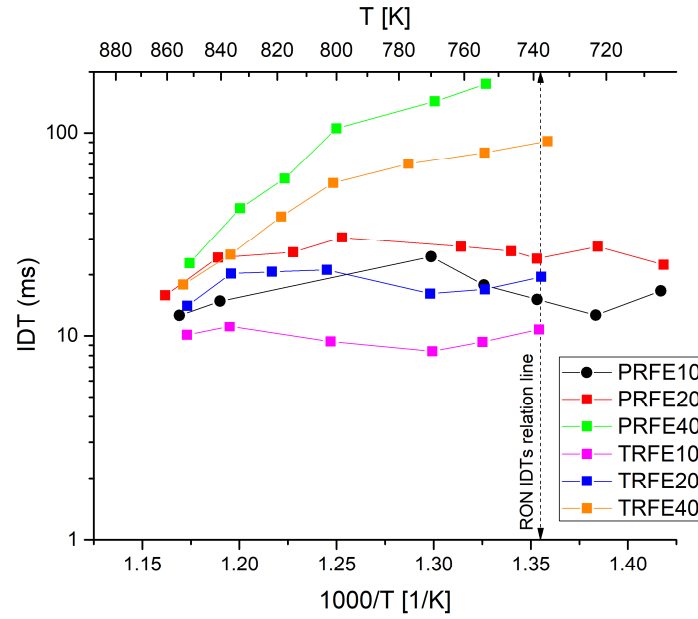


Figure 8-6 Average IDTs obtained from experiments for PRF and TRF surrogates substituted with ethanol for up to 40% by volumes.

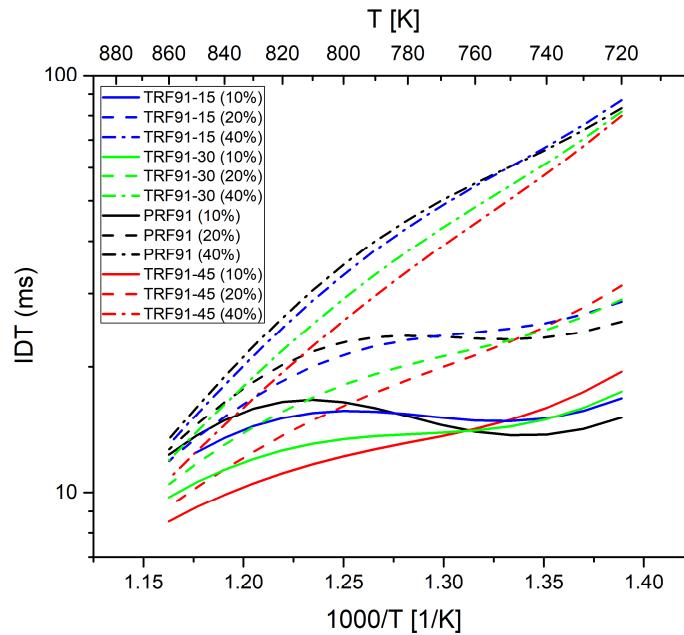


Figure 8-7 IDTs obtained from constant volume simulations for various PRF and TRF surrogates substituted with ethanol for up to 40% by volumes.

In figure 8.8, RON and IDTs are compared at the compressed condition $T_c=740\text{K}$ and $P_c=21\text{ bar}$. This compressed condition is very similar to condition (750K at 25 bar) obtained as RON vs IDT correlation by Singh et al. [60] using kinetic simulations for various non oxygenated gasoline surrogate mixtures. A curve fit is not attempted here due to limited number of data points available. The trend suggests that for sensitivity values below 11.1, the IDT lies in a narrow range, but for the higher sensitive fuels a different slope is observed. The sensitivity is imparted by ethanol and toluene contents in the fuel. Presence of high levels of ethanol and unsaturated compounds reduces the low temperature reactivity of the fuel and results in extended delay times. However, the TRFE mixtures exhibits lower delay times even for a sensitivity value of 11.1 (TRFE20). This is due to the molecular level interactions occurring between ethanol and toluene fractions of the fuel or could be due to presence of relatively higher percentages of low reactivity component such as n-heptane which could promote LTHR. This would be analyzed by looking at the reaction pathways in the next section. For the E40 blends, the mole fraction of ethanol present at TRFE40 is 60% in comparison to 65% present at PRFE40. The 5% difference is not suspected be the sole reason for the large difference in ignition delay times and the RON values. Hence a rate of production analysis using chemkin-pro is carried out in the next section to identify the kinetic reason for this behavior.

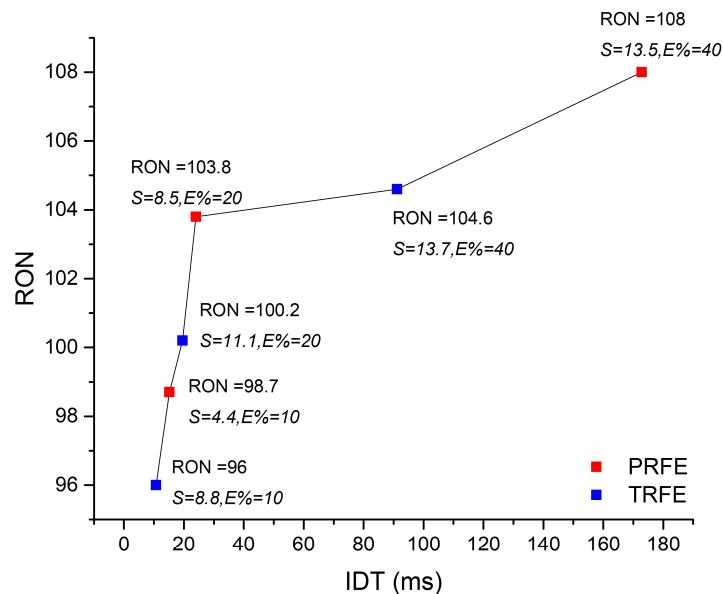


Figure 8-8 RON vs IDT relationship obtained at $T_c=740\text{K}$ and $P_c=21$ bar for PRFE and TRFE mixtures. RON values, sensitivity values and ethanol % are shown for each data point. Note: Data shown for PRFE40 is at $T_c=750\text{K}$, $P_c=21$ bar.

OH rate of production (ROP) analysis was performed using Chemkin PRO software and the results are discussed here. H atom abstraction reactions from parent molecules by OH radicals are one of the major reaction classes that control ignition in the intermediate temperature region [60]. In this work in order to understand the chemistry of toluene and ethanol in the NTC region ROP analysis is performed for OH and HO₂ radicals. ROP at 2/3 reaction time of OH peak, which also corresponds to 2/3 of the ignition delay time was used by Javed et al. [178]. 10% of OID was used by Kukadapu et al. [52] for comparing ROP of OH to understand the initial radical pool formation. In this work, ROP analysis was performed at 80% OID following the recommendation of Fan et al. [192].

From figure 8.9 for the PRFE10 mixture, isooctane-the largest fraction of fuel, consumes the majority of the OH in the high temperature range, but at lower temperatures the relative

importance of ethanol increases. Consumption by n-heptane remains constant for all the temperatures studied for PRFE10. For PRFE20, with increasing ethanol mole fraction (%), ethanol shows higher consumption in comparison to the PRFE10, however isooctane is responsible for the ignition behavior at 860K and at lower temperatures isooctane and ethanol are equally responsible for ignition. For PRFE40, which has ethanol in the highest mole fraction, the ethanol strongly controls the ignition process and is followed by the isooctane. Temperature dependence in ROP, as observed in PRFE20 and PRFE10 is not seen at PRFE40. The contribution of n-heptane remains similar for all of these fuels and at all temperatures and n-heptane does not control the ignition process significantly. This can be mainly attributed to the lower concentrations of n-heptane present in the PRFE mixtures.

In figure 8.10, for the TRFE10 mixture it can be observed that toluene strongly controls the ignition by abstracting the OH radicals with a high consumption rate exhibited at the lower temperature. This indicates that toluene levels in the mixture completely dictate the ignition behavior for this blend. N-heptane and ethanol shows very similar OH abstraction rates. In the TRFE20 mixtures toluene continues to dominate the reactivity of the mixture even though equal mole fractions of ethanol and toluene are present. This indicates that ignition is primarily controlled by the toluene and this could be the reason for the antagonistic effect observed in the blends. N-heptane competes equally with ethanol for the TRFE10 mixture. In the TRFE40 mixture with 60% of ethanol by mole fraction, ethanol strongly dictates the ignition behavior, and this explains the similarity of the ignition curve with PRF40 since both of these fuels contain very similar levels of ethanol by mole fraction.

For TRFE10 with respect to n-heptane OH-abstraction, a different behavior is observed in comparison to the PRFE mixtures. The TRFE mixtures contain a higher % of n-heptane and at

high temperature n-heptane consumes the most OH, in comparison to isooctane and ethanol. Excluding toluene, for the TRFE10 mixture, high temperature combustion is strongly controlled by n-heptane. But as the temperature decreases contributions from ethanol and isooctane become equally important to the n-heptane. However, as ethanol concentration increases, the ethanol strongly controls ignition at all temperatures, followed by n-heptane with the isooctane having very similar reactivity to the n-heptane. For TRFE40 fuel, like in PRFE40, ethanol strongly contributes to ignition and the relative importance among n-heptane and isooctane remains similar to TRFE20. TRFE40 and PRFE40 have similar sensitivity, but TRFE40 has a lower MON compared to the PRF. The lower MON can be attributed to the high temperature reactivity of the n-heptane. It is interesting to note that the toluene reaction pathway $\text{C}_6\text{H}_5\text{CH}_3 + \text{OH} \rightleftharpoons \text{HOC}_6\text{H}_4\text{CH}_3 + \text{H}$ does not actively participate in OH abstraction and hence is not included in this analysis.

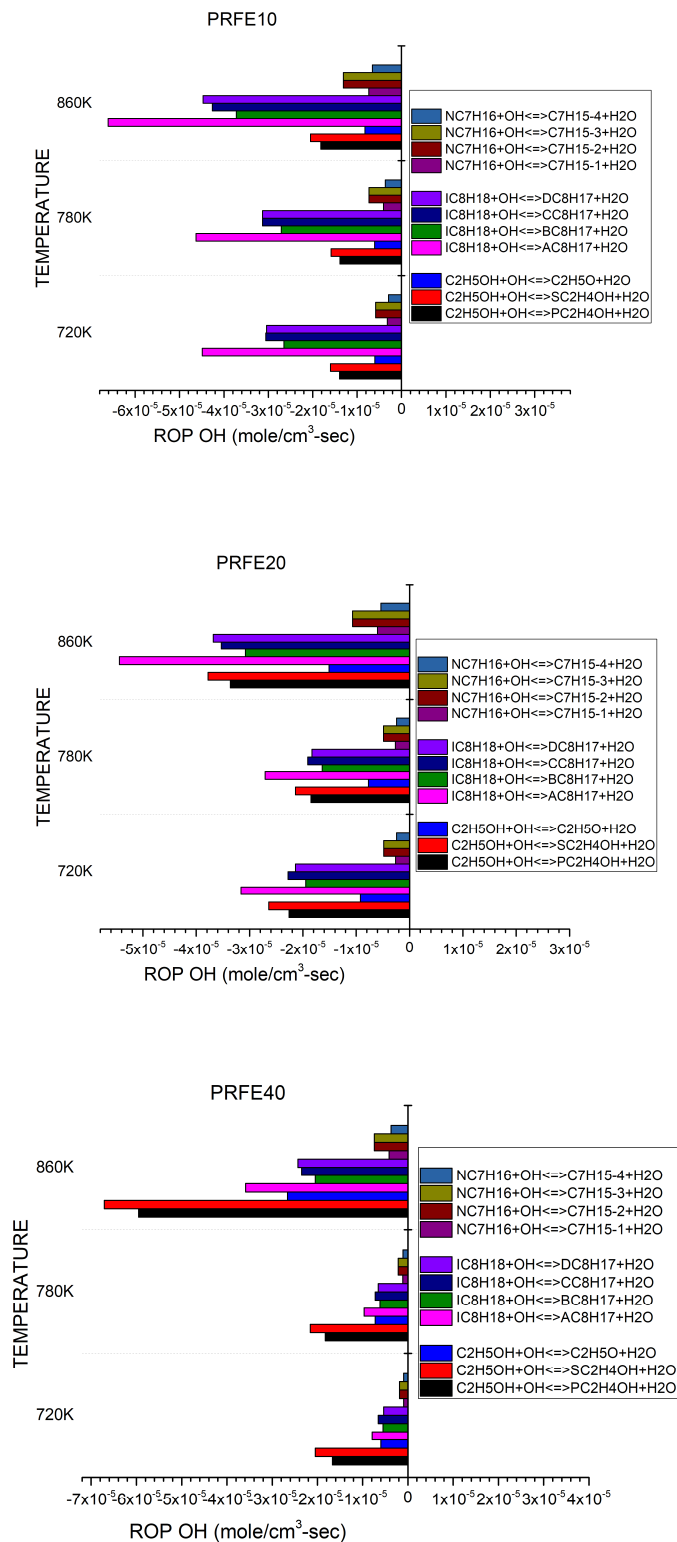


Figure 8-9 OH consumption rate by fuel components at different temperatures at 80% of ignition delay time for PRFE10 (top), PRFE20 (middle) and PRFE40 (bottom).

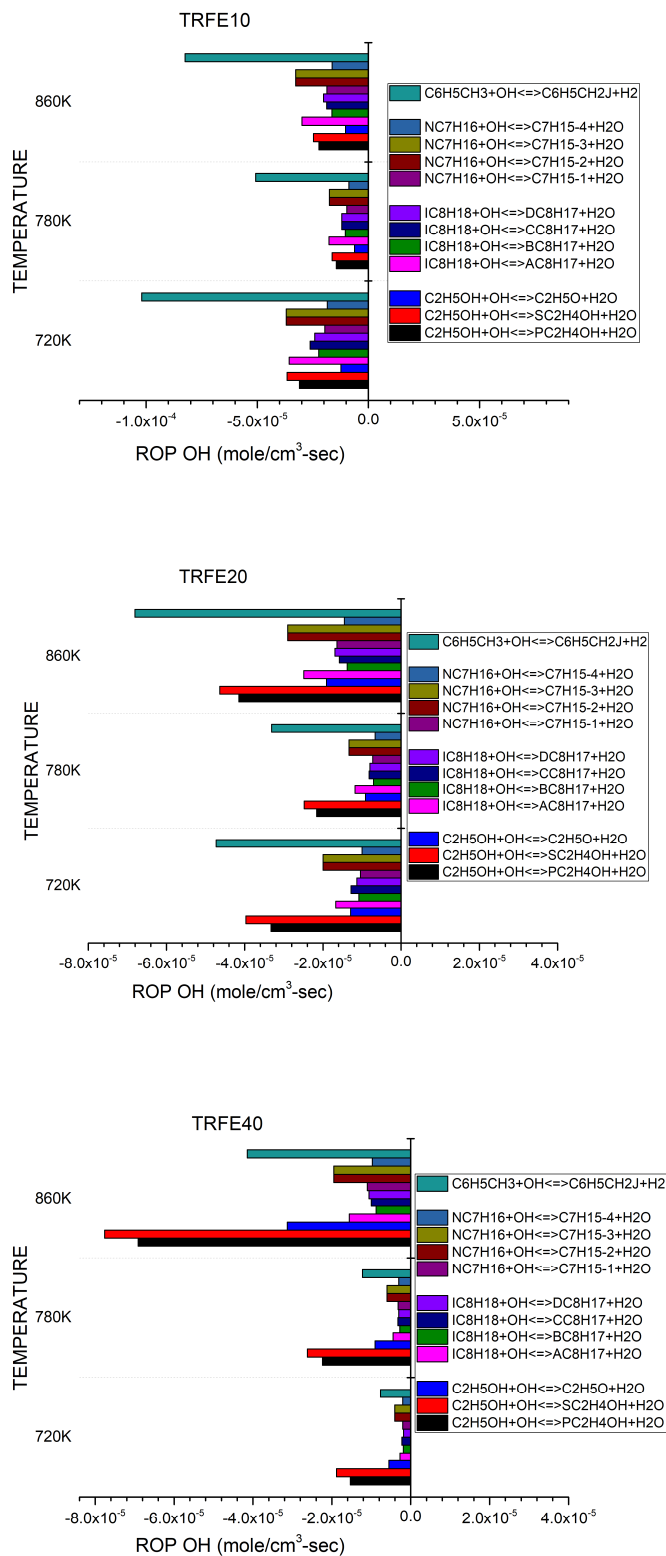


Figure 8-10 OH consumption rate by fuel components at different temperatures at 80% of ignition delay time for TRFE10(top), TRFE20(middle) and TRFE40(bottom).

8.8.2 HO₂ ROP Analysis

Aromatics, when present in fuel blends, tends to increase the reactivity of the fuel mixtures in the intermediate temperature range (800-950K) due to abstraction of HO₂ radicals and accelerated formation of H₂O₂ [194]. In addition, HO₂ reacts with benzylic radicals to form benzoyl radicals and highly reactive OH radicals. In the NTC region, these reactions increases OH production and prevent the OH radical consumption as seen in the PRFs [58]. Ethanol has rapid consumption of HO₂ via $\text{C}_2\text{H}_5\text{OH} + \text{HO}_2 \rightleftharpoons \text{CH}_3\dot{\text{C}}\text{HOH} + \text{H}_2\text{O}$, in the low temperature range [173]. In order to further analyze the participation of toluene and ethanol in reactions with the other ignition controlling radical HO₂[60], a similar ROP analysis is carried out for HO₂ at 80% OID. Alkenes and aromatics are also known to abstract HO₂ radicals produced by alkanes at intermediate temperatures [1].

For TRFE10 the mole fraction of toluene is twice that of the ethanol. For this fuel toluene is effective in consuming HO₂ radicals in comparison to ethanol. A similar trend was observed with the OH ROP analysis, but we can see that ethanol competes more effectively in HO₂ consumption with toluene. As we move to TRFE20, in which equal mole fractions of ethanol and toluene are present, ethanol is more effective than toluene in abstracting HO₂ radicals. In the case of TRFE40, ethanol now exhibits a significantly higher HO₂ abstraction rate. It can be concluded that given equal amounts of ethanol and toluene in the fuel, ethanol shows very high a HO₂ abstraction and is also effective in abstracting OH radicals. Additionally, it can be observed that the HO₂ abstraction potential of ethanol and toluene are temperature invariant unlike the alkanes as seen earlier for the OH abstraction process.

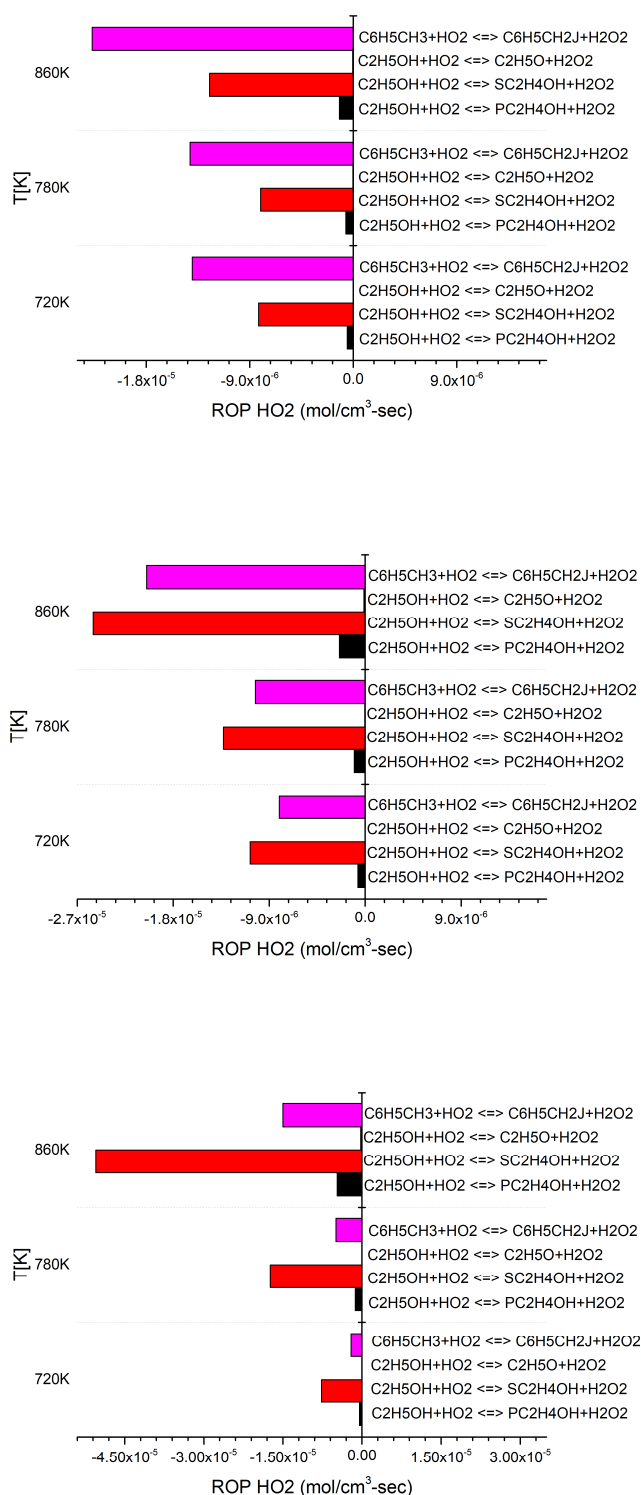


Figure 8-11 HO2 consumption rate by toluene and ethanol at different temperatures at 80% of ignition delay time for TRFE10(top), TRFE20(middle) and TRFE40(bottom).

8.8.3 Average Pressure Rise Rate (PRR) Analysis

In figure 8.12, the average pressure rise rate for the CR9.6 and CR13.8 cases are presented for the PRFE and TRFE mixtures. The intention of analyzing the PRR data is to get a preliminary idea of the autoignition intensity depending upon the end gas conditions. At CR9.6, for the PRFE mixtures, the pressure rise rates lies in the 150 to 225 bar/ms range with the max PRR located in the 740K and 760K compressed temperature range. The lowest PRRs are located at outer ends of the test conditions, i.e. at the lowest temperature and the highest temperature for 9.6 compression ratio. The PRFE10 and PRFE20 fuels do not show different autoignition intensity except at 720K. The PRFE40 blend shows much lower PRR at 760K and 780K, however these tests also had very long ignition delay times in excess of 150ms. In such circumstances the toroidal combustion core region would be cooler than the estimated compressed temperature and this could be the primary reason for the lower autoignition intensity. Moving on to the TRF mixtures a similar trend to the PRF mixtures is seen. The TRFE10 and TRFE20 have very similar pressure rise rates, with lower pressure rise rates exhibited by the TRFE40 mixtures. This suggests that higher ignition delay times could potentially reduce autoignition intensity. For the PRF mixtures the ignition delay times are similar at 710K and 760K, with 710K showing the lowest intensity. Hence it is possible that other than longer delay times the higher ethanol content in the fuel is also affecting the PRRs.

Moving onto the CR13.8 test points, at 860K, IDT values for all six fuels are available.

Comparing the IDTs for the six fuels, it can be seen that the PRRs scales with IDTs and a similar observation was made from the PRF plots by comparing the average delay times 760K and 780K for all six fuels. This shows that shortened delay times are associated with higher pressure rise rates or heat release and hence autoignition intensity observed in the engine could be based on

how soon the end gas autoignites. However, this is only true at a given temperature condition, since at 800, 840 and 860K compressed conditions the TRFE10 ignition delay times are 11.3, 12.33, and 9.96 ms respectively but the lowest PRR is observed at the shortest delay time.

Hence, the maximum PRR depends upon thermodynamic conditions and does not necessarily scale with temperature and for a given compressed condition the maximum PRR depends upon the reactivity of the fuel-air mixture.

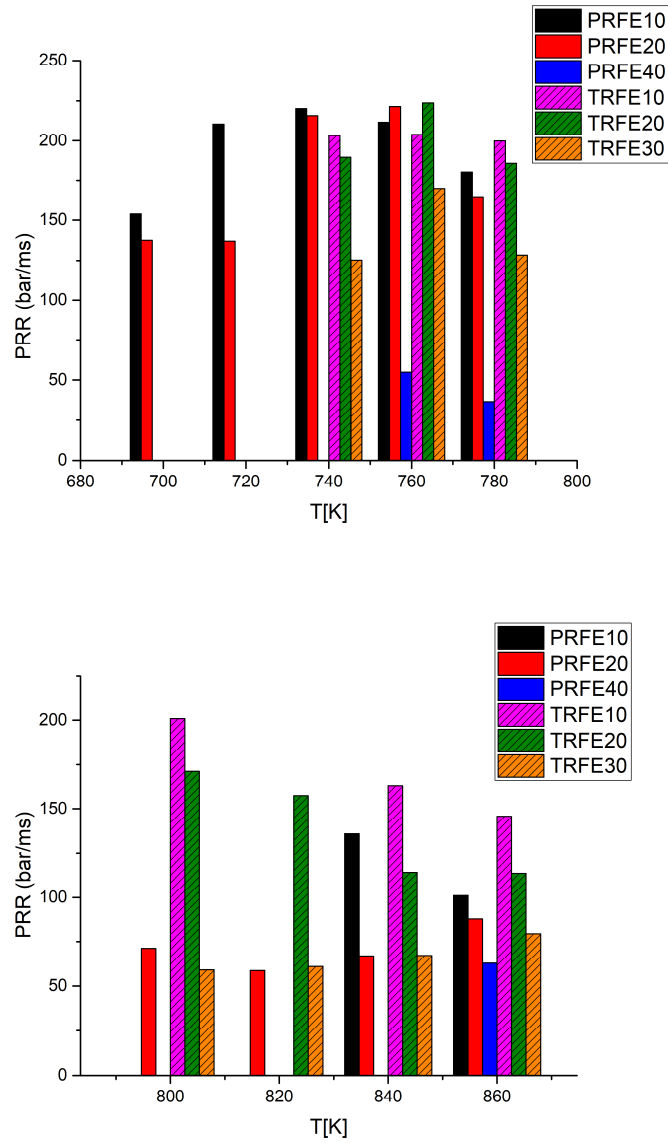


Figure 8-12 Average pressure rise rates (PRR) for all the tested fuels at CR9.6 (top) and CR13.8 (bottom).

8.9 Chapter Summary

In this work a preliminary attempt is made to relate RON values with IDTs obtained from the MSU RCM facility. Several past and recent works [61,78,190,195] in this essence have been done using numerical analysis and not using experimentally measured delay times. Such methods depend upon the accuracy of the available reaction mechanisms. The results from our current study indicates that for the experiments performed at the MSU RCM facility, a qualitative RON value can be obtained by measuring the fuels IDT at 740K and 21 bar for gasoline surrogate blends containing a range of sensitivity values. This presents a valid case for testing new second generation biofuel blends in the RCM as a next step. For such blends, experimentally measured octane numbers, well-validated reaction mechanism or blending laws to estimate ON seldom exists. Hence this approach enables us to record both the reactivity of the fuel and to assess the qualitative RON value of the resulting blends. The major conclusions in this chapter is listed below,

- 1) Variable volume simulations improved the predictions of the C-V simulations. The longer delay times observed in the RCM data due to heat loss effect is properly captured when the volume profile is imported. However, the variable volume simulations follows the trend of the constant volume simulations. The NTC region in PRF mixtures with lower ethanol content is underpredicted by both of these simulations.
- 2) In the 720K -850K range at 21 bar, RON values of the fuel were represented by ignition delay times at 740K. A correlation is not attempted in this chapter due to limited number of data points.

- 3) A dependence for MON values vs IDT was not found in the tested range. Mittal et al [59] suggested that MON tests capture chemical kinetics occurring above 900K and the limited range could be a possible reason for lack of correlation. For eg PRF91E10 and PRF91E40 have very similar MON values and but are spaced apart at 850K. Judging by the slope of the curves, since Arrhenius behaviour is expected at high temperatures, a possible crossover might occur at the higher temperatures.
- 4) The numerical simulations reveal that ethanol strongly controls the ignition process for PRF fuels with ethanol content greater than 10% by volume. Toluene actively participates in the OH abstraction, hence controlling ignition, in comparison to ethanol for ethanol content less than 40% by volume in the blend. Toluene scavenges HO₂ radicals more effectively compared to ethanol when toluene has higher mole fraction than ethanol. However, when equal mole fractions are present ethanol strongly scavenges HO₂ radicals.
- 5) In the TRF mixtures, n-heptane actively competes with ethanol in scavenging the OH radicals when 10% ethanol is present by volume.
- 6) Comparing the average pressure rise rates, it was found that the PRR depended upon compressed conditions and did not necessarily increase with temperature. For the same compressed conditions, the PRR of different fuels shows a one to one relation with their ignition delay times.

Chapter 9 Summary and Conclusions

This dissertation presented experimental results supporting efficiency improving strategies for SI engines through the use of excess air or EGR dilution, and by altering the composition of the fuel used. Although conclusions have been drawn at the end of each chapter with respect to the applied test strategies and the obtained results, concluding remarks and discussions based on the research questions raised in Chapter 1 are presented here.

1- For a methane fueled TJI system, how does a single jet and/or converging jets compare with the burn durations and lean limit extension observed with diverging jets?

Chapter 3 focused on this aspect and a set of experiments were carried out for varying main chamber lambda starting from $\lambda=1.78$ up to the lean limit. The prechamber lambda was fixed $\lambda=0.8$ for all the tests. It was found that until $\lambda\sim 2.5$ the diverging jets had shorter 10-90 burn durations and up to 50% reduction in duration was recorded. Hence for practical applications, diverging jets would be a better choice with the added benefit of reduced impingement.

However, the single jet and converging jet had a slightly higher lean limit extension and exhibited a similar burn duration to the diverging jets as the lean limit was approached. Hence these configurations exhibited better dilution tolerance.

2- Performance metrics derived from main chamber pressure such as 0-10%, 10-90% burn durations, and the durations of the peak first and third derivative values of pressure are compared for various TJI configurations. Can this information be used to evaluate and compare TJI performance in both active and passive configurations?

This question was partly investigated in Chapter 3 and exclusively investigated in Chapter 4. The 0-10% burn duration values for varying nozzle designs and main chamber lambda values

remained constant for a fixed prechamber lambda value. A series of tests were performed by varying the prechamber lambda and holding the main chamber at $\lambda=1.8$. It was concluded that 0-10% burn duration was a strong function of prechamber lambda and hence it is a suitable metric to evaluate prechamber mixture conditions. However, the overall performance of nozzles was indicated by the 10-90% burn durations without any ambiguity.

In the main chamber pressure trace, two maximum peak pressure rise points were located during combustion, one during the jet ignition phase and other during the main chamber phase. The jet ignition and the main chamber combustion dp/dt values were a stronger function of main chamber lambda. The duration of the jet ignition phase was further measured using 3rd derivative pressure peaks. The jet ignition duration measurements remove the effect of spark timing and the time required for flame propagation within the prechamber. Longer jet ignition durations typically corresponded to the delay in strong main chamber ignition which in turn delayed the flow reversal events.

3- Can the direct test chamber (DTC) charge preparation technique replace the traditional mixing tank-based charge preparation approach for ignition delay studies in an RCM?

The DTC approach avoids issues with traditional mixing tank techniques such as thermal cracking of fuel molecules and condensation of fuel along the transfer lines. Hence in order to study the ignition delay times of different gasolines and their surrogates the DTC approach was used. The results were validated by comparing the ignition delay times of iso-octane air mixtures across different facilities in Chapter 5. For full blend gasolines, a GCMS study was conducted to ensure complete evaporation of non-volatile fractions of the gasoline fuel, when the DTC technique was used. The results indicated that reasonable RCM wall temperatures together with 2 minutes of mixing time were enough to prepare a homogenous gas-phase mixture. By

employing the DTC approach combined with the use of premixed gas bottles, air-fuel mixtures at different equivalence ratios can be quickly prepared relative to the only fixed equivalence ratios possible with the mixing tank technique.

4- What is the effect of CO₂ dilution on ignition delay times for full blend gasolines, and their simple and multicomponent surrogate-air mixtures?

For gasoline-air and surrogates-air mixtures, the addition of CO₂ retarded the ignition delay times significantly in the NTC region when compared to the low temperature and the high-temperature region. CO₂ addition did not show significant chemical reactivity since the effect of dilution on delay times resembled the case of reduced reactivity due to a reduction in the concentration of fuel in the final mixture. If significant chemical reactivity existed, then it is possible that the ignition delay times of the diluted mixture would be very similar to the undiluted mixture [72]. Also, the CO₂ dilution effect was found to scale with the octane numbers for the full blend gasoline. However, such behavior was not noted for the multi-component surrogates suggesting the CO₂ retardation potential depends both on the octane number and the chemical make-up of the fuel.

5-Can CO₂ dilution provide any octane relaxation potential?

Octane differences in terms of ignition delay times is manifested in the NTC region as observed in Chapters 6 and 7. Similarly the effect of CO₂ dilution was pronounced in the NTC region as well. It was seen that with increasing dilution, ignition delay times of low RON gasoline overlapped with undiluted high RON gasoline in the NTC region. Since knock typically occurs in the NTC region CO₂ dilution can provide octane relaxation potential.

5-Ethanol is an octane booster and it blends antagonistically with aromatics such as toluene and synergistically with alkanes. What are the resulting trends in ignition delay times when ethanol is blended by up to 40% by volume to PRF (alkane only) and TRF (alkane aromatics) mixtures? What is the reason for the observed trends in terms of underlying fuel chemistry?

ROP analysis from the numerical simulations indicated that when only 10% ethanol was present in a PRF91 mixture, iso-octane controlled the final ignition in the NTC region. However, for the increased levels of ethanol, ethanol controlled the ignition and resulted in reduced reactivity of these mixtures. However, for the TRF mixtures, toluene influenced the final ignition and ethanol-controlled ignition only at 40% volume levels. This was the kinetic reason for antagonistic blending behavior since ethanol was not actively controlling the final ignition. The trends indicated that mixtures with a higher percentage of ethanol largely showed Arrhenius behavior while the other mixtures generally showed a region of no change in reactivity with increasing temperature in the tested temperature range.

6-Is there a relationship between measured ignition delay times in the RCM and measured RON and MON values from a CFR engine?

The experiments conducted in Chapter 8 indicated a trend of increasing RON values with decreasing reactivity at 740K and 21 bar. But no such relation was identified for the MON values. MON value correlation is expected at higher temperatures and it is possible that the tested range did not cover the corresponding compressed temperature condition.

9.1 Recommendation for Future Work

In the first part of this work, TJI nozzle design optimization for a methane fueled TJI system was carried out. The second part of the work focused on cold-EGR strategy and the implementation of the DTC approach for studying gasoline fuels and their surrogates in a RCM. It was noted that higher RON fuels exhibited lower reactivity in the NTC region, indicating a potential correlation between the RON numbers and ignition delay times of the fuel-air mixture in the NTC region. Finally, in order to confirm if any RON vs IDTs correlation existed, the effect of fuel composition on reactivity and RON values was studied from experimental and numerical results. Various PRF and TRF fuels blended with varying levels of ethanol were tested in the RCM and trends regarding reactivity and kinetic activity were identified. In order to answer some of the new questions that were raised in the dissertation chapters, additional avenues of future work were identified and are discussed below,

- In the TJI experiments, the converging jets appeared as a single jet instead of two separate jets. Also, during the later stages of combustion, a tail like flame front appeared in the right portion of the combustion chamber as observed from the high-speed images. The reason for this single-jet appearance and tail formation for the converging jets is not completely understood and supporting CFD simulation needs to be performed in order to understand the physics of the converging jets.
- Also, the effects of the cold jet (unburned charge pushed out from the prechamber due to the propagating flame) on pressure rise rates during the jet ignition phase is not completely understood. In the TJI experiments, it was found that pressure rise rates were a strong function of main chamber λ . However, for a fixed main and prechamber

lambda, the large hole nozzle had higher pressure rise rate compared to the small hole nozzle and it is suspected that the behavior is due to the issuance of a relatively larger fraction of the cold jet from the large hole configuration. Visualization of the cold jets using schlieren techniques would be useful to understand the main chamber fuel stratification just before the hot reacting jets begins to consume the main chamber charge.

- In Chapter 5, the DTC approach was introduced, and validation was performed by comparing ignition delay times and by conducting GCMS analysis. As an additional validation, the delay times obtained from the DTC approach can be directly compared with delay times obtained using a mixing tank technique to verify if homogenous mixing is achieved. For these tests, a high volatile fuel would be preferred in order to remove problems related to condensation of fuel along the transfer lines.
- CO₂ dilution did not show any significant chemical reactivity in the diluted mixtures as observed from the delay times. Additional test results using known inert components such as N₂ would confirm if any reactivity existed at all.
- In Chapter 8, reactivity trends of the fuel-air mixtures matched the relative RON values of the tested fuels at 740K and 21 bar despite the high alkane fuels showing reduced reactivity in the NTC regions. However, no such relation was identified for the MON values. MON value correlation is expected in the high-temperature range and hence additional tests using additional fuel mixtures could be performed at higher temperatures to identify the MON relation.
- The RON and MON values of TRFE40 were lower in comparison to the PRFE40 even though higher fractions of octane boosting components like ethanol and toluene were

present in the mixture. This is due to the antagonistic blending nature of ethanol with toluene and this blending behavior will vary depending on other fuel components [191]. Anisole a second-generation biofuel can potentially replace the toluene fraction in gasoline as an octane booster. The presence of ethanol increases the vapor pressure of the anisole in a gasoline surrogate blend and hence could prove to be a viable blend for future use [196]. Preliminary RCM experiments for anisole-air mixtures at stoichiometric conditions compared with numerical predictions are shown in the Appendix. Experiments can be conducted with the toluene fraction in the TRFE blends replaced by Anisole.

- The effect of fuel composition on ignition delay times was explored in Chapter 8. The effect of fuel composition on ignition by a TJI system can be explored in a future study. This would show the impact of fuel composition on burn rates and dilution tolerance of a TJI system.

APPENDIX

APPENDIX Additional Ignition Delay Data for Iso-Octane and Anisole-Air Mixtures

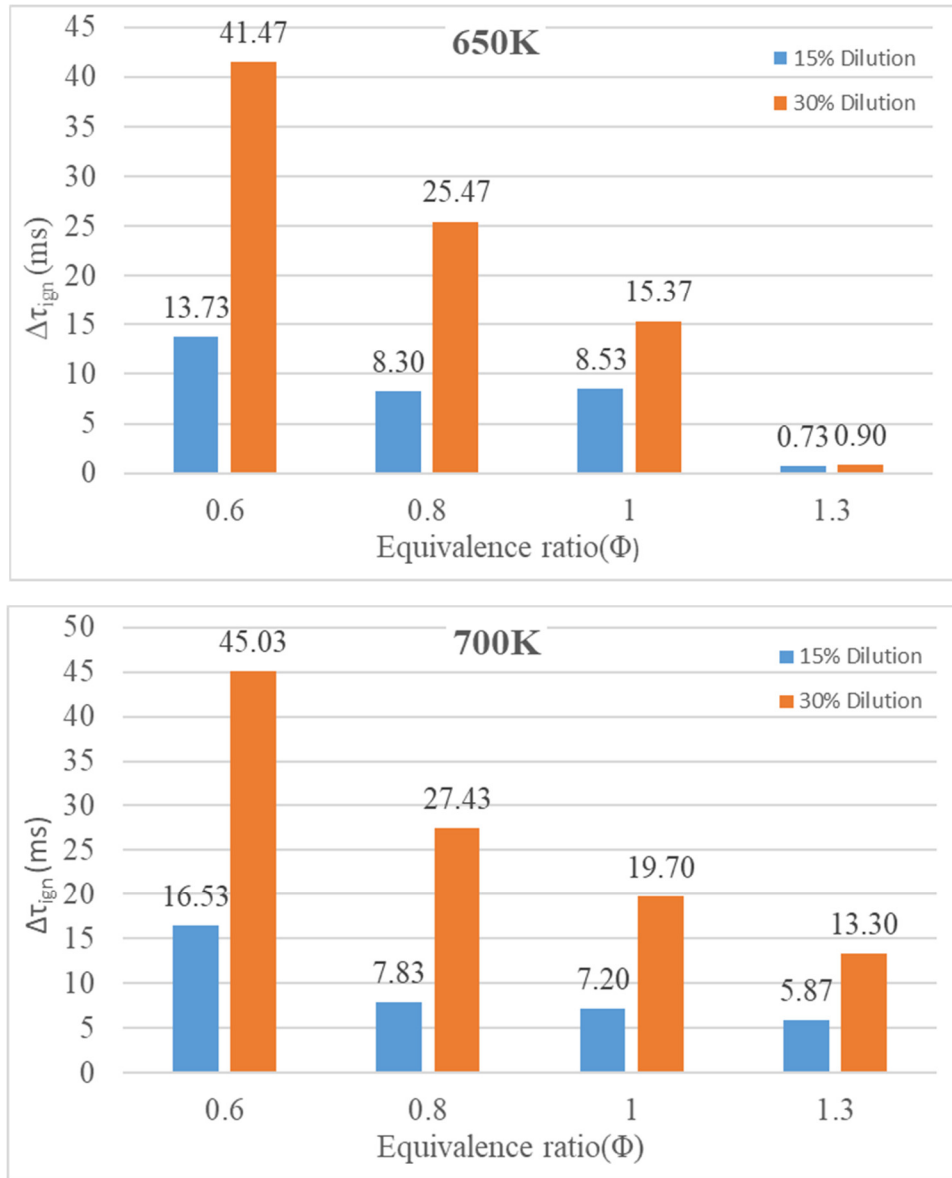


Figure A-1 Bar charts showing average increase in ignition delay times with increasing dilution levels with 0% dilution delay times used as baseline with $T_c = 650K$ and $700K$ and $P_c = 20 \pm 0.5 \text{ bar}$. (Chapter 5)

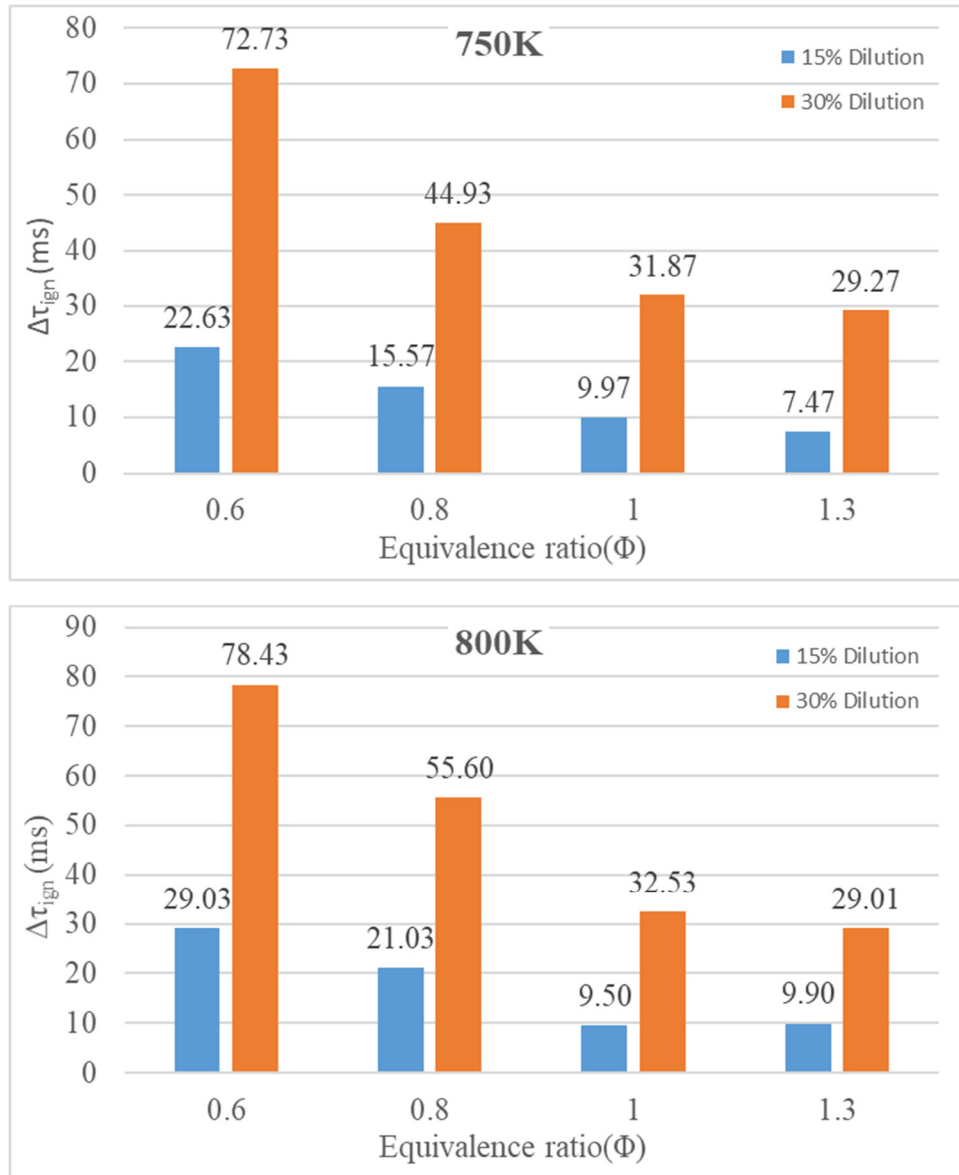


Figure A-2 Bar charts showing average increase in ignition delay times with increasing dilution levels with 0% dilution delay times used as baseline with $T_c = 750\text{K}$ and 800K and $P_c = 20 \pm 0.5\text{bar}$.

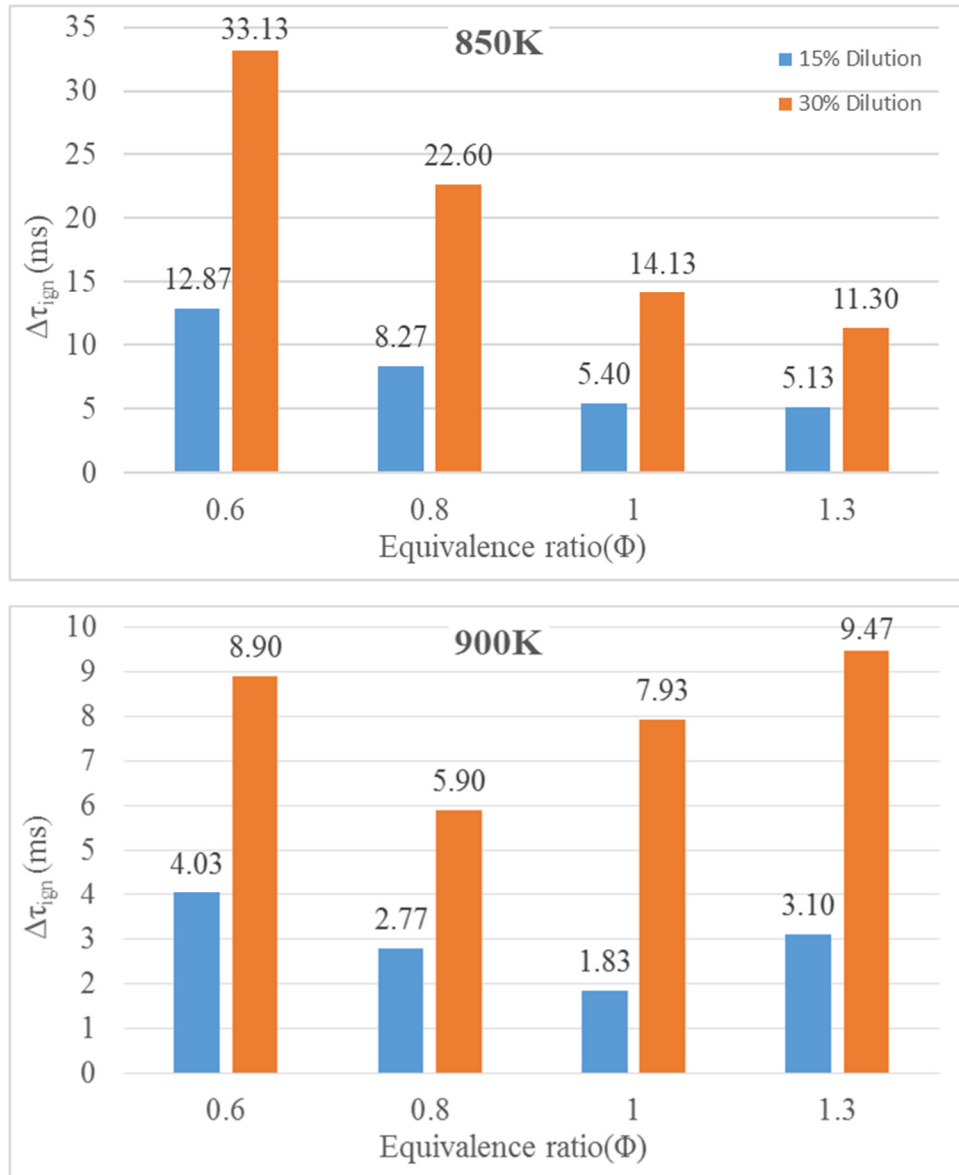


Figure A-3 Bar charts showing average increase in ignition delay times with increasing dilution levels with 0% dilution delay times used as baseline with $T_c = 850$ and 900K and $P_c = 20 \pm 0.5\text{bar}$.

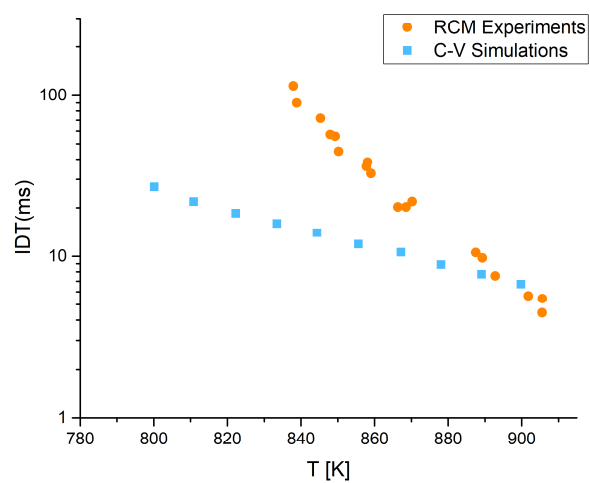


Figure A-4 Ignition delay times of anisole-air mixtures at stoichiometric condition and 20 bar compressed pressure. Preliminary experimental and numerical results for chapter 9

BIBLIOGRAPHY

BIBLIOGRAPHY

1. Sarathy, S.M., Farooq, A., and Kalghatgi, G.T., “Recent progress in gasoline surrogate fuels,” *Prog. Energy Combust. Sci.* 65:67–108, 2018, doi:10.1016/j.pecs.2017.09.004.
2. Aleiferis, P.G., Behringer, M.K., OudeNijeweme, D., and Freeland, P., “Insights into Stoichiometric and Lean Combustion Phenomena of Gasoline–Butanol, Gasoline–Ethanol, Iso-Octane–Butanol, and Iso-Octane–Ethanol Blends in an Optical Spark-Ignition Engine,” *Combust. Sci. Technol.* 189(6):1013–1060, 2017, doi:10.1080/00102202.2016.1271796.
3. Fifth Assessment Report: Climate Change 2014: Mitigation of Climate Change, Sep. 2014.
4. Lane, J., “Biofuels Mandates Around the World: 2014,” *Biofuels Digest*, 2013.
5. Annual Energy Outlook 2018 with projections to 2050, 74.
6. Kalghatgi, G.T., “The outlook for fuels for internal combustion engines,” *Int. J. Engine Res.* 15(4):383–398, 2014, doi:10.1177/1468087414526189.
7. Kalghatgi, G., “Fuel/Engine Interactions,” SAE International, Warrendale, PA, ISBN 978-0-7680-6458-2, 2013, doi:10.4271/R-409.
8. Caton, J.A., “A Comparison of Lean Operation and Exhaust Gas Recirculation: Thermodynamic Reasons for the Increases of Efficiency,” 2013, doi:10.4271/2013-01-0266.
9. Manivannan, A., Porai, P.T., Chandrasekaran, S., and Ramprabhu, R., “Lean Burn Natural Gas Spark Ignition Engine - An Overview,” 2003, doi:10.4271/2003-01-0638.
10. Kumano, K. and Yamaoka, S., “Analysis of Knocking Suppression Effect of Cooled EGR in Turbo-Charged Gasoline Engine,” 2014, doi:10.4271/2014-01-1217.
11. Heywood, J.B., “Internal Combustion Engine Fundamentals,” McGraw-Hill, 1988.
12. Clasen, K., Koopmans, L., and Dahl, D., “Homogeneous Lean Combustion in a 2lt Gasoline Direct Injected Engine with an Enhanced Turbo Charging System,” 2018, doi:10.4271/2018-01-1670.
13. Toulson, E., “Applying Alternative Fuels in Place Of Hydrogen To The Jet Ignition Process,” University of Melbourne, PhD Thesis 2008.
14. Toulson, E., Watson, H.C., and Attard, W.P., “The Lean Limit and Emissions at Near-Idle for a Gasoline HAJI System with Alternative Pre-Chamber Fuels,” 2007, doi:10.4271/2007-24-0120.

15. Hashimoto, K., Inaba, O., and Akasaka, Y., "Effects of Fuel Properties on the Combustion and Emission of Direct-Injection Gasoline Engine," 2000, doi:10.4271/2000-01-0253.
16. Kiyota, Y., Akishino, K., and Ando, H., "Concept of Lean Combustion by Barrel-Stratification," 1992, doi:10.4271/920678.
17. Johnson, J. and Den Braven, K.R., "Comparison of Homogeneous, Stratified and High-Squish Stratified Combustion in a Direct-Injected Two-Stroke Engine," 2008, doi:10.4271/2008-32-0030.
18. Johansson, A.N., Hemdal, S., and Dahlander, P., "Experimental Investigation of Soot in a Spray-Guided Single Cylinder GDI Engine Operating in a Stratified Mode," 2013, doi:10.4271/2013-24-0052.
19. Yamamoto, H., "Investigation on Relationship Between Thermal Efficiency and NO_x Formation in Ultra-Lean Combustion," 1999, doi:10.4271/1999-01-3328.
20. Dober, G.G. and Watson, H.C., "Quasi-Dimensional and CFD Modelling of Turbulent and Chemical Flame Enhancement in an Ultra Lean Burn S.I. Engine," 2000, doi:10.4271/2000-01-1263.
21. Kuo, T.-W., "What Causes Slower Flame Propagation in the Lean-Combustion Engine?," *J. Eng. Gas Turbines Power* 112(3):348, 1990, doi:10.1115/1.2906502.
22. Toulson, E., Schock, H.J., and Attard, W.P., "A Review of Pre-Chamber Initiated Jet Ignition Combustion Systems," 2010, doi:10.4271/2010-01-2263.
23. Wolk, B., DeFilippo, A., Chen, J.-Y., Dibble, R., Nishiyama, A., and Ikeda, Y., "Enhancement of flame development by microwave-assisted spark ignition in constant volume combustion chamber," *Combust. Flame* 160(7):1225–1234, 2013, doi:10.1016/j.combustflame.2013.02.004.
24. Starikovskiy, A. and Aleksandrov, N., "Plasma-assisted ignition and combustion," *Prog. Energy Combust. Sci.* 39(1):61–110, 2013, doi:10.1016/j.pecs.2012.05.003.
25. L. A. Gussak and V. P. Karpov, "The application of LAG process in the pre-chamber engines."
26. Attard, W.P. and Blaxill, H., "A Lean Burn Gasoline Fueled Pre-Chamber Jet Ignition Combustion System Achieving High Efficiency and Low NO_x at Part Load," 2012, doi:10.4271/2012-01-1146.
27. Attard, W.P. and Blaxill, H., "A Gasoline Fueled Pre-Chamber Jet Ignition Combustion System at Unthrottled Conditions," *SAE Int. J. Engines* 5(2):315–329, 2012, doi:10.4271/2012-01-0386.

28. Attard, W.P., Kohn, J., and Parsons, P., "Ignition Energy Development for a Spark Initiated Combustion System Capable of High Load, High Efficiency and Near Zero NOx Emissions," *SAE Int. J. Engines* 3(2):481–496, 2010, doi:10.4271/2010-32-0088.
29. Bunce, M. and Blaxill, H., "Sub-200 g/kWh BSFC on a Light Duty Gasoline Engine," 2016, doi:10.4271/2016-01-0709.
30. Hensinger, D.M., Maxson, J.A., Hom, K., and Oppenheim, A.K., "Jet Plume Injection and Combustion," 1992, doi:10.4271/920414.
31. Murase, E., Ono, S., Hanada, K., and Oppenheim, A.K., "Pulsed Combustion Jet Ignition in Lean Mixtures," 1994, doi:10.4271/942048.
32. Maxson, J.A., Hensinger, D.M., Hom, K., and Oppenheim, A.K., "Performance of Multiple Stream Pulsed Jet Combustion Systems," 1991, doi:10.4271/910565.
33. Boretti, A.A. and Watson, H.C., "The Lean Burn Direct-Injection Jet-Ignition Flexi Gas Fuel LPG/CNG Engine," 2009, doi:10.4271/2009-01-2790.
34. Boretti, A.A., "Modelling auto ignition of hydrogen in a jet ignition pre-chamber," *Int. J. Hydrog. Energy* 35(8):3881–3890, 2010, doi:10.1016/j.ijhydene.2010.01.114.
35. Murase, E. and Hanada, K., "Ignition timing control of homogeneous charge compression ignition engines by pulsed flame jets," *Combust. Sci. Technol.* 174(5–6):129–140, 2002, doi:10.1080/713713034.
36. Gentz, G., Thelen, B., Litke, P., Hoke, J., and Toulson, E., "Combustion Visualization, Performance, and CFD Modeling of a Pre-Chamber Turbulent Jet Ignition System in a Rapid Compression Machine," *SAE Int. J. Engines* 8(2):538–546, 2015, doi:10.4271/2015-01-0779.
37. Kyaw, Z.H. and Watson, H.C., "Hydrogen Assisted Jet Ignition For Near Elimination Of No~ And Cyclic Variability In The S.I. Engine," doi:10.4271/2014-01-1217.
38. Toulson, E., Huisjen, A., Chen, X., Squibb, C., Zhu, G., Schock, H., and Attard, W.P., "Visualization of Propane and Natural Gas Spark Ignition and Turbulent Jet Ignition Combustion," *SAE Int. J. Engines* 5(4):1821–1835, 2012, doi:10.4271/2012-32-0002.
39. Wang, Z., Liu, H., and Reitz, R.D., "Knocking combustion in spark-ignition engines," *Prog. Energy Combust. Sci.* 61:78–112, 2017, doi:10.1016/j.pecs.2017.03.004.
40. Griffiths, J.F., Halford-Maw, P.A., and Mohamed, C., "Spontaneous Ignition Delays as a Diagnostic of the Propensity of Alkanes to Cause Engine Knock," doi:10.4271/2014-01-121 .
41. Bates, L. and Bradley, D., "Deflagrative, auto-ignitive, and detonative propagation regimes in engines," *Combust. Flame* 175:118–122, 2017, doi:10.1016/j.combustflame.2016.05.023.

42. Cavina, N., Rojo, N., Ceschini, L., Balducci, E., Poggio, L., Calogero, L., and Cevolani, R., "Investigation of Knock Damage Mechanisms on a GDI TC Engine," 2017, doi:10.4271/2017-24-0060.
43. D. ASTM and 2699, "Standard Test Method for Research Octane Number of Spark-Ignition Engine Fuel," *Am. Soc. Test. Mater. ASTM*, 2013.
44. D. ASTM and 2700, "Standard Test Method for Motor Octane Number of Spark-Ignition Engine Fuel," *Am. Soc. Test. Mater.*, 2014.
45. Amer, A., Babiker, H., Chang, J., Kalghatgi, G., Adomeit, P., Brassat, A., and Günther, M., "Fuel Effects on Knock in a Highly Boosted Direct Injection Spark Ignition Engine," *SAE Int. J. Fuels Lubr.* 5(3):1048–1065, 2012, doi:10.4271/2012-01-1634.
46. Boot, M.D., Tian, M., Hensen, E.J.M., and Mani Sarathy, S., "Impact of fuel molecular structure on auto-ignition behavior – Design rules for future high performance gasolines," *Prog. Energy Combust. Sci.* 60:1–25, 2017, doi:10.1016/j.pecs.2016.12.001.
47. Szybist, J.P. and Splitter, D.A., "Understanding chemistry-specific fuel differences at a constant RON in a boosted SI engine," *Fuel* 217:370–381, 2018, doi:10.1016/j.fuel.2017.12.100.
48. Ji, W., Zhao, P., He, T., He, X., Farooq, A., and Law, C.K., "On the controlling mechanism of the upper turnover states in the NTC regime," *Combust. Flame* 164:294–302, 2016, doi:10.1016/j.combustflame.2015.11.028.
49. Greenspan, J., "Chemical Kinetics and Chain Reactions (Semenoff, N.)," *J. Chem. Educ.* 12(6):298, 1935, doi:10.1021/ed012p298.3.
50. Turns, S.R., "An Introduction to Combustion: Concepts and Applications," 3rd ed., McGraw-Hill Companies.
51. CURRAN, H.J., GAFFURI, P., PITZ, W.J., and WESTBROOK, C.K., "A Comprehensive Modeling Study of n-Heptane Oxidation," 29.
52. Kukkadapu, G., Kumar, K., Sung, C.-J., Mehl, M., and Pitz, W.J., "Autoignition of gasoline surrogates at low temperature combustion conditions," *Combust. Flame* 162(5):2272–2285, 2015, doi:10.1016/j.combustflame.2015.01.025.
53. Atef, N., Kukkadapu, G., Mohamed, S.Y., Rashidi, M.A., Banyon, C., Mehl, M., Heufer, K.A., Nasir, E.F., Alfazazi, A., Das, A.K., Westbrook, C.K., Pitz, W.J., Lu, T., Farooq, A., Sung, C.-J., Curran, H.J., and Sarathy, S.M., "A comprehensive iso-octane combustion model with improved thermochemistry and chemical kinetics," *Combust. Flame* 178:111–134, 2017, doi:10.1016/j.combustflame.2016.12.029.
54. Curran, H., "A comprehensive modeling study of iso-octane oxidation," *Combust. Flame* 129(3):253–280, 2002, doi:10.1016/S0010-2180(01)00373-X.

55. Nakagome, K., Shimazaki, N., Niimura, K., and Kobayashi, S., "Combustion and Emission Characteristics of Premixed Lean Diesel Combustion Engine," 1997, doi:10.4271/970898.
56. Kukkadapu, G., Kumar, K., Sung, C.-J., Mehl, M., and Pitz, W.J., "Experimental and surrogate modeling study of gasoline ignition in a rapid compression machine," *Combust. Flame* 159(10):3066–3078, 2012, doi:10.1016/j.combustflame.2012.05.008.
57. Liang, W. and Law, C.K., "Theory of first-stage ignition delay in hydrocarbon NTC chemistry," *Combust. Flame* 188:162–169, 2018, doi:10.1016/j.combustflame.2017.10.003.
58. Westbrook, C.K., Mehl, M., Pitz, W.J., and Sjöberg, M., "Chemical kinetics of octane sensitivity in a spark-ignition engine," *Combust. Flame* 175:2–15, 2017, doi:10.1016/j.combustflame.2016.05.022.
59. Mittal, V., Heywood, J.B., and Green, W.H., "The Underlying Physics and Chemistry behind Fuel Sensitivity," *SAE Int. J. Fuels Lubr.* 3(1):256–265, 2010, doi:10.4271/2010-01-0617.
60. Singh, E., Badra, J., Mehl, M., and Sarathy, S.M., "Chemical Kinetic Insights into the Octane Number and Octane Sensitivity of Gasoline Surrogate Mixtures," *Energy Fuels* 31(2):1945–1960, 2017, doi:10.1021/acs.energyfuels.6b02659.
61. Badra, J.A., Bokhumseen, N., Mulla, N., Sarathy, S.M., Farooq, A., Kalghatgi, G., and Gaillard, P., "A methodology to relate octane numbers of binary and ternary n-heptane, iso-octane and toluene mixtures with simulated ignition delay times," *Fuel* 160:458–469, 2015, doi:10.1016/j.fuel.2015.08.007.
62. Grandin, B., Ångström, H.-E., Stålhammar, P., and Olofsson, E., "Knock Suppression in a Turbocharged SI Engine by Using Cooled EGR," 1998, doi:10.4271/982476.
63. Li, T., Yin, T., and Wang, B., "Anatomy of the cooled EGR effects on soot emission reduction in boosted spark-ignited direct-injection engines," *Appl. Energy* 190:43–56, 2017, doi:10.1016/j.apenergy.2016.12.105.
64. Shen, K., Li, F., Zhang, Z., Sun, Y., and Yin, C., "Effects of LP and HP cooled EGR on performance and emissions in turbocharged GDI engine," *Appl. Therm. Eng.* 125:746–755, 2017, doi:10.1016/j.applthermaleng.2017.07.064.
65. Toulson, E., Watson, H.C., and Attard, W.P., "The Effects of Hot and Cool EGR with Hydrogen Assisted Jet Ignition," 2007, doi:10.4271/2007-01-3627.
66. Cairns, A., Blaxill, H., and Irlam, G., "Exhaust Gas Recirculation for Improved Part and Full Load Fuel Economy in a Turbocharged Gasoline Engine," 2006, doi:10.4271/2006-01-0047.
67. Grandin, B. and Ångström, H.-E., "Replacing Fuel Enrichment in a Turbo Charged SI Engine: Lean Burn or Cooled EGR," 1999, doi:10.4271/1999-01-3505.

68. U.S Department of Energy, “Alternative Fuels Data Center – Natural Gas Vehicle” <https://www.afdc.energy.gov>.
69. U.S. Energy Information Administration, “How much natural gas does the United States have, and how long will it last?,” <https://www.eia.gov>.
70. Schlatter, S., Schneider, B., Wright, Y.M., and Boulouchos, K., “Comparative Study of Ignition Systems for Lean Burn Gas Engines in an Optically Accessible Rapid Compression Expansion Machine,” 2013, doi:10.4271/2013-24-0112.
71. Burke, U., Somers, K.P., O’Toole, P., Zinner, C.M., Marquet, N., Bourque, G., Petersen, E.L., Metcalfe, W.K., Serinyel, Z., and Curran, H.J., “An ignition delay and kinetic modeling study of methane, dimethyl ether, and their mixtures at high pressures,” *Combust. Flame* 162(2):315–330, 2015, doi:10.1016/j.combustflame.2014.08.014.
72. Yu, Y., Vanhove, G., Griffiths, J.F., De Ferrières, S., and Pauwels, J.-F., “Influence of EGR and Syngas Components on the Autoignition of Natural Gas in a Rapid Compression Machine: A Detailed Experimental Study,” *Energy Fuels* 27(7):3988–3996, 2013, doi:10.1021/ef400336x.
73. Heyne, S., Roubaud, A., Ribaucour, M., Vanhove, G., Minetti, R., and Favrat, D., “Development of a natural gas reaction mechanism for engine simulations based on rapid compression machine experiments using a multi-objective optimisation strategy,” *Fuel* 87(13–14):3046–3054, 2008, doi:10.1016/j.fuel.2008.04.004.
74. Healy, D., Curran, H.J., Simmie, J.M., Kalitan, D.M., Zinner, C.M., Barrett, A.B., Petersen, E.L., and Bourque, G., “Methane/ethane/propane mixture oxidation at high pressures and at high, intermediate and low temperatures,” *Combust. Flame* 155(3):441–448, 2008, doi:10.1016/j.combustflame.2008.07.003.
75. Healy, D., Kopp, M.M., Polley, N.L., Petersen, E.L., Bourque, G., and Curran, H.J., “Methane/ *n* -Butane Ignition Delay Measurements at High Pressure and Detailed Chemical Kinetic Simulations,” *Energy Fuels* 24(3):1617–1627, 2010, doi:10.1021/ef901292j.
76. Mehl, M., Faravelli, T., Giavazzi, F., Ranzi, E., Scorletti, P., Tardani, A., and Terna, D., “Detailed Chemistry Promotes Understanding of Octane Numbers and Gasoline Sensitivity,” *Energy Fuels* 20(6):2391–2398, 2006, doi:10.1021/ef060339s.
77. Sarathy, S.M., Javed, T., Karsenty, F., Heufer, A., Wang, W., Park, S., Elwardany, A., Farooq, A., Westbrook, C.K., Pitz, W.J., Oehlschlaeger, M.A., Dayma, G., Curran, H.J., and Dagaut, P., “A comprehensive combustion chemistry study of 2,5-dimethylhexane,” *Combust. Flame* 161(6):1444–1459, 2014, doi:10.1016/j.combustflame.2013.12.010.
78. Westbrook, C.K., Sjöberg, M., and Cernansky, N.P., “A new chemical kinetic method of determining RON and MON values for single component and multicomponent mixtures of engine fuels,” *Combust. Flame* 195:50–62, 2018, doi:10.1016/j.combustflame.2018.03.038.

79. Allen, C., Valco, D., Toulson, E., Edwards, T., and Lee, T., "Ignition behavior and surrogate modeling of JP-8 and of camelina and tallow hydrotreated renewable jet fuels at low temperatures," *Combust. Flame* 160(2):232–239, 2013, doi:10.1016/j.combustflame.2012.10.008.
80. Allen, C., Toulson, E., Edwards, T., and Lee, T., "Application of a novel charge preparation approach to testing the autoignition characteristics of JP-8 and camelina hydroprocessed renewable jet fuel in a rapid compression machine," *Combust. Flame* 159(9):2780–2788, 2012, doi:10.1016/j.combustflame.2012.03.019.
81. Gentz, G., Gholamisheeri, M., and Toulson, E., "A study of a turbulent jet ignition system fueled with iso-octane: Pressure trace analysis and combustion visualization," *Appl. Energy* 189:385–394, 2017, doi:10.1016/j.apenergy.2016.12.055.
82. Gholamisheeri, M., Thelen, B., Gentz, G., and Toulson, E., "CFD Modeling of an Auxiliary Fueled Turbulent Jet Ignition System in a Rapid Compression Machine," 2016, doi:10.4271/2016-01-0599.
83. Johansson, B. and Olsson, K., "Combustion Chambers for Natural Gas SI Engines Part I: Fluid Flow and Combustion," 1995, doi:10.4271/950469.
84. Cho, H.M. and He, B.-Q., "Spark ignition natural gas engines—A review," *Energy Convers. Manag.* 48(2):608–618, 2007, doi:10.1016/j.enconman.2006.05.023.
85. Einewall, P., Tunestål, P., and Johansson, B., "Lean Burn Natural Gas Operation vs. Stoichiometric Operation with EGR and a Three Way Catalyst," 2005, doi:10.4271/2005-01-0250.
86. Loudon, Marc., *Organic Chemistry*, 5th edition. ISBN-13: 978- 0981519432.
87. Attard, W.P. and Blaxill, H., "A Single Fuel Pre-Chamber Jet Ignition Powertrain Achieving High Load, High Efficiency and Near Zero NO_x Emissions," *SAE Int J Engines* 5(3):734–746, 2011, doi:10.4271/2011-01-2023.
88. Bunce, M., Blaxill, H., Kulatilaka, W., and Jiang, N., "The Effects of Turbulent Jet Characteristics on Engine Performance Using a Pre-Chamber Combustor," 2014, doi:10.4271/2014-01-1195.
89. Noguchi, N., Sanda, S. and Nakamura, N., "Development of Toyota Lean Burn Engine," *SAE Tech. Pap.* 760757, 1976, doi:10.4271/760757.
90. Date, T. and Yagi, S., "Research and Development of Honda CVCC Engine," 1974, doi:10.4271/740605.
91. Boston, P.M., Bradley, D., Lung, F.K.-K., Vince, I.M., and Weinberg, F.J., "Flame initiation in lean, quiescent and turbulent mixtures with various igniters," *Symp. Int. Combust.* 20(1):141–149, 1985, doi:10.1016/S0082-0784(85)80497-5.

92. Couet, S., Higelin, P., and Moreau, B., "APIR: A New Firing Concept for the Internal Combustion Engines - sensitivity to knock and in-cylinder aerodynamics," 2001, doi:10.4271/2001-01-1954.
93. http://www.me.berkeley.edu/gri_mech/.
94. Gholamisheeri, M., Thelen, B., and Toulson, E., "CFD Modeling and Experimental Analysis of a Homogeneously Charged Turbulent Jet Ignition System in a Rapid Compression Machine," 2017, doi:10.4271/2017-01-0557.
95. Reddy, H. and Abraham, J., "A numerical study of vortex interactions with flames developing from ignition kernels in lean methane/air mixtures," *Combust. Flame* 158(3):401–415, 2011, doi:10.1016/j.combustflame.2010.09.008.
96. Reddy, H. and Abraham, J., "Influence of turbulence–kernel interactions on flame development in lean methane/air mixtures under natural gas-fueled engine conditions," *Fuel* 103:1090–1105, 2013, doi:10.1016/j.fuel.2012.07.074.
97. Baumgartner, L.S., Wohlgemuth, S., Zirngibl, S., and Wachtmeister, G., "Investigation of a Methane Scavenged Prechamber for Increased Efficiency of a Lean-Burn Natural Gas Engine for Automotive Applications," *SAE Int J Engines* 8(2):921–933, 2015, doi:10.4271/2015-01-0866.
98. Yamanaka, K., Shiraga, Y., and Nakai, S., "Development of Pre-chamber Sparkplug for Gas Engine," 2011, doi:10.4271/2011-01-1870.
99. Roethlisberger, R.P. and Favrat, D., "Investigation of the prechamber geometrical configuration of a natural gas spark ignition engine for cogeneration: part I. Numerical simulation," *Int. J. Therm. Sci.* 42(3):223–237, 2003, doi:10.1016/S1290-0729(02)00023-6.
100. Shah, A., Tunestal, P., and Johansson, B., "Investigation of Performance and Emission Characteristics of a Heavy Duty Natural Gas Engine Operated with Pre-Chamber Spark Plug and Dilution with Excess Air and EGR," *SAE Int. J. Engines* 5(4):1790–1801, 2012, doi:10.4271/2012-01-1980.
101. Gentz, G., Thelen, B., Gholamisheeri, M., Litke, P., Brown, A., Hoke, J., and Toulson, E., "A study of the influence of orifice diameter on a turbulent jet ignition system through combustion visualization and performance characterization in a rapid compression machine," *Appl. Therm. Eng.* 81:399–411, 2015, doi:10.1016/j.applthermaleng.2015.02.026.
102. Gussak, L.A., Turkish, M.C., and Siegl, D.C., "High Chemical Activity of Incomplete Combustion Products and a Method of Prechamber Torch Ignition for Avalanche Activation of Combustion in Internal Combustion Engines," *SAE Automobile Engineering and Manufacturing Meeting*, SAE International, 1975, doi:https://doi.org/10.4271/750890.
103. Alvarez, C.E.C., Couto, G.E., Roso, V.R., Thiriet, A.B., and Valle, R.M., "A review of prechamber ignition systems as lean combustion technology for SI engines," *Appl. Therm. Eng.* 128:107–120, 2018, doi:10.1016/j.applthermaleng.2017.08.118.

104. Karimi, A., Rajagopal, M., and Nalim, R., "Traversing Hot-Jet Ignition in a Constant-Volume Combustor," *J. Eng. Gas Turbines Power* 136(4):041506, 2013, doi:10.1115/1.4025659.
105. Wolfhard, H.G., "The Ignition of Combustible Mixtures by Hot Gases," *J. Jet Propuls.* 28(12):798–804, 1958, doi:10.2514/8.7472.
106. Kammerstätter, S., Bauer, S., and Sattelmayer, T., "Jet-Penetration in Prechamber-Ignited Lean Large-Bore Natural Gas Engines," 23–33, 2012, doi:10.1115/ICEF2012-92031.
107. Mastorakos, E., Allison, P., Giusti, A., De Oliveira, P., Benekos, S., Wright, Y., Frouzakis, C., and Boulouchos, K., "Fundamental Aspects of Jet Ignition for Natural Gas Engines," *SAE Int. J. Engines* 10(5), 2017, doi:10.4271/2017-24-0097.
108. Kawabata, Y. and Mori, D., "Combustion Diagnostics & Improvement of a Prechamber Lean-Burn Natural Gas Engine," 2004, doi:10.4271/2004-01-0979.
109. Olsen, D.B. and Lisowski, J.M., "Prechamber NO_x formation in low BMEP 2-stroke cycle natural gas engines," *Appl. Therm. Eng.* 29(4):687–694, 2009, doi:10.1016/j.applthermaleng.2008.03.049.
110. Simpson, D.J. and Olsen, D.B., "Precombustion Chamber Design for Emissions Reduction From Large Bore NG Engines," *J. Eng. Gas Turbines Power* 132(12):122802–122802–7, 2010, doi:10.1115/1.4001293.
111. Duong, J., Wellander, R., Hyvönen, J., Andersson, Ö., Richter, M., Johansson, B., and Ålden, M., "High Speed Combustion Imaging in a Large Bore Gas Engine: The Relationship Between Pre- and Main Chamber Heat Release," (56345):V08AT09A022, 2013, doi:10.1115/IMECE2013-64286.
112. Shah, A., Tunestal, P., and Johansson, B., "Effect of Pre-Chamber Volume and Nozzle Diameter on Pre-Chamber Ignition in Heavy Duty Natural Gas Engines," SAE International, 2015, doi:10.4271/2015-01-0867.
113. Attard, W.P., Toulson, E., Huisjen, A., Chen, X., Zhu, G., and Schock, H., "Spark Ignition and Pre-Chamber Turbulent Jet Ignition Combustion Visualization," 2012, doi:10.4271/2012-01-0823.
114. Gentz, G.R. and Toulson, E., "Experimental Studies of a Liquid Propane Auxiliary Fueled Turbulent Jet Igniter in a Rapid Compression Machine," *SAE Int J Engines* 9(2):777–785, 2016, doi:10.4271/2016-01-0708.
115. Chinnathambi, P., Bunce, M., and Cruft, L., "RANS Based Multidimensional Modeling of an Ultra-Lean Burn Pre-Chamber Combustion System with Auxiliary Liquid Gasoline Injection," 2015, doi:10.4271/2015-01-0386.
116. Thelen, B.C. and Toulson, E., "A computational study on the effect of the orifice size on the performance of a turbulent jet ignition system," *Proc. Inst. Mech. Eng. Part J. Automob. Eng.* 231(4):536–554, 2016, doi:10.1177/0954407016659199.

117. Maxson, J.A., Hensinger, D.M., Hom, K., and Oppenheim, A.K., "Performance of Multiple Stream Pulsed Jet Combustion Systems," 1991, doi:10.4271/910565.
118. Assanis, D., Engineer, N., Neuman, P., and Wooldridge, M., "Computational Development of a Dual Pre-Chamber Engine Concept for Lean Burn Combustion," SAE International, 2016, doi:10.4271/2016-01-2242.
119. Shiga, S., Ozone, S., Machacon, H.T.C., Karasawa, T., Nakamura, H., Ueda, T., Jingu, N., Huang, Z., Tsue, M., and Kono, M., "A study of the combustion and emission characteristics of compressed-natural-gas direct-injection stratified combustion using a rapid-compression-machine," *Combust. Flame* 129(1):1–10, 2002, doi:10.1016/S0010-2180(01)00367-4.
120. Gentz, G., Gholamisheeri, M., and Toulson, E., "A study of a turbulent jet ignition system fueled with iso-octane: Pressure trace analysis and combustion visualization," *Appl. Energy* 189:385–394, 2017, doi:10.1016/j.apenergy.2016.12.055.
121. ImageJ, <https://imagej.nih.gov/ij/>, Nov. 2018.
122. Attard, W.P. and Blaxill, H., "A Single Fuel Pre-Chamber Jet Ignition Powertrain Achieving High Load, High Efficiency and Near Zero NOx Emissions," *SAE Int J Engines* 5(3):734–746, 2011, doi:10.4271/2011-01-2023.
123. Chinnathambi, P., Bunce, M., and Cruft, L., "RANS Based Multidimensional Modeling of an Ultra-Lean Burn Pre-Chamber Combustion System with Auxiliary Liquid Gasoline Injection," 2015, doi:10.4271/2015-01-0386.
124. Mastorakos, E., Allison, P., Giusti, A., De Oliveira, P., Benekos, S., Wright, Y., Frouzakis, C., and Boulouchos, K., "Fundamental Aspects of Jet Ignition for Natural Gas Engines," *SAE Int. J. Engines* 10(5), 2017, doi:10.4271/2017-24-0097.
125. Allison, P.M., Oliveira, M. de, Giusti, A., and Mastorakos, E., "Pre-chamber ignition mechanism: Experiments and simulations on turbulent jet flame structure," *Fuel* 230:274–281, 2018, doi:10.1016/j.fuel.2018.05.005.
126. Kammerstätter, S., Bauer, S., and Sattelmayer, T., "Jet-Penetration in Prechamber-Ignited Lean Large-Bore Natural Gas Engines," *ASME 2012 Internal Combustion Engine Division Fall Technical Conference*, ASME, Vancouver, BC, Canada, ISBN 978-0-7918-5509-6: 23, 2012, doi:10.1115/ICEF2012-92031.
127. Biswas, S. and Qiao, L., "Ignition of ultra-lean premixed H₂/air using multiple hot turbulent jets generated by pre-chamber combustion," *Appl. Therm. Eng.* 132:102–114, 2018, doi:10.1016/j.applthermaleng.2017.11.073.
128. Biswas, S., Tanvir, S., Wang, H., and Qiao, L., "On ignition mechanisms of premixed CH₄ /air and H₂ /air using a hot turbulent jet generated by pre-chamber combustion," *Appl. Therm. Eng.* 106:925–937, 2016, doi:10.1016/j.applthermaleng.2016.06.070.

129. Thelen, B.C. and Toulson, E., “A computational study on the effect of the orifice size on the performance of a turbulent jet ignition system,” *Proc. Inst. Mech. Eng. Part J. Automob. Eng.* 231(4):536–554, 2016, doi:10.1177/0954407016659199.
130. Gholamisheeri, M., Thelen, B.C., Gentz, G.R., Wichman, I.S., and Toulson, E., “Rapid compression machine study of a premixed, variable inlet density and flow rate, confined turbulent jet,” *Combust. Flame* 169:321–332, 2016, doi:10.1016/j.combustflame.2016.05.001.
131. ImageJ, <https://imagej.nih.gov/ij/>, 2018.
132. Pomraning, E., Richards, K., and Senecal, P.K., “Modeling Turbulent Combustion Using a RANS Model, Detailed Chemistry, and Adaptive Mesh Refinement,” 2014, doi:10.4271/2014-01-1116.
133. Anderson, E.K., Attard, W.P., Brown, A., Litke, P., Grinstead, K., and Hoke, J., “Experimental Study of a Pre-Chamber Jet Igniter in a Turbocharged Rotax 914 Aircraft Engine,” 2013, doi:10.4271/2013-01-1629.
134. Benim, A.C. and Syed, K.J., “Chapter 7 - Flashback Due to Turbulent Flame Propagation in the Core Flow,” in: Benim, A. C. and Syed, K. J., eds., *Flashback Mechanisms in Lean Premixed Gas Turbine Combustion*, Academic Press, Boston, ISBN 978-0-12-800755-6: 45–57, 2015, doi:10.1016/B978-0-12-800755-6.00007-6.
135. Gentz, G.R. and Toulson, E., “Experimental Studies of a Liquid Propane Auxiliary Fueled Turbulent Jet Igniter in a Rapid Compression Machine,” *SAE Int J Engines* 9(2):777–785, 2016, doi:10.4271/2016-01-0708.
136. Gentz, G., Thelen, B., Gholamisheeri, M., Litke, P., Brown, A., Hoke, J., and Toulson, E., “A study of the influence of orifice diameter on a turbulent jet ignition system through combustion visualization and performance characterization in a rapid compression machine,” *Appl. Therm. Eng.* 81:399–411, 2015, doi:10.1016/j.applthermaleng.2015.02.026.
137. Hamori, F. and Eng, B., “Exploring the Limits of Hydrogen Assisted Jet Ignition,” 419.
138. Bunce, M.P., Chinnathambi, P., and Blaxill, H.R., “The Effects of Pre-Chamber-Initiated Lean- Burn Combustion on Engine Efficiency and Emissions,” 19.
139. Donohoe, N., Heufer, A., Metcalfe, W.K., Curran, H.J., Davis, M.L., Mathieu, O., Plichta, D., Morones, A., Petersen, E.L., and Güthe, F., “Ignition delay times, laminar flame speeds, and mechanism validation for natural gas/hydrogen blends at elevated pressures,” *Combust. Flame* 161(6):1432–1443, 2014, doi:10.1016/j.combustflame.2013.12.005.
140. Bunce, M.P., Blaxill, H.R., and Gurney, D.C., “Design and Development of a Jet Ignition Engine for Stable Ultra-Lean Operation,” 22.
141. Chinnathambi, P., Bunce, M., and Cruft, L., “RANS Based Multidimensional Modeling of an Ultra-Lean Burn Pre-Chamber Combustion System with Auxiliary Liquid Gasoline Injection,” 2015, doi:10.4271/2015-01-0386.

142. Tingas, E.A., Im, H.G., Kyritsis, D.C., and Goussis, D.A., "The use of CO₂ as an additive for ignition delay and pollutant control in CH₄/air autoignition," *Fuel* 211:898–905, 2018, doi:10.1016/j.fuel.2017.09.022.
143. Quader, A.A., "Why Intake Charge Dilution Decreases Nitric Oxide Emission from Spark Ignition Engines," *SAE Trans.* 80:20–30, 1971.
144. Kumano, K. and Yamaoka, S., "Analysis of Knocking Suppression Effect of Cooled EGR in Turbo-Charged Gasoline Engine," 2014, doi:10.4271/2014-01-1217.
145. Grandin, B., Ångström, H.-E., Stålhammar, P., and Olofsson, E., "Knock Suppression in a Turbocharged SI Engine by Using Cooled EGR," 1998, doi:10.4271/982476.
146. Grandin, B. and Ångström, H.-E., "Replacing Fuel Enrichment in a Turbo Charged SI Engine: Lean Burn or Cooled EGR," 1999, doi:10.4271/1999-01-3505.
147. Hwang, K., Hwang, I., Lee, H., Park, H., Choi, H., Lee, K., Kim, W., Kim, H., Han, B., Lee, J., Shin, B., and Chae, D., "Development of New High-Efficiency Kappa 1.6L GDI Engine," 2016, doi:10.4271/2016-01-0667.
148. Matsuo, S., Ikeda, E., Ito, Y., and Nishiura, H., "The New Toyota Inline 4 Cylinder 1.8L ESTEC 2ZR-FXE Gasoline Engine for Hybrid Car," 2016, doi:10.4271/2016-01-0684.
149. Vanhove, G., Petit, G., and Minetti, R., "Experimental study of the kinetic interactions in the low-temperature autoignition of hydrocarbon binary mixtures and a surrogate fuel," *Combust. Flame* 145(3):521–532, 2006, doi:10.1016/j.combustflame.2006.01.001.
150. Davidson, D.F., Gauthier, B.M., and Hanson, R.K., "Shock tube ignition measurements of iso-octane/air and toluene/air at high pressures," *Proc. Combust. Inst.* 30(1):1175–1182, 2005, doi:10.1016/j.proci.2004.08.004.
151. Di, H., He, X., Zhang, P., Wang, Z., Wooldridge, M.S., Law, C.K., Wang, C., Shuai, S., and Wang, J., "Effects of buffer gas composition on low temperature ignition of iso-octane and n-heptane," *Combust. Flame* 161(10):2531–2538, 2014, doi:10.1016/j.combustflame.2014.04.014.
152. He, X., Donovan, M.T., Zigler, B.T., Palmer, T.R., Walton, S.M., Wooldridge, M.S., and Atreya, A., "An experimental and modeling study of iso-octane ignition delay times under homogeneous charge compression ignition conditions," *Combust. Flame* 142(3):266–275, 2005, doi:10.1016/j.combustflame.2005.02.014.
153. GRIFFITHS, J.F., HALFORD-MAW, P.A., and ROSE, D.J., "Fundamental Features of Hydrocarbon Autoignition in a Rapid Compression Machine," 16.
154. Mittal, G. and Bhari, A., "A rapid compression machine with crevice containment," *Combust. Flame* 160(12):2975–2981, 2013, doi:10.1016/j.combustflame.2013.06.027.

155. Walton, S., He, X., Zigler, B., Wooldridge, M., and Atreya, A., "An experimental investigation of iso-octane ignition phenomena," *Combust. Flame* 150(3):246–262, 2007, doi:10.1016/j.combustflame.2006.07.016.
156. Mehl, M., Pitz, W.J., Westbrook, C.K., and Curran, H.J., "Kinetic modeling of gasoline surrogate components and mixtures under engine conditions," *Proc. Combust. Inst.* 33(1):193–200, 2011, doi:10.1016/j.proci.2010.05.027.
157. Goldsborough, S.S., Hochgreb, S., Vanhove, G., Wooldridge, M.S., Curran, H.J., and Sung, C.-J., "Advances in rapid compression machine studies of low- and intermediate-temperature autoignition phenomena," *Prog. Energy Combust. Sci.* 63:1–78, 2017, doi:10.1016/j.pecs.2017.05.002.
158. Healy, D., Curran, H.J., Simmie, J.M., Kalitan, D.M., Zinner, C.M., Barrett, A.B., Petersen, E.L., and Bourque, G., "Methane/ethane/propane mixture oxidation at high pressures and at high, intermediate and low temperatures," *Combust. Flame* 155(3):441–448, 2008, doi:10.1016/j.combustflame.2008.07.003.
159. Ladommatos, N., Abdelhalim, S.M., Zhao, H., and Hu, Z., "The Dilution, Chemical, and Thermal Effects of Exhaust Gas Recirculation on Diesel Engine Emissions - Part 4: Effects of Carbon Dioxide and Water Vapour," 21.
160. Gallagher, S.M., Curran, H.J., Metcalfe, W.K., Healy, D., Simmie, J.M., and Bourque, G., "A rapid compression machine study of the oxidation of propane in the negative temperature coefficient regime," *Combust. Flame* 153(1–2):316–333, 2008, doi:10.1016/j.combustflame.2007.09.004.
161. Chen, Z., Zhang, P., Yang, Y., Brear, M.J., He, X., and Wang, Z., "Impact of nitric oxide (NO) on n-heptane autoignition in a rapid compression machine," *Combust. Flame* 186:94–104, 2017, doi:10.1016/j.combustflame.2017.07.036.
162. Mittal, G., Raju, M.P., and Bhari, A., "A numerical assessment of the novel concept of crevice containment in a rapid compression machine," *Combust. Flame* 158(12):2420–2427, 2011, doi:10.1016/j.combustflame.2011.04.013.
163. Dec, J.E., Yang, Y., and Dronniou, N., "Boosted HCCI - Controlling Pressure-Rise Rates for Performance Improvements using Partial Fuel Stratification with Conventional Gasoline," *SAE Int. J. Engines* 4(1):1169–1189, 2011, doi:10.4271/2011-01-0897.
164. Allen, C., Toulson, E., Edwards, T., and Lee, T., "Application of a novel charge preparation approach to testing the autoignition characteristics of JP-8 and camelina hydroprocessed renewable jet fuel in a rapid compression machine," *Combust. Flame* 159(9):2780–2788, 2012, doi:10.1016/j.combustflame.2012.03.019.
165. Toulson, E., Schock, H.J., and Attard, W.P., "A Review of Pre-Chamber Initiated Jet Ignition Combustion Systems," 2010, doi:10.4271/2010-01-2263.

166. GRIFFITHS, J.F., HALFORD-MAW, P.A., and ROSE, D.J., "Fundamental Features of Hydrocarbon Autoignition in a Rapid Compression Machine," 16.
167. Tingas, E.A., Im, H.G., Kyritsis, D.C., and Goussis, D.A., "The use of CO₂ as an additive for ignition delay and pollutant control in CH₄/air autoignition," *Fuel* 211:898–905, 2018, doi:10.1016/j.fuel.2017.09.022.
168. Gauthier, B.M., Davidson, D.F., and Hanson, R.K., "Shock tube determination of ignition delay times in full-blend and surrogate fuel mixtures," *Combust. Flame* 139(4):300–311, 2004, doi:10.1016/j.combustflame.2004.08.015.
169. Javed, T., Ahmed, A., Lovisotto, L., Issayev, G., Badra, J., Sarathy, S.M., and Farooq, A., "Ignition studies of two low-octane gasolines," *Combust. Flame* 185:152–159, 2017, doi:10.1016/j.combustflame.2017.07.006.
170. Javed, T., Lee, C., AlAbbad, M., Djebbi, K., Beshir, M., Badra, J., Curran, H., and Farooq, A., "Ignition studies of n-heptane/iso-octane/toluene blends," *Combust. Flame* 171:223–233, 2016, doi:10.1016/j.combustflame.2016.06.008.
171. Lee, C., Ahmed, A., Nasir, E.F., Badra, J., Kalghatgi, G., Sarathy, S.M., Curran, H., and Farooq, A., "Autoignition characteristics of oxygenated gasolines," *Combust. Flame* 186:114–128, 2017, doi:10.1016/j.combustflame.2017.07.034.
172. Kukkadapu, G., Kumar, K., Sung, C.-J., Mehl, M., and Pitz, W.J., "Experimental and surrogate modeling study of gasoline ignition in a rapid compression machine," *Combust. Flame* 159(10):3066–3078, 2012, doi:10.1016/j.combustflame.2012.05.008.
173. Lee, C., Ahmed, A., Nasir, E.F., Badra, J., Kalghatgi, G., Sarathy, S.M., Curran, H., and Farooq, A., "Autoignition characteristics of oxygenated gasolines," *Combust. Flame* 186:114–128, 2017, doi:10.1016/j.combustflame.2017.07.034.
174. Chung, J., Lee, S., An, H., Song, S., and Chun, K.M., "Rapid-compression machine studies on two-stage ignition characteristics of hydrocarbon autoignition and an investigation of new gasoline surrogates," *Energy* 93:1505–1514, 2015, doi:10.1016/j.energy.2015.09.077.
175. Xie, Y., Wang, J., Zhang, M., Gong, J., Jin, W., and Huang, Z., "Experimental and Numerical Study on Laminar Flame Characteristics of Methane Oxy-fuel Mixtures Highly Diluted with CO₂," *Energy Fuels* 27(10):6231–6237, 2013, doi:10.1021/ef401220h.
176. Somers, K.P., Simmie, J.M., Gillespie, F., Burke, U., Connolly, J., Metcalfe, W.K., Battin-Leclerc, F., Dirrenberger, P., Herbinet, O., Glaude, P.-A., and Curran, H.J., "A high temperature and atmospheric pressure experimental and detailed chemical kinetic modelling study of 2-methyl furan oxidation," *Proc. Combust. Inst.* 34(1):225–232, 2013, doi:10.1016/j.proci.2012.06.113.
177. Chinnathambi, P., Wadkar, C., and Toulson, E., "Impact of CO₂ dilution on ignition delay times of iso-octane at 15% and 30% dilution levels in a rapid compression machine."

178. Javed, T., Lee, C., AlAbbad, M., Djebbi, K., Beshir, M., Badra, J., Curran, H., and Farooq, A., "Ignition studies of n -heptane/ iso -octane/toluene blends," *Combust. Flame* 171:223–233, 2016, doi:10.1016/j.combustflame.2016.06.008.
179. Zádor, J., Taatjes, C.A., and Fernandes, R.X., "Kinetics of elementary reactions in low-temperature autoignition chemistry," *Prog. Energy Combust. Sci.* 37(4):371–421, 2011, doi:10.1016/j.pecs.2010.06.006.
180. Leppard, W.R., "The Chemical Origin of Fuel Octane Sensitivity," 1990, doi:10.4271/902137.
181. Sarathy, S.M., Kukkadapu, G., Mehl, M., Wang, W., Javed, T., Park, S., Oehlschlaeger, M.A., Farooq, A., Pitz, W.J., and Sung, C.-J., "Ignition of alkane-rich FACE gasoline fuels and their surrogate mixtures," *Proc. Combust. Inst.* 35(1):249–257, 2015, doi:10.1016/j.proci.2014.05.122.
182. Chinnathambi, P., Thelen, B., Naylor, M., Cook, D., and Toulson, E., "Performance Assessment of a Single Jet, Dual Diverging Jets, and Dual Converging Jets in an Auxiliary Fueled Turbulent Jet Ignition System," 2018, doi:10.4271/2018-01-1135.
183. Kukkadapu, G., Kumar, K., Sung, C.-J., Mehl, M., and Pitz, W.J., "Autoignition of gasoline and its surrogates in a rapid compression machine," *Proc. Combust. Inst.* 34(1):345–352, 2013, doi:10.1016/j.proci.2012.06.135.
184. Won, S.H., Haas, F.M., Dooley, S., Edwards, T., and Dryer, F.L., "Reconstruction of chemical structure of real fuel by surrogate formulation based upon combustion property targets," *Combust. Flame* 183:39–49, 2017, doi:10.1016/j.combustflame.2017.04.032.
185. Kuwahara, K., Tada, T., Furutani, M., Sakai, Y., and Ando, H., "Chemical Kinetics Study on Two-Stage Main Heat Release in Ignition Process of Highly Diluted Mixtures," *SAE Int. J. Engines* 6(1):520–532, 2013, doi:10.4271/2013-01-1657.
186. Knop, V., Loos, M., Pera, C., and Jeuland, N., "A linear-by-mole blending rule for octane numbers of n-heptane/iso-octane/toluene mixtures," *Fuel* 115:666–673, 2014, doi:10.1016/j.fuel.2013.07.093.
187. Morgan, N., Smallbone, A., Bhave, A., Kraft, M., Cracknell, R., and Kalghatgi, G., "Mapping surrogate gasoline compositions into RON/MON space," *Combust. Flame* 157(6):1122–1131, 2010, doi:10.1016/j.combustflame.2010.02.003.
188. Andrae, J.C.G., "Development of a detailed kinetic model for gasoline surrogate fuels," *Fuel* 87(10):2013–2022, 2008, doi:10.1016/j.fuel.2007.09.010.
189. Kalghatgi, G., Babiker, H., and Badra, J., "A Simple Method to Predict Knock Using Toluene, N-Heptane and Iso-Octane Blends (TPRF) as Gasoline Surrogates," *SAE Int. J. Engines* 8(2):505–519, 2015, doi:10.4271/2015-01-0757.

190. Naser, N., Sarathy, S.M., and Chung, S.H., “Estimating fuel octane numbers from homogeneous gas-phase ignition delay times,” *Combust. Flame* 188:307–323, 2018, doi:10.1016/j.combustflame.2017.09.037.
191. Foong, T.M., Morganti, K.J., Brear, M.J., Silva, G. da, Yang, Y., and Dryer, F.L., “The octane numbers of ethanol blended with gasoline and its surrogates,” *Fuel* 115:727–739, 2014, doi:10.1016/j.fuel.2013.07.105.
192. Fan, Q., Wang, Z., Qi, Y., and Wang, Y., “Investigating auto-ignition behavior of n-heptane/iso-octane/ethanol mixtures for gasoline surrogates through rapid compression machine measurement and chemical kinetics analysis,” *Fuel* 241:1095–1108, 2019, doi:10.1016/j.fuel.2018.12.112.
193. Mehl, M., Pitz, W.J., Westbrook, C.K., and Curran, H.J., “Kinetic modeling of gasoline surrogate components and mixtures under engine conditions,” *Proc. Combust. Inst.* 33(1):193–200, 2011, doi:10.1016/j.proci.2010.05.027.
194. Li, Y., Alfazazi, A., Mohan, B., Alexandros Tingas, E., Badra, J., Im, H.G., and Mani Sarathy, S., “Development of a reduced four-component (toluene/n-heptane/iso-octane/ethanol) gasoline surrogate model,” *Fuel* 247:164–178, 2019, doi:10.1016/j.fuel.2019.03.052.
195. Yuan, H., Yang, Y., Brear, M.J., Foong, T.M., and Anderson, J.E., “Optimal octane number correlations for mixtures of toluene reference fuels (TRFs) and ethanol,” *Fuel* 188:408–417, 2017, doi:10.1016/j.fuel.2016.10.042.
196. McCormick, R.L., Ratcliff, M.A., Christensen, E., Fouts, L., Luecke, J., Chupka, G.M., Yanowitz, J., Tian, M., and Boot, M., “Properties of Oxygenates Found in Upgraded Biomass Pyrolysis Oil as Components of Spark and Compression Ignition Engine Fuels,” *Energy Fuels* 29(4):2453–2461, 2015, doi:10.1021/ef502893g.